Nonlinear diffusion in mathematical biology

Yifei Li
Msc

Submitted in fulfilment of the requirements for the degree of
Doctor of Philosophy

School of Mathematical Sciences
Faculty of Science
Queensland University of Technology

2022

Copyright in Relation to This Thesis

© Copyright 2022 by Yifei Li. All rights reserved.

Statement of Original Authorship

The work contained in this thesis has not been previously submitted to meet requirements for an award at this or any other higher education institution. To the best of my knowledge and belief, the thesis contains no material previously published or written by another person except where due reference is made.

Signature:

Date:

Abstract

Using mathematical models to study population dynamics is fundamental in ecology and biology, for example, to predict long-term survival or extinction of species and to analyse biological invasion processes. To investigate spatial effects, such as moving invasion fronts, reaction-diffusion equations are widely considered for studying population dynamics. In such models the evolution of populations is governed by the interplay between reaction and diffusion, where reaction refers to population growth mechanisms such as logistic growth or growth that includes Allee effects, and diffusion refers to population migration mechanisms. While most reaction-diffusion models consider linear diffusion, nonlinear diffusion mechanisms have increasingly received attention in population models, since they capture some phenomena more realistically, such as sharp moving fronts.

In this thesis, we explore the influence of nonlinear diffusion on population dynamics in reaction-diffusion models. The thesis comprises two main parts. First, we focus on the role of nonlinear diffusion in determining the long-term survival or extinction of bistable populations. We construct a discrete-continuum modelling framework, which connects the behaviour of individuals described in discrete models to population dynamics in continuous descriptions, so that we can explore the relationship between nonlinear diffusion and the movement mechanism of individuals. Through this framework, we also illustrate that the shape of initial spatial distributions plays an important role on the fate of bistable populations.

The second part of this thesis is devoted to the mathematical analysis of travelling waves in reaction-diffusion models with nonlinear diffusion. We consider a reaction-diffusion equation derived from the continuum limit of a discrete model proposed in Johnston et al. (2017), where the movement mechanism of individuals leads to a nonlinear diffusion term with negative values in a sub-interval of population densities, and the growth mechanism leads to a source term associated with either logistic growth or strong Allee effect. Based on using geometric singular perturbation theory, we study the existence and stability properties of both smooth travelling wave solutions, and shock-fronted travelling wave solutions.

Acknowledgments

First and foremost, I would like to express my sincere thanks to both **Professor Peter van Heijster** and **Professor Matthew Simpson**. **Professor Peter van Heijster** was my principal supervisor and is currently my external supervisor. Thank you Peter, for providing me the excellent opportunity to pursue this PhD research project under your supervision. **Professor Matthew Simpson** was my associate supervisor, and is currently my principal supervisor. Thank you, Mat. This thesis would not have existed without your supervision and support. I am grateful for both of your guidance and for all opportunities and help provided for enhancing my training for a career in research.

Second, I would like to express my sincere gratitude to my associate supervisor, **Dr Pascal Buenzli**, for his supervision, support, patience and enthusiasm.

In addition to my supervisors, I would like to thank all the co-authors of the papers involved in this thesis. I am sincerely thankful to **Dr Robert Marangell** and **Professor Martin Wechselberger** for providing technical help and insightful comments. Many thanks also go to **Dr Stuart Johnston** for his helpful comments.

I would like to acknowledge the financial support from **QUT** through a **QUT Postgraduate Research Award (QUTPRA)** and **QUT HDR Tuition Fee Sponsorship**, and travel funding provided throughout my candidature by the **School of Mathematical Sciences**.

I would also like to thank my colleagues and friends at QUT for their support, care, and advice during my PhD study. In particular, I want to thank **Dr Claudio Arancibia-Ibarra**, **Dr Paige Davis**, **Dr Wang Jin** and **Dr Alexander Browning** for their help.

Last but not the least, I am wholeheartedly grateful for my parents, **Senlin** and **Aiping**, my love **Huicui**, and all other family and friends back in China for their continual love and support. This journey would not have been possible without your love and care.

Publication List

---

1. **Li, Y.**, Johnston, S. T., Buenzli, P. R., van Heijster, P., Simpson, M.J., 2022. Extinction of bistable populations is affected by the shape of their initial spatial distribution. *Bulletin of Mathematical Biology*, 84: 21. DOI:10.1007/s11538-021-00974-5. arXiv Preprint

This publication corresponds to Chapter 2 of this thesis.

2. **Li, Y.**, Buenzli, P. R., Simpson, M. J., 2022. Interpreting how nonlinear diffusion affects the fate of bistable populations using a discrete modelling framework (submitted to *Proceedings of the Royal Society A: Mathematical, Physical and Engineering Sciences*). arXiv Preprint.

This publication corresponds to Chapter 3 of this thesis.

3. **Li, Y.**, van Heijster, P., Marangell, R., Simpson, M. J., 2020. Travelling wave solutions in a negative nonlinear diffusion–reaction model. *Journal of Mathematical Biology*, 81: 1495-1522. DOI:10.1007/s00285-020-01547-1. arXiv Preprint

This publication corresponds to Chapter 4 of this thesis.

4. **Li, Y.**, van Heijster, P., Simpson, M.J., Wechselberger, M., 2021. Shock-fronted travelling waves in a reaction–diffusion model with nonlinear forward-backward-forward diffusion. *Physica D: Nonlinear Phenomena*. 423: 132916. DOI:10.1016/j.physd.2021.132916. arXiv Preprint

This publication corresponds to Chapter 5 of this thesis.

Table of Contents

Chapter 1

Introduction

1.1 Background

Mathematical models provide a framework for exploring mechanisms that influence the evolution of populations (Murray 1989; Jin et al. 2016b; Johnston et al. 2017; Fadai et al. 2020; Chaplain et al. 2020). Both continuum and discrete models are widely used in studying population dynamics. In this section we introduce mathematical models where the evolution of populations is described by either continuum equations or discrete simulations. We pay particular attention to two questions in mathematical biology: the question of when a population will eventually survive or go extinct, and whether a population can form a travelling wave to propagate through space.

1.1.1 Ordinary differential equations and well mixed populations

A classical continuum population model is the ordinary differential equation (ODE) model,

$$\frac{\mathrm{d}C(t)}{\mathrm{d}t} = C(t)f(C(t)), \tag{1.1}$$

where $C(t) > 0$ is the population density, and $f(C)$ is the per capita growth rate of the population (Kot 2001; Edelstein-Keshet 2005; Courchamp et al. 2008). Equation (1.1) models the temporal evolution of well-mixed populations. There are some popular models based on the ODE (1.1) and choice of $f(C)$, such as the exponential growth model, the logistic growth model and the weak or strong Allee effect model (Murray 1989; Kot 2001; Courchamp et al. 2008).

- The **exponential growth** model considers a positive constant per capita growth rate, $f(C) = \lambda > 0$, see Figure 1.1(a)–(c). Although some low-density population dynamics are captured by the exponential growth model, exponential growth drives the population density to infinity (Murray 1989; Sarapata and de Pillis 2014).

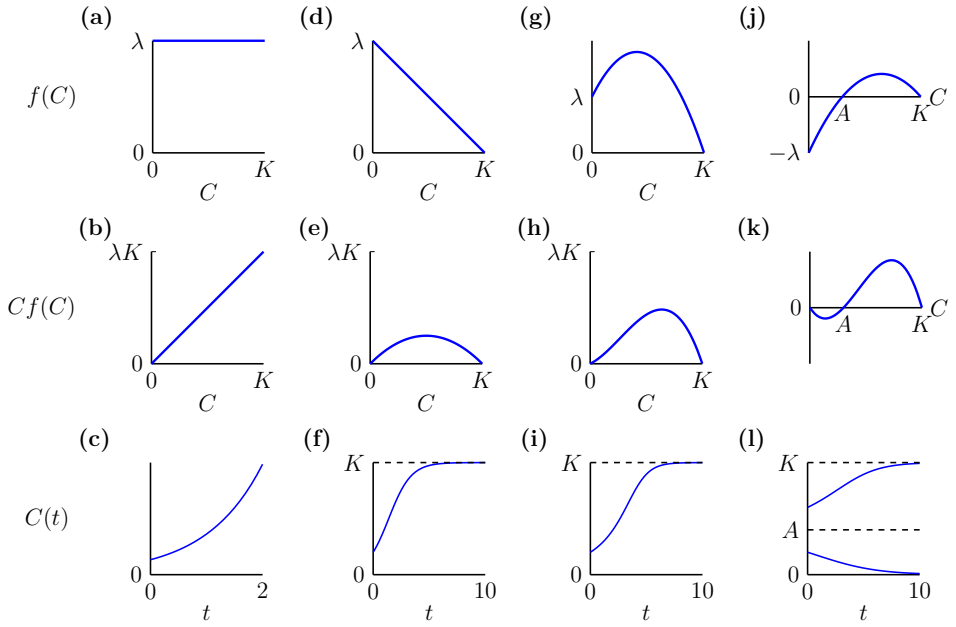

Figure 1.1: **Different mechanisms and the corresponding population dynamics.** (a)–(c) $f(C)$, $Cf(C)$ and $C(t)$ with exponential growth. (d)–(f) $f(C)$, $Cf(C)$ and $C(t)$ with logistic growth. (g)–(i) $f(C)$, $Cf(C)$ and $C(t)$ with weak Allee effect. (j)–(l) $f(C)$, $Cf(C)$ and $C(t)$ with strong Allee effect.

- The **logistic growth** model is perhaps the most widely used model in population biology. The classical logistic growth model incorporates a linearly decreasing per capita growth rate, $f(C) = \lambda(1 - C/K)$, where $\lambda > 0$ now denotes the intrinsic growth rate, and $K > 0$ is the carrying capacity density, see Figure 1.1(d)–(f). In such models population density increases to approach the carrying capacity density, K, as $t \to \infty$ (Courchamp et al. 1999; Kot 2001; Murray 1989; Sarapata and de Pillis 2014).

- In the **weak Allee effect** model, population density also approaches K as $t \to \infty$, see an example with $f(C) = \lambda(1 - C/K)(C/A + 1)$, where $0 < A < K$ is a positive constant, as shown in Figure 1.1(g)–(i). However, unlike the logistic growth model where $f(C)$ is decreasing with respect to C, $f(C)$ achieves its peak at a positive density in the weak Allee effect model (Taylor and Hastings 2005; Courchamp et al. 2008).

- Different to these models where $f(C)$ is always positive, the **strong Allee effect** model has a negative per capita growth rate at low densities (Allee and Bowen 1932; Stephens et al. 1999; Taylor and Hastings 2005; Courchamp et al. 2008). A simple example of the strong Allee effect is given by $f(C) = \lambda(1 - C/K)(C/A - 1)$, where $0 < A < K$ is now called the Allee threshold, see Figure 1.1(j)–(l).

In the classical logistic growth and weak Allee effect models, any population, no matter

how small, will always grow to reach the carrying capacity density and survive. In contrast, as population density may decrease in strong Allee effect models, populations governed by strong Allee effects will either approach the carrying capacity density and survive, or reduce to zero density and go extinct (Allee and Bowen 1932; Stephens et al. 1999; Taylor and Hastings 2005; Courchamp et al. 2008). The only factor determining the fate of populations in the strong Allee effect model is the initial density $C(0)$. That is, the population will survive if $C(0) > A$, and go extinct if $C(0) < A$, see Figure 1.1(l).

1.1.2 Reaction-diffusion equations and spatially-structured populations

To model populations with spatial structures, such as cells with moving fronts as shown in Figure 1.2, some studies consider using reaction-diffusion equations (Hadeler and Rothe 1975; Lewis and Kareiva 1993; Holmes et al. 1994; Hastings et al. 2005; Maciel and Lutscher 2015; Johnston et al. 2017; Neufeld et al. 2017; El-Hachem et al. 2019). Here we present a reaction-diffusion equation with one spatial dimension as an example,

$$\frac{\partial C(x,t)}{\partial t} = D\frac{\partial^2 C(x,t)}{\partial x^2} + C(x,t)f(C(x,t)), \tag{1.2}$$

where $D > 0$ is the constant diffusivity coefficient specifying the diffusion mechanism, and $C(x,t)f(C(x,t))$ is the source term specifying the reaction mechanism. Unlike Equation (1.1) where the survival or extinction of populations solely depends upon initial density, many factors influence the fate of populations in reaction-diffusion models, such as initial spatial distributions, boundary conditions, the size of domain and the interplay between diffusion and reaction mechanisms (Skellam 1951; Bradford and Philip 1970a,b; Lewis and Kareiva 1993; Holmes et al. 1994; Lutscher 2019). For example, when the reaction mechanism associates with strong Allee effects, populations can only survive if the initial occupied area and the initial density are sufficiently large (Lewis and Kareiva 1993). Furthermore, the spatial-temporal dynamics described by reaction-diffusion equations allow populations to form spatial structures, which are suitable for studying a variety of realistic phenomena in population biology, such as the invasion processes of cells (Mack et al. 2000; Johnston et al. 2017).

In population biology, a travelling wave solution of Equation (1.2) represents that a population travels through space with a constant speed and a constant wave shape (Allee and Bowen 1932; Maini et al. 2004a; Johnston et al. 2017). We now consider boundary conditions $C(x,t) = 1$ as $x \to -\infty$ and $C(x,t) = 0$ as $x \to \infty$. Introducing the travelling wave coordinate $z = x - vt$, where v is a constant wave speed, functions

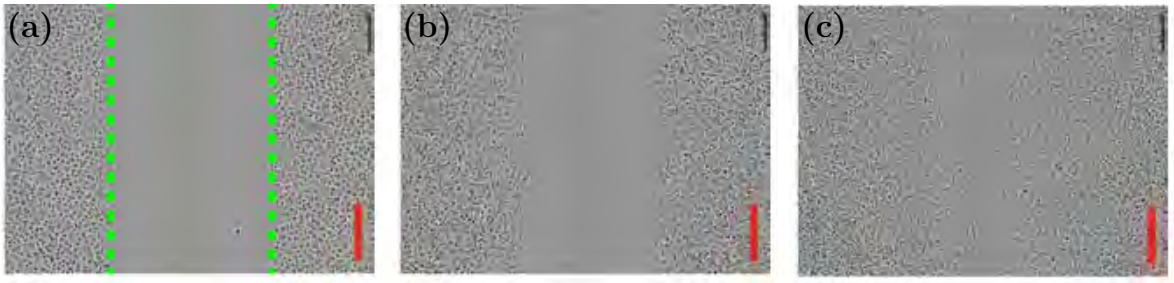

Figure 1.2: **Moving fronts of cells.** (a)–(c) Images of cells in an experiment of *in vitro* cell migration assays at $t = 0\,\text{h}$, $t = 12\,\text{h}$ and $t = 24\,\text{h}$, respectively. The scale bar corresponds to 300 µm. The dashed green lines in (a) show the approximate location of the position of leading edge. This figure is adapted from Figure 1 in Jin et al. (2016b).

$C(z,t) = C(x - vt, t)$ satisfying Equation (1.2) can be written as

$$\frac{\partial C(z,t)}{\partial t} = \frac{\partial^2 C(z,t)}{\partial z^2} + v\frac{\partial C(z,t)}{\partial z} + C(z,t)f(C(z,t)). \tag{1.3}$$

If $C(z,t) = c(z)$ is a stationary solution to (1.3), that is, $\partial C/\partial t = 0$, then it is a travelling wave solution to (1.2) satisfying

$$\frac{\mathrm{d}^2 c(z)}{\mathrm{d}z^2} + v\frac{\mathrm{d}c(z)}{\mathrm{d}z} + c(z)f(c(z)) = 0, \tag{1.4}$$

A dynamical system approach can be used to analyse (1.4) (Fife 2013). By introducing $p = \mathrm{d}c/\mathrm{d}z$, Equation (1.4) can be transformed into a system of first-order ODEs

$$\begin{cases} \dfrac{\mathrm{d}c}{\mathrm{d}z} = p, \\ \dfrac{\mathrm{d}p}{\mathrm{d}z} = -vp - cf(c). \end{cases} \tag{1.5}$$

The heteroclinic orbits on the phase plane of system (1.5), which connect the equilibrium point associated with state $c = 1$ to the equilibrium point associated with state $c = 0$, indicate the existence of travelling wave solutions to (1.2).

If we consider a logistic growth source term, Equation (1.2) becomes the well-known Fisher-KPP equation (Fisher 1937; Kolmogorov et al. 1937),

$$\frac{\partial C(x,t)}{\partial t} = D\frac{\partial^2 C(x,t)}{\partial x^2} + \lambda C(x,t)(1 - C(x,t)), \tag{1.6}$$

where we, without loss of generality, consider a carrying capacity $K = 1$. Phase plane analysis of system (1.5) indicates that there exists travelling wave solutions with positive speeds $v \geq v^*$, where $v^* = 2\sqrt{\lambda D}$ is called the *minimum wave speed*, and with a smooth front where $C(x,t) \to 0$ as $x \to \infty$ (Fife 2013). We show the smooth travelling wave solutions of the Fisher-KPP equation in Figure 1.3(a). When we change the logistic growth

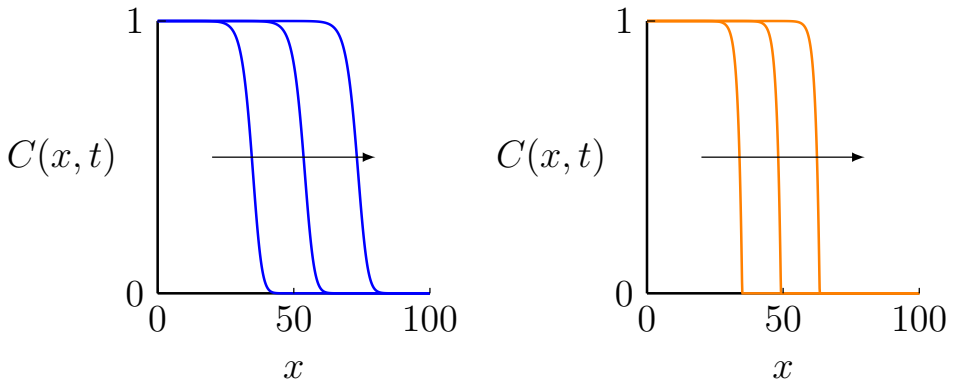

Figure 1.3: **Smooth and sharp-fronted travelling wave solutions.** We show the numerical solutions of reaction-diffusion equations using an implicit finite difference method with space step $\delta x = 0.1$ and time step $\delta t = 0.01$, considering the Heaviside initial condition $C = 1$ for $x \in [0, 20]$ and $C = 0$ elsewhere, and no-flux boundary conditions. (a) Smooth travelling wave solutions of the Fisher-KPP equation (1.6) with $D = 1$ and $f(C) = 1 - C$, at $t = 10$, $t = 20$ and $t = 30$. (b) Sharp-fronted travelling wave solutions of (1.7) with $D(C) = C$ and $f(C) = 1 - C$, at $t = 20$, $t = 40$ and $t = 60$. The black arrows show the moving direction of waves.

source term to a weak or strong Allee effect source term, there still exists travelling wave solutions in Equation (1.2). Similar to the logistic growth source term, the weak Allee effect leads to travelling wave solutions with positive speeds greater than a threshold (Hadeler and Rothe 1975). In contrast, the strong Allee effect leads to a unique wave speed which is either positive or negative (Hadeler and Rothe 1975; Fife and McLeod 1977). However, it is challenging to calculate the explicit solution of reaction-diffusion equations. For the Fisher-KPP equation, there are two currently known explicit travelling wave solutions with particular speeds Ablowitz and Zeppetella (1979); Malfliet (1992); McCue et al. (2021). Instead of explicitly solving reaction-diffusion equations, numerical techniques such as the finite difference method are used to approximate solutions in reaction-diffusion equations and provide evidence of the existence of corresponding solutions (Ames 2014; Johnston et al. 2017).

1.1.3 Nonlinear diffusion in population models

Most reaction-diffusion models in mathematical biology consider a constant diffusivity (Hadeler and Rothe 1975; Murray 1989; Holmes et al. 1994; Kot 2001; Hastings et al. 2005; Maciel and Lutscher 2015; Neufeld et al. 2017). However, reaction-diffusion equations with linear diffusion cannot describe population dynamics in some well-documented circumstances. For example, the smooth travelling wave solution in the Fisher-KPP equation cannot provide sharp wave fronts to replicate observations in cell migration assays (Maini et al. 2004a,b; Jin et al. 2016b). Therefore, reaction-diffusion equations with

nonlinear diffusion are considered in many applications (Shigesada 1980; Sengers et al. 2007; Cai et al. 2007; Martínez-García et al. 2015; Jin et al. 2016b; McCue et al. 2019; Bubba et al. 2020). For example, $D(C) = C$ is considered in cell migration assays so that the travelling wave has a sharp front that reaches 0 within a finite distance (Sengers et al. 2007; Jin et al. 2016b). In one spatial dimension, the reaction-diffusion equation is

$$\frac{\partial C(x,t)}{\partial t} = \frac{\partial}{\partial x}\left(D(C(x,t))\frac{\partial C(x,t)}{\partial x}\right) + C(x,t)f(C(x,t)), \tag{1.7}$$

where we call $D(C)$ the nonlinear diffusivity function. We show numerical results of the sharp-fronted travelling wave solutions of Equation (1.7) with $D(C) = C$ and a logistic growth source term in Figure 1.3(b). Compared to the smooth travelling wave solutions in Figure 1.3(a), the front position of population density profiles in sharp-fronted travelling waves can be intuitively defined.

1.1.4 Discrete models and continuum limits

While continuum models capture population dynamics in many situations, they cannot reflect the behaviour of individuals underlying the population dynamics. In contrast, discrete models explicitly consider each individual as an agent that can undergo events in a stochastic process. The lattice-based random walk model is a popular discrete model for describing population dynamics (Codling et al. 2008; Baker and Simpson 2010; Simpson et al. 2010a; Jin et al. 2016a; Johnston et al. 2017). In lattice-based models, individuals such as cells are represented as agents on lattice sites, and evolve in time governed by simple rules associated with agent-to-agent interactions. A basic rule is that two agents are not able to occupy the same lattice site at the same time, which leads to an exclusion process and reflects that it is impossible for cells to penetrate each other (Liggett and Liggett 1985; Simpson et al. 2010a). One agent generally only occupies one lattice site, while more lattice sites could be occupied by one agent (Turner et al. 2004; Alber et al. 2006; Lushnikov et al. 2008). The random sequential update method is used to simulate the evolution of agents in lattice-based models (Chowdhury et al. 2005). If there are $Q(t)$ agents on the lattice at time t, then during the next time step of duration τ, the algorithm selects $Q(t)$ agents, one at a time with replacement, to advance the stochastic simulation from time t to time $t + \tau$ (Simpson et al. 2010a).

The averaged population dynamics in lattice-based discrete simulations can be related to a continuous description in an appropriate continuum limit (Hughes 1995; Deroulers et al. 2009; Simpson et al. 2010a; Fernando et al. 2010; Johnston et al. 2012; Liggett 2013; Jin et al. 2016b; Johnston et al. 2017). For example, the undirected random motion of individuals leads to the heat equation in continuum limit (Liggett 2013). If the discrete

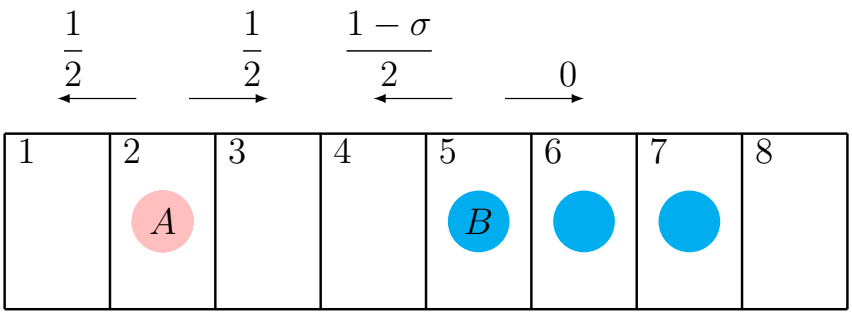

Figure 1.4: **Schematic of the movement mechanism associated with a parameter σ.** Each lattice site can be occupied by, at most, one agent. Sites are indexed by i where $i = 1, 2, ..., 6$, and have locations $x = i\Delta$. The red circle represents an isolated agent. The blue circles represent three grouped agents. The isolated agent at site 2 would step to site 1 or site 3 with probability 1/2 per computational step. The movement probability of the grouped agent at site 5 is influenced by contact effects. It would step to site 4 with probability $(1 - \sigma)/2$, where $\sigma \in [-1, 1]$ represents the contact effect, and would step to site 6 with probability 0 since the target site is occupied.

model considers a more complicated agent-to-agent interactions, the resulting continuous description may incorporate nonlinear diffusion mechanisms. For example, Johnston et al. (2012) use a parameter σ to reflect the contact effect, which represents either adhesion or repulsion between neighbouring cells in microscopic transport processes. We provide a schematic illustration of the one-dimensional lattice with spacing Δ, and the movement mechanism of agents associated with σ in Figure 1.4, where isolated and grouped agents have different movement mechanisms. The corresponding continuum limit of the discrete model described in Johnston et al. (2012) is

$$\frac{\partial C(x,t)}{\partial t} = \frac{\partial}{\partial x}\left(D(C(x,t))\frac{\partial C(x,t)}{\partial x}\right), \tag{1.8}$$

with nonlinear diffusivity function

$$D(C) = D_0\left[1 - \sigma C(4 - 3C)\right], \tag{1.9}$$

where

$$D_0 = \lim_{\Delta,\tau\to 0}\frac{\Delta^2}{2\tau}. \tag{1.10}$$

Here, $D_0 > 0$ is a constant as $\Delta \to 0$ and $\tau \to 0$ with the ratio Δ^2/τ held constant (Codling et al. 2008; Simpson et al. 2010a; Johnston et al. 2012).

Except for movement mechanisms, growth mechanisms such as the proliferation and death of individuals can also be incorporated into discrete models (Etienne et al. 2002; Cai et al. 2007; Yates et al. 2015; Johnston et al. 2017; Surendran et al. 2020; Fadai et al. 2020). In particular, Johnston et al. (2017) consider a one-dimensional lattice-based discrete model incorporating the movement, proliferation and death of isolated and grouped individuals.

The continuum limit of this discrete model is a reaction-diffusion equation with nonlinear diffusivity function

$$D(C) = D_i(1 - 4C + 3C^2) + D_g(4C - 3C^2), \tag{1.11}$$

and reaction term

$$Cf(C) = C\left[\lambda_g(1 - C) + (\lambda_i - \lambda_g - K_i + K_g)(1 - C)^2 - K_g C\right], \tag{1.12}$$

where $D_i > 0$ and $D_g > 0$ correspond to the movement probability of isolated and grouped agents, respectively; $\lambda_i > 0$ and $\lambda_g > 0$ correspond to the proliferation probability of isolated and grouped agents, respectively; $K_i > 0$ and $K_g > 0$ correspond to the death probability of isolated and grouped agents, respectively. When isolated and grouped agents have equal proliferation rates $\lambda = \lambda_i = \lambda_g$, and no agent death, $K_i = K_g = 0$, the reaction term represents a logistic kinetic

$$Cf(C) = \lambda C(1 - C). \tag{1.13}$$

If isolated and grouped agents have different proliferation rates and death rates, that is, $\lambda_i \neq \lambda_g$ and $K_i \neq K_g$, the reaction term represents a strong Allee kinetic,

$$Cf(C) = rC(1 - C)(C - A), \tag{1.14}$$

where $r = K_i - \lambda_i + \lambda_g$ and $A = 1 - \lambda_g/r$. The nonlinear diffusivity function, $D(C)$, depends on the choices of D_i and D_g. In particular, when $D_i > 4D_g$, $D(C)$ is a convex function and has a sign condition

$$D(C) > 0 \quad \text{for} \quad C \in [0, \alpha) \cup (\beta, 1], \quad D(C) < 0 \quad \text{for} \quad C \in (\alpha, \beta), \tag{1.15}$$

where the interval of negative $D(C)$ is centred around $C = 2/3$, with $1/3 < \alpha < 2/3$ and $2/3 < \beta < 1$. Interestingly, numerical solutions of the reaction-diffusion equation with such $D(C)$ and logistic kinetics provide smooth travelling wave solutions, while numerical solutions with such $D(C)$ and strong Allee kinetics provide shock-fronted travelling wave solutions, where solutions jump from one value to another (Johnston et al. 2017). Furthermore, unlike smooth travelling wave solutions which always have positive speeds, that is, solutions with wave speeds $v > 0$ in the moving frame $z = x - vt$, shock-fronted travelling wave solutions may have either positive or negative speeds. We provide a schematic illustration of smooth and shock-fronted travelling wave solutions in Figure 1.5.

Modelling population dynamics based on a discrete model that leads to a well-defined

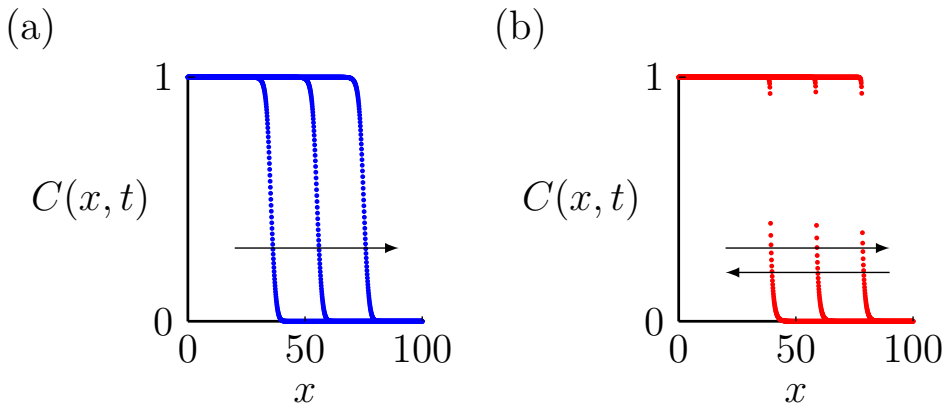

Figure 1.5: **Schematic of smooth and shock-fronted travelling wave solutions obtained by a numerical method.** We show the numerical solutions of (1.7) with $D(C) = 0.6C^2 - 0.8C + 0.25$ obtained from (1.11) with $D_i = 0.25$ and $D_g = 0.05$, using an implicit finite difference method with space step $\delta x = 0.1$ and time step $\delta t = 0.01$. We consider the Heaviside initial condition $C = 1$ for $x \in [0, 20]$ and $C = 0$ elsewhere, and no-flux boundary conditions. (a) Smooth travelling wave solutions at $t = 20$, $t = 40$ and $t = 60$, obtained with a logistic growth source term $Cf(C) = C(1 - C)$. (b) Shock-fronted travelling wave solutions at $t = 1000$, $t = 2000$ and $t = 3000$, obtained with a strong Allee effect source term $Cf(C) = C(1 - C)(C - 0.2)$, where the solution jumps from one value to another. The black arrows show the moving direction of waves. We note that the speed of shock-fronted travelling wave solutions, v, can be either positive or negative.

continuum limit provides a powerful discrete-continuum framework. The discrete model performs realistic simulations incorporating fluctuations, and intuitively reflects the behaviour of individuals which cannot be easily obtained from the continuum model. On the other hand, the continuum model precisely describes population dynamics, and does not have the additional computational overhead which may be intractable in discrete simulations. However, although some discrete models derive appropriate continuum limits associated with nonlinear diffusion mechanisms (Deroulers et al. 2009; Fernando et al. 2010; Yates et al. 2015; Chappelle and Yates 2019), constructing a framework to connect general nonlinear diffusion terms in reaction-diffusion equations to the intuitive mechanisms of individual-level behaviours described by discrete models is challenging.

1.1.5 Existence of travelling wave solutions with nonlinear diffusion

Since nonlinear diffusion plays an important role in population biology, many studies focus on the mathematical analysis of travelling wave solutions to reaction-diffusion equations with nonlinear diffusion (Malaguti and Marcelli 2003; Maini et al. 2006, 2007; Ferracuti et al. 2009; Kuzmin and Ruggerini 2011). In particular, Ferracuti et al. (2009) prove the existence of travelling wave solutions for reaction-diffusion equations with general convex $D(C)$ that changes signs twice on $C \in (0, 1)$ and logistic growth source terms, based on

the *comparison method* (Aronson and Weinberger 1978). In this case travelling waves exist if their speed is greater than a minimum wave speed (Aronson and Weinberger 1978). However, their method cannot be extended for studying the shock-fronted travelling wave solutions when the source term is associated with strong Allee effects (Johnston et al. 2017).

To study shock-fronted travelling wave solutions, perturbation theory is a good choice. Shocks associated with nonlinear diffusion but no source terms have been studied in the context of many physical phenomena, such as the movement of moisture in partially saturated porous media (DiCarlo et al. 2008) and the motion of nanofluids (Landman and White 2011). For example, we can find a shock-fronted travelling wave solution for a convection-diffusion equation of the form

$$\frac{\partial C(x,t)}{\partial t} + C(x,t)\frac{\partial C(x,t)}{\partial x} = \frac{\partial^2}{\partial x^2}\left(g(C(x,t)) - \varepsilon^2 \frac{\partial^2 C(x,t)}{\partial x^2}\right), \tag{1.16}$$

where $g(C)$ is a cubic function representing the chemical potential and $0 < \varepsilon \ll 1$ (Witelski 1995b). When the continuous description includes a reaction mechanism, properties of shock-fronted travelling wave solutions can be studied through using the geometric singular perturbation theory (GSPT) (Jones 1995; Fenichel 1979; Hek 2010; Sewalt et al. 2016) and canard theory (Szmolyan and Wechselberger 2001; Wechselberger and Pettet 2010; Wechselberger 2012). GSPT is a geometric approach dealing with problems with singular perturbations. The standard GSPT method using Fenichel's theory is based on the normal hyperbolicity of subsets of the critical manifold. However, the requirement of normal hyperbolicity in singularly perturbed systems cannot be satisfied in some contexts. In such situations, canard theory can overcome the loss of normal hyperbolicity and can be used to study the geometric structure of the perturbed systems (Fenichel 1979; Wechselberger 2012). Canards were first studied to analyse the van der Pol oscillator (Benoit 1981), and further developed to the context of GSPT (Dumortier et al. 1996). The existence of smooth or shock-fronted travelling wave solutions in coupled advection-reaction-diffusion models has been proved by using GSPT with canard theory in Wechselberger and Pettet (2010), and Wechselberger and Pettet (2010) also point the equivalent relationship between the holes in the walls (Pettet et al. 2000) obtained with phase plane analysis and specific types of canard points (Szmolyan and Wechselberger 2001).

1.1.6 Stability of travelling wave solutions

The problem of stability naturally arises after proving the existence of travelling wave solutions (Harley et al. 2015; Davis et al. 2017, 2019). The stability of a travelling wave solution predicts the long-term behaviour of the solution. If the addition of arbitrarily

small perturbations into the travelling wave solution leads the solution to eventually leave a small neighbourhood of the set of travelling wave solutions, the travelling wave solution is unstable (Sandstede 2002). The stability of a travelling wave solution indicates observation results in numerical simulations. That is, we believe numerical simulations only provide stable solutions after a long time period.

There are various approaches to study the stability of travelling waves (Volpert et al. 1994; Sandstede 2002). One widely used approach is to linearise the PDE about the travelling wave solution with small perturbations $q(z,t)$, and to study the resulting linear operator $\mathcal{L}$. The spectrum of $\mathcal{L}$ provides useful information for the stability of travelling wave solutions. If the spectrum of $\mathcal{L}$ is contained in the open left half plane, or the origin, the travelling wave solution is spectrally stable. The spectrum of a linear operator naturally breaks up into two sets: the point spectrum and the essential spectrum (Sandstede 2002; Kapitula and Promislow 2013). The point spectrum is the set of isolated eigenvalues with finite multiplicity. It deals with the stability of the actual wave front. The essential spectrum is the complement of the point spectrum. It deals with instabilities at infinity and it is related to the spectrum of the background linear operator $\mathcal{L}$ as $z \to \pm\infty$.

1.2 Research questions

This thesis explores and answers the following questions:

1. **What is the role of initial shape of spatial distributions on the fate of bistable populations?**

   The strong Allee effect model reflecting bistable population dynamics, where a population will end in either survival or extinction, is often considered to model situations where the potential for population extinction is thought to be important (Saltz and Rubenstein 1995; Taylor and Hastings 2005; Courchamp et al. 2008; Fadai et al. 2020). Unlike the classical ordinary differential equation models, where the fate of populations solely depends upon whether the initial density is above or below the Allee threshold, many factors influence population extinction in reaction-diffusion models such as initial spatial distributions and boundary conditions (Bradford and Philip 1970a,b; Lewis and Kareiva 1993; Soboleva et al. 2003; Lewis et al. 2016).

   Formal asymptotic analysis of the reaction-diffusion equation, which incorporates linear diffusion and the strong Allee effects, reveals that the area of the initial population distribution has to exceed a threshold, so that the population avoids extinction (Lewis and Kareiva 1993). However, Lewis and Kareiva (1993) only consider a radially symmetric initial distribution on a two-dimensional domain. An interesting question is whether other shapes of spatial distributions lead to different long-term outcomes. Both discrete and continuous models allow us to explore whether

the population will survive or go extinct with different initial distributions, while this requires us to construct the discrete model with a well-defined continuum limit, and carefully consider the interactive effects of shapes and other initial conditions.

2. **How does nonlinear diffusion affect the fate of bistable populations?**

   Predicting whether a population will survive or become extinct is a key question in population biology (Berger 1990; Cantrell and Cosner 1998; Axelrod et al. 2006; Ovaskainen and Meerson 2010; Kéfi et al. 2011). In reaction-diffusion models, population dynamics are governed by the interplay between diffusion and reaction mechanisms. It is known that nonlinear diffusion can impact the conditions of the reaction-diffusion model leading to population extinction (Lee et al. 2006). This brings the interest of exploring the relationship between nonlinear diffusion and the fate of bistable populations. For a given nonlinear diffusivity function, whether it encourages or suppresses population extinction relative to the classical linear diffusion model is an interesting question. To physically interpret the role of nonlinear diffusion on bistable population dynamics, we consider a discrete-continuum modelling framework, which can connect the behaviour of individuals to the population dynamics in reaction-diffusion equations. Through such a framework, we are able to gain insight into how the complicated interplay between diffusion and reaction mechanisms associated with individual-level behaviours affects the fate of bistable populations.

3. **What are the existence and stability properties of smooth travelling wave solutions with nonlinear diffusion and logistic growth source terms?**

   Travelling wave solutions of reaction-diffusion equations are useful in studying population dynamics in invasion processes, where individuals migrate to new areas in which they persist, proliferate, and spread (Murray 1989; Mack et al. 2000; Taylor and Hastings 2005). For example, the travelling wave solutions of the famous Fisher-KPP equation describe that a population will spread through space with a fixed shape and a constant speed depending on the initial population distribution (Fisher 1937; Kolmogorov et al. 1937; Murray 1989). However, when the reaction-diffusion model incorporates a nonlinear diffusion mechanism, such as a nonlinear diffusivity function that changes signs, studying the existence and stability properties of travelling wave solutions becomes challenging (Malaguti and Marcelli 2003; Maini et al. 2006; Ferracuti et al. 2009).

   Through deriving reaction-diffusion equations from the continuum limit of a discrete model, Johnston et al. (2017) incorporate information about individual-level behaviours including movement, proliferation and death into the continuum model. When the migration rate of isolated individuals is much larger than the migration

rate of grouped individuals, the nonlinear diffusivity function changes sign twice in the domain of our interest. Considering reaction-diffusion equations with such nonlinear diffusivity functions and logistic growth kinetics, we aim to prove the existence of smooth travelling wave solutions by using a geometric approach, and investigate the relationship between the wave speed and the spectral stability of the travelling wave solutions.

4. **Do shock-fronted travelling wave solutions exist with nonlinear diffusion and strong Allee effect source terms?**

   With a nonlinear diffusivity function changing signs twice, the reaction-diffusion equation incorporating logistic growth kinetics exits smooth travelling wave solutions with positive speeds (Li et al. 2020). However, when we consider a strong Allee effect source term, numerical observations suggest the existence of shock-fronted travelling wave solutions (Johnston et al. 2017). Furthermore, the speed of shock-fronted travelling wave solutions can be either positive or negative.

   Geometric approaches, such as the geometric singular perturbation theory (GSPT), have been used to study shock-fronted travelling wave solutions (Harley et al. 2014a; Sewalt et al. 2016). To apply GSPT, the shock-fronted travelling waves are smoothed out by regularising the reaction-diffusion equation with a smaller higher order perturbation term. We aim to consider two typical forms of perturbation terms (Pego and Penrose 1989; Padrón 2004), and apply GSPT to analyse the shock-fronted travelling waves in reaction-diffusion equations with nonlinear diffusivity functions changing signs twice and strong Allee effect source terms.

1.3 Structure of the thesis

This thesis comprises two main parts. Chapters 2 and 3 explore the factors that affect the survival or extinction of bistable populations. Chapters 4 and 5 focus on the mathematical analysis of travelling waves in population models. Since the thesis is presented as a thesis by published papers, main chapters (Chapters 2, 3, 4 and 5) are comprised of publications. This thesis consists of the four following publications:

1. **Li, Y.**, Johnston, S. T., Buenzli, P. R., van Heijster, P., Simpson, M.J., 2022. Extinction of bistable populations is affected by the shape of their initial spatial distribution. *Bulletin of Mathematical Biology*, 84: 21. DOI:10.1007/s11538-021-00974-5. arXiv Preprint.

2. **Li, Y.**, Buenzli, P. R., Simpson, M. J., 2022. Interpreting how nonlinear diffusion affects the fate of bistable populations using a discrete modelling framework (submitted to *Proceedings of the Royal Society A: Mathematical, Physical and Engineering*

Sciences). arXiv Preprint.

3. **Li, Y.**, van Heijster, P., Marangell, R., Simpson, M. J., 2020. Travelling wave solutions in a negative nonlinear diffusion–reaction model. *Journal of Mathematical Biology*, 81: 1495-1522. DOI:10.1007/s00285-020-01547-1. arXiv Preprint.

4. **Li, Y.**, van Heijster, P., Simpson, M.J., Wechselberger, M., 2021. Shock-fronted travelling waves in a reaction–diffusion model with nonlinear forward-backward-forward diffusion. *Physica D: Nonlinear Phenomena*. 423: 132916. DOI:10.1016/j.physd.2021.132916. arXiv Preprint.

To make the style and layout consistent, minor changes have been made to each of the papers, such as Table 2.1, while most of the content in these chapters are exactly the same as the original papers that have been either published or submitted. Since all main chapters are independent publications, some overlapped contents appear in the background information of these different chapters. The Chapter 2.9, 3.9 and 5.7 correspond to the supplementary materials associated with the respective publications. The PhD candidate has contributed significantly and is the primary author of all the four papers. The work presented in this thesis fulfils the requirements for the award of thesis by published papers at Queensland University of Technology.

Chapter 1 constitutes the introduction for the thesis. This chapter introduces the relevant background information of mathematical modelling in population biology and ecology. The major research questions of the thesis are then stated. The details about the contribution of the candidate and all co-authors to each of the publication are described in Section 1.4.

Chapter 2 addresses the first question described in Section 1.2. Chapter 2 contains publication 1, where we construct a new discrete-continuum modelling framework and study the role of initial shape on the fate of bistable populations. This chapter also contains additional information such as the simulation algorithm and more detailed derivations associated with publication 1.

Chapter 3 addresses the second question described in Section 1.2. Chapter 3 contains publication 2, where we interpret the role of nonlinear diffusion on the fate of bistable populations. This chapter also contains additional results associated with publication 2.

Chapter 4 addresses the third question described in Section 1.2. Chapter 4 contains publication 3, where we study the existence and stability properties of travelling wave solutions of a reaction-diffusion equation with nonlinear diffusion and logistic growth kinetics.

Chapter 5 addresses the fourth question described in Section 1.2. Chapter 5 contains publication 4, where we study the properties of shock-fronted travelling wave solutions of

the reaction-diffusion equation with nonlinear diffusion and strong Allee kinetics. This chapter also contains additional results associated with publication 4.

Chapter 6 outlines a summary of the research findings from this thesis, and discusses possible future work based on the results achieved and the limitations of our work.

1.4 Statement of joint authorship

In this section we summarise the contributions of the PhD candidate and the co-authors to each publication. All co-authors have agreed to the presentation of these publications in this thesis.

1.4.1 Chapter 2: The role of initial shape of spatial distributions on the fate of bistable populations

The associated publication for this chapter is:

Li, Y., Johnston, S. T., Buenzli, P. R., van Heijster, P., Simpson, M.J., 2022. Extinction of bistable populations is affected by the shape of their initial spatial distribution. *Bulletin of Mathematical Biology*, 84: 21. DOI:10.1007/s11538-021-00974-5. arXiv Preprint

The work was divided as follows:

- **Li, Y. (Candidate)** designed the study, derived the continuum limit equations, developed the codes for numerical simulations, performed numerical simulations, generated results, composed all figures and supplementary material, interpreted the results, drafted the manuscript, and critically reviewed and revised the manuscript.
- Johnston, S. T. designed the study, provided technical assistance, helped interpret the results, critically reviewed and revised the manuscript and supplementary material.
- Buenzli, P. R. designed the study, helped interpret the results, oversaw drafting and redrafting of the manuscript, critically reviewed and revised the manuscript and supplementary material.
- van Heijster, P. provided technical assistance, critically reviewed and revised the manuscript and supplementary material.
- Simpson, M.J. initiated the concept for this paper, designed the study, supervised the research, helped interpret the results, oversaw drafting and redrafting of the manuscript, critically reviewed and revised the manuscript and supplementary material, and acted as the corresponding author.

1.4.2 Chapter 3: The role of nonlinear diffusion on the fate of bistable populations

The associated publication for this chapter is:

Li, Y., Buenzli, P. R., Simpson, M. J., 2022. Interpreting how nonlinear diffusion affects the fate of bistable populations using a discrete modelling framework (submitted to *Proceedings of the Royal Society A: Mathematical, Physical and Engineering Sciences*). arXiv Preprint

The work was divided as follows:

- **Li, Y. (Candidate)** designed the study, derived the continuum limit equations, developed the codes for numerical simulations, performed numerical simulations, generated results, composed all figures and supplementary material, interpreted the results, drafted the manuscript, and critically reviewed and revised the manuscript.
- Buenzli, P. R. designed the study, helped interpret the results, oversaw drafting and redrafting of the manuscript, critically reviewed and revised the manuscript and supplementary material.
- Simpson, M.J. initiated the concept for this paper, designed the study, supervised the research, helped interpret the results, oversaw drafting and redrafting of the manuscript, critically reviewed and revised the manuscript and supplementary material, and acted as the corresponding author.

1.4.3 Chapter 4: Smooth travelling waves in reaction-diffusion equations with nonlinear diffusion and logistic growth source terms

The associated publication for this chapter is:

Li, Y., van Heijster, P., Marangell, R., Simpson, M. J., 2020. Travelling wave solutions in a negative nonlinear diffusion–reaction model. *Journal of Mathematical Biology*, 81: 1495-1522. DOI:10.1007/s00285-020-01547-1. arXiv Preprint

The work was divided as follows:

- **Li, Y. (Candidate)** designed the study, derived the continuum limit equations, developed the codes for calculating numerical solutions, performed numerical simulations, generated results, composed all figures and supplementary material, interpreted the results, drafted the manuscript, and critically reviewed and revised the manuscript.

- van Heijster, P. initiated the concept for this paper, designed the study, supervised the research, helped interpret the results, contributed to the writing of the manuscript, oversaw drafting and redrafting of the manuscript, critically reviewed and revised the manuscript and supplementary material, and acted as the corresponding author.
- Marangell, R. provided technical assistance, contributed to the writing of the manuscript, critically reviewed and revised the manuscript.
- Simpson, M. J. provided technical assistance, oversaw drafting and redrafting of the manuscript, critically reviewed and revised the manuscript and supplementary material.

1.4.4 Chapter 5: Shock-fronted travelling waves in reaction-diffusion equations with nonlinear diffusion and strong Allee effect source terms

The associated publication for this chapter is:

Li, Y., van Heijster, P., Simpson, M.J., Wechselberger, M., 2021. Shock-fronted travelling waves in a reaction–diffusion model with nonlinear forward-backward-forward diffusion. *Physica D: Nonlinear Phenomena.* 423: 132916. DOI:10.1016/j.physd.2021.132916. arXiv Preprint

The work was divided as follows:

- **Li, Y. (Candidate)** designed the study, developed the codes for calculating numerical solutions, performed numerical simulations, generated results, composed all figures and supplementary material, interpreted the results, drafted the manuscript, and critically reviewed and revised the manuscript.
- van Heijster, P. initiated the concept for this paper, supervised the research, provided technical assistance, supervised the research, contributed to the writing of the manuscript, oversaw drafting and redrafting of the manuscript, critically reviewed and revised the manuscript and supplementary material, and acted as the corresponding author.
- Simpson, M. J. provided technical assistance, oversaw drafting and redrafting of the manuscript, critically reviewed and revised the manuscript and supplementary material.
- Wechselberger, M. provided technical assistance, critically reviewed and revised the manuscript.

Chapter 2

The role of initial shape of spatial distributions on the fate of bistable populations

---

2.1 Preamble

This chapter is a paper published in the *Bulletin of Mathematical Biology*

Li, Y., Johnston, S. T., Buenzli, P. R., van Heijster, P., Simpson, M.J., 2022. Extinction of bistable populations is affected by the shape of their initial spatial distribution. *Bulletin of Mathematical Biology*, 84: 21. DOI:10.1007/s11538-021-00974-5. arXiv Preprint

In this chapter, we address the research question 1 of the thesis: What is the role of initial shape of spatial distributions on the fate of bistable populations? We start by considering a lattice-based discrete model incorporating crowding effects into the movement, proliferation and death of individuals, where the continuum limit is a reaction-diffusion equation. We explore whether solutions of the continuum model accurately capture the appropriately averaged data from discrete simulations. Considering bistable population dynamics influenced by the strong Allee effect and linear diffusion, we systematically explore the fate of populations by varying the shape of spatial population distributions and the ratio of movement and proliferation/death rates. Note that the framework constructed here acts as a reference framework for further studies in the next chapter, where extensions are made by incorporating more complicated movement mechanisms of individuals associated with nonlinear diffusion.

2.2 Abstract

The question of whether biological populations survive or are eventually driven to extinction has long been examined using mathematical models. In this work we study population survival or extinction using a stochastic, discrete lattice-based random walk model where individuals undergo movement, birth and death events. The discrete model is defined on a two-dimensional hexagonal lattice with periodic boundary conditions. A key feature of the discrete model is that crowding effects are introduced by specifying two different crowding functions that govern how local agent density influences movement events and birth/death events. The continuum limit description of the discrete model is a nonlinear reaction-diffusion equation, and we focus on crowding functions that lead to linear diffusion and a bistable source term that is often associated with the strong Allee effect. Using both the discrete and continuum modelling tools we explore the complicated relationship between the long-term survival or extinction of the population and the initial spatial arrangement of the population. In particular, we study different spatial arrangements of initial distributions: (i) a well-mixed initial distribution where the initial density is independent of position in the domain; (ii) a vertical strip initial distribution where the initial density is independent of vertical position in the domain; and, (iii) several forms of two-dimensional initial distributions where the initial population is distributed in regions with different shapes. Our results indicate that the shape of the initial spatial distribution of the population affects extinction of bistable populations. All software required to solve the discrete and continuum models used in this work are available on GitHub.

2.3 Introduction

The classical logistic growth model is widely adopted in mathematical biology and mathematical ecology (Kot 2001; Murray 1989; Edelstein-Keshet 2005). In the logistic model, small initial population densities increase over time to approach a maximum carrying-capacity density (Maini et al. 2004a,b). An implicit assumption in using the logistic growth model is that any population, no matter how small, will always grow and survive. This limitation also applies to models based on the weak Allee effect, which incorporates a reduced per-capita growth rate relative to the logistic model when the density is small (Taylor and Hastings 2005). To address this limitation, more complicated models have been developed, including models based on the strong Allee effect (Allee and Bowen 1932; Lewis and Kareiva 1993; Stephens et al. 1999; Courchamp et al. 1999; Taylor and Hastings 2005; Courchamp et al. 2008; Arroyo-Esquivel and Hastings 2020). In the strong Allee effect model, initial densities greater than a threshold, called the *Allee threshold*, grow to eventually reach the carrying capacity, whereas initial densities less than the Allee threshold eventually go extinct (Allee and Bowen 1932; Courchamp et al. 1999;

Taylor and Hastings 2005; Courchamp et al. 2008; Fadai and Simpson 2020b). This kind of population dynamics, also referred to as *bistable* population dynamics (Kot 2001), is often adopted to model situations where the potential for population extinction is thought to be important (Saltz and Rubenstein 1995; Courchamp et al. 1999; Drake 2004; Böttger et al. 2015; Vortkamp et al. 2020). Bistable population dynamics are often studied using mathematical models that take the form of an ordinary differential equation (ODE). In this case, the eventual extinction or survival of the population is dictated solely by whether the initial density is greater than, or less than, the Allee threshold density. Such ODE models assume that the population is well-mixed, and hence neglect spatial effects. Spatial effects, such as moving invasion fronts, can be incorporated by considering partial differential equation (PDE) models where the density of individuals depends explicitly upon position and time (Lewis and Kareiva 1993; Holmes et al. 1994; Hastings et al. 2005). A common PDE framework is to consider a reaction-diffusion equation (RDE) with a cubic bistable source term (Neufeld et al. 2017; Johnston et al. 2017).

When spatial effects are taken into consideration, even the logistic model with linear diffusion may not always lead to the survival of populations. For example, for a population on a finite domain with homogeneous Dirichlet boundary conditions, the population will go extinct when reproduction cannot balance the loss through boundaries (Skellam 1951; Grindrod 1991). The size of the domain must exceed a critical value, called the *critical patch size*, so that a population persists (Holmes et al. 1994; Lutscher 2019). Similar results also hold for diffusing bistable populations, where loss through the boundaries is not the only mechanism of interest since the source term can become negative (Bradford and Philip 1970a,b). For a population governed by the strong Allee effect, enough individuals must aggregate together so that the population can reproduce and balance the loss due to the death of individuals. This motivates the concept of the *critical initial area* (also known as critical aggregation or critical initial radius) which indicates that the initial population can only survive if the initial occupied area and the initial density are sufficiently large (Lewis and Kareiva 1993; Soboleva et al. 2003; Lewis et al. 2016). See Table 2.1 for a brief review of relevant models and known results.

Current RDE models of bistable populations on two-dimensional domains often consider an infinite domain and a radially symmetric initial distribution (Lewis and Kareiva 1993; Petrovskii and Shigesada 2001). In particular, Lewis and Kareiva (1993) use formal asymptotics to derive expressions for the critical initial area for a radially distributed bistable population with linear diffusion, and their results are valid in the limit that the time scale of reproduction is much faster than the time scale of migration. In contrast, here we develop a mathematical modelling framework for studying bistable population dynamics on two-dimensional domains with periodic boundary conditions. Using this framework we extend the previous results by showing that bistable populations with the

References	Model	Coordinate	Domain	Boundary conditions	Initial conditions	Properties
Bradford and Philip (1970a)	$\frac{\partial C(x,t)}{\partial t} = \frac{\partial^2 C(x,t)}{\partial x^2} + f(C(x,t))$, where f is a general bistable form.	One-dimensional Cartesian	$0 \leq x < L$ where $L < \infty$ or $L \to \infty$	• Homogeneous Neumann at $x = 0$ • Homogeneous or inhomogeneous Dirichlet at $x = L$	• No initial conditions for the steady-state solution $C(x)$. • Perturbed steady-state solutions for stability analysis.	• There exist stable steady-state solutions, which represent population survival, if L and $C(0)$ are greater than the thresholds.
Bradford and Philip (1970b)	$\frac{\partial C(r,t)}{\partial t} = \frac{1}{r}\frac{\partial}{\partial r}\left(r\frac{\partial C(r,t)}{\partial r}\right) + f(C(r,t))$, where f is a general bistable form.	Two-dimensional, radially symmetric	$0 \leq r < R$ where $R < \infty$ or $R \to \infty$	• Homogeneous Neumann at $r = 0$ • Homogeneous or inhomogeneous Dirichlet at $r = R$	• No initial conditions for the steady-state solution $C(r)$. • Perturbed steady-state solutions for stability analysis.	• There exist stable steady-state solutions, which represent population survival, if L and $C(0)$ are greater than the thresholds. • The threshold of $C(0)$ is significantly greater than it in Bradford and Philip (1970a).

Table 2.1: The comparison of models studying the critical initial area or critical patch size (Bradford and Philip 1970a,b) and our model. All models include the strong Allee effect, while Etienne et al. (2002) further considers a competition mechanism.

References	Model	Coordinate	Domain	Boundary conditions	Initial conditions	Properties
Lewis and Kareiva (1993)	$\frac{\partial C(x,y,t)}{\partial t} = D\nabla^2 C(x,y,t) + kC(1-C)(C-A)$	Two-dimensional Cartesian	$\mathbb{R}^2$	• Homogeneous Neumann	• $C = 1$ in a square region and $C = 0$ elsewhere.	• Numerical simulations indicate that the initial distribution converges to a travelling wave solution.
				• Homogeneous Dirichlet	• $C = 1$ in a circular region with radius r^*, and $C = 0$ elsewhere.	• There exists a threshold $r_{\min}$ determined by D, k and A. If $r^* > r_{\min}$, the initial distribution forms a radially expanding wave which leads to population survival; if $r^* < r_{\min}$, the initial distribution forms a radially shrinking wave which leads to population extinction.
Soboleva et al. (2003)	$\frac{\partial C(x,y,t)}{\partial t} = D\nabla^2 C(x,y,t) + f(C(x,y,t))$, where f is cubic and bistable with $f(0) = f(1) = 0$.	Two-dimensional Cartesian	$\mathbb{R}^2$	• Homogeneous Dirichlet	• Perturbed radially symmetric unstable steady-state solutions. • Perturbed radially asymmetric unstable steady-state solutions.	• The unstable steady-state solution provides threshold initial distribution where populations above the threshold distribution will survive and populations below the threshold distribution will go extinct. • The symmetric one-dimensional threshold distribution has a smaller maximum density relative to the radially symmetric two-dimensional threshold distribution.

Table 2.1 Continued.

References	Model	Coordinate	Domain	Boundary conditions	Initial conditions	Properties
Kot et al. (1996)	Integrodifference equation (discrete time n, continuous space x): $C^{n+1}(x) = \int_{-\infty}^{\infty} k(x-\hat{x}) f[C^n(\hat{x})] \mathrm{d}\hat{x}$, where $f = 0$ if $0 < C^n < C_\mathrm{A}$ and $f = K$ if $C_\mathrm{A} < C^n < K$.	One-dimensional Cartesian	$-\infty < x < \infty$	• Homogeneous Dirichlet	• $C = B$ for $-l^* < x < l^*$ and $C = 0$ elsewhere.	• The initial distribution will form an expanding travelling wave front, which leads to population survival, if $B > C_\mathrm{A}$ and if l^* is greater than a threshold.
Etienne et al. (2002)	Integrodifference equation (discrete time n, continuous space x, y): $L^{n+1}(x,y) = g(R) \iint_\Omega k(x-\hat{x}, y-\hat{y}) A^n(\hat{x},\hat{y}) \mathrm{d}\hat{x}\mathrm{d}\hat{y}$, where $A^n = 0$ if $L^n < L_\mathrm{min}$ or $L^n > L_\mathrm{max}$ and $A^n = L^n/2$ elsewhere. Here, L^n is the larval population in generation n, A^n is the female adult population in generation n and $g(R)$ represents the resource availability.	Two-dimensional Cartesian	$[0, L] \times [0, L]$	• Periodic • Homogeneous Neumann • Homogeneous Dirichlet	• $C = B$ in the whole domain. • $C = B$ in different-sized central square regions and $C = 0$ elsewhere.	• Numerical simulations indicate that the initial distribution and density of individuals, resource availability and heterogeneity influence the fate of populations.
Li et al. (2021) (this paper)	Discrete model with the continuum limit: $\frac{\partial C(x,y,t)}{\partial t} = D\nabla^2 C(x,y,t) + kC(1-C)(C-A)$	Two-dimensional Cartesian	$[0, L] \times [0, L]$	• Periodic	• $C = B$ in the whole domain. • $C = B$ in regions with different shapes and $C = 0$ elsewhere.	• Both discrete and numerical simulations indicate that initial shapes affect the fate of populations. The key feature of these shapes is their dimensionality.

Table 2.1 Continued.

same initial area can either lead to survival or extinction depending upon the initial shape of the population distribution.

Our modelling framework is based on a two-dimensional stochastic discrete random walk model on a hexagonal lattice (Jin et al. 2016a; Fadai et al. 2020). The discrete model is an exclusion process, so that each lattice site can be occupied by no more than one agent. Individuals in the model undergo a birth-death process that is modulated by localised crowding effects (Jin et al. 2016a; Johnston et al. 2017). The continuum limit of the discrete model leads to a two-dimensional RDE with a bistable source term. This framework allows us to explore discrete simulations together with solutions of the RDE. This approach is convenient because the discrete model is more realistic in the sense that it incorporates fluctuations, but this benefit incurs additional computational overhead (West et al. 2016; Macfarlane et al. 2018; Chaplain et al. 2020). Moreover, the discrete framework provides additional information such as the age structure and individual trajectories which cannot be easily obtained using a continuum approach. In contrast, the continuum RDE model can be solved numerically very efficiently, but the continuum approach is only accurate if the time scale of migration is small compared to the time scale of proliferation (Simpson et al. 2010a). Moreover, the continuum RDE model does not provide any information about the role of stochasticity (West et al. 2016; Macfarlane et al. 2018; Chaplain et al. 2020). So, to take advantages of both approaches, we use both a stochastic model and the continuum limit description.

In all cases we study population dynamics on a square domain of side length L, with periodic boundary conditions along all boundaries. We explore the role of the initial population distribution by considering different initial spatial arrangements of agents. We first distribute agents uniformly across the entire domain as shown in Figure 2.1(a), which leads to a well-mixed population. For the vertical strip initial distribution we distribute agents uniformly within a column of width w_1 as shown in Figure 2.1(b), which may represent a population of individuals along a one-dimensional river environment (Lutscher et al. 2010). For the initial distributions restricted in both spatial dimensions, we first consider a simple shape and distribute agents uniformly within a square region of area $w_1 \times w_1$ as shown in Figure 2.1(c), which may represent a population of cells in a scratch assay (Treloar et al. 2014). We further consider several other initial spatial arrangements of agents, see Figures 2.6–2.8.

This work is organised as follows. In Section 2.4 we describe the discrete individual-based model, paying particular attention to incorporating realistic movement and growth mechanisms. For simplicity, we use the generic term *growth* to refer to the birth/death process in the discrete model. The reason why we make a distinction between birth and death will become clear when we describe the modelling framework. In Section 2.5 we explain how to analyse the discrete model using a mean-field assumption to

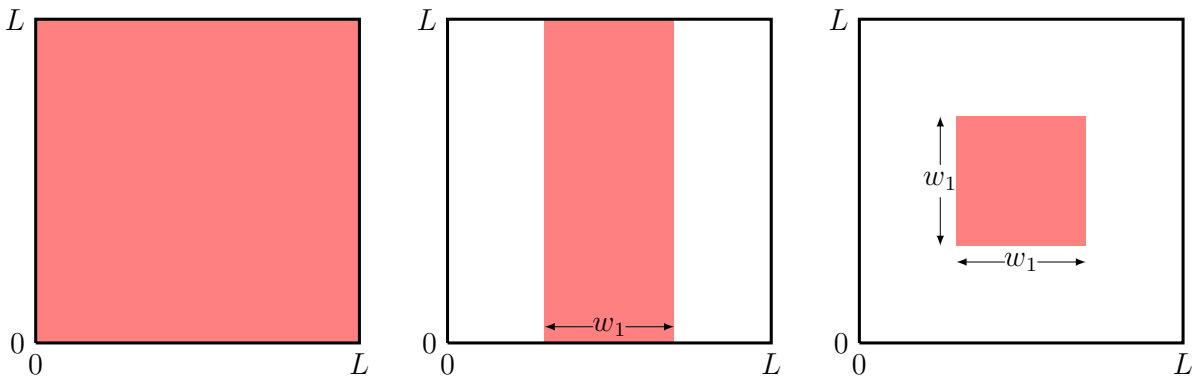

(a) well-mixed **(b)** vertical strip **(c)** square

Figure 2.1: **Initial spatial distributions of the population with different shapes on an $L \times L$ square domain.** In (a), individuals are distributed uniformly across the entire $L \times L$ domain. In (b), individuals are distributed uniformly in a vertical strip of width w_1 and height L. In (c), individuals are distributed uniformly in the central square region of length and width w_1.

arrive at an approximate continuum limit description in terms of a classical RDE. Our discrete-continuous framework incorporates crowding functions into both movement and birth/death mechanisms, which extends the previous work that only considers a crowding function in birth/death mechanisms (Jin et al. 2016a). Moreover, our model is very flexible since it describes a wide range of movement and birth/death mechanisms influenced by crowding effects. Results in Section 2.6 show how both the discrete and continuum models compare. In Section 2.7, we systematically explore how population survival or extinction depends upon the shape of the initial distribution. All software required to solve the discrete and continuum models used in this work are available on GitHub.

2.4 Discrete model

We consider a lattice-based discrete model describing movement, birth and death events in a population of individuals on a hexagonal lattice, with lattice spacing $\Delta > 0$. Each lattice site is indexed by (i, j), and has a unique Cartesian coordinate,

$$(x, y) = \begin{cases} \left(i\Delta, j\dfrac{\Delta\sqrt{3}}{2} \right), & \text{if } j \text{ is even,} \\ \left(\left(i + \dfrac{1}{2} \right) \Delta, j\dfrac{\Delta\sqrt{3}}{2} \right), & \text{if } j \text{ is odd.} \end{cases} \tag{2.1}$$

In any single realisation of the stochastic model, a lattice site $\mathbf{s}$ is either occupied, $C_{\mathbf{s}} = 1$, or vacant, $C_{\mathbf{s}} = 0$. If there are $Q(t)$ agents on the lattice at time t, we advance the stochastic simulation from time t to time $t + \tau$ by randomly selecting $Q(t)$ agents, one at a time, with replacement, so that any particular agent may be selected more than once, and

allowing those agents to *attempt* to move. Once the $Q(t)$ potential movement events have been assessed, we then select $Q(t)$ agents at random, one at a time, with replacement, to *attempt* to undergo a growth event, which could be either a birth or death event depending upon the local crowding conditions. Although altering the order of these events leads to different outcomes in particular discrete simulations, these differences are not important when we consider averaged data from many identically-prepared realisations of the model (Simpson et al. 2009a,b).

We now explain some features of the discrete model in terms of the schematic in Figure 2.2. In this initial description of the discrete model we consider nearest-neighbour movement and growth events only, and we will relax this assumption later. Figure 2.2(a) shows a potential movement event for an agent at site $\mathbf{s}$, where all nearest-neighbour sites are vacant. In this case, the probability of attempting to move during the next time step of duration τ, is $M \in [0, 1]$, and the attempted motility event will be successful with probability $\widehat{M} \leq M$. Here we note that the two probabilities, M and $\widehat{M}$ are, in general, different. This difference is a result of the local crowding effects. The special case in Figure 2.2(a) where the agent at site $\mathbf{s}$ is uncrowded we have $\widehat{M} = M$. If the attempted motility event is successful, the agent at site s moves to a randomly-chosen vacant site chosen among the set of vacant nearest-neighbour sites. In this case, as all six neighbour sites are vacant, the probability of moving to the target site, highlighted with a green circle, is $\widehat{M}/6$.

In Figure 2.2(b) we show a potential growth event for an agent at site $\mathbf{s}$, where again all nearest-neighbour sites are vacant. Here, the probability of attempting to grow in the next time step of duration τ is $P \in [0, 1]$, and the attempted growth event is successful with probability $\widehat{P} \leq P$. Again, the difference between P and $\widehat{P}$ is caused by local crowding effects, and since this agent is uncrowded we have $\widehat{P} = P$. If the attempted growth event is successful, there are two possible outcomes. First, the growth event is a birth event. In this case a daughter agent is placed at a randomly-chosen vacant site within the set of nearest-neighbour sites with probability $\widehat{P}$. As there are six vacant neighbour sites, the probability of placing a daughter agent at the target site, highlighted in green, is $\widehat{P}/6$. Second, the growth event is a death event, and the agent is removed from the lattice, with probability $\widehat{P}$. The distinction between the birth and death events is governed by the sign of the *growth crowding function*, F, which will be explained later.

To illustrate how crowding effects are incorporated into the movement component of the model, we now consider the schematic in Figure 2.2(c), where the agent at site $\mathbf{s}$ is surrounded by two agents, highlighted in purple. The probability of attempting to move is $M \in [0, 1]$, and the attempted movement event is successful with probability $\widehat{M} = MG(K_{\mathbf{s}}^{(\mathrm{m})})$. Here, $K_{\mathbf{s}}^{(\mathrm{m})}$ is a measure of the local density of site $\mathbf{s}$, and $G(K_{\mathbf{s}}^{(\mathrm{m})}) \in [0, 1]$ is the *movement crowding function* that specifies how the local density influences the

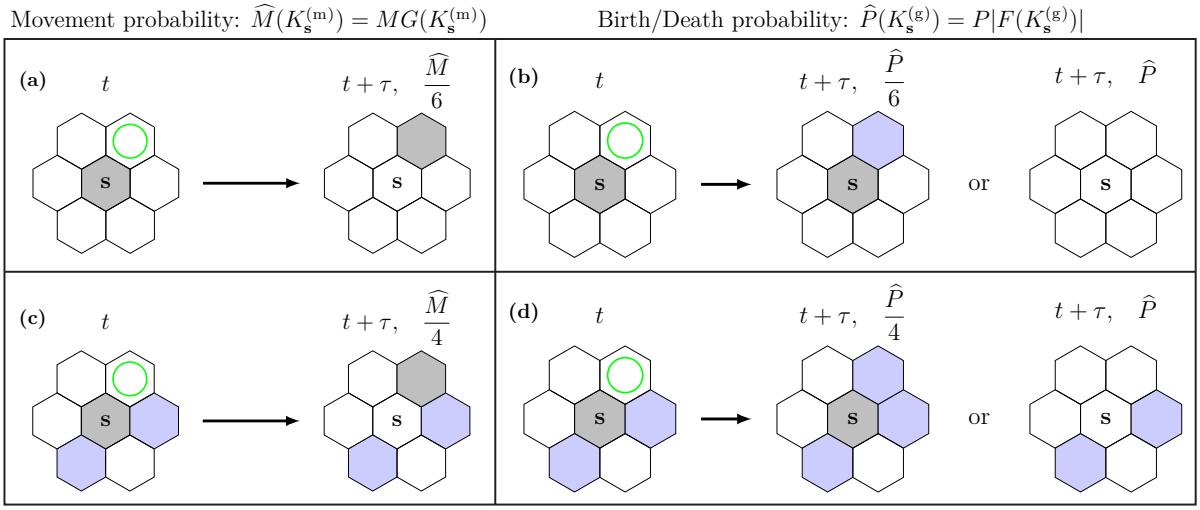

Figure 2.2: **Movement and birth/death mechanisms.** In each lattice fragment site **s** is occupied and shaded in grey, and occupied neighbouring sites are shaded in blue, while vacant neighbouring sites are unshaded (white). In (a) the agent at site **s** moves with probability $\widehat{M}$ and moves to the target site, highlighted with a green circle, with probability $\widehat{M}/6$. In (b) the agent at site **s** undergoes a birth event with probability $\widehat{P}$ and places a new agent on the target site with probability $\widehat{P}/6$ if the growth crowding function $F > 0$. In contrast, it dies with probability $\widehat{P}$ if $F < 0$. In (c) the agent moves with probability $\widehat{M}$ and moves to the target site with probability $\widehat{M}/4$. In (d) the agent undergoes a birth event with probability $\widehat{P}$ and places a new agent on the target site with probability $\widehat{P}/4$ if $F > 0$. In contrast, it dies with probability $\widehat{P}$ if $F < 0$.

probability of this agent to undergo a movement event. If this attempt is successful, as there are four vacant neighbour sites, the probability of moving to the target site, highlighted in green, is $\widehat{M}/4$.

Figure 2.2(d) illustrates how crowding effects are incorporated into the growth component of the model, where the agent at site **s** is surrounded by two agents. The probability of attempting to grow is $P \in [0, 1]$, and the attempted growth is successful with probability $\widehat{P} = P|F(K_{\mathbf{s}}^{(\mathrm{g})})|$. Here, $K_{\mathbf{s}}^{(\mathrm{g})}$ is again a measure of the local density of site **s** and the function $F(K_{\mathbf{s}}^{(\mathrm{g})}) \in [-1, 1]$ is called the growth crowding function that specifies how the local density influences the probability of this agent to undergo a growth event. If this attempt is successful, there are two possible outcomes reflected by the sign of F. If $F > 0$, the growth event is a birth event, and a daughter agent is placed at a randomly-chosen vacant site with probability $\widehat{P}$. As there are four vacant neighbour sites, the probability of placing a daughter agent at the vacant target site, highlighted in green, is $\widehat{P}/4$. Second, if $F < 0$, the growth event is a death event, and the agent is removed from the lattice with probability $\widehat{P}$. The special case where $F = 0$ leads to neither a birth or death event.

A key feature of our model is in the way that the local density about each site affects movement and growth events through the movement and growth crowding functions. To describe this we take $\mathcal{N}_r\{\mathbf{s}\}$ to denote the set of neighbouring sites around site **s**,

where $r \geq 1$ is the integer number of concentric rings of sites surrounding site $\mathbf{s}$, so that $|\mathcal{N}_r| = 3r(r+1)$ (Jin et al. 2016a; Fadai et al. 2020). The probability that any potential movement or growth event is successful depends upon the crowdedness of the local region surrounding site $\mathbf{s}$. We count neighbouring agents in $\mathcal{N}_r$, and consider

$$K_{\mathbf{s}}(r) = \frac{1}{|\mathcal{N}_r|} \sum_{\mathbf{s}' \in \mathcal{N}_r\{\mathbf{s}\}} C_{\mathbf{s}'} \in [0,1], \tag{2.2}$$

as a simple measure of the crowdedness of the local region surrounding site $\mathbf{s}$. While in Figure 2.2 we explain the model with $r = 1$ and $|\mathcal{N}_1| = 6$, it is possible to use different-sized templates, depending on the choice of r. Sometimes it is useful to use different-sized templates for the movement and growth mechanisms. For example, Simpson et al. (2010a) argues that cell movement can be modelled using a nearest-neighbour random walk with $r = 1$, whereas cell proliferation often involves non nearest-neighbour interactions since daughter cells are often deposited several cell diameters away from the location of the mother cell. This argument is supported by experimental images of cell proliferation where careful examination of timelapse movies show that daughter cells are often generated some distance from the mother cell (Druckenbrod and Epstein 2005). To simulate such dynamics, Simpson et al. (2010a) introduce proliferation mechanisms where daughter agents are placed up to four lattice sites away from the mother agent to faithfully capture this biological detail into their model. This would be similar to setting $r = 1$ for movement and $r = 4$ for growth in our model. It is thus convenient for us to make a notational distinction between the size of the templates for motility and growth. Therefore, we denote the motility template as $K_{\mathbf{s}}^{(\mathrm{m})} = K_{\mathbf{s}}(r')$ and the growth template as $K_{\mathbf{s}}^{(\mathrm{g})} = K_{\mathbf{s}}(r'')$ where $r' \geq 1$ and $r'' \geq 1$ are two, potentially different, positive integers.

We now describe the details of how crowding effects and different-sized spatial templates are incorporated into the growth component of the model with reference to the schematic illustration in Figure 2.3. Note that this figure only indicates the potential growth events without the indication of any movement events. In Figures 2.3(a)–(c), crowding of the agent at site $\mathbf{s}$ is measured using a nearest-neighbour template with $r = 1$ and the growth crowding function $F(K_{\mathbf{s}}^{(\mathrm{g})}) = 1 - K_{\mathbf{s}}^{(\mathrm{g})}$, as given in Figure 2.3(d). The probability of undergoing a birth event is $\widehat{P} = P|F(K_{\mathbf{s}}^{(\mathrm{g})})|$. In Figure 2.3(a) where $K_{\mathbf{s}}^{(\mathrm{g})} = 0$, we have $F(0) = 1$ and $\widehat{P} = P$. As there are six vacant sites in $\mathcal{N}_1$, the probability of placing a daughter agent at the target site, highlighted in green, is $\widehat{P}/6$. In Figure 2.3(b), where the agent at site $\mathbf{s}$ is surrounded by two neighbour agents, the probability of undergoing a birth event is $\widehat{P} = 2P/3$, since $K_{\mathbf{s}}^{(\mathrm{g})} = 1/3$ and $F(1/3) = 2/3$. As there are four vacant sites in $\mathcal{N}_1$, the probability of placing a daughter agent at the target site is $\widehat{P}/4$. Similarly, in Figure 2.3(c), we have $\widehat{P} = P/3$ as $K_{\mathbf{s}}^{(\mathrm{g})} = 2/3$ and $F(2/3) = 1/3$. As there are two vacant sites in $\mathcal{N}_1$, the probability of placing a daughter agent at the target site is $\widehat{P}/2$.

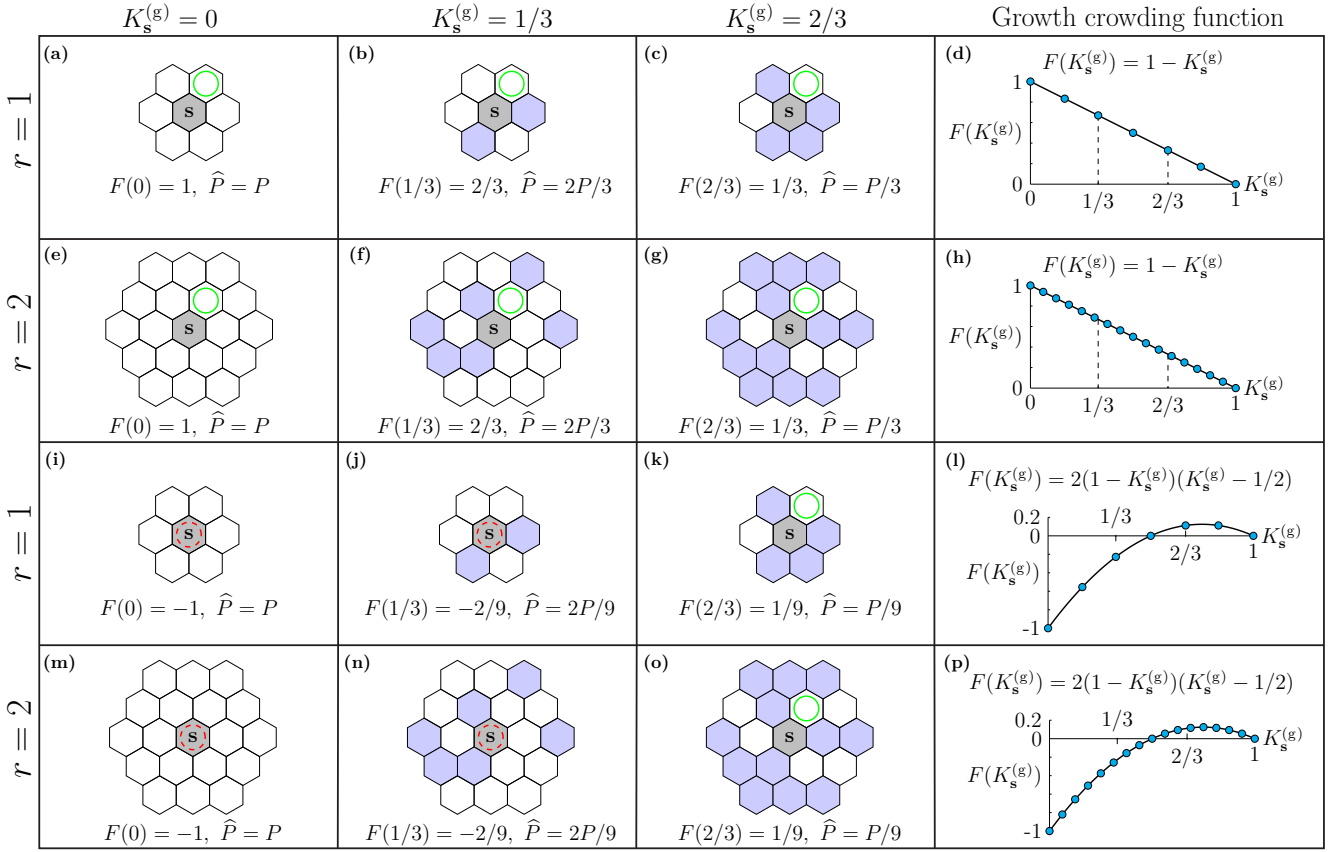

Figure 2.3: **Growth mechanisms with different-sized spatial templates and growth crowding functions**. In each lattice fragment site **s** is shaded grey, occupied sites within the template are shaded blue, and vacant sites within the template are unshaded (white). Each subfigure shows a potential outcome for an agent at site **s**. The crowdedness of $\mathcal{N}_1$ is shown in (a)–(c) and (i)–(k). The crowdedness of $\mathcal{N}_2$ is shown in (e)–(g) and (m)–(o). The agent at site **s** can undergo a birth event when $F > 0$ as in (a)–(c), (e)–(g), (k) and (o). In contrast the agent at site **s** can undergo a death event when $F < 0$ as in (i), (j), (m) and (n). The solid green circles represent the target site for the placement of a daughter agent during a successful proliferation event, and the dashed red circles indicate the location of agents that can undergo a death event.

In Figures 2.3(e)–(g) we introduce a non nearest-neighbour growth mechanism by measuring the crowdedness of the agent at site $\mathbf{s}$ using a larger spatial template with $r = 2$. Therefore, if the agent at $\mathbf{s}$ undergoes a successful birth event, the daughter agent is able to be placed at any vacant site within $\mathcal{N}_2$. The probability of undergoing a birth event is $\widehat{P} = P|F(K_{\mathbf{s}}^{(\mathrm{g})})|$, where $F(K_{\mathbf{s}}^{(\mathrm{g})}) = 1 - K_{\mathbf{s}}^{(\mathrm{g})}$. For the agent in Figure 2.3(e) where $K_{\mathbf{s}}^{(\mathrm{g})} = 0$ and $F(0) = 1$, we have $\widehat{P} = P$. In this configuration there are 18 vacant sites in $\mathcal{N}_2$ and the probability of placing a daughter agent at the target site, highlighted in green, is $\widehat{P}/18$. In Figure 2.3(f), where the agent at site $\mathbf{s}$ is surrounded by six neighbour agents, the probability of undergoing a birth event is $\widehat{P} = 2P/3$, as $K_{\mathbf{s}}^{(\mathrm{g})} = 1/3$ and $F(1/3) = 2/3$. Since there are 12 vacant sites in $\mathcal{N}_2$, the probability of placing a daughter agent at the target site is $\widehat{P}/12$. Similarly, in Figure 2.3(g), we have $\widehat{P} = P/3$, as $K_{\mathbf{s}}^{(\mathrm{g})} = 2/3$ and $F(2/3) = 1/3$. The probability of placing a daughter agent at the target site is $\widehat{P}/6$. All results in Figures 2.3(a)–(h) consider the simplest linear crowding function $F(K_{\mathbf{s}}^{(\mathrm{g})}) = 1 - K_{\mathbf{s}}^{(\mathrm{g})}$, which means that agents do not die in this case, since $F(K_{\mathbf{s}}^{(\mathrm{g})}) \geq 0$.

We now choose a nonlinear growth crowding function $F(K_{\mathbf{s}}^{(\mathrm{g})}) = 2(1-K_{\mathbf{s}}^{(\mathrm{g})})(K_{\mathbf{s}}^{(\mathrm{g})}-1/2)$ that can take on both positive and negative values, as shown in Figure 2.3(l). In this case we make a distinction between a birth event when $F(K_{\mathbf{s}}^{(\mathrm{g})}) > 0$, a death event when $F(K_{\mathbf{s}}^{(\mathrm{g})}) < 0$, and no event when $F(K_{\mathbf{s}}^{(\mathrm{g})}) = 0$. We first consider a nearest-neighbour template with $r = 1$ in Figures 2.3(i)–(k). In Figure 2.3(i), the agent at site $\mathbf{s}$ dies with probability $\widehat{P} = P|F(K_{\mathbf{s}}^{(\mathrm{g})})|$. Here, $K_{\mathbf{s}}^{(\mathrm{g})} = 0$ and $F(0) = -1$, thus $\widehat{P} = P$. In Figure 2.3(j) the agent at site $\mathbf{s}$ dies with probability $\widehat{P} = 2P/9$ as $K_{\mathbf{s}}^{(\mathrm{g})} = 1/3$ and $F(1/3) = -2/9$. In Figure 2.3(k) the agent at site $\mathbf{s}$ undergoes a birth event with probability $\widehat{P} = P/9$ as $K_{\mathbf{s}}^{(\mathrm{g})} = 2/3$ and $F(2/3) = 1/9$. As there are two vacant sites in $\mathcal{N}_1$, the probability of placing a daughter agent at the target site is $\widehat{P}/2$.

Finally, we consider a larger template with $\mathcal{N}_2$ in Figures 2.3(m)–(o). In Figure 2.3(m), the agent at site $\mathbf{s}$ dies with probability $\widehat{P} = P|F(K_{\mathbf{s}}^{(\mathrm{g})})|$, where $F(K_{\mathbf{s}}^{(\mathrm{g})}) = 2(1 - K_{\mathbf{s}}^{(\mathrm{g})})(K_{\mathbf{s}}^{(\mathrm{g})} - 1/2)$. Here $K_{\mathbf{s}}^{(\mathrm{g})} = 0$ and $F(0) = -1$, thus $\widehat{P} = P$. In Figure 2.3(n), the agent at site $\mathbf{s}$ dies with probability $\widehat{P} = 2P/9$ as $K_{\mathbf{s}}^{(\mathrm{g})} = 1/3$ and $F(1/3) = -2/9$. In Figure 2.3(o) the agent at site $\mathbf{s}$ undergoes a birth event with probability $\widehat{P} = P/9$ as $K_{\mathbf{s}}^{(\mathrm{g})} = 2/3$ and $F(2/3) = 1/9$. As there are six vacant sites in $\mathcal{N}_2$, the probability of placing a daughter agent at the target site is $\widehat{P}/6$.

The movement crowding function, $G(K_{\mathbf{s}}^{(\mathrm{m})})$, is incorporated into the model in a similar way as the growth crowding function except that it is always non-negative, $G(K_{\mathbf{s}}^{(\mathrm{m})}) \in [0, 1]$. In this section we have sought to describe the discrete mechanism as clearly as possible with the use of Figure 2.2 and Figure 2.3. For the remainder of this work we focus on results where we set $r = 1$ for movement and $r = 4$ for growth. Other choices of r can be implemented using the software available on GitHub.

2.5 Continuum limit

In this section we derive the mean-field continuum limit of the discrete model. The *averaged* occupancy of site $\mathbf{s}$, constructed from V identically-prepared realisations of the discrete model, can be written as

$$\overline{C}_{\mathbf{s}} = \frac{1}{V}\sum_{v=1}^{V} C_{\mathbf{s}}^{(v)}(t), \tag{2.3}$$

where $C_{\mathbf{s}}^{(v)}(t) \in \{0,1\}$ is the binary occupancy of site $\mathbf{s}$ at time t in the vth identically-prepared realisation of the discrete model. We note that $\overline{C}_{\mathbf{s}} \in [0,1]$, and is a function of time, t, but we suppress this dependence for notational convenience. Similarly, the *averaged* occupancy of $\mathcal{N}_r\{\mathbf{s}\}$, again constructed from V identically-prepared realisations, is given by

$$\overline{K}_{\mathbf{s}}(r) = \frac{1}{|\mathcal{N}_r|}\sum_{\mathbf{s}'\in\mathcal{N}_r\{\mathbf{s}\}} \overline{C}_{\mathbf{s}'}. \tag{2.4}$$

As we use a nearest-neighbour template, $r = 1$, for movement, and a larger template, $r = 4$, for growth, we denote the averaged occupancy of sites for potential movement events as $\overline{K}_{\mathbf{s}}^{(\mathrm{m})}$, and the averaged occupancy of sites for potential growth events as $\overline{K}_{\mathbf{s}}^{(\mathrm{g})}$.

To arrive at an approximate continuum limit description, we start by writing down an expression for the expected change in occupancy of site $\mathbf{s}$ during the time interval from t to $t+\tau$,

$$\begin{aligned}\delta(\overline{C}_{\mathbf{s}}) = &\overbrace{\frac{M}{|\mathcal{N}_1|}(1-\overline{C}_{\mathbf{s}})\sum_{\mathbf{s}'\in\mathcal{N}_1\{\mathbf{s}\}}\overline{C}_{\mathbf{s}'}\frac{G(\overline{K}_{\mathbf{s}'}^{(\mathrm{m})})}{1-\overline{K}_{\mathbf{s}'}^{(\mathrm{m})}}}^{\text{movement events into } \mathbf{s}} \quad - \quad \overbrace{M\overline{C}_{\mathbf{s}}G(\overline{K}_{\mathbf{s}}^{(\mathrm{m})})}^{\text{movement events out of } \mathbf{s}} \\ &+ \underbrace{\frac{P}{|\mathcal{N}_4|}(1-\overline{C}_{\mathbf{s}})\sum_{\mathbf{s}'\in\mathcal{N}_4\{\mathbf{s}\}}\mathbb{H}(F(\overline{K}_{\mathbf{s}'}^{(\mathrm{g})}))\overline{C}_{\mathbf{s}'}\frac{F(\overline{K}_{\mathbf{s}'}^{(\mathrm{g})})}{1-\overline{K}_{\mathbf{s}'}^{(\mathrm{g})}}}_{\text{birth events: place new agents onto } \mathbf{s}} \\ &- \underbrace{(1-\mathbb{H}(F(\overline{K}_{\mathbf{s}}^{(\mathrm{g})}))P\overline{C}_{\mathbf{s}}F(\overline{K}_{\mathbf{s}}^{(\mathrm{g})})}_{\text{death events: remove agent from } \mathbf{s}},\end{aligned} \tag{2.5}$$

where $\mathbb{H}$ is the Heaviside step function. Each term in Equation (2.5) has a relatively simple physical interpretation. The first term on the right hand side of Equation (2.5) represents the change in occupancy of site $\mathbf{s}$ owing to the expected movement of agents in $\mathcal{N}_1\{\mathbf{s}\}$ into site $\mathbf{s}$. The factor $1/(1-\overline{K}_{\mathbf{s}}^{(\mathrm{m})})$ accounts for the choice of the target site in $\mathcal{N}_1$ being randomly selected from the available vacant sites. The second term on the right hand side of Equation (2.5) represents the change in occupancy of site $\mathbf{s}$ owing to the expected movement of agents out of site $\mathbf{s}$. The third term on the right hand side of

Equation (2.5) represents the change in occupancy owing to the expected birth events of agents in $\mathcal{N}_4\{\mathbf{s}\}$ that would place daughter agents onto site $\mathbf{s}$, where $F(\overline{K}_{\mathbf{s}}^{(\mathrm{g})}) > 0$. Again, the factor $1/(1-\overline{K}_{\mathbf{s}}^{(\mathrm{g})})$ accounts for the choice of the target site in $\mathcal{N}_4$ being randomly selected from the available vacant sites. The last term on the right hand side of Equation (2.5) represents the expected change in occupancy owing to agent death at site $\mathbf{s}$, when $F(\overline{K}_{\mathbf{s}}^{(\mathrm{g})}) < 0$. Note that this approximate conservation statement (2.5) makes use of the mean-field assumption, whereby the occupancy status of lattice sites are taken to be independent (Baker and Simpson 2010).

To derive the continuum limit we replace $\overline{C}_{\mathbf{s}}$ with a continuous function, $C(x,y,t)$, and expand each term in Equation (2.5) in a Taylor series about site $\mathbf{s}$, and truncate terms of $\mathcal{O}(\Delta^3)$. Subsequently, we divide both sides of the resulting expression by τ and evaluate the resulting expressions in the limit $\Delta \to 0$ and $\tau \to 0$ jointly, with the ratio of Δ^2/τ held constant (Hughes 1995). This leads to the following nonlinear RDE,

$$\frac{\partial C(x,y,t)}{\partial t} = D_0 \nabla \cdot (D(C) \nabla C(x,y,t)) + \lambda C(x,y,t) F(C), \tag{2.6}$$

where

$$D(C) = C\frac{\mathrm{d}G(C)}{\mathrm{d}C} + \frac{1+C}{1-C}G(C), \tag{2.7}$$

and

$$D_0 = \frac{M}{4}\lim_{\Delta,\tau\to 0}\frac{\Delta^2}{\tau}, \quad \lambda = \lim_{\tau\to 0}\frac{P}{\tau}. \tag{2.8}$$

Here, D_0 is the free-agent diffusivity, $D(C)$ is a nonlinear diffusivity function that relates to the movement crowding function $G(C)$, and λ is the rate coefficient associated with the source term that is related to the growth crowding function $F(C)$. To obtain a well-defined continuum limit we require that $P = \mathcal{O}(\tau)$ (Simpson et al. 2010a). The algebraic details required to arrive at the continuum limit are outlined in the Supplementary Material.

For all simulations in this work we use $\Delta = \tau = 1$, giving $D_0 = M/4$ and $\lambda = P$. This is equivalent to working in a non-dimensional framework (Simpson et al. 2010a). If the model is to be applied to a particular dimensional problem, then Δ and τ can be re-scaled using appropriate length and time scales. In this non-dimensional framework with $\tau = 1$, we satisfy the requirement that $P = \mathcal{O}(\tau)$ by ensuring $P/M \ll 1$. The main focus of this work is on the role of the growth mechanism, and the question of whether the population survives or goes extinct. We therefore set $G(C) = 1 - C$ leading to $D(C) = 1$. This means that the nonlinear diffusion term in Equation (2.6) simplifies to a linear diffusion term, giving

$$\frac{\partial C(x,y,t)}{\partial t} = D_0 \nabla^2 C(x,y,t) + \lambda C(x,y,t) F(C). \tag{2.9}$$

We note that Equation (2.9) has been studied extensively in applications involving the spatial spread of invasive species, such as the works of Fisher (1937); Skellam (1951); Fife

(1979); Lewis and Kareiva (1993) and Hastings et al. (2005). Some previous models consider a logistic-type source term (Fisher 1937), while others consider Allee-type bistable source term (Sewalt et al. 2016). Under these conditions many results have been established. For example, if we consider Equation (2.9) on a one-dimensional infinite domain, it is well known that this model supports travelling wave solutions for both logistic (Fisher 1937) and bistable (Fife 1979) source terms. In this work, however, we take a different perspective by studying Equation (2.9) on a finite domain and so the question of analysing travelling wave solutions is not our focus. Moreover, although Lewis and Kareiva (1993) give a critical radius of a radially symmetric distribution so that the initial distribution converges to an expanding wave in an infinite domain, their analysis is valid under the assumption that the time scale of growth is much faster than the time scale of migration, which corresponds to $P/M \gg 1$ in our framework. Our discrete model does not have any such restriction and can be implemented for any $M \in [0, 1]$ and any $P \in [0, 1]$. In contrast, our continuum model requires $P/M \ll 1$ to correspond to the discrete model, and we will explore the consequences of these differences in our results.

In the rest of this work we choose

$$F(C) = a(1 - C)(C - A), \quad \text{with} \quad a = \frac{5}{2}, \quad A = \frac{2}{5}, \tag{2.10}$$

since this leads to the canonical cubic source term $\lambda CF(C)$ associated with Allee kinetics. In particular, we set $A = 2/5$ so that this choice of $F(C)$ can be used to represent birth events where $C > 2/5$ and death events where $C < 2/5$, see Figure 2.4(d). We further set $a = 5/2$ leading to $F(0) = -1$, so that attempted death events for an isolated agent, where $C = 0$, are always successful.

In summary, our discrete model requires the specification of two crowding functions: $G(C)$ and $F(C)$. These crowding functions are related to macroscopic quantities in the associated RDE model. In particular, $G(C)$ is related to a nonlinear diffusivity function, $D(C)$, and $F(C)$ is related to a nonlinear source term $\lambda CF(C)$. Figure 2.4 shows the relationship between these functions for our choice of $G(C)$ and $F(C)$.

2.6 Initial distributions and simulation data

In this section we consider the three initial distributions shown in Figure 2.1 with $L = 100$, and we introduce the corresponding continuous descriptions. In general, each of the initial distribution shown in Figure 2.1 can be written as

$$C(x, y, 0) = \begin{cases} B, & (x, y) \in \mathcal{H}, \\ 0, & \text{elsewhere}, \end{cases} \tag{2.11}$$

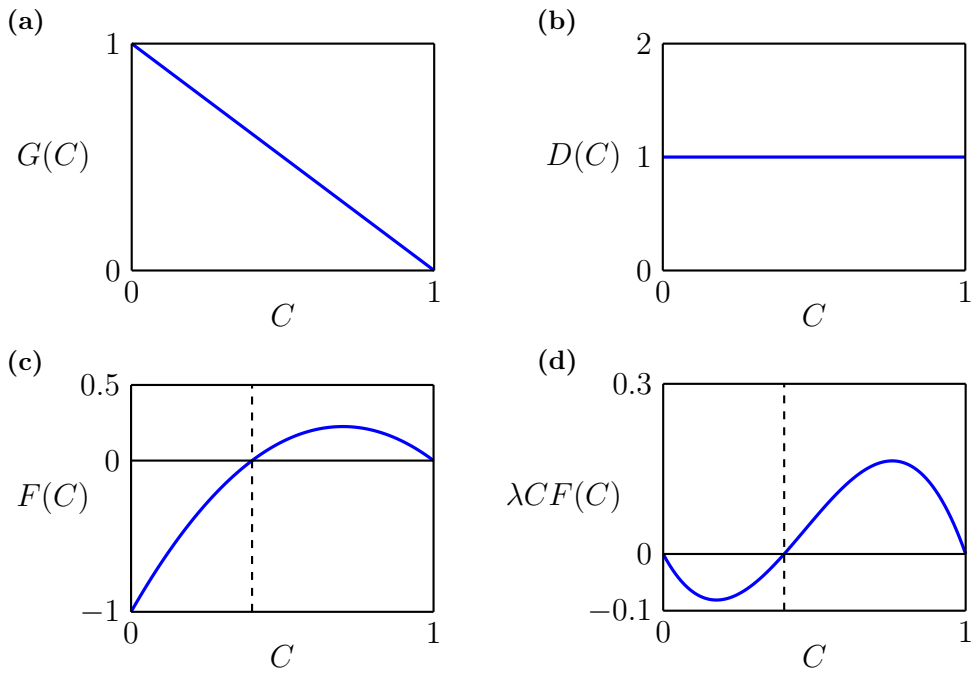

Figure 2.4: **Specific crowding functions used in this work.** (a)–(b) Setting $G(C) = 1 - C$ for the movement crowding function leads to linear diffusion, $D(C) = 1$. (c)–(d) Setting $F(C) = 5(1 - C)(C - 2/5)/2$ for the growth crowding function with $\lambda = P = 1$ leads to $\lambda CF(C) = 5C(1 - C)(C - 2/5)/2$. The dashed lines in (c)–(d) relate to the Allee threshold, $A = 2/5$.

where $\mathcal{H}$ is the region in which individuals are distributed at density $B \in (0, 1]$. For the discrete model, we randomly distribute a fixed number of agents on $\mathcal{H}$ so that the averaged density across $\mathcal{H}$ is B. For example, all agents in the discrete model are closely packed together if $B = 1$. In contrast, for the continuum model, the density is B at each position in $\mathcal{H}$.

For the three initial distributions in Figure 2.1 we will report data from the stochastic model in the following way. We denote the averaged occupancy of site $\mathbf{s}$ in V identically-prepared simulations as

$$\langle C(x, y, t)\rangle = \frac{1}{V}\sum_{v=1}^{V} C^{(v)}(i, j, n), \tag{2.12}$$

where we note that the average denoted by the angular parenthesis is taken in the same way as the average in Equation (2.3). Here, site $\mathbf{s}$, indexed by i and j, are related to position, (x, y) via Equation (2.1). The averaged occupancy $\langle C(x, y, t)\rangle$ is a measure of the local density at location (x, y), and time $t = n\tau$ after the nth time step in the stochastic discrete model. Although (2.12) describes the averaged occupancy of any distribution, there are more concise forms for the vertical strip distributions in Figure 2.1(b). As the initial occupancy is independent of the vertical position, we denote the averaged occupancy

of any site as

$$\langle C(x,t)\rangle = \frac{1}{VJ}\sum_{v=1}^{V}\sum_{j=1}^{J} C^{(v)}(i,j,n), \tag{2.13}$$

which is a measure of the density at location x and at time $t = n\tau$. Note that, as we will show through simulation, the density of agents remains independent of the vertical position for all $t > 0$ because we use periodic boundary conditions. Similarly, for simulations relating to the well-mixed initial distribution as in Figure 2.1(a), where the initial density is independent of position, we denote the averaged occupancy of any site as

$$\langle C(t)\rangle = \frac{1}{VIJ}\sum_{v=1}^{V}\sum_{j=1}^{J}\sum_{i=1}^{I} C^{(v)}(i,j,n), \tag{2.14}$$

which is a measure of the total population density at time $t = n\tau$. As we will show through simulation, in this case the density of agents remains independent of position for all $t > 0$. The total population density $\langle C(t)\rangle$ is also useful to describe simulations starting from the square and vertical strip initial distributions. In summary, data from the discrete models can be summarised by calculating $\langle C(x,y,t)\rangle$, $\langle C(x,t)\rangle$, and $\langle C(t)\rangle$.

For the well-mixed initial distribution, as shown in Figure 2.1(a), Equation (2.9) simplifies to

$$\frac{\mathrm{d}C(t)}{\mathrm{d}t} = \lambda C(t)F(C), \tag{2.15}$$

where $C(t)$ represents the total density of the population (Simpson et al. 2010a). This separable ODE can be solved to give an implicit solution for our choice of $F(C)$.

For the vertical strip initial distribution, as shown in Figure 2.1(b), Equation (2.9) simplifies to

$$\frac{\partial C(x,t)}{\partial t} = D_0\frac{\partial^2 C(x,t)}{\partial x^2} + \lambda C(x,t)F(C), \tag{2.16}$$

where $C(x,t)$ represents the column-averaged density of agents (Simpson et al. 2010a). An extensive discussion and exploration of the implications of simplifying the two-dimensional nonlinear RDE into this simpler one-dimensional RDE is given in Simpson (2009). Given a numerical solution of Equation (2.16), as outlined in the Supplementary Material, we compute

$$\mathcal{C}(t) = \frac{1}{L}\int_0^L C(x,t)\ \mathrm{d}x, \tag{2.17}$$

which is the total density of the population in the whole domain, and corresponds to $\langle C(t)\rangle$ in the discrete model.

For the square initial distribution, to compare averaged data from the discrete model with the solution of the continuum model we solve Equation (2.9) numerically to give $C(x,y,t)$. Full details of the numerical methods are presented in the Supplementary

Material. Using the numerical solution for $C(x, y, t)$ we calculate

$$\mathcal{C}(t) = \frac{1}{L^2} \int_0^L \int_0^L C(x, y, t) \, \mathrm{d}x \, \mathrm{d}y, \tag{2.18}$$

which, again, is the total density of the population in the whole domain.

We now show the evolution of the total population density in both the discrete and continuum models with these three initial distributions. Setting all three initial distributions with $\mathcal{C}(0) = 0.25$ and considering $P/M = 1/1000$ or $P/M = 8/1000$, representing two kinds of populations with different ratios of time scale of migration and growth, we show $\mathcal{C}(t)$ and $\langle C(t) \rangle$ in Figure 2.5, where we calculate $\langle C(t) \rangle$ with 40 identically-prepared realisations. In all cases the continuum model accurately captures the averaged data from the discrete model. The well-mixed initial distribution leads to population survival with both $P/M = 1/1000$ and $P = 8/1000$, whereas the vertical strip and square initial distributions lead to population extinction when $P/M = 1/1000$, but population survival when $P/M = 8/1000$, as shown in Figures 2.5(e)–(f) and Figures 2.5(h)–(i). This is interesting as the global density averaged across the whole domain is smaller than the Allee threshold. This comparison indicates that the vertical strip and square initial distributions may sometimes lead to the survival of the population whereas the same initial number of individuals in a well-mixed environment would lead to extinction. These differences are due to the interplay between the role of the initial spatial distribution and the ratio of time scale of migration to the time scale of proliferation and death. Additional results in the Supplementary Material provide more detailed comparisons of the solutions of the continuum model and appropriately averaged data from the discrete model. Additional results relating to the robustness of the averaged data is also explored in the Supplementary Material. Overall, the numerical solution of the continuum model provides a useful way of accurately studying the expected behaviour of the discrete model. Of interest is that the long-term fate of populations varies with the spatial arrangement of the initial distributions. Our aim now is to study these differences more carefully.

2.7 Role of the shape of the initial distribution

In this section we explore the influence of more complicated two-dimensional shapes of the initial distribution on the fate of populations. Our results in Section 2.6 indicate that several factors are at play when we consider the long-term fate of bistable populations. First, the spatial arrangement of the initial population plays an important role. Second, the ratio P/M also influences the fate of populations. Since the initial distribution of the population is given by Equation (2.11), the initial distribution varies with both B and the size of the initially occupied region $\mathcal{H}$ except that the well-mixed initial distribution only varies with B. In the remainder of the main document we fix $B = 1$ and alter the

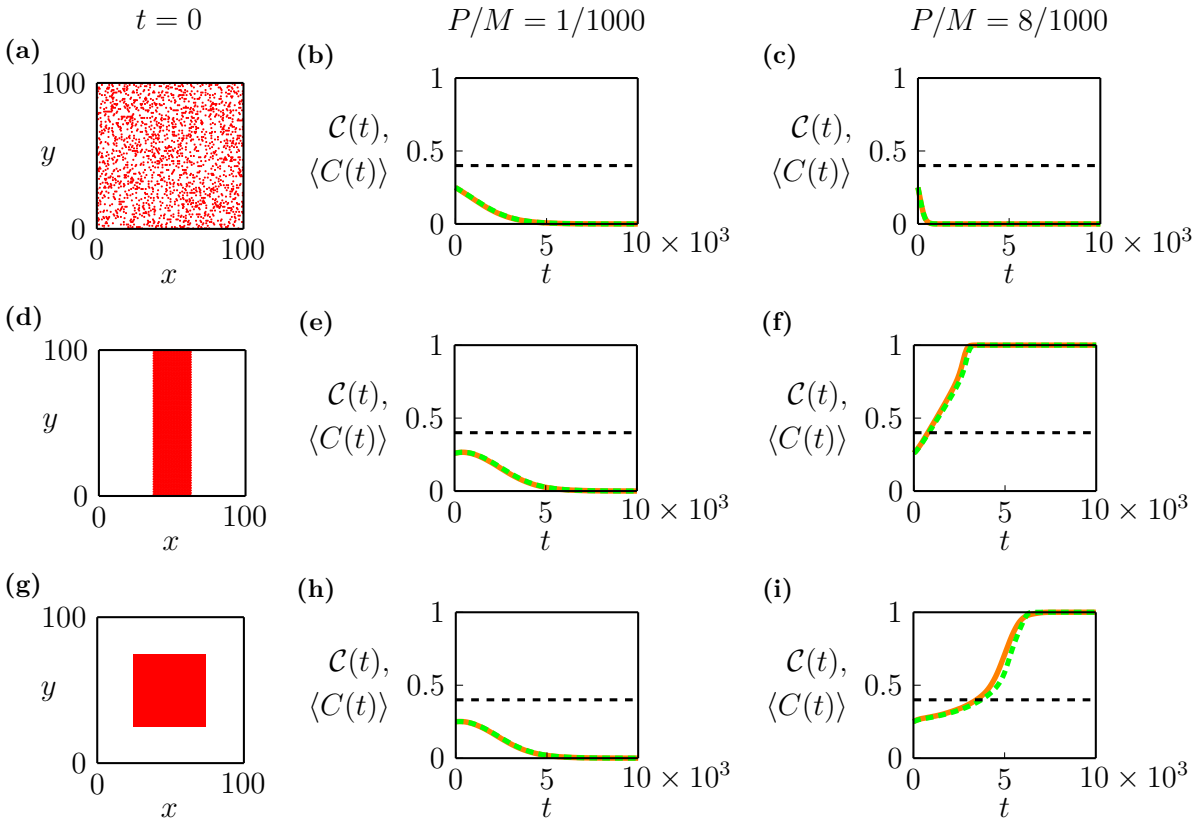

Figure 2.5: **The ratio P/M and the shape of the initial spatial distribution influence the fate of populations.** (a) Well-mixed initial distribution with $B = 0.25$ leading to $\mathcal{C}(0) = 0.25$. (b) $\langle C(t)\rangle$ (solid orange) and $\mathcal{C}(t)$ (dashed green) for the well-mixed initial distribution with $P/M = 1/1000$. (c) $\langle C(t)\rangle$ (solid orange) and $\mathcal{C}(t)$ (dashed green) for the well-mixed initial distribution with $P/M = 8/1000$. (d) Vertical strip initial distribution with width $w_1 = 25$ leading to $\mathcal{C}(0) = 0.25$. (e) $\langle C(t)\rangle$ (solid orange) and $\mathcal{C}(t)$ (dashed green) for the vertical strip initial distribution with $P/M = 1/1000$. (f) $\langle C(t)\rangle$ (solid orange) and $\mathcal{C}(t)$ (dashed green) for the vertical strip initial distribution with $P/M = 8/1000$. (g) Square initial distribution with width $w_1 = 50$ leading to $\mathcal{C}(0) = 0.25$. (h) $\langle C(t)\rangle$ (solid orange) and $\mathcal{C}(t)$ (dashed green) for the square initial distribution with $P/M = 1/1000$. (i) $\langle C(t)\rangle$ (solid orange) and $\mathcal{C}(t)$ (dashed green) for the square initial distribution with $P/M = 8/1000$. The dashed black horizontal lines in (b)–(c), (e)–(f) and (h)–(i) indicate the Allee threshold, $A = 0.4$.

initial population size by adjusting the size of $\mathcal{H}$ for the initial distributions that are not well-mixed. Additional results in the Supplementary Material indicate that varying B does not change our overall observations and conclusions.

To systematically study the transition between population extinction to population survival, we take the $(\mathcal{C}(0), P/M)$ phase space and discretise it uniformly into a rectangular mesh, with 51×40 nodes in Figure 2.6(n). We vary $\mathcal{C}(0)$ by changing B in the well-mixed initial distribution, whereas we vary $\mathcal{C}(0)$ by changing the size of $\mathcal{H}$ in the vertical strip and square initial distributions as shown in Figures 2.6(a)–(c) and Figure 2.6(d)–(f), respectively. We also vary the ratio P/M by holding $M = 1$ and choosing $P \in [1/1000, 4/100]$ in the discrete model. As $P/M = \lambda/(4D_0)$, we hold $D_0 = 1/4$ and vary λ in the continuum model. With each pair of parameters, we run the numerical simulation of the continuum model after a sufficiently long period of time so that the population either leads to survival or extinction. In Figure 2.6(n), we draw the survival/extinction thresholds from the continuum model with the well-mixed, vertical strip and square initial distributions. In the vertical strip and square cases we see that the long-term survival is strongly dependent upon P/M whereas in the well-mixed initial distribution this dependence is less pronounced. Additional results in the Supplementary Material show the good agreement in the prediction of survival or extinction between the continuum and discrete models, and further show the role of stochasticity in discrete simulations.

A key feature of the initial shape is the dimension of the shape. The well-mixed, vertical strip and square initial distributions can be thought of as zero-, one- and two-dimensional shapes, respectively. To highlight the influence of the dimensionality on the fate of the population, we consider a rectangular distribution of varying initial heights, see Figures 2.6(g)–(i). The initially occupied region $\mathcal{H}$ is a rectangle with width $w_1 = 40$ and height $w_2 \in [25, 100]$, which leads to $\mathcal{C}(0) \in [0.1, 0.4]$. When $\mathcal{C}(0) = 0.16$ with $w_2 = 40$, the rectangular initial distribution is the same as the square initial distribution, as shown in Figures 2.6(e) and (h). When $\mathcal{C}(0) = 0.4$ with $w_2 = 100$, the rectangular initial distribution is the same as the vertical strip initial distribution, as shown in Figures 2.6(c) and (i). Note that we use $\mathcal{C}(0)$ as the horizontal axis in the phase diagram so that we can compare the results with different shapes of initial distributions. We show the evolution of the total population density in the continuum model with $M = 1$ and $P = 0.0028$, leading to $D_0 = 1/4$ and $\lambda = 0.0028$, and different $\mathcal{C}(0)$ in Figures 2.6(j)–(m). When $\mathcal{C}(0) = 0.2$ and $\mathcal{C}(0) = 0.3$, the rectangular initial distribution leads to extinction, which is the same as the results obtained from the square initial distribution. While the vertical strip initial distribution leads to survival with $\mathcal{C}(0) = 0.3$. In contrast, when $\mathcal{C}(0) = 0.33$ and $\mathcal{C}(0) = 0.36$, the rectangular initial distribution leads to survival, which is the same as the results obtained from the vertical strip initial distribution. While the square initial distribution leads to extinction with $\mathcal{C}(0) = 0.33$. This indicates a switch of the influence of

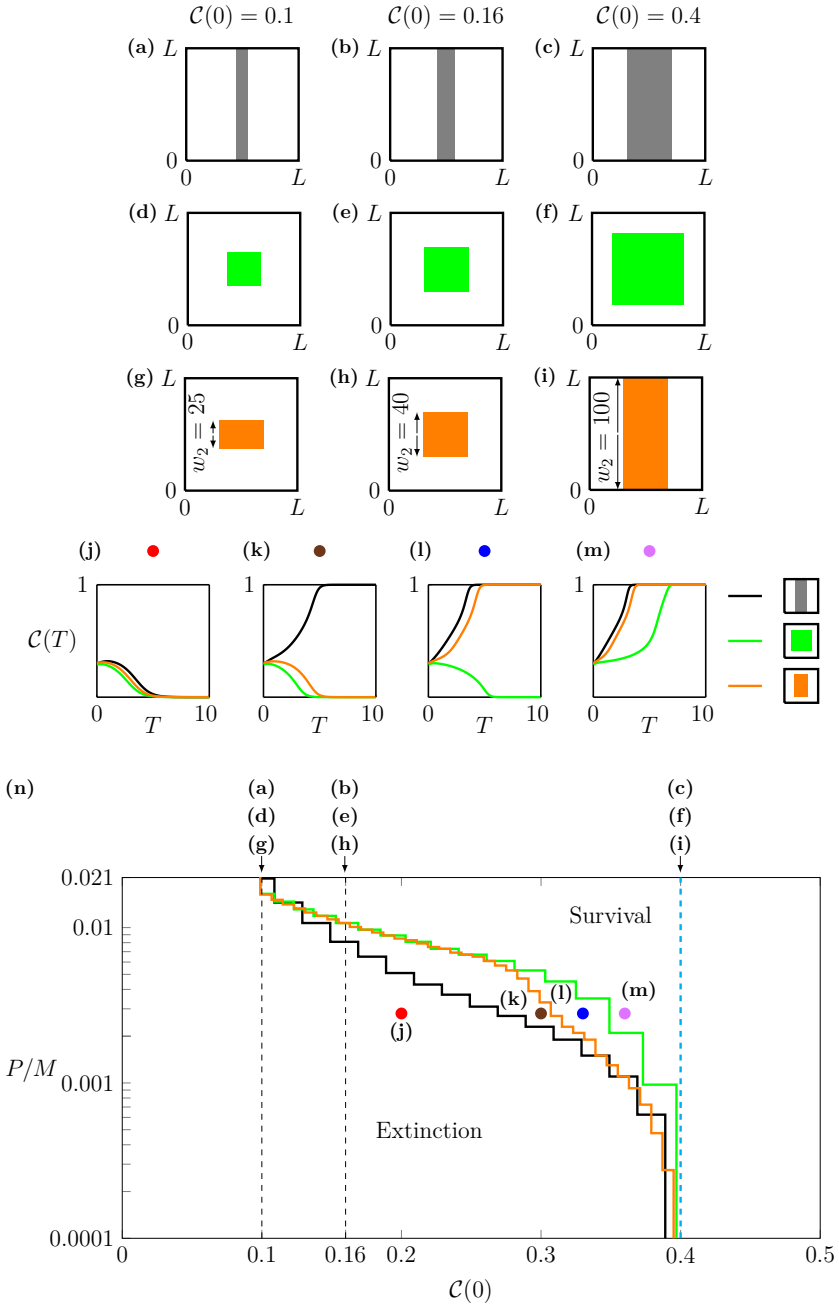

Figure 2.6: **Influence of dimensionality in rectangular initial distributions.** (a)–(c) Vertical strip (one-dimensional) initial distributions varied with the width $w_1 \in [10, 40]$. (d)–(f) Square (two-dimensional) initial distributions varied with the width $w_1 \in [32, 64]$. (g)–(i) The rectangular initial distributions varied with the height $w_2 \in [25, 100]$ with a fixed width $w_1 = 40$. (j)–(m) The evolution of the total population density $\mathcal{C}(T)$ where $T = 10^3 t$ with $P/M = 0.0028$, $\mathcal{C}(0) = 0.2$ in (j), 0.3 in (k), 0.33 in (l) and 0.36 in (m), and with the vertical strip (black), square (green) and rectangular (orange) initial distributions. (n) Phase diagram showing the survival/extinction boundaries constructed from a 151×120 array of $\mathcal{C}(0) \in [1/10, 1/40]$ and $P/M \in [1/10000, 21/1000]$. Three curves indicate the survival/extinction thresholds from the continuum model of the vertical strip (black), square (green) and rectangular (orange) initial distributions. Three dashed lines represent $\mathcal{C}(0) = 0.1, 0.16$ and 0.4, where $\mathcal{C}(0) = 0.4$ (cyan) is also the survival/extinction threshold of the well-mixed initial distributions. Note that we use a logarithmic scale for the P/M axis.

the rectangular initial distribution on the fate of populations from a manner similar to the square initial distribution to a manner similar to the vertical strip initial distribution. In Figure 2.6(n), we draw the survival/extinction boundary from the continuum model with the rectangular initial distribution in the $(\mathcal{C}(0), P/M)$ phase space for $\mathcal{C}(0) \in [0.1, 0.4]$ and $P/M = [1/10000, 21/1000]$, and compare them to the results obtained from the vertical strip initial distribution and from the square initial distribution. Although the results are from the continuum model, we still use P/M as the vertical axis to reflect the connection between the discrete and continuum models in our framework. We observe that there is a clear transition of the survival/extinction boundary for the rectangular initial distribution. The survival/extinction boundary of the rectangular initial distribution is close to the survival/extinction boundary obtained from the square initial distribution when $\mathcal{C}(0)$ is small, and is close to the survival/extinction boundary obtained from the vertical strip initial distribution when $\mathcal{C}(0)$ is large. This transition indicates that the dimensionality of the initial shape of a population plays a role in determining the ultimate fate of the population.

Many more spatial arrangements of the population can be considered. We first consider a circle with radius r as the initially occupied region $\mathcal{H}$, as shown in Figure 2.7(a). We draw the phase diagram on the $(\mathcal{S}, P/M)$ space, where $\mathcal{S}$ denotes the area of the initially occupied region $\mathcal{H}$, from the continuum model with $L = 100$ by varying $P/M \in [1/1000, 21/1000]$ where $M = 1$ and $\mathcal{S} = \pi r^2 \in [1000, 5000]$ with $r \in [17.8, 39.9]$ in Figure 2.7(b). We then consider the critical initial radius

$$r_{\text{crit}} = \sqrt{\frac{2D_0}{\lambda a}} \frac{1}{1-2A}, \tag{2.19}$$

derived by Lewis and Kareiva (1993), which leads to the critical initial area $\mathcal{S}_{\text{crit}} = \pi r_{\text{crit}}^2$. As λ and D_0 depend on P and M in our framework, we derive the survival/extinction threshold of the initial area

$$\mathcal{S}_{\text{crit}} = \frac{\pi M}{2aP} \frac{1}{(1-2A)^2}, \tag{2.20}$$

and draw the extinction/survival boundary in the $(\mathcal{S}, P/M)$ phase space based on (2.20) in Figure 2.7(b). Although the critical initial radius is formally derived in the limit $P/M \gg 1$, this result also appears to work well here where P/M is not that large. We now consider a larger domain with $L = 200$ in Figure 2.7(c), in this case the match between the survival/extinction boundary of the circular initial distribution and the critical initial area is better because the role of boundaries becomes less important. Furthermore, we compare the survival/extinction boundary to the result obtained from the square initial distribution with $L = 100$ and $L = 200$ in Figure 2.7(b) and Figure 2.7(c), respectively. Note that in the square initial distribution the area of $\mathcal{H}$ is given by $\mathcal{S} = w_1^2$. The survival/extinction boundaries obtained with the circular and square initial distributions are very close, which

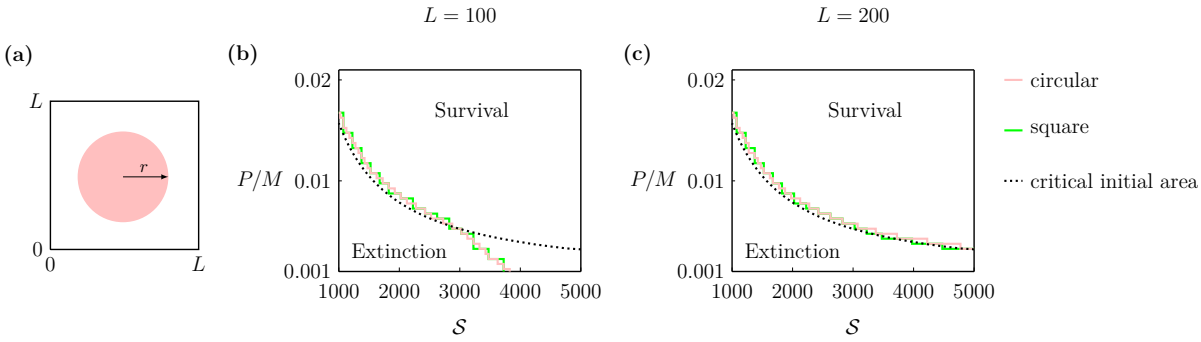

Figure 2.7: **Phase diagram for survival/extinction with the circular initial distributions.** (a) A circular initial distribution with radius r. (b)–(c) Phase diagrams on a rectangular mesh with 81×41 nodes for $\mathcal{S} \in [0.1, 0.5]$ and $P/M \in [1/1000, 21/1000]$ where $M = 1$. We consider $L = 100$ in (b) and $L = 200$ in (c). Pink curves indicate the survival/extinction thresholds in the continuum model with the circular initial distributions. Green curves indicate the survival/extinction thresholds in the continuum model with the square initial distributions. Black dotted curves indicate the survival/extinction thresholds obtained from (2.20).

indicates that these two initial distributions give rise to similar outcomes. This could be attributed to the fact that they are both compact initial distributions with a small perimeter to area ratio.

A natural question is whether populations with other two-dimensional initial distributions have the similar critical initial area determined by (2.19). To explore this, we now consider a square annulus in the middle of the domain as the initially occupied region, as shown in Figure 2.8(a). The area of the region is determined by a fixed outer width $w_1 = 64$ and a variable inner width w_2. We also consider a circle as the initially occupied region, as shown in Figure 2.8(b). The area of the region varies with radius r. We show the evolution of the total population density in the continuum model with these two initial shapes at $P/M = 0.01$, where $M = 1$ and $P = 0.01$ leading to $D_0 = 1/4$ and $\lambda = 0.01$, and different $\mathcal{C}(0)$. We further show the results obtained from the vertical strip initial distributions and the square initial distributions in Figure 2.8(c). All four initial distributions lead to population extinction when $\mathcal{C}(0) = 0.1$. When $\mathcal{C}(0) = 0.15$, only the vertical strip initial distribution leads to population survival. When $\mathcal{C}(0) = 0.2$, the square and circular initial distributions also lead to population survival. In contrast, the square annular initial distribution still leads to population extinction. Note that $P/M = 0.01$ leads to $A_{\text{crit}} \approx 1570$ and $\mathcal{C}(0)_{\text{crit}} = 0.157 < 0.2$. This suggests that, although the area of the square annulus exceeds the critical initial area given in Lewis and Kareiva (1993), it still leads to population extinction. When $\mathcal{C}(0) = 0.3$, all four initial distributions lead to population survival. These results indicate that, although some initial distributions have the same area of the initially occupied region, they may lead to different fates of the population. It is the shape of the initially occupied region that dictates whether a bistable population

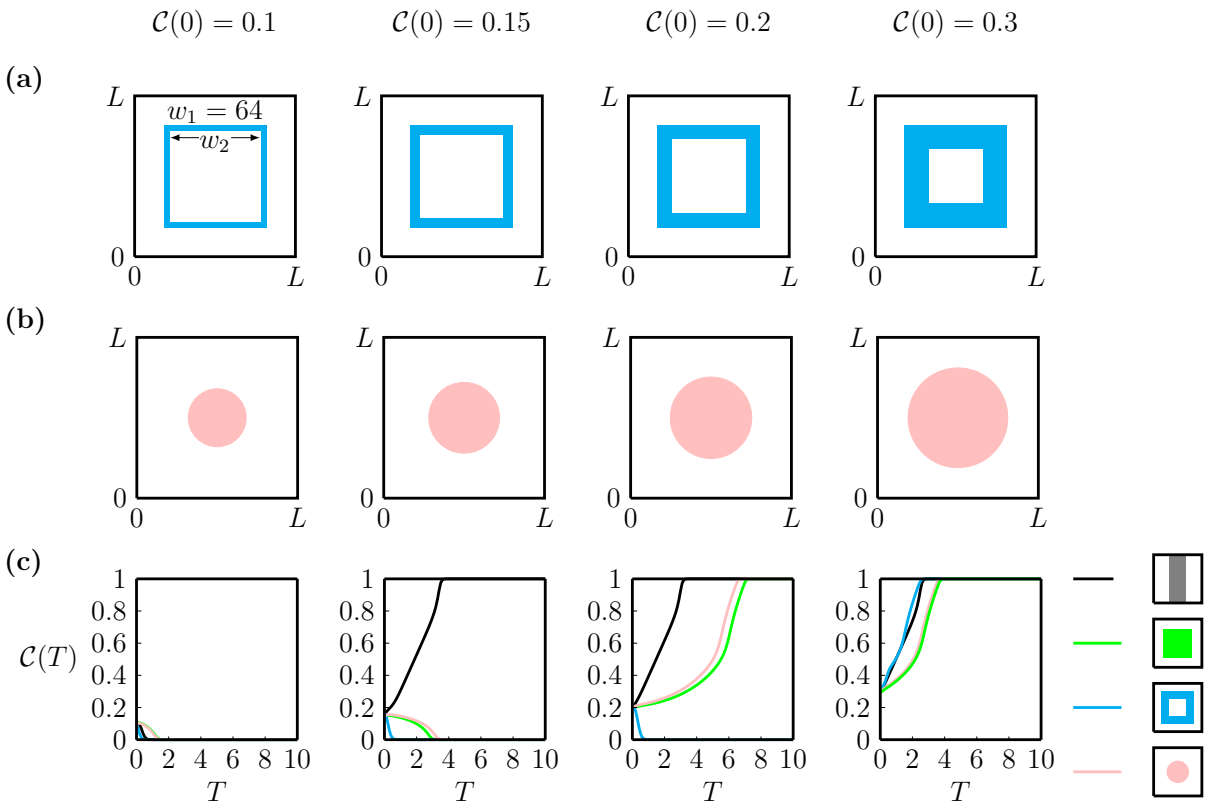

Figure 2.8: **Population dynamics with more complicated initial spatial distributions**. (a) Square annular initial distributions with a fixed outer width $w_1 = 64$ and different values of inner width w_2. (b) Circular initial distributions with different values of radius r. (c) The evolution of the total population density $\mathcal{C}(T)$ which considers $T = \lambda t$, $P/M = 0.01$ with $P = 0.01$ and $M = 1$ leading to $\lambda = 0.01$ and $D_0 = 1/4$, and $\mathcal{C}(0) = 0.1, 0.15, 0.2, 0.3$ with different initial distributions. Black curves are generated by the vertical strip initial distributions. Green curves are generated by the square initial distributions. Cyan curves are generated by the square annular initial distributions. Pink curves are generated by the circular initial distributions.

survives or goes extinct. This suggests the importance of considering the influence of the spatial arrangements of individuals on the long-term survival of populations.

2.8 Conclusions and Outlook

In this work we design, analyse and implement a new two-dimensional stochastic discrete model incorporating movement, birth and death events with crowding effects to study population extinction. The continuum limit of the discrete model is a nonlinear RDE which can be used to study a wide range of macroscopic phenomena including linear diffusion, nonlinear diffusion, as well as logistic and bistable growth kinetics. Since the aim of this work is to focus on long term survival or extinction, we choose the movement crowding function to be $G(C) = 1 - C$ which corresponds to macroscopic linear diffusion. In addition, we choose the growth crowding function to be $F(C) = a(1-C)(C-A)$ which leads to a classical cubic bistable source term with Allee threshold A.

The focus of our work is to use the discrete and continuum models to explore the factors that influence the long-term fate of the bistable population. In particular, we explore different spatial arrangements of the population on a finite $L \times L$ domain with periodic boundary conditions. The well-mixed initial distribution involves distributing agents evenly across the entire $L \times L$ domain, the vertical strip initial distribution involves distributing agents along a vertical strip within the $L \times L$ domain so that the initial density is independent of vertical position in the domain, and the two-dimensional initial distributions involve distributing agents in a square, circular, rectangular or square annular region within the $L \times L$ domain. Our results show that the shape of initial distributions plays an important role in determining the fate of populations. This suggests the importance of considering the influence of spatial arrangements of individuals in studies of population dynamics.

There are many avenues for extending the work presented in this study. The stochastic model provides very detailed information including the age structure of the population and individual trajectories, see the results in the Supplementary Material. Furthermore, Other shapes of initial distributions than those investigated here can be considered and similar numerical explorations of the long-term survival or extinction of the populations can be conducted using the software provided on GitHub for both the continuum and discrete models. Another feature of this work that could be explored is the choice of crowding functions. As we pointed out, all simulations here focus on $G(C) = 1 - C$, which gives rise to linear diffusion, and $F(C) = a(1 - C)(C - A)$ which gives rise to the classical cubic bistable term. Other choices of $G(C)$ and $F(C)$ can be incorporated into the discrete model to explore how the results presented here depend upon the precise details of these choices of crowding functions. We note that other choices of $G(C)$ lead to

different motility mechanisms that are associated with nonlinear diffusion mechanisms, and that these can be important for applications where adhesion (Deroulers et al. 2009) and inertial effects (Zhang et al. 2019) are relevant. While we have not explicitly explored these effects in this work, our framework is sufficiently general that these mechanisms can be incorporated and explored, if required. Moreover, other boundary conditions could be incorporated in our model. In the Supplementary Material, we show that no-flux boundary conditions lead to the same result as when we consider periodic boundary conditions with symmetric rectangular initial distributions, while homogeneous Dirichlet boundary conditions only lead to the same result when the initial area is small. Furthermore, if we consider an asymmetric initial distribution, these three boundary conditions lead to different outcomes. Another interesting extension would be to consider Allee-type dynamics with populations of interacting species (Simpson et al. 2009a). Under these conditions interactions can also contribute to the eventual survival or extinction of any of the subpopulations (Taylor et al. 2020; Krause and Van Gorder 2020).

2.9 Additional results

2.9.1 Derivation of the continuum limit

We recall Equation (5), that is, the expected change in occupancy of site $\mathbf{s}$ during the time interval from t to $t+\tau$,

$$\begin{aligned}\delta(\overline{C}_{\mathbf{s}}) =& \frac{M}{|\mathcal{N}_1|}(1-\overline{C}_{\mathbf{s}}) \sum_{\mathbf{s}'\in\mathcal{N}_1\{\mathbf{s}\}} \overline{C}_{\mathbf{s}'} \frac{G(\overline{K}^{(\mathrm{m})}_{\mathbf{s}'})}{1-\overline{K}^{(\mathrm{m})}_{\mathbf{s}'}} - M\overline{C}_{\mathbf{s}} G(\overline{K}^{(\mathrm{m})}_{\mathbf{s}}) \\ &+ \frac{P}{|\mathcal{N}_4|}(1-\overline{C}_{\mathbf{s}}) \sum_{\mathbf{s}'\in\mathcal{N}_4\{\mathbf{s}\}} \mathbb{H}(F(\overline{K}^{(\mathrm{g})}_{\mathbf{s}'}))\overline{C}_{\mathbf{s}'} \frac{F(\overline{K}^{(\mathrm{g})}_{\mathbf{s}'})}{1-\overline{K}^{(\mathrm{g})}_{\mathbf{s}'}} \\ &- (1-\mathbb{H}(F(\overline{K}^{(\mathrm{g})}_{\mathbf{s}}))P\overline{C}_{\mathbf{s}} F(\overline{K}^{(\mathrm{g})}_{\mathbf{s}}).\end{aligned} \tag{2.21}$$

As we know that the continuum limit of the last two terms in Equation (2.21) leads to a source term $\lambda CF(C)$ (Jin et al. 2016a), we focus on the movement mechanism, that is, the first two terms on the right hand side of Equation (2.21). For convenience, we will omit the overlines on notations in the following content.

It is useful to first write the general form of the Taylor series relating the occupancy of sites $(x+a, y+b)$,

$$\begin{aligned}C_{x+a,y+b} =& C_{x,y} + \frac{(a\Delta)^1}{1!}\frac{\partial C_{x,y}}{\partial x} + \frac{(b\Delta)^1}{1!}\frac{\partial C_{x,y}}{\partial y} \\ &+ \frac{(a\Delta)^2}{2!}\frac{\partial C^2_{x,y}}{\partial x^2} + \frac{2ab\Delta^2}{2!}\frac{\partial C^2_{x,y}}{\partial x\partial y} + \frac{(b\Delta)^2}{2!}\frac{\partial C^2_{x,y}}{\partial y^2} + \mathcal{O}(\Delta^3).\end{aligned} \tag{2.22}$$

We represent the six nearest neighbouring sites of site $\mathbf{s}$ located at (x, y) as site $\mathbf{s}_1$ with $(x-\Delta, y)$; site $\mathbf{s}_2$ with $(x+\Delta, y)$; site $\mathbf{s}_3$ with $(x-\Delta/2, y+\Delta\sqrt{3}/2)$; site $\mathbf{s}_4$ with $(x+\Delta/2, y+\Delta\sqrt{3}/2)$; site $\mathbf{s}_5$ with $(x-\Delta/2, y-\Delta\sqrt{3}/2)$ and site $\mathbf{s}_6$ with $(x+\Delta/2, y-\Delta\sqrt{3}/2)$. That is, $\mathcal{N}_1 = \{\mathbf{s}_1, \mathbf{s}_2, \mathbf{s}_3, \mathbf{s}_4, \mathbf{s}_5, \mathbf{s}_6\}$. The truncated Taylor series of these sites are

$$C_{\mathbf{s}_1} = C_{\mathbf{s}} - \frac{\partial C_{\mathbf{s}}}{\partial x}\Delta + \frac{\partial^2 C_{\mathbf{s}}}{\partial x^2}\frac{\Delta^2}{2} + \mathcal{O}(\Delta^3), \tag{2.23}$$

$$C_{\mathbf{s}_2} = C_{\mathbf{s}} + \frac{\partial C_{\mathbf{s}}}{\partial x}\Delta + \frac{\partial^2 C_{\mathbf{s}}}{\partial x^2}\frac{\Delta^2}{2} + \mathcal{O}(\Delta^3), \tag{2.24}$$

$$C_{\mathbf{s}_3} = C_{\mathbf{s}} - \frac{\partial C_{\mathbf{s}}}{\partial x}\frac{\Delta}{2} + \frac{\partial C_{\mathbf{s}}}{\partial y}\frac{\sqrt{3}\Delta}{2} + \left[\frac{1}{4}\frac{\partial^2 C_{\mathbf{s}}}{\partial x^2} + \frac{3}{4}\frac{\partial^2 C_{\mathbf{s}}}{\partial y^2} - \frac{\sqrt{3}}{2}\frac{\partial^2 C_{\mathbf{s}}}{\partial x \partial y}\right]\frac{\Delta^2}{2} + \mathcal{O}(\Delta^3), \tag{2.25}$$

$$C_{\mathbf{s}_4} = C_{\mathbf{s}} + \frac{\partial C_{\mathbf{s}}}{\partial x}\frac{\Delta}{2} + \frac{\partial C_{\mathbf{s}}}{\partial y}\frac{\sqrt{3}\Delta}{2} + \left[\frac{1}{4}\frac{\partial^2 C_{\mathbf{s}}}{\partial x^2} + \frac{3}{4}\frac{\partial^2 C_{\mathbf{s}}}{\partial y^2} + \frac{\sqrt{3}}{2}\frac{\partial^2 C_{\mathbf{s}}}{\partial x \partial y}\right]\frac{\Delta^2}{2} + \mathcal{O}(\Delta^3), \tag{2.26}$$

$$C_{\mathbf{s}_5} = C_{\mathbf{s}} - \frac{\partial C_{\mathbf{s}}}{\partial x}\frac{\Delta}{2} - \frac{\partial C_{\mathbf{s}}}{\partial y}\frac{\sqrt{3}\Delta}{2} + \left[\frac{1}{4}\frac{\partial^2 C_{\mathbf{s}}}{\partial x^2} + \frac{3}{4}\frac{\partial^2 C_{\mathbf{s}}}{\partial y^2} + \frac{\sqrt{3}}{2}\frac{\partial^2 C_{\mathbf{s}}}{\partial x \partial y}\right]\frac{\Delta^2}{2} + \mathcal{O}(\Delta^3), \tag{2.27}$$

$$C_{\mathbf{s}_6} = C_{\mathbf{s}} + \frac{\partial C_{\mathbf{s}}}{\partial x}\frac{\Delta}{2} - \frac{\partial C_{\mathbf{s}}}{\partial y}\frac{\sqrt{3}\Delta}{2} + \left[\frac{1}{4}\frac{\partial^2 C_{\mathbf{s}}}{\partial x^2} + \frac{3}{4}\frac{\partial^2 C_{\mathbf{s}}}{\partial y^2} - \frac{\sqrt{3}}{2}\frac{\partial^2 C_{\mathbf{s}}}{\partial x \partial y}\right]\frac{\Delta^2}{2} + \mathcal{O}(\Delta^3). \tag{2.28}$$

The local density of $\mathbf{s}$ is obtained by summing the Taylor series of sites in $\mathcal{N}_1\{\mathbf{s}\}$, that is,

$$\begin{aligned} K_{\mathbf{s}}^{(\mathrm{m})} &= \frac{1}{6}\sum_{\mathbf{s}'' \in \mathcal{N}_1\{\mathbf{s}\}} C_{\mathbf{s}''} \\ &= C_{\mathbf{s}} + \left(\frac{\partial^2 C_{\mathbf{s}}}{\partial x^2} + \frac{\partial^2 C_{\mathbf{s}}}{\partial y^2}\right)\frac{\Delta^2}{4} + \mathcal{O}(\Delta^3). \end{aligned} \tag{2.29}$$

Similarly, the local density of $\mathbf{s_1}$ is obtained by summing the Taylor series of sites in $\mathcal{N}_1\{\mathbf{s}_1\}$, that is,

$$\begin{aligned} K_{\mathbf{s}_1}^{(\mathrm{m})} &= \frac{1}{6}\sum_{\mathbf{s}'' \in \mathcal{N}_1\{\mathbf{s}_1\}} C_{\mathbf{s}''} \\ &= C_{\mathbf{s}_1} + \left(\frac{\partial^2 C_{\mathbf{s}_1}}{\partial x^2} + \frac{\partial^2 C_{\mathbf{s}_1}}{\partial y^2}\right)\frac{\Delta^2}{4} + \mathcal{O}(\Delta^3), \\ &= C_{\mathbf{s}} - \frac{\partial C_{\mathbf{s}}}{\partial x}\Delta + \frac{\partial^2 C_{\mathbf{s}}}{\partial x^2}\frac{\Delta^2}{2} + \left(\frac{\partial^2 C_{\mathbf{s}}}{\partial x^2} + \frac{\partial^2 C_{\mathbf{s}}}{\partial y^2}\right)\frac{\Delta^2}{4} + \mathcal{O}(\Delta^3). \end{aligned} \tag{2.30}$$

For simplification we rewrite Equation (2.30) as $K_{\mathbf{s}_1}^{(\mathrm{m})} = C_{\mathbf{s}} + \widetilde{C}_{\mathbf{s}_1}$, where $\widetilde{C}_{\mathbf{s}_1} \sim \mathcal{O}(\Delta)$. Subsequently, the movement crowding function at $\mathbf{s}_1$ can be expanded as

$$\begin{aligned} G\left(K_{\mathbf{s}_1}^{(\mathrm{m})}\right) &= G\left(C_{\mathbf{s}} + \widetilde{C}_{\mathbf{s}_1}\right), \\ &= G\left(C_{\mathbf{s}}\right) + \frac{\mathrm{d}G\left(C_{\mathbf{s}}\right)}{\mathrm{d}C}\widetilde{C}_{\mathbf{s}_1} + \frac{\mathrm{d}^2 G\left(C_{\mathbf{s}}\right)}{\mathrm{d}C^2}\frac{\widetilde{C}_{\mathbf{s}_1}^2}{2}. \end{aligned} \tag{2.31}$$

The expansions of $G(K_{\mathbf{s}_2}^{(\mathrm{m})})$, $G(K_{\mathbf{s}_3}^{(\mathrm{m})})$,...,$G(K_{\mathbf{s}_6}^{(\mathrm{m})})$ have similar forms to (2.31). We then

go back to the first term on the right hand side of (2.21), which gives

$$\frac{M}{6}(1-C_{\mathbf{s}})\sum_{\mathbf{s}'\in\mathcal{N}_1\{\mathbf{s}\}}C_{\mathbf{s}'}\frac{G(K_{\mathbf{s}'}^{(\mathrm{m})})}{1-K_{\mathbf{s}'}^{(\mathrm{m})}}. \tag{2.32}$$

For convenience we further drop the $\mathbf{s}$ notation so that $C_{\mathbf{s}}$ becomes C and $C_{\mathbf{s}_1}$ becomes C_1. Subsequently, (2.32) becomes

$$\frac{M}{6}(1-C)\sum_{i=1}^{6}C_i\frac{G(K_{\mathbf{s}_i}^{(\mathrm{m})})}{1-K_{\mathbf{s}_i}^{(\mathrm{m})}}. \tag{2.33}$$

Moreover, we will use two notations

$$\mathcal{A}=\left(\frac{\partial^2 C_{\mathbf{s}}}{\partial x^2}+\frac{\partial^2 C_{\mathbf{s}}}{\partial y^2}\right)\frac{\Delta^2}{4},\quad \mathcal{B}=\left(\left(\frac{\partial C_{\mathbf{s}}}{\partial x}\right)^2+\left(\frac{\partial C_{\mathbf{s}}}{\partial y}\right)^2\right)\frac{\Delta^2}{4}, \tag{2.34}$$

in the following content. Expanding the term related to site $\mathbf{s}_1$ in (2.33) gives

$$\begin{aligned}
&\frac{M}{6}(1-C)\left(C+\widetilde{C}_1-\mathcal{A}\right)\frac{\left(G(C)+G'(C)\widetilde{C}_1+G''(C)\dfrac{\widetilde{C}_1^2}{2}\right)}{1-\left(C+\widetilde{C}_1\right)}\\
=&\frac{M}{6}\left[CG(C)+\left(CG'(C)+\frac{G(C)}{1-C}\right)\widetilde{C}_1\right]\\
&+\frac{M}{6}\left[\left(\frac{G(C)}{(1-C)^2}+\frac{G'(C)}{1-C}+\frac{CG''(C)}{2}\right)\widetilde{C}_1^2-G(C)\mathcal{A}\right]+\mathcal{O}(\Delta^3).
\end{aligned}$$

The terms related to other sites can be obtained in a similar way. Therefore, expanding all terms in (2.33) and neglecting terms of order $\mathcal{O}(\Delta^3)$ gives

$$\begin{aligned}
&\frac{M}{6}\left[6CG(C)+\left(CG'(C)+\frac{G(C)}{1-C}\right)\sum_{k=1}^{6}\widetilde{C}_k\right]\\
&+\frac{M}{6}\left[\left(\frac{G(C)}{(1-C)^2}\frac{G'(C)}{1-C}+\frac{CG''(C)}{2}\right)\sum_{k=1}^{6}\widetilde{C}_k^2-6G(C)\mathcal{A}\right].
\end{aligned} \tag{2.35}$$

Furthermore, since we have

$$\begin{aligned}
\sum_{k=1}^{6}\widetilde{C}_k&=12\left(\frac{\partial^2 C}{\partial x^2}+\frac{\partial^2 C}{\partial y^2}\right)\frac{\Delta^2}{4}+\mathcal{O}(\Delta^3),\\
&=12\mathcal{A}+\mathcal{O}(\Delta^3),
\end{aligned} \tag{2.36}$$

and

$$\begin{aligned}\sum_{k=1}^{6}\widetilde{C}_k^2 &= 12\left(\left(\frac{\partial C}{\partial x}\right)^2+\left(\frac{\partial C}{\partial y}\right)^2\right)\frac{\Delta^2}{4}+\mathcal{O}(\Delta^3),\\ &= 12\mathcal{B}+\mathcal{O}(\Delta^3),\end{aligned} \tag{2.37}$$

Equation (2.35) becomes

$$\begin{aligned}&MCG(C)+M\left(2CG'(C)-G(C)+\frac{2G(C)}{1-C}\right)\mathcal{A}\\ &+M\left(CG''(C)+\frac{2G(C)}{(1-C)^2}+\frac{2G'(C)}{1-C}\right)\mathcal{B}+\mathcal{O}(\Delta^3).\end{aligned} \tag{2.38}$$

Remind that the second term in (2.21) is

$$\begin{aligned}MCG(\overline{K}_{\mathbf{s}}^{(\mathrm{m})}) &= MCG(C)+MCG'(C)\widetilde{C},\\ &= MCG(C)+MCG'(C)\mathcal{A}+\mathcal{O}(\Delta^3).\end{aligned} \tag{2.39}$$

Then combining (2.38) and (2.39) gives

$$\begin{aligned}\delta(C_{\mathbf{s}}) = &\left(CG'(C)+\frac{1+C}{1-C}G(C)\right)M\mathcal{A}\\ &+\left(CG''(C)+\frac{2G(C)}{(1-C)^2}+\frac{2G'(C)}{1-C}\right)M\mathcal{B}+\mathcal{O}(\Delta^3).\end{aligned} \tag{2.40}$$

Dividing both sides of the resulting expression by τ, and letting $\Delta\to 0$ and $\tau\to 0$ jointly, with the ratio Δ^2/τ held constant, leads to the following nonlinear reaction-diffusion equation,

$$\frac{\partial C}{\partial t} = D_0\nabla\cdot\left[\left(CG'(C)+\frac{1+C}{1-C}G(C)\right)\nabla C\right]+\lambda CF(C), \tag{2.41}$$

where

$$D_0 = \frac{M}{4}\lim_{\Delta,\tau\to 0}\frac{\Delta^2}{\tau},\quad \lambda = \lim_{\tau\to 0}\frac{P}{\tau}. \tag{2.42}$$

If we define

$$D(C) = CG'(C)+\frac{1+C}{1-C}G(C), \tag{2.43}$$

then the continuum limit is written as

$$\frac{\partial C}{\partial t} = D_0\nabla\cdot[D(C)\nabla C]+\lambda CF(C). \tag{2.44}$$

2.9.2 Algorithm for discrete simulations

Algorithm 1: Pseudo-code for a single realisation of the stochastic model

Create a two-dimensional $I \times J$ hexagonal lattice; Distribute agents with specific initial conditions; The total number of lattice site is IJ;
Set $t = 0$; Calculate total agents $Q(t)$;
while $t < t_{\text{end}}$ and $Q(t) > 0$ and $Q(t) \leq IJ$ **do**
    $t = t + \tau$;
    $Q(t) = Q(t - \tau)$;
    $B_1 = 0$; $B_2 = 0$;
    Draw two random variables: $\beta_1 \sim U[0, 1]$, $\beta_2 \sim U[0, 1]$;
    while $B_1 < Q(t)$ **do**
        $B_1 = B_1 + 1$;
        Randomly choose an agent $\mathbf{s}$;
        if $\beta_1 < M$ **then**
            Calculate $\overline{K}_{\mathbf{s}}^{(\mathrm{m})}$ and $G(\overline{K}_{\mathbf{s}}^{(\mathrm{m})})$;
            Draw a random variable: $\gamma_1 \sim U[0, 1]$;
            if $\gamma_1 < G(\overline{K}_{\mathbf{s}}^{(\mathrm{m})})$ **then**
                Randomly choose a vacant site in $\mathcal{N}_1(\mathbf{s})$ and move agent to chosen site
            else
                Nothing happens;
            end
        else
            Nothing happens;
        end
    end
    while $B_2 < Q(t)$ **do**
        $B_2 = B_2 + 1$;
        Randomly choose an agent $\mathbf{s}$;
        if $\beta_2 < P$ **then**
            Calculate $K_{\mathbf{s}}^{(\mathrm{g})}$ and $F(\overline{K}_{\mathbf{s}}^{(\mathrm{g})})$;
            Calculate a random variable: $\gamma_2 \sim U[0, 1]$;
            if $F(\overline{K}_{\mathbf{s}}^{(\mathrm{g})}) > 0$ **then**
                if $\gamma_2 < F(\overline{K}_{\mathbf{s}}^{(\mathrm{g})})$ **then**
                    Randomly choose a vacant site in $\mathcal{N}_4(\mathbf{s})$ and place a new agent on chosen site;
                    $Q(t) = Q(t) + 1$
            else if $F(\overline{K}_{\mathbf{s}}^{(\mathrm{g})}) < 0$ **then**
                if $\gamma_2 < -F(\overline{K}_{\mathbf{s}}^{(\mathrm{g})})$ **then**
                    Remove agent;
                    $Q(t) = Q(t) - 1$;
            else
                Nothing happens;
            end
        else
            Nothing happens;
        end
    end
end

2.9.3 Numerical methods

Here, we introduce the method of lines to numerically calculate solutions of the PDE

$$\frac{\partial C}{\partial t} = D_0 \nabla^2 C + \lambda C F(C), \tag{2.45}$$

on a square domain $\Omega = \{(x, y), 0 < x < L,\ 0 < y < L\}$. We first discretise the spatial derivative in Equation (2.45) with an $(I + 1) \times (I + 1)$ mesh. Nodes on the mesh are uniformly distributed with spacing $\delta x > 0$ and indexed by x_i and y_j with $i = 0, 1, 2, ..., I$ and $j = 0, 1, 2, ..., I$ satisfying $I = L/\delta x$. We leave the time derivative continuous and obtain

$$\frac{\mathrm{d}C_{i,j}}{\mathrm{d}t} = \frac{D_0}{\delta x^2}(C_{i+1,j} + C_{i-1,j} + C_{i,j+1} + C_{i,j-1} - 4C_{i,j}) + \lambda C_{i,j} F(C_{i,j}). \tag{2.46}$$

This equation is valid for interior nodes, and is modified on the boundary nodes to simulate periodic boundary conditions. This system of $I \times I$ coupled ordinary differential equations is then integrated through time using MATLABs function ode45 (MATLAB 2020). Following similar steps, we can also calculate the numerical solution of the PDE

$$\frac{\partial C}{\partial t} = D_0 \frac{\partial^2 C}{\partial x^2} + \lambda C F(C). \tag{2.47}$$

2.9.4 Comparisons of discrete and continuum results

In this section we compare the averaged data from the discrete simulations to the continuum solutions with the well-mixed, vertical strip and square initial distributions. Results in Figure 2.9 compare the discrete and continuum solutions for the well-mixed initial distribution. In Figure 2.9(a), a fixed number of agents are randomly distributed in the entire domain at $T = \lambda t = 0$, leading to $\langle C(0) \rangle = 0.25$. Figures 2.9(b)–(c) show discrete snapshots as the population evolves with $M = 1$ and $P = 1/1000$, leading to $\lambda = 1/1000$. We superimpose the solution of Equation (15) in the main document with averaged data from the discrete model in Figure 2.9(d). The continuum model gives a good approximation to the averaged discrete data, and in this case we see that the population becomes extinct. Note that we generate $V = 40$ identically-prepared realisations to obtain $\langle C(T) \rangle$ in Figure 2.9(d) and (h).

We now consider the exact same discrete mechanism with a larger initial number of agents giving $\langle C(0) \rangle = 0.64$ in Figure 2.9(e). Figures 2.9(f)–(g) again show discrete snapshots as the population evolves, and we observe that $C(T)$ approximates $\langle C(T) \rangle$ well in Figure 2.9(h). In this case the population survives and grows to reach the maximum

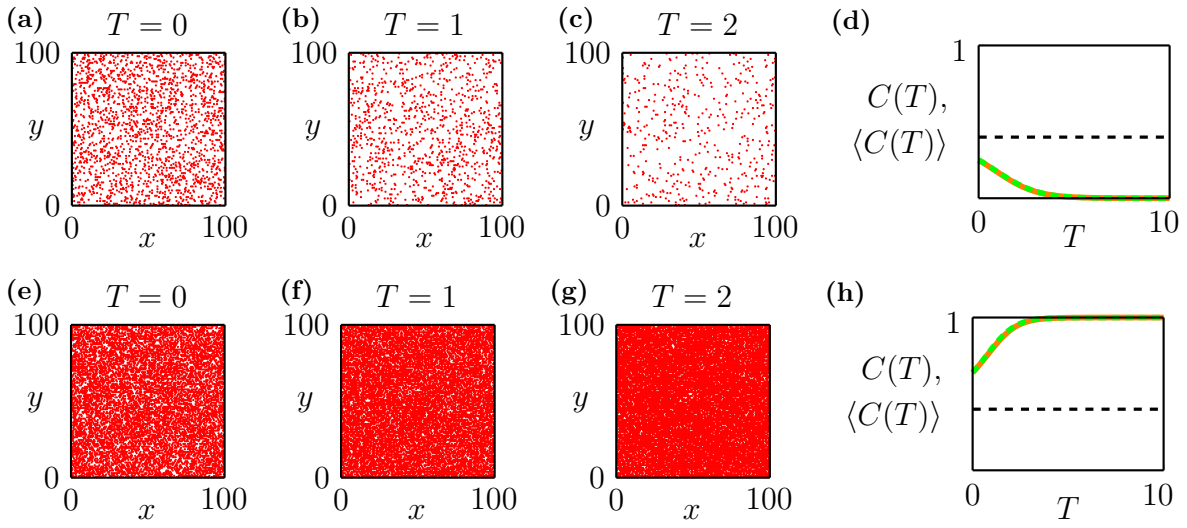

Figure 2.9: **Comparison of data from the discrete model with the solution of the continuum model for the well-mixed initial distribution.** (a)–(c) Snapshots of discrete simulations at time $T = \lambda t = 0, 1, 2$. At $T = 0$ a fixed number of agents are randomly distributed on the lattice so that $\langle C(0)\rangle = 0.25$. (d) $\langle C(T)\rangle$ (solid orange) and $C(T)$ (dashed green). (e)–(g) Snapshots of discrete simulations at time $T = 0, 1, 2$ with $\langle C(0)\rangle = 0.64$. (h) $\langle C(T)\rangle$ (solid orange) and $C(T)$ (dashed green). The dashed black horizontal lines in (d) and (h) are the Allee threshold, $A = 0.4$.

density.

Results in Figure 2.10 give a comparison between the discrete and continuum solutions for the vertical strip initial distribution. Simulations are performed with $M = 1$ and $P = 1/1000$, leading to $D_0 = 1/4$ and $\lambda = 1/1000$. The initial distribution in Figure 2.10(a) shows that the central strip of width 25 is occupied with density $B = 1$. Figures 2.10(b)–(c) show snapshots from the discrete model as the population spreads into the domain. Figure 2.10(d) compares the numerical solution of Equation (2.47), $C(x, T)$, with averaged data from the discrete model, $\langle C(x, T)\rangle$. The evolution of the total population density in the discrete model, $\langle C(T)\rangle$, and in the continuum model, $\mathcal{C}(T)$, is compared in Figure 2.10(e). In all cases the continuum model accurately captures the averaged data from the discrete model, and in this case the population eventually becomes extinct. This is an interesting result given that the initial density in the central strip is greater than the Allee threshold, yet the total population eventually becomes extinct as the migration of individuals reduces the population density locally to below the Allee threshold.

We then consider a second set of discrete-continuum comparisons for precisely the same mechanisms except that the spatial arrangement of the vertical strip initial distribution, shown in Figure 2.10(f), is wider and occupies the central vertical strip of width 64 with density $B = 1$. Figures 2.10(g)–(h) show discrete snapshots as the population spreads. The comparisons between $C(x, T)$ and $\langle C(x, T)\rangle$ in Figure 2.10(i), and between $\mathcal{C}(T)$ and $\langle C(T)\rangle$ in Figure 2.10(j) are excellent. In this case we see that the population eventually

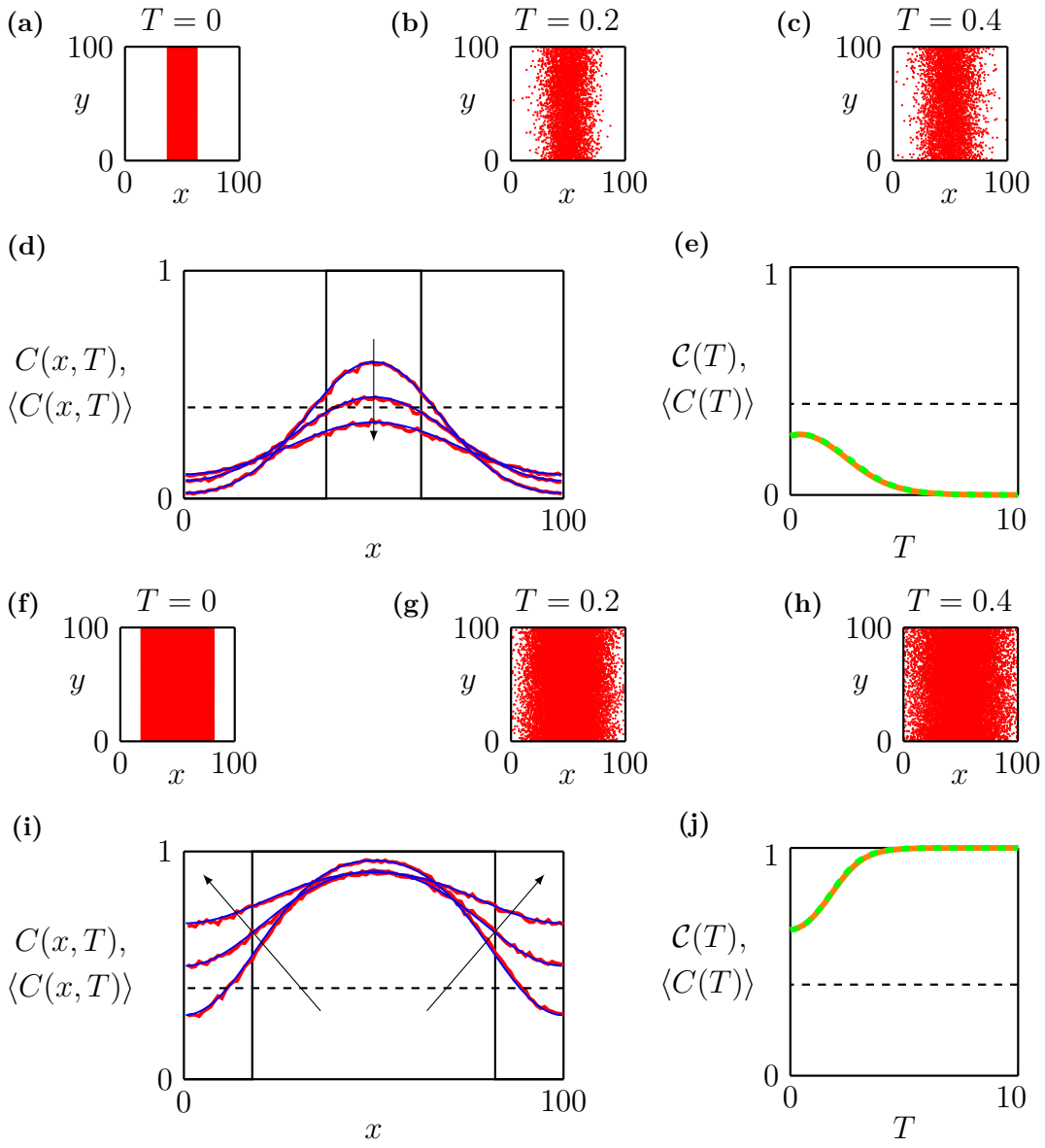

Figure 2.10: **Comparison of data from the discrete model with the solution of the continuum model for the vertical strip initial distribution.** (a) Agents are initially placed within a vertical strip where $x \in [37.5, 62.5]$, with $B = 1$. (b)–(c) Snapshots from the discrete model at $T = 0.1$ and $T = 0.2$, respectively. (d) $\langle C(x,T)\rangle$ (red) and $C(x,T)$ (blue) at time $T = 0.6, 1, 2, 1.8$. (e) $\langle C(t)\rangle$ (solid orange) and $\mathcal{C}(t)$ (dashed green). (f) Agents are initially placed within a vertical strip where $x \in [18, 82]$, with $B = 1$. (g)–(h) Snapshots from the discrete model at $T = 0.1$ and $T = 0.2$, respectively. (i) $\langle C(x,T)\rangle$ (red) and $C(x,T)$ (blue) at time $T = 0.6, 1.2, 1.8$. (j) $\langle C(t)\rangle$ (solid orange) and $\mathcal{C}(t)$ (dashed green). The dashed black horizontal lines in (d), (e), (i) and (j) indicate the Allee threshold, $A = 0.4$. Arrows in (d) and (i) show the direction of increasing time. Note that we generate 40 identically-prepared realisations to obtain $\langle C(x,T)\rangle$ in (d) and (i), and $\langle C(T)\rangle$ in (e) and (j).

grows to reach the maximum density. For the vertical strip initial distribution the same discrete mechanism again leads to different long-term outcomes in Figures 2.10(a)–(e) and Figures 2.10(f)–(j), where the population eventually becomes extinct in the former case, while surviving in the latter case. The only difference is in the width of the initial population.

In Figure 2.11, we compare data from the discrete model with numerical solutions of the continuum model for the square initial distribution. Again, simulations are performed with $M = 1$ and $P = 1/1000$, leading to $D_0 = 1/4$ and $\lambda = 1/1000$. The initial distribution in Figure 2.11(a) shows a square region of size 50×50 that is occupied with density $B = 1$. Figure 2.11(b) shows a snapshot from the discrete model at $T = \lambda t = 0.5$ where we see the agents spreading into the domain. The numerical solution of Equation (2.45) in Figure 2.11(c) shows the solution of the continuum model at $T = 0.5$. The visual comparison between the spatial arrangement of agents in the discrete model and the density of the profiles in Figure 2.11(b) and Figure 2.11(c) matches well. To make a more quantitative comparison we examine the density along the horizontal dashed lines shown in Figures 2.11(b)–(c) at $y = 50$. Figure 2.11(d) compares the evolution of $C(x, 50, T)$ and $\langle C(x, 50, T)\rangle$, and we see that the match between the solution of the continuum model and appropriately averaged data from the discrete model is excellent. Finally, in Figure 2.11(e) we compare the averaged total occupancy from the discrete model, $\langle C(T)\rangle$, with $\mathcal{C}(T)$ from the solution of the continuum model. Again, we see that the discrete-continuum comparison is excellent, and that the continuum model predicts the eventual extinction of this population. Similar to the outcomes from the one-dimensional initial distributions, although the initial density of agents in the central of the domain exceeds the Allee threshold, the migration of individuals reduces the density locally to below the Allee threshold, resulting in extinction.

We now consider a second set of discrete-continuum comparisons for precisely the same mechanisms except that the spatial arrangement of the square initial distribution, shown in Figure 2.11(f), is larger and occupies the central 80×80 region of the domain. As before, the match between the discrete averaged data and numerical solutions of Equation (2.45) is excellent in Figures 2.11(g)–(j). In this case the population eventually grows to reach the maximum density.

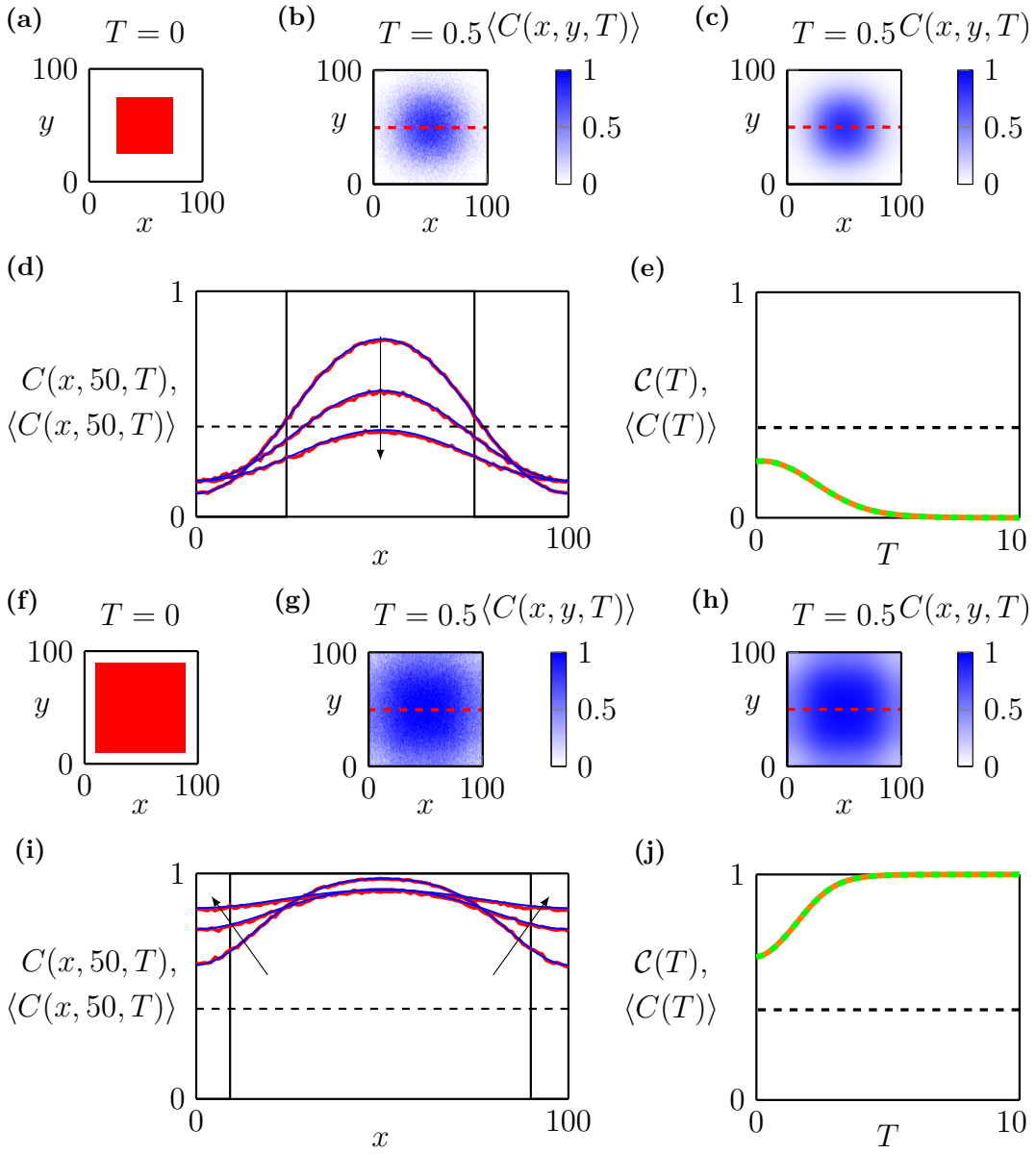

Figure 2.11: **Comparison of data from the discrete model with the solution of the continuum model for the square initial distribution.** (a) Agents are initially located in a square region of size 40×40 with $B = 1$. (b) $\langle C(x,y,T) \rangle$ at $T = \lambda t = 0.5$. (c) $C(x,y,T)$ at $T = \lambda t = 0.5$. (d) $\langle C(x,50,T) \rangle$ (red) and $C(x,50,T)$ (blue) at $T = 0.6, 1.2, 1.8$. (e) $\langle C(T) \rangle$ (solid grey) and $\mathcal{C}(T)$ (dashed green). (f) Agents are initially located at a square region of size 80×80 with $B = 1$. (g) $\langle C(x,y,T) \rangle$ at $T = \lambda t = 0.5$. (h) $C(x,y,T)$ at time $T = \lambda t = 0.5$. (i) $\langle C(x,50,T) \rangle$ (red) and $C(x,50,T)$ (blue) at $T = 0.6, 1.2, 1.8$. (j) $\langle C(T) \rangle$ (solid grey) and $\mathcal{C}(T)$ (dashed green). The dashed red lines in (b), (e), (g), (h) indicate the line $y = 50$, where we obtain the density along the horizontal direction. The dashed black horizontal lines in (d), (e), (i) and (j) indicate the Allee threshold, $A = 0.4$. Arrows in (d) and (i) show the direction of increasing time. Note that we generate 40 identically-prepared realisations to obtain $\langle C(x,y,T) \rangle$ in (b) and (g), and $\langle C(T) \rangle$ in (e) and (j). While we use 4000 identically-prepared realisations to obtain $\langle C(x,50,T) \rangle$ in (d) and (i).

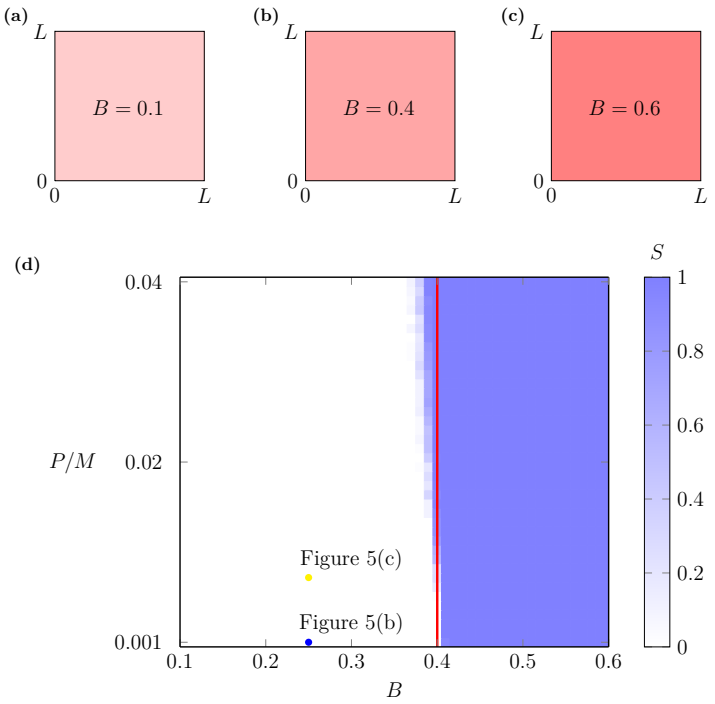

Figure 2.12: **Phase diagram for survival/extinction with the well-mixed initial distribution**. (a)–(c) show how we vary the initial density with $C(0) = B$ for this initial distribution. (d) Phase diagram of a rectangular mesh with 51×40 nodes for $C(0) = B \in [1/10, 6/10]$, and $P/M \in [1/1000, 4/100]$. The vertical red line indicates the survival/extinction threshold from the continuum model and the blue shading shows the survival probability S measured by 40 identically-prepared realisations. The blue dot indicates the parameters in Figure 5(b) in the main document. The yellow dot indicates the parameters in Figure 5(c) in the main document.

2.9.5 Phase diagrams with $B = 1$

In this section we summarise the long-term outcomes of a range of scenarios with the well-mixed, vertical strip and square initial distributions with $B = 1$. Results in Figure 2.12 show the results obtained with the well-mixed initial distribution. In this case $\mathcal{H}$ corresponds to the entire $L \times L$ domain and $C(0) = B$. We vary the initial distribution by varying B, as indicated in Figures 2.12(a)–(c), and vary the ratio P/M by holding $M = 1$ and varying $P \in [1/1000, 4/100]$ in the discrete model. As $P/M = \lambda/(4D_0)$, we hold $D_0 = 1/4$ and vary λ in the continuum model. To systematically study the transition between population extinction to population survival, we take the $(B, P/M)$ phase space and discretise it uniformly into a rectangular mesh, with 51×40 nodes. We note that, unlike the continuum approach that always leads to the same outcome when using the same choice of parameters, different identically-prepared realisations of the stochastic model can lead to different outcomes (Surendran et al. 2020; Johnston et al. 2020). Therefore, for each value of B and P/M considered, we generate 40 identically-prepared realisations of the discrete model and we compute the survival probability, $S \in [0, 1]$, as the fraction of realisations in which

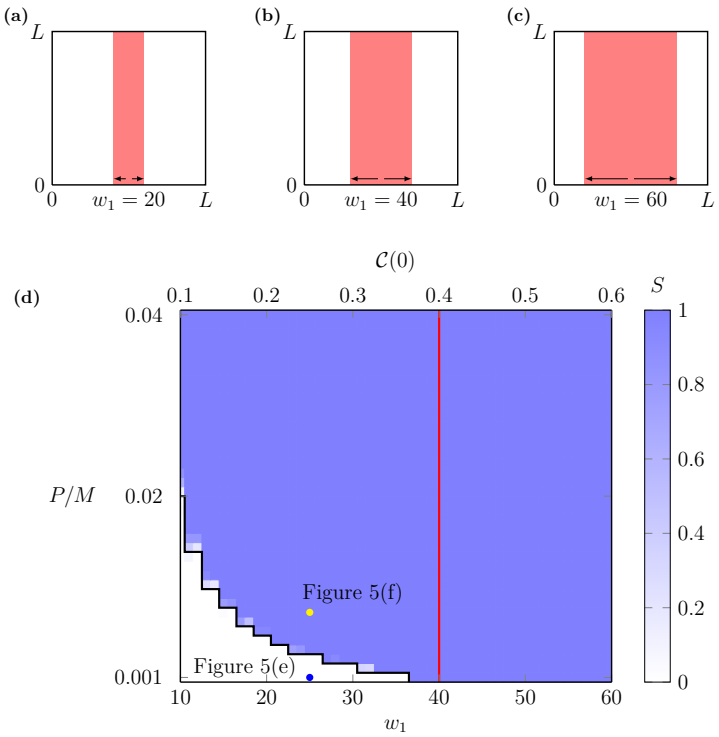

Figure 2.13: **Phase diagram for survival/extinction with the vertical strip initial distribution**. (a)–(c) Three different initial distributions where $\mathcal{C}(0) = w_1/L$, and we vary w_1. (d) Phase diagram of a rectangular mesh with 51×40 nodes for $w_1 \in [10, 60]$, $\mathcal{C}(0) \in [1/10, 6/10]$ and $P/M \in [1/1000, 4/100]$. The black curve indicates the survival/extinction threshold from the continuum model and the blue shading shows the survival probability S measured by 40 identically-prepared realisations. The vertical red line is $\mathcal{C}(0) = 0.4$ which relates to the Allee threshold, $A = 0.4$. The blue dot indicates the parameters in Figure 5(e) in the main document. The yellow dot indicates the parameters in Figure 5(f) in the main document.

the population survives after a sufficiently long period of time $\mathcal{T}$, which we take to be $\mathcal{T} = \max(30/P, 10^4)$. Figure 2.12(d) summarises the outcomes of the simulations in terms of a phase diagram. In this case the survival outcome for the continuum model is a simple vertical line at $C(0) = A$. In general we see good agreement between the prediction of survival or extinction between the continuum and discrete models.

There are some small discrepancies as P/M increases. In discrete simulations, the local clustering caused by larger P/M leads to higher local densities and thus contributes to the survival of populations, which reflects the influence of stochasticity in the discrete model. This difference is consistent with the fact that for the continuum model P/M has to be sufficiently small, otherwise the mean-field approximation is invalid and the solution of the continuum model does not necessarily provide an accurate description of the discrete mechanism (Baker and Simpson 2010; Simpson et al. 2010a). In summary, for the well-mixed initial distribution the long-term population survival depends simply upon whether the initial density is above or below the Allee threshold, as expected.

We now explore how the simple outcome for the well-mixed initial distribution becomes more complicated when we consider different initial spatial arrangements of the population. For the vertical strip initial distribution we vary the size of $\mathcal{H}$ by changing the width of the vertical strip, w_1. Varying the width of the strip leads to a change in the initial density across the entire domain, $\mathcal{C}(0) = w_1/L$. For example, Figures 2.13(a)–(c) shows three vertical strip initial distributions with different widths. For these initial distributions we vary the ratio $P/M = \lambda/(4D_0)$ by holding $M = 1$ and varying P in the discrete model, and by holding $D_0 = 1/4$ and varying λ in the continuum model. This allows us to consider the $(w_1, P/M)$ phase space, which we discretise into a rectangular mesh with 51×40 nodes. Figure 2.13(b) shows a phase diagram illustrating how the survival probability, S, depends upon w_1 and P/M. The boundary that separates the eventual survival and extinction in the continuum model is shown in solid black, and the survival probability from the discrete simulations is shown in blue shading. Overall, the long-term predictions in terms of survival or extinction are consistent between the continuum and discrete models. For completeness we also show the red vertical line indicating the Allee threshold in the sense of global population density averaged across the whole $L \times L$ domain. It is interesting to compare the results in Figure 2.12(d) and Figure 2.13(d). In the vertical strip case we see that the long-term survival is strongly dependent upon P/M whereas in the well-mixed initial distribution this dependence is less pronounced.

For the square initial distribution, we vary the size of $\mathcal{H}$ by changing w_1 as shown in Figures 2.14(a)–(c). Varying w_1 allows us to vary the initial density across the entire domain, $\mathcal{C}(0) = w_1^2/L^2$. Similar to Figure 2.13, we construct a phase diagram in Figure 2.14(d) that summarises the long-term survival outcome as a function of w_1^2 and P/M, by discretising the $(w_1^2, P/M)$ phase space using a rectangular mesh with 51×40 nodes. The phase diagram in Figure 2.14(d) is very similar to the phase diagram in Figure 2.13(d). We see that the long-term survival strongly depends upon P/M, and the distinction between survival and extinction predicted by the continuum limit model is a good approximation of the discrete simulation data.

Results in Figures 2.12–2.14 show that the long-term survival of a population depends upon P/M and the initial arrangement of the population in a complicated manner. Stochasticity only plays a role on the fate of populations in the discrete model when parameters are close to the boundary that separates the eventual survival and extinction in the continuum model.

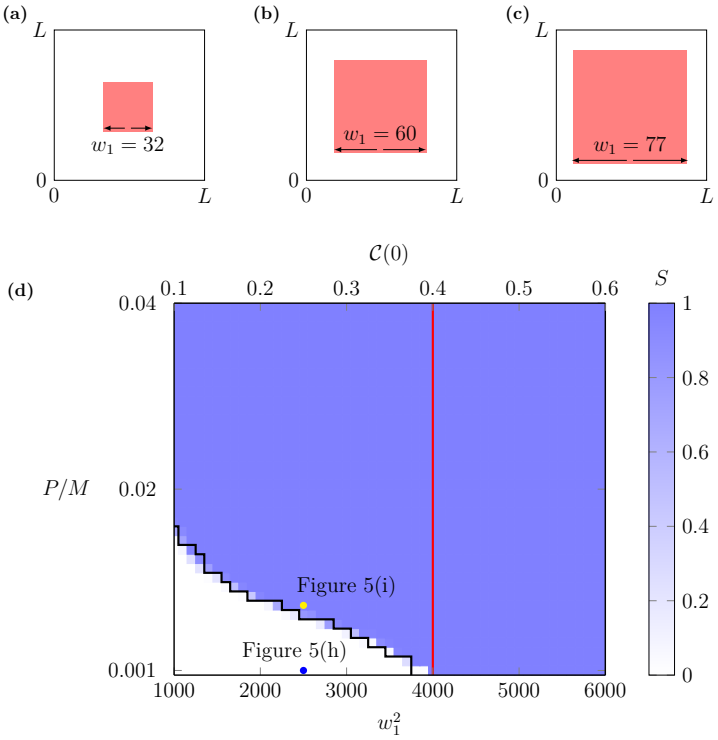

Figure 2.14: **Phase diagram for survival/extinction with the square initial distribution**. (a)–(c) Three different initial distributions where $\mathcal{C}(0) = w_1^2/L^2$, and we vary w_1. (d) Phase diagram of a rectangular mesh with 51×40 nodes for $w_1^2 \in [1000, 6000]$, $\mathcal{C}(0) \in [1/10, 6/10]$ and $P/M \in [1/1000, 4/100]$ where $M = 1$. The black curve indicates the survival/extinction threshold from the continuum model and the blue shading shows the survival probability S measured by 40 identically-prepared realisations. The vertical red line is $\mathcal{C}(0) = 0.4$ which relates to the Allee threshold, $A = 0.4$. The blue dot indicates the parameters in Figure 5(h) in the main document. The yellow dot indicates the parameters in Figure 5(i) in the main document.

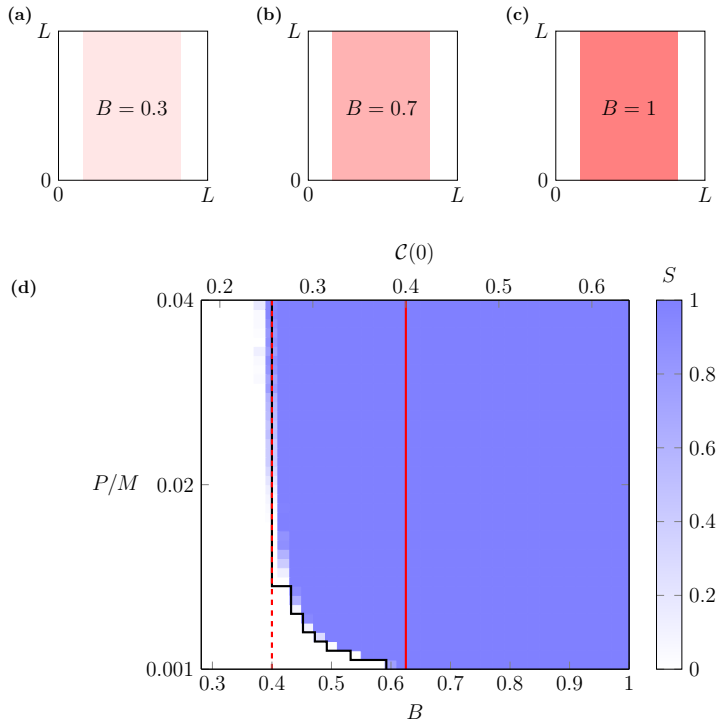

Figure 2.15: **Phase diagram for survival/extinction with the vertical strip initial distribution**. (a)–(c) Three different initial distributions where $\mathcal{C}(0) = Bw_1/L$, and we fix $w_1 = 64$ and vary B. (d) Phase diagram on a rectangular mesh with 36×40 nodes for $B \in [0.3, 1]$, $\mathcal{C}(0) \in [0.192, 0.64]$ and $P/M \in [1/1000, 4/100]$. The black curve indicates the survival/extinction threshold from the continuum model and the blue shading shows the survival probability S from the discrete simulations measured by 40 identically-prepared realisations. The vertical solid red line is $\mathcal{C}(0) = 0.4$. The vertical dashed line is $B = 0.4$. They both relate to the Allee threshold, $A = 0.4$.

2.9.6 Phase diagrams with $B \neq 1$

Instead of varying the size of $\mathcal{H}$, we now vary $\mathcal{C}(0)$ by varying B. We constrain the region $\mathcal{H}$ as a vertical strip with width $w_1 = 64$, as shown in Figure 2.15(a). As $\mathcal{C}(0) = Bw_1/L$, where we fix $w_1/L = 0.64$, the initial density $\mathcal{C}(0)$ varies from 0.192 to 0.64 when B varies from 0.3 to 1 as illustrated in Figures 2.15(a)–(c). We vary $P/M = \lambda/(4D_0)$ by holding $M = 1$ and varying $P \in [1/1000, 4/100]$ and we discretise the $(B, P/M)$ space into a rectangular mesh with 36×40 nodes. Figure 2.15(d) shows a phase diagram illustrating how the survival probability, S, depends upon B and P/M. The boundary that separates the eventual survival and extinction in the continuum model is shown in solid black, and the survival probability from the discrete simulations is shown in blue shading. The long–term predictions in terms of survival or extinction are consistent between the continuum and discrete models. Furthermore, we observe a different phenomenon compared to the results in Figure 10: There is a lower bound on $\mathcal{C}(0)$ for survival in Figure 2.15(d). This lower bound relates to $B = 0.4$, and indicates the Allee threshold $A = 0.4$. Unlike the solid

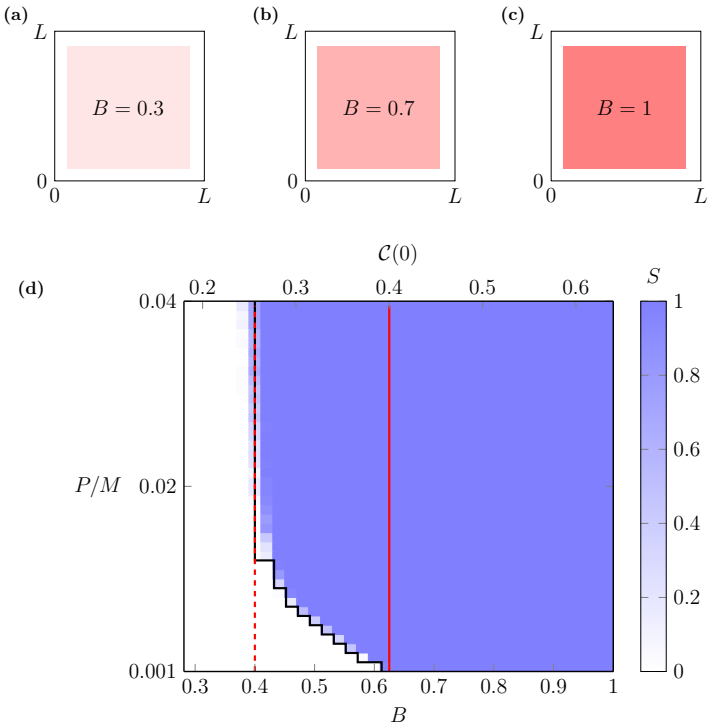

Figure 2.16: **Phase diagram for survival/extinction with the square initial distribution**. (a)–(c) Three different initial distributions where $\mathcal{C}(0) = Bw^2/L^2$, and we fix $w = 80$ and vary B. (d) Phase diagram on a rectangular mesh with 36×40 nodes for $B \in [0.3, 1]$, $\mathcal{C}(0) \in [0.192, 0.64]$ and $P/M \in [1/1000, 4/100]$. The black curve indicates the survival/extinction threshold from the continuum model and the blue shading shows the survival probability S from the discrete simulations measured by 40 identically-prepared realisations. The vertical solid red line is $\mathcal{C}(0) = 0.4$. The vertical dashed line is $B = 0.4$. They both relate to the Allee threshold, $A = 0.4$.

line, $\mathcal{C}(0) = 0.4$, which indicates a threshold of survival in the sense of global density, the dashed line, $B = 0.4$, indicates a threshold of survival in the sense of local density.

Next, we consider the square initial distribution and constrain the region with width $w_1 = 80$ in Figures 2.16(a)–(c). As $\mathcal{C}(0) = Bw_1^2/L^2$, where we fix $w_1^2/L^2 = 0.64$, the initial density $\mathcal{C}(0)$ varies from 0.192 to 0.64 when B varies from 0.3 to 1. We again change $P/M = \lambda/(4D_0)$ by holding $M = 1$ and varying $P \in [1/1000, 4/100]$ and we discretise the $(B, P/M)$ space into a rectangular mesh with 36×40 nodes. With this initial condition we construct a phase diagram summarising the long–term survival outcomes as a function of B and P/M in Figure 2.16(d), which is very similar to the phase diagram in Figure 2.15(d) where we see that the long-term survival depends on P/M and the two red lines indicating the Allee threshold.

To highlight the different fates of various populations, we compare the outcomes from the continuum model in Figure 2.17(a), where we superimpose the boundaries that separate regions of survival and extinction for the well-mixed initial distribution (red), the vertical strip initial distribution (black) and the square initial distribution (green) described by

Figure 1. Superimposing these curves divides the $(\mathcal{C}(0), P/M)$ plane into four regions with different long-term outcomes depending on the shape of the initial distributions. To emphasise these differences we compare solutions of the continuum model with different values of $\mathcal{C}(0)$ and P/M in Figures 2.17(b)–(g). The solutions in Figures 2.17(b)–(g) correspond to various illustrative choices of $\mathcal{C}(0)$ and P/M. For example, the profiles in Figure 2.17(b) related to region $\mathcal{R}_0$ all lead to extinction regardless of the shape of the initial distributions, whereas the profiles in Figure 2.17(c) related to region $\mathcal{R}_1$ lead to extinction for the well-mixed and square distributions, whereas the vertical distribution leads to survival.

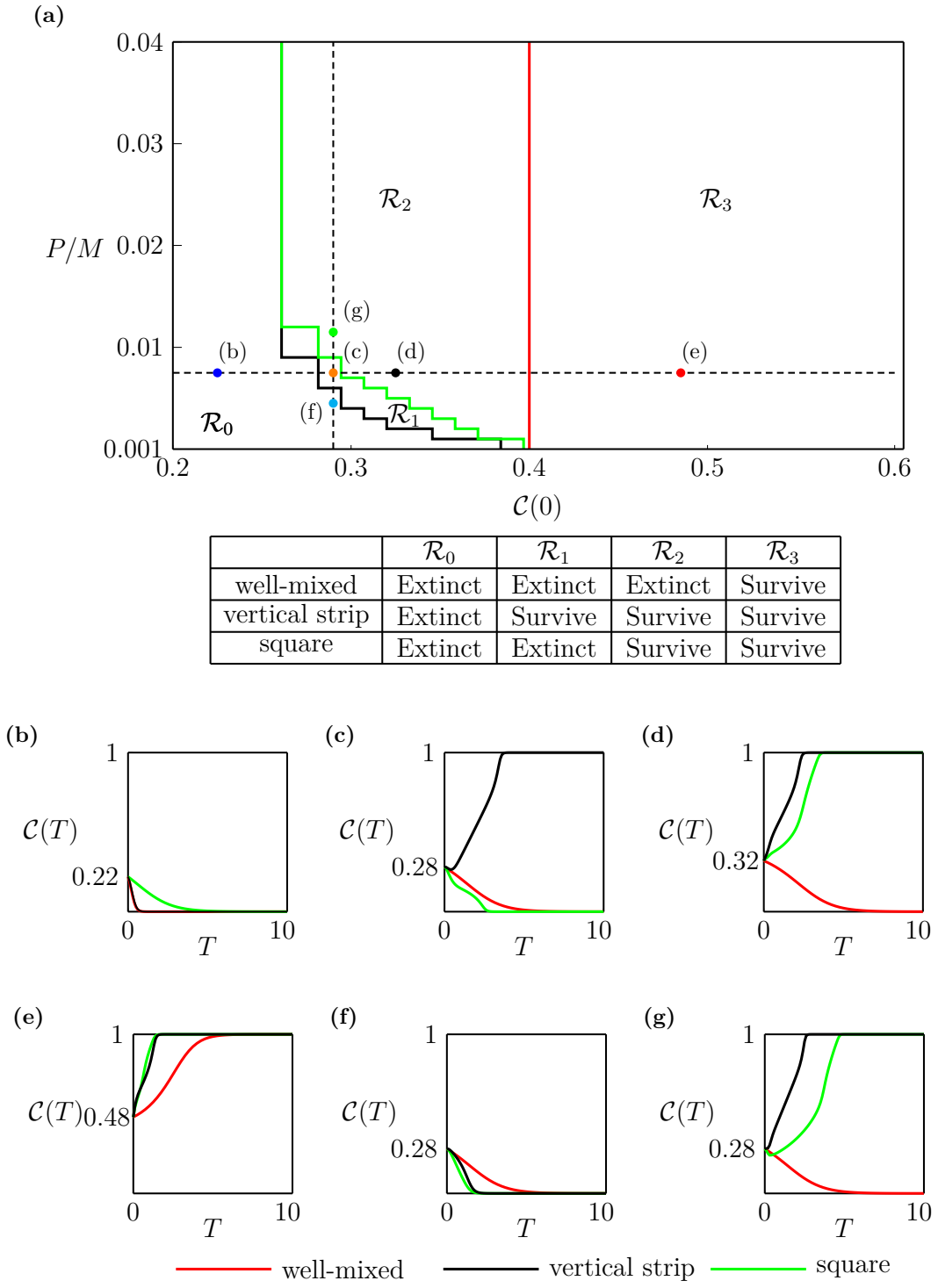

	$\mathcal{R}_0$	$\mathcal{R}_1$	$\mathcal{R}_2$	$\mathcal{R}_3$
well-mixed	Extinct	Extinct	Extinct	Survive
vertical strip	Extinct	Survive	Survive	Survive
square	Extinct	Extinct	Survive	Survive

Figure 2.17: **Role of dimensionality in long-term survival and extinction.** (a) The combined phase diagrams from the continuum model where the red, black and green curves highlight the boundaries separating extinction and survival for the well-mixed, vertical strip and square initial distributions, respectively. (b)–(g) Profiles of $\mathcal{C}(T)$ with $T = 10^3 t$ for six different choices of P/M and $\mathcal{C}(0)$. Parameters in (b)–(g) relate to the coloured discs superimposed in (a): (b) relates to the blue disc; (c) relates to the orange disc; (d) relates to the black disc; (e) relates to the red disc; (f) relates to the cyan disk and (g) relates to the green disc.

2.9.7 Phase diagrams with other boundary conditions

We consider two kinds of rectangular initial distributions on the $L \times L$ domain with $L = 100$. One is centred on the domain, as shown in Figure 2.18(a). Another one is not centred on the domain, as shown in Figure 2.18(b). Through varying w_2 and P/M, we generate the survival/extinction thresholds of the rectangular initial distributions with no-flux boundary conditions and homogeneous Dirichlet boundary conditions along all boundaries, and compare them to the result obtained from the periodic boundary conditions in Figures 2.18(c)–(d). When the initial distribution is centred on the domain, the survival/extinction threshold from the continuum model with the no-flux boundary conditions is the same as the result obtained from the periodic boundary conditions. Interestingly, the homogeneous Dirichlet boundary conditions also provide the same results when the initial area is small. Furthermore, when we consider the initial distribution which is not centred on the domain, these three boundary conditions provide different survival/extinction thresholds. Note that, when we apply the homogeneous Dirichlet boundary condition, we judge that the population survives if there exists any location leading to $C(x, y, \mathcal{T}) > A$, where we consider $\mathcal{T} = \max(30/P, 10^4)$ in practice.

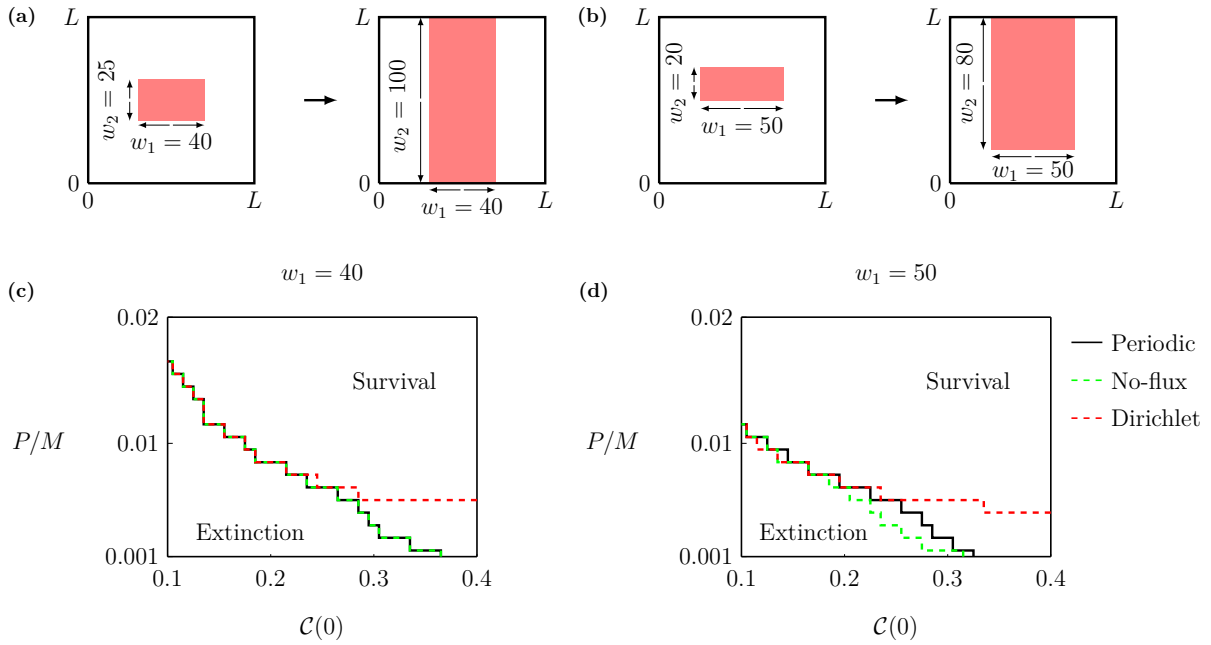

Figure 2.18: **Phase diagrams for survival/extinction with the rectangular initial distributions and different boundary conditions.** (a) The rectangular initial distribution centred on the domain with $w_1 = 40$. We vary $\mathcal{C}(0) = w_1 w_2 / L^2 \in [1/10, 4/10]$ by varying $w_2 \in [25, 100]$. (b) The rectangular initial distribution which is not centred on the domain with $w_1 = 50$. We vary $\mathcal{C}(0) = w_1 w_2 / L^2 \in [1/10, 4/10]$ by varying $w_2 \in [20, 80]$. (c)–(d) Phase diagrams of a rectangular mesh with 31×20 nodes for $\mathcal{C}(0) \in [1/10, 4/10]$ and $P/M \in [1/1000, 2/100]$ where $M = 1$. The survival/extinction thresholds in (c) are obtained with the rectangular initial distributions described in (a). The survival/extinction thresholds in (d) are obtained with the rectangular initial distributions described in (b). The black solid, green dashed and red dashed curves are the survival/extinction thresholds from the continuum model with the periodic, no-flux and homogeneous Dirichlet boundary conditions, respectively.

2.9.8 Robustness of the stochastic simulations

In this section we investigate the robustness of the stochastic simulations which generate discrete data from V identically-prepared realisations. The variance of the total population density is

$$\sigma^2 = \frac{1}{V}\sum_{i=1}^{V}\left\|\left\langle C^i(t)\right\rangle - \langle C(t)\rangle\right\|, \tag{2.48}$$

where $\langle C^i(t)\rangle$ denotes the total population density estimated from the discrete simulation in the ith realisation and $\langle C(t)\rangle$ denotes the averaged total population density. In practice, we consider $t \in [0, 10^4]$. As we calculate the total population density via averaging 40 times identically-prepared realisations in the main document, we also consider $V = 40$ in this section. We calculate the variance with the well-mixed, vertical strip and square initial distributions in Figure 2.19. For the well-mixed initial distribution, $C(0)$ varies with $B \in [0.1, 0.6]$. Note that we use $\mathcal{C}(0)$ as the x-axis in Figure 2.19 as it is only equivalent to $C(0)$ for the well-mixed initial distribution. For the vertical strip initial distribution, we hold $B = 1$ and change $\mathcal{C}(0)$ by varying the width of the strip. For the square initial distribution, we hold $B = 1$ and change $\mathcal{C}(0)$ by varying the width of the square. The variance is small when $P/M = 0.001$ for all three initial distributions in Figure 2.19(a), which indicates that averaging the data from our discrete simulations leads to a robust estimate of the average occupancy. When we consider $P/M = 0.02$, the variance is also low for vertical strip and square initial distributions. However, the variance becomes much larger when $\mathcal{C}(0)$ approaches 0.4, which is the Allee threshold, in the well-mixed initial distribution. This is not surprising as the discrete simulations either lead to survival or extinction depending on fluctuations in the density.

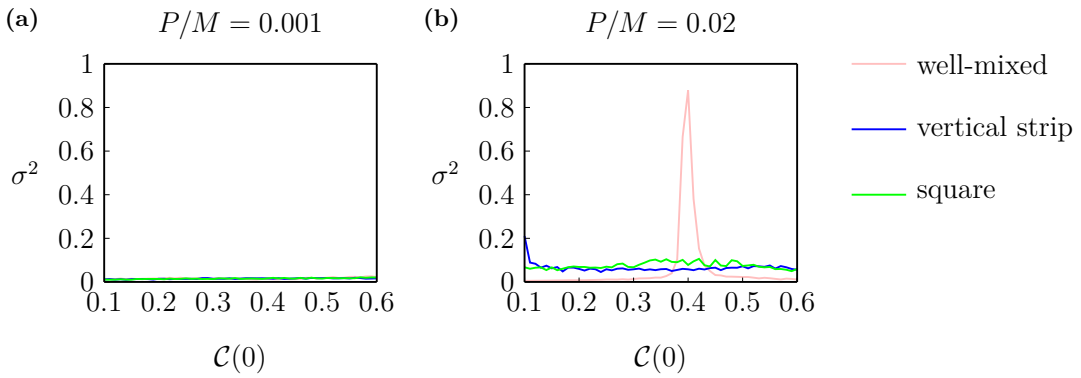

Figure 2.19: **The robustness of the stochastic simulations.** (a) Variance of the difference between the averaged total population density, $\langle C(t)\rangle$ and the total population density of the ith realisation, $\langle C^i(t)\rangle$, where $i = 1, 2, ..., 40$, with $P/M = 0.001$. (b) Variance of the difference between the averaged total population density, $\langle C(t)\rangle$ and the total population density of the ith realisation, $\langle C^i(t)\rangle$, where $i = 1, 2, ..., 40$, with $P/M = 0.02$. Pink curves are generated with the well-mixed initial distribution. Blue curves are generated with the vertical strip initial distribution. Green curves are generated with the square initial distribution.

2.9.9 Value of the combined discrete-continuum framework

Although the discrete simulations and continuous solutions match well in our framework, there is additional information in the discrete model that cannot be easily extracted from the continuum modelling approach. For example, it is unclear from the continuum model whether a population survives mostly because of a high number of births, or because of a low number of deaths. Tracking the age of agents in the discrete model gives indications as to where agents of different ages are located in space. In Figures 2.20(a)–(d), we show the age group of a population in one realisation with vertical strip and square initial distributions. Both initial distributions lead to the survival of populations, but the age structure of the two populations is different, see Figure 2.20(e) for the number of agents in different generations when the population occupies the whole domain.

Another advantage of the discrete model is the ability to track the individual behaviours of the agents. For example, in the discrete model one can trace the trajectory of individuals, which provides insights into the motility mechanisms (Cai et al. 2006; Simpson et al. 2009b). In Figure 2.21, we initially select five agents and trace them until the population occupies the whole domain or until the agent dies. We observe that those agents closer to free space are more motile. Furthermore, once they move into a less crowded region, they have higher probability of dying. This phenomenon is consistent with the growth mechanism governed by the strong Allee kinetics.

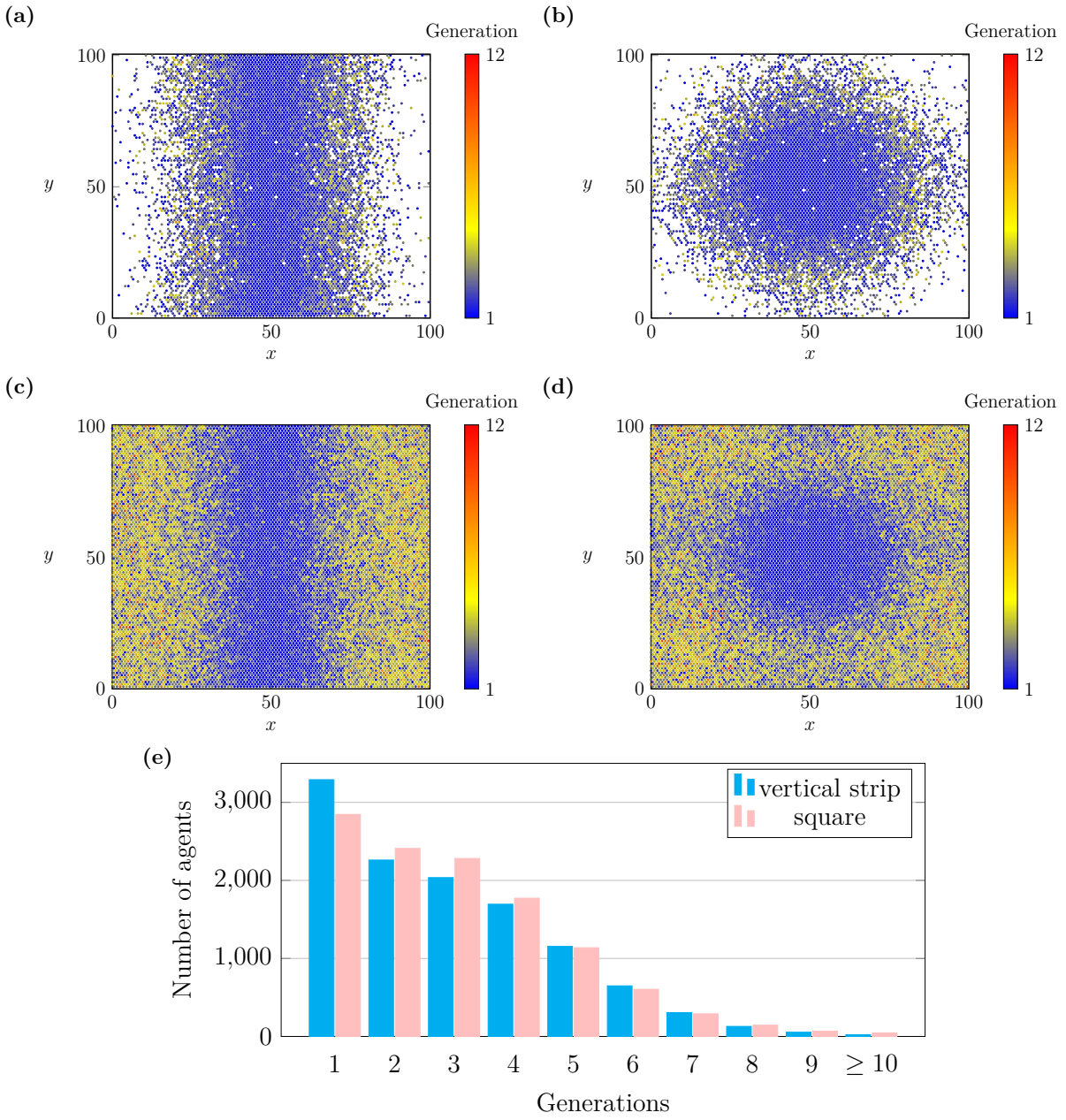

Figure 2.20: **The age group of the population with vertical strip and square initial distributions where $\mathcal{C}(0) = 0.4$ and $P/M = 0.01$, where $P = 0.01$ and $M = 1$.** (a) Snapshot of the discrete simulation with the vertical strip initial distribution at $t = 1000$. The agents initially placed on the domain are the first generation (blue). (b) Snapshot of the discrete simulation with the square initial distribution at $t = 1000$. (c) Snapshot of the discrete simulation with the vertical strip initial distribution when the population occupies the whole domain. (d) Snapshot of the discrete simulation with the square initial distribution when the population occupies the whole domain. (e) The number of agents in different generations.

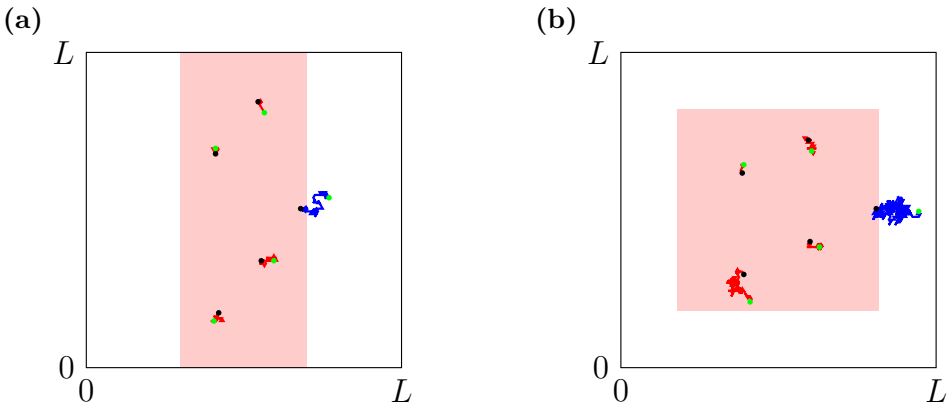

Figure 2.21: **Trajectories of agents in discrete simulations with the vertical strip and square initial distributions where $\mathcal{C}(0) = 0.4$ and $P/M = 0.01$, where $P = 0.01$ and $M = 1$.** (a) Trajectories of five agents with the vertical strip initial distribution. (b) Trajectories of five agents with the square initial distribution. The pink area indicates the initially occupied region with $B = 1$. The black points indicate the initial positions of the five individuals. The green points indicate the final positions of the five individuals when the population occupies the whole domain. Note that both agents whose trajectories are highlighted in blue in (a) and (b) died before the population occupies the whole domain .

Chapter 3

The role of nonlinear diffusion on the fate of bistable populations

---

3.1 Preamble

This chapter is a paper submitted to *Proceedings of the Royal Society A: Mathematical, Physical and Engineering Sciences*

Li, Y., Buenzli, P. R., Simpson, M. J., 2021. Interpreting how nonlinear diffusion affects the fate of bistable populations using a discrete modelling framework. arXiv Preprint.

In this chapter, we address the research question 2 of the thesis: How does nonlinear diffusion affect the fate of bistable populations? We extend the work in Chapter 2 by considering more complicated movement mechanisms associated with nonlinear diffusion in the continuum limit reaction-diffusion equation. We build a connection between the crowding function, which quantifies the movement mechanism of individuals in the discrete model, and the nonlinear diffusivity function in the continuum model. We compare solutions of the continuum model with nonlinear diffusion to the averaged data of discrete simulations. To physically interpret the influence of nonlinear diffusion on population dynamics, we derive the density-depend flux of populations based on the discrete model. Through exploring the relationship between the density-dependent flux and the fate of bistable populations, we identify features of the nonlinear diffusivity functions that either encourage or suppress the extinction of bistable populations

3.2 Abstract

Understanding whether a population will survive and flourish or become extinct is a central question in population biology. One way of exploring this question is to study population dynamics using reaction-diffusion equations, where migration is usually represented as a linear diffusion term, and birth-death is represented with a bistable source term. While linear diffusion is most commonly employed to study migration, there are several limitations of this approach, such as the inability of linear diffusion-based models to predict a well-defined population front. One way to overcome this is to generalise the constant diffusivity, D, to a nonlinear diffusivity function $D(C)$, where $C > 0$ is the density. While it has been formally established that the choice of $D(C)$ affects long-term survival or extinction of a bistable population, working solely in a classical continuum framework makes it difficult to understand precisely how the choice of $D(C)$ affects survival or extinction. Here, we address this question by working with a simple discrete simulation model that is easy to interpret. The continuum limit of the discrete model is a nonlinear reaction-diffusion equation, where the flux involves a nonlinear diffusion term and the source term is given by the strong Allee effect bistable model. We study population extinction/survival using this very intuitive discrete framework together with numerical solutions of the reaction-diffusion continuum limit equation. This approach provides clear insight into how the choice of $D(C)$ either encourages or suppresses population extinction relative to the classical linear diffusion model.

3.3 Introduction

Predicting whether a population will survive or go extinct is a key question in population biology (Berger 1990; Cantrell and Cosner 1998; Axelrod et al. 2006; Ovaskainen and Meerson 2010; Kéfi et al. 2011). For example, predicting whether a species released into a wild area will survive is crucial in protecting endangered animals (Saltz and Rubenstein 1995). Similarly, whether cancer spreads to a different body part from a primary tumour site depends on the survival of small numbers of tumour cells growing successfully in new locations (Korolev et al. 2014; Gerlee et al. 2021). A classical continuum model for studying the survival of biological populations is the strong Allee effect model, based on an ordinary differential equation (ODE),

$$\frac{\mathrm{d}C(t)}{\mathrm{d}t} = \lambda C(t)\left(1 - \frac{C(t)}{K}\right)\left(\frac{C(t)}{A} - 1\right), \tag{3.1}$$

where $C(t) \geq 0$ is the population density at time $t \geq 0$, $\lambda > 0$ is the intrinsic growth rate, $K > 0$ is the carrying capacity density, and $0 < A < K$ is the Allee threshold density (Allee and Bowen 1932; Kot 2001; Edelstein-Keshet 2005; Courchamp et al. 2008; Taylor and

Hastings 2005; Surendran et al. 2020; Fadai and Simpson 2020b). The fate of a population described by (3.1) depends solely upon the initial density, $C(0)$. Extinction occurs if $C(0) < A$, leading to $C(t) \to 0$ as $t \to \infty$. In contrast, the population survives if $C(0) > A$, leading to $C(t) \to K$ as $t \to \infty$. Such dynamics, leading to either eventual survival or extinction, are sometimes called *bistable* population dynamics. The strong Allee effect model belongs to a broader class of population models, called bistable population dynamics models, and the key feature of these models is that they involve three equilibrium points: $C = 0$ and $C = K > 0$ are stable equilibrium points, and $C = A$, where $0 < A < K$ is unstable. There are many ODE models of this kind, not just the classical cubic form in (3.1) (Johnston et al. 2020; Fadai and Simpson 2020b; Alkhayuon et al. 2021; Gerlee et al. 2021).

To investigate spatial effects, such as moving invasion fronts, some studies consider incorporating Equation (3.1) into a reaction-diffusion equation, where the population density depends upon both position and time (Hadeler and Rothe 1975; Lewis and Kareiva 1993; Holmes et al. 1994; Hastings et al. 2005; Maciel and Lutscher 2015; Johnston et al. 2017; Neufeld et al. 2017; El-Hachem et al. 2019; Li et al. 2020, 2021). In reaction-diffusion models, the dynamics of bistable populations involve a more complicated interaction between the bistable source term and the diffusion term. Unlike ODE models where the fate of a bistable population is solely determined by the initial density, many factors influence whether the population will survive or go extinct in reaction-diffusion models (Lewis and Kareiva 1993; Bradford and Philip 1970a,b; Johnston et al. 2020; Li et al. 2022). For example, the initial area of a bistable population on an infinite domain needs to be greater than a threshold, called the *critical initial area*, so that the population avoids extinction (Lewis and Kareiva 1993).

Most reaction-diffusion models in population biology consider a constant diffusivity associated with Fick's first law of diffusion, which states that the diffusive flux is proportional to the spatial gradient of density (Hadeler and Rothe 1975; Holmes et al. 1994; Kot 2001; Hastings et al. 2005; Jin et al. 2016a; Murray 1989; Maciel and Lutscher 2015; Neufeld et al. 2017). In one spatial dimension the diffusive flux is $J = -D\partial C(x,t)/\partial x$, where $D > 0$ is the constant diffusivity. Linear diffusion is popular in modelling biological populations, since this model is very simple, and has a straightforward connection with a range of underlying stochastic models, such as conceptualising the motion of individuals in the population as a simple unbiased random walk in the dilute limit, where interactions between individuals are weak (Hughes 1995; Kot 2001; Murray 1989; Liggett 2013). However, despite the immense popularity of linear diffusion, there are well-documented circumstances where population dynamics cannot be described by this simple model. For example, sharp moving fronts in cell migration assays cannot be represented by linear diffusion, and so there has been great interest in modelling the motion of well-defined fronts

using degenerate nonlinear diffusion terms (Maini et al. 2004a,b; Sengers et al. 2007; Jin et al. 2016b; McCue et al. 2019). Similar to cell biology applications, mathematical models of insect dispersal with linear diffusion are unable to replicate observations where well-defined sharp fronts play an important role (Shigesada 1980; Murray 1989). Therefore, reaction-diffusion equations with nonlinear diffusion are considered in a variety of applications where, in one spatial dimension, the flux is $J = -D(C(x,t))\partial C(x,t)/\partial x$, with the key difference that the constant linear diffusivity D is now generalised to a nonlinear function $D(C) > 0$ (Shigesada 1980; Murray 1989; Painter and Sherratt 2003; Maini et al. 2004a; Sengers et al. 2007; Cai et al. 2007; Deroulers et al. 2009; Fernando et al. 2010; Johnston et al. 2012; Martínez-García et al. 2015; Yates et al. 2015; Jin et al. 2016b; McCue et al. 2019; Bubba et al. 2020). Unlike the constant diffusivity that can be interpreted as undirected random motion of individuals without interaction (Hughes 1995; Liggett 2013), identifying the behaviour of individuals corresponding to a given nonlinear diffusion term is less clear. Therefore, it is not always obvious which nonlinear diffusion term is appropriate to model a particular situation (Sherratt and Murray 1990; Murray 1989; Cai et al. 2007; Jin et al. 2016b). Since it is known that nonlinear diffusion can impact the conditions required for survival of a bistable population (Cantrell and Cosner 2004; Lee et al. 2006), exploring the behaviour of individuals is helpful to provide a simple interpretation of how $D(C)$ affects the fate of bistable populations subject to a nonlinear diffusion migration mechanism. Therefore, it is valuable to study the connection between the behaviour of individuals and the nonlinear diffusion term in reaction-diffusion equations.

To connect continuum models with the behaviour of individuals, we work with a physically intuitive discrete framework. The discrete model incorporates straightforward crowding effects into birth, death and movement of individuals on a two-dimensional hexagonal lattice (Li et al. 2022). In particular, we quantify the influence of crowdedness on the motility of individuals by using a crowding function $G(C) > 0$, which explicitly describes how the local crowding affects the ability of individuals to move. The continuum limit of the discrete model is a reaction-diffusion equation with a strong Allee effect source term, and a general nonlinear diffusivity function $D(C)$. This framework allows us to investigate population dynamics through repeated simulation of the discrete model, as well as solving the associated reaction-diffusion continuum limit model numerically. Through the mathematical relationship between the nonlinear diffusivity function $D(C)$ and the underlying crowding function $G(C)$, we develop an intuitive understanding of how different choices of $D(C)$ affect the extinction or survival of the population. To improve our understanding, we derive expressions for the density-dependent flux of populations associated with the discrete model. The expression for the flux can be re-written as the flux associated with a linear diffusion mechanism plus a term, which we interpret as a correction that is associated with the effects of nonlinear diffusion. Writing the flux in

this way allows us to directly relate how different choices of $D(C)$ either encourage or suppress extinction. All interpretations of our modelling framework are supported by a suite of stochastic simulations and numerical solutions of the associated continuum limit reaction-diffusion equation. All numerical algorithms required to replicate our work are available on Github.

3.4 The discrete model and the continuum limit

In this section we introduce a lattice-based discrete model and the corresponding continuum limit model description that is closely related to our previous work (Li et al. 2022). Unlike the work in Li et al. (2022), which only considers examples where the motility of individuals is given by a linear diffusion mechanism, here we focus on a more broad range of motility mechanisms that include a range of choices of nonlinear diffusivity functions.

In the discrete model individuals are represented as agents on a two-dimensional hexagonal lattice with spacing $\Delta > 0$. A lattice site $\mathbf{s}$, indexed by (i, j) with a unique Cartesian coordinate (x, y), is either occupied $C_{\mathbf{s}} = 1$, or vacant $C_{\mathbf{s}} = 0$. Stochastic simulations include birth, death and movement events, and we will now explain the details of these mechanisms.

If there are $Q(t)$ agents on the lattice, we use a random sequential updating method to evolve the discrete model from time t to time $t + \tau$. To achieve this we select $Q(t)$ agents at random, with replacement, and give those agents an opportunity to undergo a movement event. We then select another $Q(t)$ agents, at random, with replacement, and give those agents an opportunity to undergo a birth/death event. Once these two sets of events have been assessed, we advance time from t to $t + \tau$ and repeat until the desired output time is reached (Simpson et al. 2010a).

For a potential motility event, if the agent in question is at site $\mathbf{s}$, that agent will move with probability $\widehat{M} = MG(K_{\mathbf{s}})$, where M is the probability that an isolated agent will attempt to move during a time interval of duration τ, and $G(K_{\mathbf{s}}) \in [0, 1]$ is a *movement crowding function* which quantities how crowding in a small neighbourhood of $\mathbf{s}$ influences motility. We interpret $G(K_{\mathbf{s}})$ to be a measure of the influence of the local density upon movement since $K_{\mathbf{s}}$ is a simple measure of density around site $\mathbf{s}$, given by

$$K_{\mathbf{s}} = \frac{1}{|\mathcal{N}_r|} \sum_{s' \in \mathcal{N}_r\{\mathbf{s}\}} C_{\mathbf{s}'} \in [0, 1], \tag{3.2}$$

where $\mathcal{N}_r\{\mathbf{s}\}$ denotes the set of neighbouring sites surrounding site $\mathbf{s}$. Since the local density can be measured with different-sized spatial templates, we use r to represent the diameter of concentric rings surrounding site $\mathbf{s}$, so that the number of neighbouring sites of any site is $|\mathcal{N}_r| = 3r(r + 1)$, as shown in Figure 3.1(a).

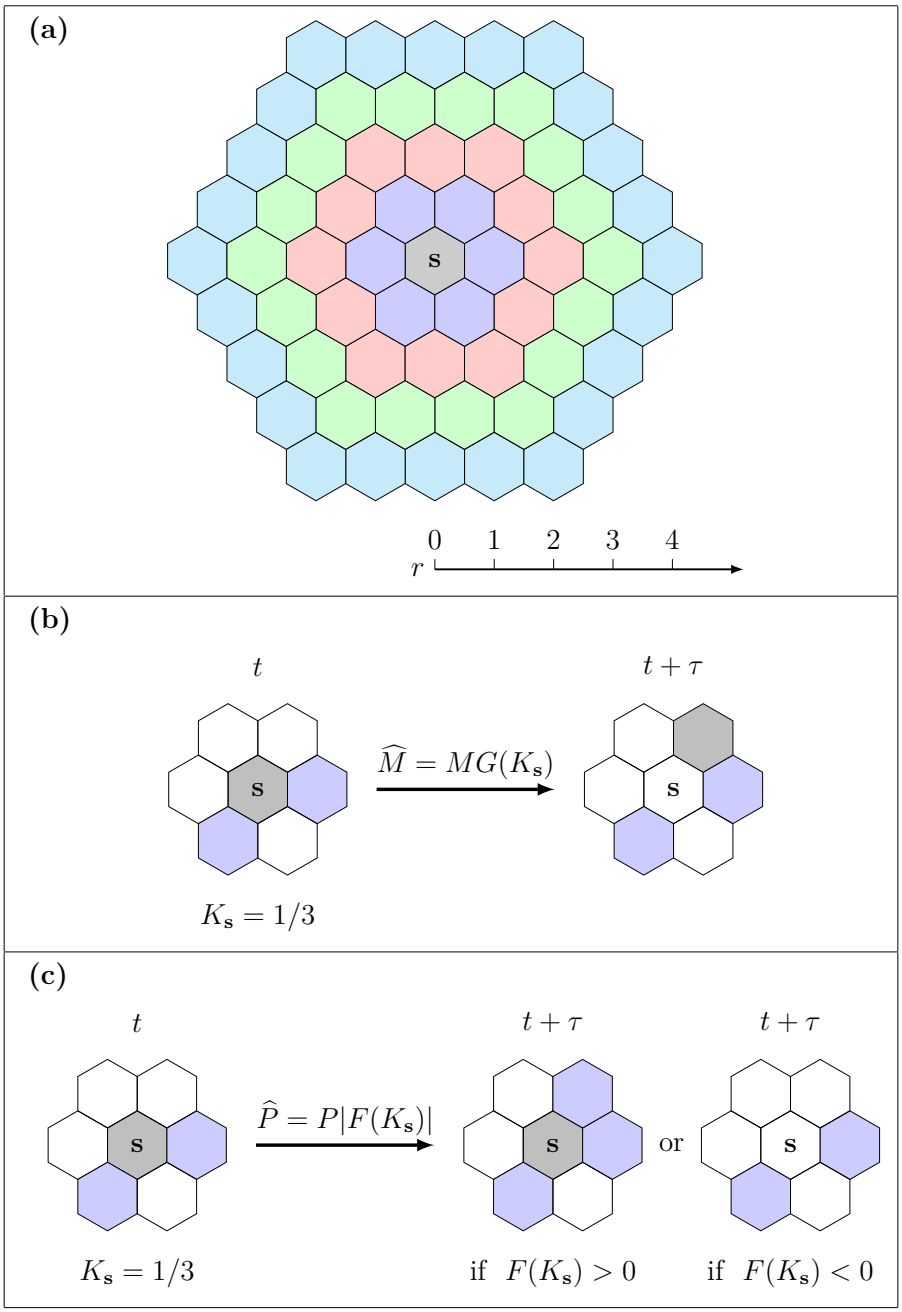

Figure 3.1: **Movement and growth mechanisms.** (a) Different-sized spatial templates $\mathcal{N}_r$, where r is the diameter of the concentric rings surrounding site $\mathbf{s}$. (b) Movement mechanism with $r = 1$. (c) Growth mechanism with $r = 1$. In (b) and (c), there are two neighbouring agents (blue) surrounding the agent at site $\mathbf{s}$ (grey) at time t. The agent at site $\mathbf{s}$ undergoes a movement event with probability $\widehat{M} = MG(K_{\mathbf{s}})$, where $K_{\mathbf{s}} = 1/3$, as shown in (b). As there are four vacant neighbouring sites, the probability of moving to one of the vacant sites is $\widehat{M}/4$. Similarly, the agent undergoes a growth event with probability $\widehat{P} = P|F(K_{\mathbf{s}})|$, where $K_{\mathbf{s}} = 1/3$, as shown in (c). If $F(K_{\mathbf{s}}) > 0$, the potential growth event is a birth event. As there are four vacant neighbouring sites, the probability of placing a new agent in one of the vacant sites is $\widehat{P}/4$. If $F(K_{\mathbf{s}}) < 0$, the potential growth event is a death event. That is, the agent will be removed out of the lattice with probability $\widehat{P}$.

If a movement event occurs, the agent at site $\mathbf{s}$ will move into a randomly chosen vacant site in $\mathcal{N}_r\{\mathbf{s}\}$. Therefore, the probability for the agent at site $\mathbf{s}$ moving to one of the vacant sites is $\widehat{M}/(|\mathcal{N}_r|(1-K_{\mathbf{s}}))$. We show the movement mechanism with $r=1$ leading to $|\mathcal{N}_r|=6$ in Figure 3.1(b). In this particular configuration the agent at site $\mathbf{s}$ has two neighbouring agents, giving $K_{\mathbf{s}}=1/3$. The probability of undergoing a movement event is $\widehat{M}=MG(1/3)$. As there are four vacant sites in $\mathcal{N}_1\{\mathbf{s}\}$, the probability of moving to one of the vacant sites is $\widehat{M}/4$. Note that we require $G(1)=0$ as individuals have no space to move if their neighbouring sites are all occupied.

For a potential growth event, if the agent in question is at site $\mathbf{s}$, that agent will undergo a growth event with probability $\widehat{P}=PF(K_{\mathbf{s}})$, where P is the probability that an isolated agent will attempt to undergo a growth event during a time interval of duration τ, and $F(K_{\mathbf{s}})\in[-1,1]$ is the *growth crowding function* which quantities how crowding in a small neighbourhood of $\mathbf{s}$ influences the propensity of agents to proliferate or die. Since the growth mechanism includes both proliferation and death as potential outcomes, we define $F(K_{\mathbf{s}})\in[-1,1]$ such that a proliferation event takes place when $F(K_{\mathbf{s}})>0$ and a death event takes place when $F(K_{\mathbf{s}})<0$. In the case of a proliferation event, a new daughter agent will be placed on a randomly chosen vacant site in $\mathcal{N}_r(\mathbf{s})$, whereas if a death event takes place the agent at site $\mathbf{s}$ will be removed from the simulation. After $Q(t)$ potential growth events have been assessed, the value of $Q(t)$ is updated accordingly.

We show the growth mechanism with $r=1$ in Figure 3.1(c). As the agent at site $\mathbf{s}$ has two neighbouring agents, we have $K_{\mathbf{s}}=1/3$. Therefore, the probability of undergoing a growth event is $\widehat{P}=P|F(1/3)|$. If $F(1/3)>0$, as there are four vacant sites in $\mathcal{N}_1\{\mathbf{s}\}$, the agent will place a new agent on one of the vacant sites with probability $\widehat{P}/4$. If $F(1/3)<0$, the agent will be removed from the lattice with probability $\widehat{P}$.

A key feature of the discrete model is that we use $G(K_{\mathbf{s}})$ to explicitly describe the influence of crowding effects on the movement of individuals. We provide several examples of $G(K_{\mathbf{s}})$ and show how they influence the movement of agents on the spatial template with $r=1$ in Figure 3.2. We first consider $G(K_{\mathbf{s}})=1-K_{\mathbf{s}}$ which has a constant slope, as shown in Figure 3.2(a). The probability of a movement event with $K_{\mathbf{s}}=0$, $K_{\mathbf{s}}=1/3$, and $K_{\mathbf{s}}=2/3$ is given in Figures 3.2(b)–(d), respectively. With this simple movement crowding function, the probability of the agent at site $\mathbf{s}$ moving to one of its neighbouring vacant sites is always $M/6$, which is independent of the local density, $K_{\mathbf{s}}$. We then consider a concave down function, $G(K_{\mathbf{s}})=(1-K_{\mathbf{s}})(1+K_{\mathbf{s}}/2)$ in Figure 3.2(e). The probability of a movement event with $K_{\mathbf{s}}=0$, $K_{\mathbf{s}}=1/3$, and $K_{\mathbf{s}}=2/3$ is given in Figures 3.2(f)–(h), respectively. Compared to the simplest crowding function $G(K_{\mathbf{s}})=1-K_{\mathbf{s}}$, the agent has a larger net movement probability for $K_{\mathbf{s}}\in(0,1)$. Finally, we consider a concave up function, $G(K_{\mathbf{s}})=(1-K_{\mathbf{s}})(1-K_{\mathbf{s}}/2)$ in Figure 3.2(i). The probability of a movement event with $K_{\mathbf{s}}=0$, $K_{\mathbf{s}}=1/3$, and $K_{\mathbf{s}}=2/3$ is shown in Figures 3.2(j)–(l), respectively.

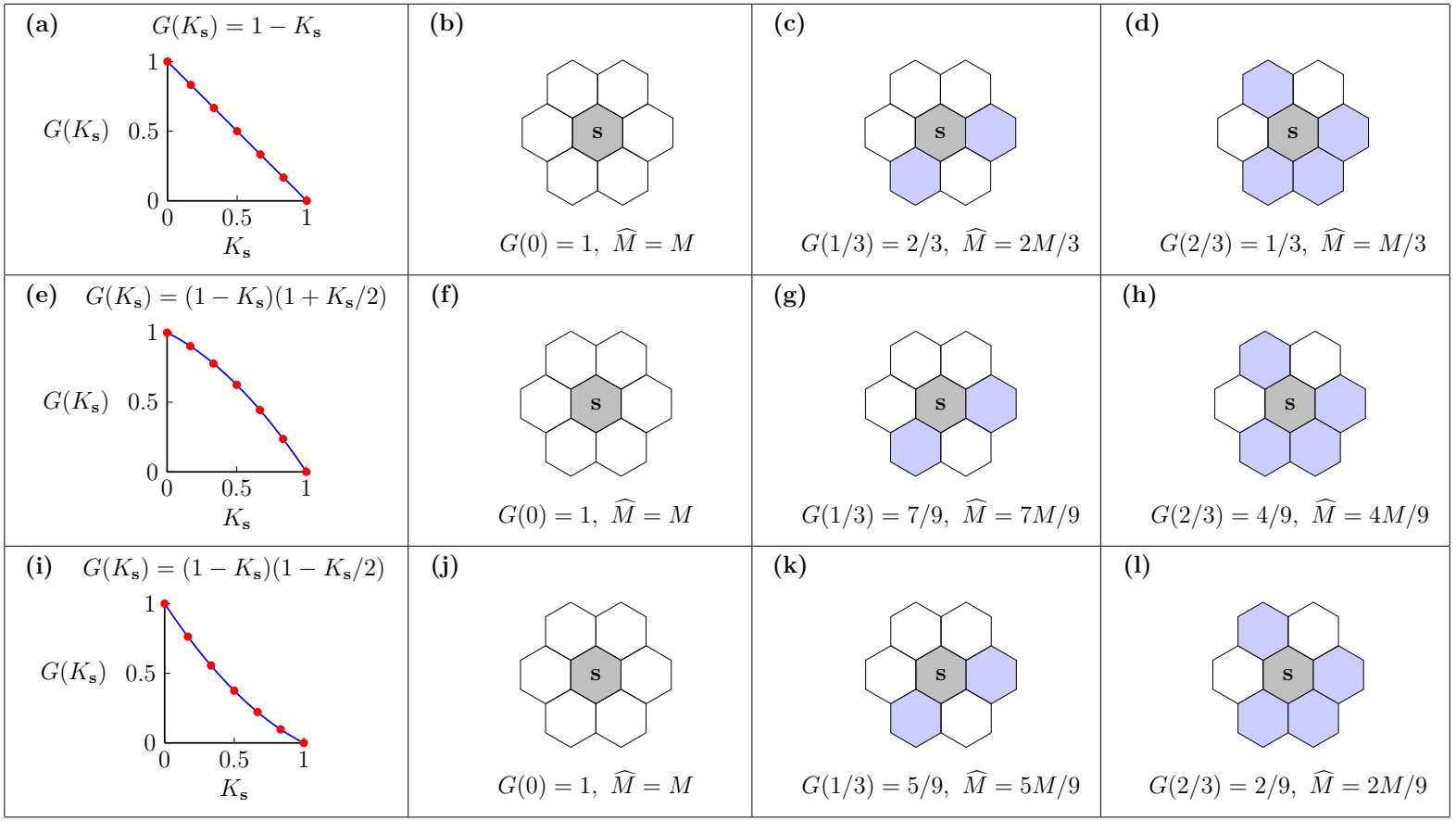

Figure 3.2: **Movement mechanism with different movement crowding functions on a spatial template with $r = 1$.** In each subfigure we represent the agent at site $\mathbf{s}$ with grey, the neighbouring agents with blue, and the vacant neighbouring sites with white. (a) $G(K_\mathbf{s}) = 1 - K_\mathbf{s}$. The red dots represent the values of $G(K_\mathbf{s})$ that can be measured from the discrete model. (b)–(d) Probabilities of undergoing a movement event for the agent at site $\mathbf{s}$ associated with the $G(K_\mathbf{s})$ in (a). (e) $G(K_\mathbf{s}) = (1 - K_\mathbf{s})(1 + K_\mathbf{s}/2)$. (f)–(h) Probabilities of undergoing a movement event for the agent at site $\mathbf{s}$ associated with the $G(K_\mathbf{s})$ in (e). (i) $G(K_\mathbf{s}) = (1 - K_\mathbf{s})(1 - K_\mathbf{s}/2)$. (j)–(l) Probabilities of undergoing a movement event for the agent at site $\mathbf{s}$ associated with the $G(K_\mathbf{s})$ in (i).

In this case, the agent has a reduced probability of movement for $K_{\mathbf{s}} \in (0,1)$, relative to the simplest case $G(K_{\mathbf{s}}) = 1 - K_{\mathbf{s}}$. The growth mechanism of agents applies a similar way of incorporating the influence of crowding effects into the discrete model (Li et al. 2022). We present the pseudo-code for implementing a single realisation of the discrete model in the Supplementary Material document.

If we consider the spatial template with $r = 1$ for the movement mechanism and $r \geq 1$ for the growth mechanism of agents, the continuum limit of the discrete model is

$$\frac{\partial C(x,y,t)}{\partial t} = \nabla \cdot (D(C(x,y,t))\nabla C(x,y,t)) + R(C), \tag{3.3}$$

with nonlinear diffusivity function

$$D(C) = D_0 \left[C\frac{\mathrm{d}G(C)}{\mathrm{d}C} + \frac{1+C}{1-C}G(C) \right], \tag{3.4}$$

and a source term $R(C) = \lambda C F(C)$, where

$$D_0 = \lim_{\Delta,\tau \to 0} \frac{M\Delta^2}{4\tau}, \quad \lambda = \lim_{\tau \to 0} \frac{P}{\tau}. \tag{3.5}$$

Here, $D_0 > 0$ is a constant in the limit that $\Delta \to 0$ and $\tau \to 0$ with the ratio Δ^2/τ held constant, and $\lambda > 0$ is constant when $P = \mathcal{O}(\tau)$, which implies that the continuum limit is valid when $P \ll M$. Note that in the discrete model we have K as the argument of the crowding function, and that in the continuum limit the argument of the crowding function is C. This difference can be reconciled through carrying out the full details of the discrete-to-continuum averaging arguments. Full algebraic details of the intermediate steps required to derive the continuum limit is given in the Supplementary Material. Throughout this study we work with dimensionless simulations by setting $\Delta = \tau = 1$ in the discrete model, which leads to $D_0 = M/4$ and $\lambda = P$ in the continuum limit. In cell biology, experimental observations imply that cell motility is reasonably well approximated by a nearest neighbour random walk whereas cell proliferation involves the disposition of daughter agents at some distance from the mother agent (Simpson et al. 2010a). Therefore, throughout this work we set $r = 1$ for the motility mechanism and $r = 4$ for the proliferation mechanism, which is consistent with previous modelling (Simpson et al. 2010a; Li et al. 2022). Moreover, as we are interested in the survival and extinction of populations, we choose a growth crowding function $F(C) = 2.5(1-C)(C-A)$ with $A = 0.4$, which leads to a cubic source term, $R(C)$, associated with the strong Allee effect. With this choice of growth crowding function, we have $F(0) = -1$ indicating that isolated agents have the largest probability of dying.

3.5 Relationship between *D(C)* and *G(C)*

Based on Equation (3.4), we are now in a unique position where we can specify an intuitive crowding function for the discrete model, $G(C)$, and use the discrete-to-continuum framework to understand how this translates into a population-level nonlinear diffusivity function, $D(C)$. This approach is very different to the more usual approach of simply specifying some phenomenological $D(C)$ function, without any detailed understanding of how a particular choice of nonlinear diffusivity impacts the underlying discrete mechanism (Sherratt and Murray 1990; Maini et al. 2004a,b; Sengers et al. 2007; McCue et al. 2019).

There are two ways of taking advantage of (3.4) to study population dynamics. First, for a given movement mechanism of individuals described by $G(C)$, we can simply substitute into this expression to give the corresponding $D(C)$. To demonstrate this first approach, we present three examples of $G(C)$, which were examined in Figure 3.2, and study the corresponding $D(C)$,

$$G(C) = 1 - C, \qquad D(C) = D_0, \tag{3.6}$$

$$G(C) = (1 - C)\left(1 + \frac{C}{2}\right), \qquad D(C) = D_0\left[1 + C\left(1 - \frac{C}{2}\right)\right], \tag{3.7}$$

$$G(C) = (1 - C)\left(1 - \frac{C}{2}\right), \qquad D(C) = D_0\left[1 - C\left(1 - \frac{C}{2}\right)\right], \tag{3.8}$$

see Figures 3.3(a)–(b). In each of these three crowding functions we always have $G(0) = 1$, which is reasonable since this condition implies that isolated agents are unaffected by crowding (Jin et al. 2016a). We first consider $G(C) = 1 - C$, which has a constant slope and leads to a constant diffusivity $D(C) = D_0$. As we mentioned in Section 3.4, the probability of an agent moving to one of its neighbouring vacant sites is always $M/6$, which is independent of density. This is consistent with the continuum model where the standard linear diffusion mechanism means that the diffusivity is independent of density. Next we consider the concave down crowding function $G(C) = (1 - C)(1 + C/2)$, which has the property that $G(C) > 1 - C$ for all $C \in (0, 1)$. For this crowding function we obtain an increasing nonlinear diffusivity function $D(C) > D_0$, which is reasonable since the motility of individuals is reduced less by crowding than in the case where $G(C) = 1 - C$, corresponding to linear diffusion. Similarly, the concave up crowding function $G(C) = (1 - C)(1 - C/2)$, which has the property that $G(C) < 1 - C$ for all $C \in (0, 1)$. For this crowding function we obtain a decreasing nonlinear diffusivity function $D(C) < D_0$, which again is reasonable since the motility of individuals is reduced more by crowding than in the case where $G(C) = 1 - C$, corresponding to linear diffusion.

The first approach to use (3.4) involves specifying a physically reasonable crowding function, $G(C)$, and using the discrete-to-continuum conservation argument to understand

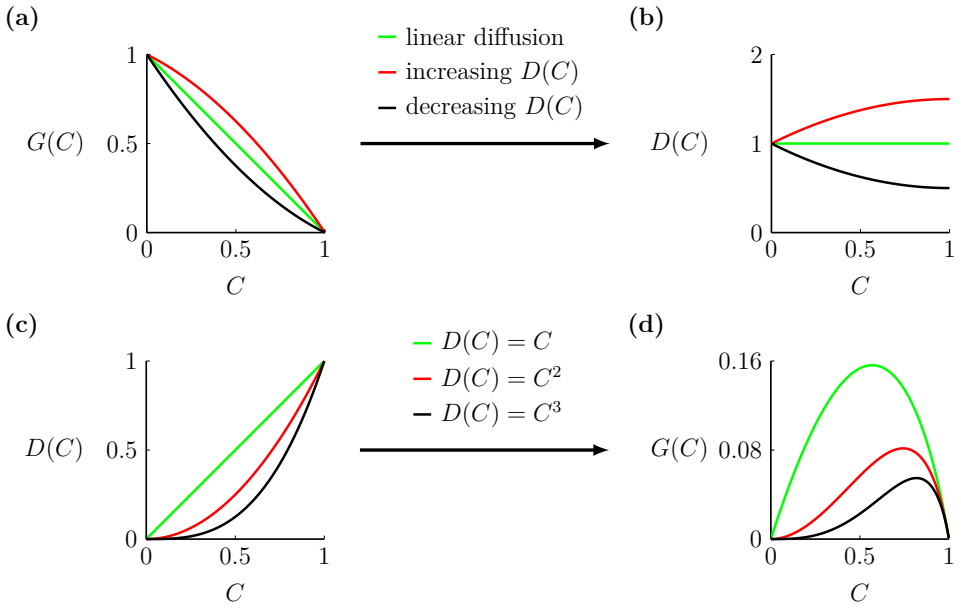

Figure 3.3: **Two approaches of connecting the movement crowding function and the diffusivity function.** (a) Movement crowding functions $G(C) = 1 - C$ (green), $G(C) = (1 - C)(1 + C/2)$ (red) and $G(C) = (1 - C)(1 - C/2)$ (black). (b) Diffusivity functions associated with the movement crowding functions in (a) with $D_0 = 1$. (c) Diffusivity functions $D(C) = D_0 C$ (green), $D(C) = D_0 C^2$ (red) and $D(C) = D_0 C^3$ (black) with $D_0 = 1$. (d) Movement crowding functions associated with the nonlinear diffusivity functions in (c).

the corresponding population-level nonlinear diffusivity function, $D(C)$. Of course, we can also view (3.4) as allowing us to specify a particular nonlinear diffusivity function $D(C)$, and to understand which particular crowding function is associated with that choice of $D(C)$. One of the challenges associated with this second approach is that a given $D(C)$ may not lead to a physically realistic crowding function, as we will now explore. One of the most standard choices of nonlinear diffusivity is a power law diffusivity, $D(C) = D_0 C^m$, where m is some constant exponent. This model has played a very important role in population biology models (Simpson et al. 2011; McCue et al. 2019), since combining this nonlinear diffusivity term with a logistic source term gives rise to the well-studied Porous-Fisher model (Sherratt and Murray 1990; Witelski 1995a; Murray 1989; Jin et al. 2016b; Buenzli et al. 2020). If we consider $m \geq 0$ and $G(C) \in [0, 1]$ we can solve (3.4) to give

$$G(C) = \left(C^{m+2} - 2C^{m+1} + C^m\right) \frac{{}_2F_1(2, m+1; m+2; C)}{m+1}, \tag{3.9}$$

where ${}_2F_1(2, m+1; m+2; C)$ is the hypergeometric function (Abramowitz and Stegun

1964). We present three examples with $m = 1, 2$ and 3, given by

$$D(C) = D_0 C, \qquad G(C) = (1-C)\left(1 + \frac{1-C}{C}\ln(1-C)\right), \tag{3.10}$$

$$D(C) = D_0 C^2, \qquad G(C) = (1-C)\left(2 - C + \frac{2(1-C)}{C}\ln(1-C)\right), \tag{3.11}$$

$$D(C) = D_0 C^3, \qquad G(C) = (1-C)\left(\frac{-C^2 - 3C + 6}{2} + \frac{3(1-C)}{C}\ln(1-C)\right). \tag{3.12}$$

Figures 3.3(c)–(d) compare the specified $D(C)$ with the associated $G(C)$. Here we see that each $D(C)$ is associated with some particular crowding function, but some of the properties of these crowding functions are not as physically reasonable as those in Figures 3.3(a)–(b). One attractive property of the crowding function in Figure 3.3(d) is that $G(1) = 0$ for each case, and this is reasonable since we expect motility to cease when the lattice is packed to maximum density. One less appealing feature of the crowding function in Figure 3.3(d) is that each case has $G(0) = 0$, which means that isolated agents do not move, and clearly this is at odds with our intuition, and experimental evidence, that crowding reduces motility (Lee et al. 1994; Tremel et al. 2009). Despite this limitation, it is still insightful and interesting that we are able to take canonical choices of nonlinear diffusivity function $D(C)$, and to explore what choice of crowding function $G(C)$ leads to those nonlinear diffusivities.

3.6 Nonlinear diffusion influences population dynamics

In this section we quantify various population dynamics using both the discrete and associated continuum models. In all simulations, we consider an $L \times L$ domain where $L = 100$, and we impose periodic boundary conditions along all boundaries. Agents are initially located in a central vertical strip of width w, which may represent a species along a river (Lutscher et al. 2010) or a population of cells in a scratch assay (Jin et al. 2016b). For the continuum model, since the initial distribution is independent of the vertical location and evolves with periodic boundary conditions, the population density remains independent of the vertical position for all $t > 0$ (Simpson 2009). Therefore, Equation (3.3) simplifies to

$$\frac{\partial C(x,t)}{\partial t} = \frac{\partial}{\partial x}\left(D(C(x,t))\frac{\partial C(x,t)}{\partial x}\right) + R(C(x,t)), \tag{3.13}$$

where $C(x,t)$ represents the average column density of population (Simpson et al. 2010a; Simpson 2009). We numerically solve Equation (3.13) and compute

$$\mathcal{C}(t) = \frac{1}{L}\int_0^L C(x,t)\ \mathrm{d}x, \tag{3.14}$$

which is the total population density across the whole domain. We apply the method of lines to solve (3.13) numerically and full details of the numerical method is given in the Supplementary Material.

To quantify results from the discrete model we always consider performing V identically prepared realisations, and use this data to calculate the average occupancy of site $\mathbf{s}$,

$$\bar{C}_{\mathbf{s}} = \frac{1}{V}\sum_{v=1}^{V} C_{\mathbf{s}}^{(v)}(t), \tag{3.15}$$

where $C_{\mathbf{s}}^{(v)}(t) \in \{0, 1\}$ is the occupancy of site $\mathbf{s}$ at time t in the vth identically-prepared realisation. As the initial occupancy is independent of the vertical position, we can denote the average column density at time $t = n\tau$ as

$$\langle C(x,t)\rangle = \frac{1}{VJ}\sum_{v=1}^{V}\sum_{j=1}^{J} C^{(v)}(i,j,n), \tag{3.16}$$

which corresponds to $C(x,t)$ in the continuum model, where indexes i and j, indicating the position of site $\mathbf{s}$, relate to position (x, y). We also compute the total population density across the whole domain at time $t = n\tau$ as

$$\langle C(t)\rangle = \frac{1}{VIJ}\sum_{v=1}^{V}\sum_{j=1}^{J}\sum_{i=1}^{I} C^{(v)}(i,j,n), \tag{3.17}$$

which corresponds to $\mathcal{C}(t)$ in the continuum model.

Figures 3.4(a)-(b) show results from both the discrete and continuum models with $G(C) = 1 - C$ and $D(C) = D_0$, corresponding to linear diffusion. Discrete simulations are performed with $M = 1$ and $P = 6/1000$, leading to $D_0 = 1/4$ and $\lambda = 6/1000$ in the continuum model. For the discrete model, we initially locate agents in the central vertical strip with width $w = 10$, which means that the initial condition for (3.13) is $C(x, 0) = 1$ for $x \in [45, 55]$ and $C(x, 0) = 0$ elsewhere. Comparing $C(x,t)$ and $\langle C(x,t)\rangle$ shows that the match between the discrete and continuum results is excellent. Moreover, the density eventually reaches zero everywhere, which suggests that the population goes extinct. We then consider a larger width $w = 30$, and compare $\langle C(x,t)\rangle$ with $C(x,t)$ at $t = 800, 1600, 2400$ in Figure 3.4(b). The solutions of (3.14) also match well with the averaged data from discrete simulations. In this case, the column density eventually reaches the carrying capacity everywhere, which suggests that the population survives.

Next, we consider the same initial conditions except that we use $G(C) = (1-C)(1+C/2)$ in the discrete model and the increasing $D(C)$, given by (3.7), in the continuum model. Results in Figure 3.4(c)-(d) correspond to $w = 10$ and $w = 30$, respectively. Again, the continuum and discrete results match well. The population goes extinct with $w = 10$, but

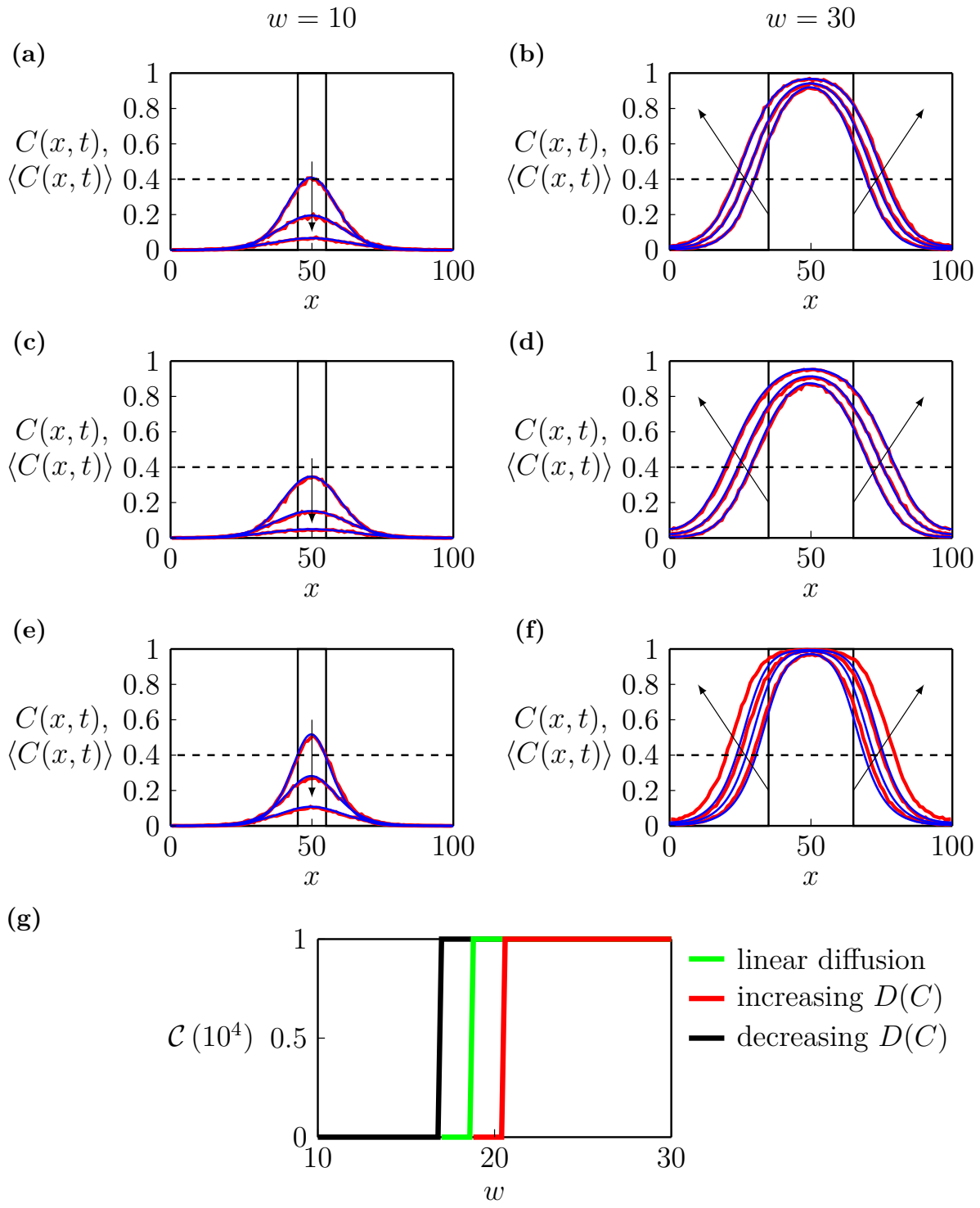

Figure 3.4: **Comparisons of discrete and continuum results.** (a)–(f) $\langle C(x,t)\rangle$ (red) and $C(x,t)$ (blue). We use the linear diffusion given by (3.6) in (a)–(b), the increasing $D(C)$ given by (3.7) in (c)–(d), and the decreasing $D(C)$ given by (3.8) in (e)–(f). The solid black lines in (a), (c), (e) indicate that we consider an initial vertical strip with $w = 10$. Similarly, the solid black lines in (b), (d), (f) indicate that we consider an initial vertical strip with $w = 30$. We show the column density at $t = 200, 400, 600$ in (a), (c) and (e), at $t = 800, 1600, 2400$ in (b) and (d), and at $t = 1600, 3200, 4800$ in (f). The arrows in (a)–(f) show the direction of increasing time. (g) The total population density obtained from the continuum model, $\mathcal{C}(t)$, at $t = 10^4$ with the linear diffusion (green), the increasing $D(C)$ (red) and the decreasing $D(C)$ (black).

survives with $w = 30$. Comparing results in Figure 3.4(a)-(b) with those in Figure 3.4(c)-(d) shows that the evolution of $C(x,t)$ is different, and this difference is due to the role of nonlinear diffusion. Traditionally, if we were working with the continuum model alone, it would be difficult to provide a physical interpretation of these differences, but in our framework we can explain these differences through our simple crowding function, $G(C)$. We then use $G(C) = (1-C)(1-C/2)$ in the discrete model and the decreasing $D(C)$ given by (3.8) in the continuum model in Figures 3.4(e)–(f). In this case the continuum and discrete results reasonably match. Again, the population goes extinct with $w = 10$, but survives with $w = 30$.

Results in Figure 3.4(a)–(f) indicate the continuum limit of our discrete model provides an accurate approximation of the stochastic population dynamics for these three choices of crowding functions. In the Supplementary Material, we show that the discrete and continuum results also match well when we consider the power law diffusivity. A natural question that arises when confronted with these results is the following: introducing a nonlinear diffusivity function changes the rate at which the population spreads across the domain, and we wish to understand how these differences affect the long-term survival or extinction of the bistable population. To begin to explore this question we now vary the initial width of the vertical strip $w \in [10, 30]$, and show the total population density of the continuum model after a long period of time $t = 10^4$, with the three $D(C)$ functions, given by (3.6)–(3.8) in Figure 3.4(g). Results in Figure 3.4(g) show that solutions of the continuum model with these three $D(C)$ functions lead to different critical values of w that separate long-term survival from long-term extinction. This numerical exploration shows that the fate of bistable populations depends upon the choice of $D(C)$. We will now take advantage of our discrete-to-continuum framework to interpret how different choices of $D(C)$ either enhance or suppress population extinction.

3.7 Interpretation of how *D(C)* affects extinction

To understand how different choices of $D(C)$ affect long-term survival or extinction, we now derive mathematical expressions for the average flux of agents in the discrete model in a general setting. We consider an agent at site $\mathbf{s}$, at location (x, y), where the occupancy is $C(x, y, t)$. Assuming that the density is sufficiently smooth, the densities at the neighbouring sites can be obtained by expanding $C(x, y, t)$ in a truncated Taylor series,

$$C_{1,2} = C \mp \Delta \frac{\partial C}{\partial x} + \mathcal{O}(\Delta^2),$$
$$C_{3,5} = C - \frac{\Delta}{2}\frac{\partial C}{\partial x} + \mathcal{O}(\Delta^2),$$
$$C_{4,6} = C + \frac{\Delta}{2}\frac{\partial C}{\partial x} + \mathcal{O}(\Delta^2),$$

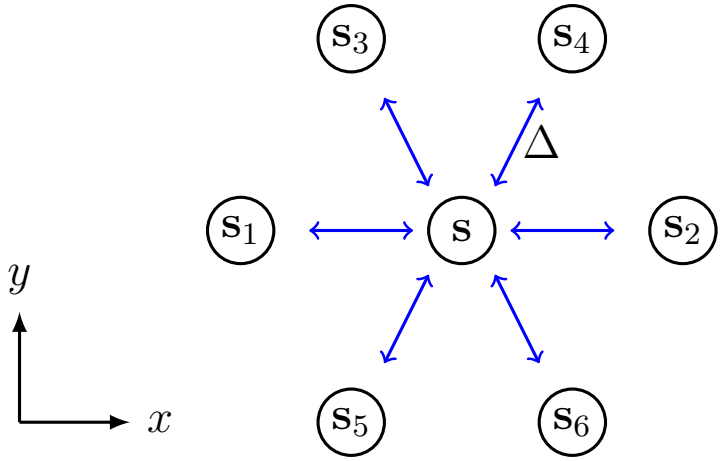

Figure 3.5: **Schematic diagram showing the six neighbouring sites surrounding site s.** The blue arrows indicate potential movement events that could change the occupancy of site $\mathbf{s}$. The spacing between site $\mathbf{s}$ and its neighbouring sites is Δ.

where, for convenience, we denote $C(x, y, t)$ as C and index the densities at neighbouring sites with subscripts as shown in Figure 3.5. The transition probability of an agent moving out of site $\mathbf{s}$ to one of its neighbouring sites $\mathbf{s}_i$, for $i = 1, 2, 3, \ldots, 6$, is

$$P_i^- = \frac{MCG(K)}{6(1-K)}(1 - C_i).$$

Similarly, the transition probability of an agent moving from site $\mathbf{s}_i$ into site $\mathbf{s}$ is

$$P_i^+ = \frac{MC_iG(K_i)}{6(1-K_i)}(1 - C).$$

Therefore, combining these expressions for the transition probabilities with the geometry of the lattice in Figure 3.5, allows us to write down an expression for the horizontal component of the net flux of agents at site $\mathbf{s}$,

$$\begin{aligned} J_x = &\frac{\Delta}{2\tau}\left[\left(2P_2^- + P_4^- + P_6^-\right) + \left(2P_1^+ + P_3^+ + P_5^+\right)\right] \\ &- \frac{\Delta}{2\tau}\left[\left(2P_2^+ + P_4^+ + P_6^+\right) + \left(2P_1^- + P_3^- + P_5^-\right)\right]. \end{aligned} \tag{3.18}$$

Substituting the expressions for the transition probabilities into (3.18) and then expanding the resulting terms in truncated Taylor series about site $\mathbf{s}$ gives

$$J_x = -\frac{M\Delta^2}{4\tau}\left[C\frac{\mathrm{d}G(C)}{\mathrm{d}C} + \frac{1+C}{1-C}G(C)\right]\frac{\partial C}{\partial x} + \mathcal{O}(\Delta^3), \tag{3.19}$$

We note that (3.19) can be written as

$$J_x = -D(C)\frac{\partial C}{\partial x}, \tag{3.20}$$

where $D(C)$ is the same as (3.4). Following a similar conservation argument, the flux of agents in the vertical direction can be written as

$$J_y = -D(C)\frac{\partial C}{\partial y}. \tag{3.21}$$

For all simulations in this work our initial condition is independent of vertical position so we have $J_y = 0$ throughout. It is useful to compare the nonlinear diffusive flux term with the classical linear diffusion flux. Thus, we re-write (3.20) as

$$J_x = -D_0\left(1 + H(C)\right)\frac{\partial C}{\partial x}, \tag{3.22}$$

where $H(C)$ can be regarded as a correction that is associated with the effects of nonlinear diffusion. For example, setting $H(C) = 0$ means that out nonlinear diffusion term simplifies to the classical linear diffusion term, whereas setting $H(C) > 0$ means that the nonlinear diffusion term is larger than the associated linear diffusion term.

To explore how different choices of $D(C)$ affect the long-term fate of bistable populations, we repeat the kinds of simulations we considered in Figure 3.4, and summarise the results in Figure 3.6 where we consider the linear diffusion, increasing $D(C)$ and decreasing $D(C)$ functions given by (3.6)–(3.8), respectively. For each diffusivity function we plot $H(C)$ in Figure 3.6(a). The increasing $D(C)$ leads to $H(C) \geq 0$ showing that the nonlinear flux is greater than the flux associated with the linear diffusion model for $C \in (0, 1]$. In contrast, the decreasing $D(C)$ leads to $H(C) \leq 0$ showing that the nonlinear flux is less than the flux associated with the linear diffusion model for $C \in (0, 1]$. We consider an initial condition with width $w = 20$ together with $M = 1$ and $P = 6/1000$, which corresponds to $D_0 = 1/4$ and $\lambda = 6/1000$ in the continuum model. Profiles in Figure 3.6(b) show the solution of the continuum model at $t = 200$, where we see that the density profile associated with the increasing $D(C)$ spreads further than the linear diffusion model. Similarly, the profile associated with the decreasing $D(C)$ spreads less than the linear diffusion model. These differences in spatial spreading mean that the maximum density for the increasing $D(C)$ model is less than the maximum density for the linear diffusion model, which encourages extinction since the bistable source term becomes negative across a larger area of the domain. This is consistent with the results in Figure 3.6(c) showing the long-term evolution of $\mathcal{C}(t)$, where we see that the population with increasing $D(C)$ goes extinct whereas the populations with linear diffusion and decreasing $D(C)$ lead to long-term survival.

Next, we investigate the population dynamics with the nonlinear diffusivity functions $D(C) = D_0C^m$ for $m = 1, 2$ and 3, with the associated $H(C)$ functions in Figure 3.6(d). With the same initial conditions and discrete parameters in Figure 6, we show various

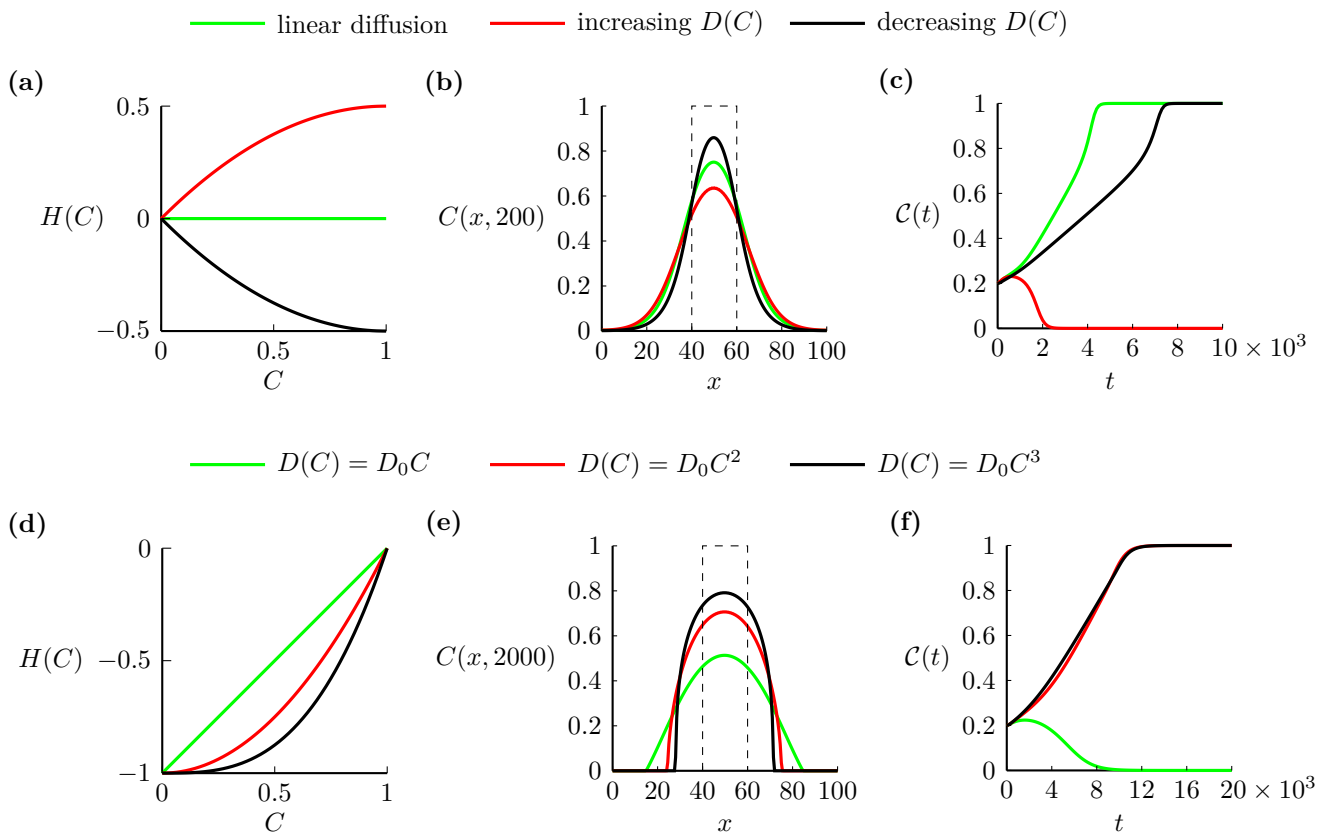

Figure 3.6: **Population dynamics with different $D(C)$.** (a) $H(C)$ associated with the linear diffusion given by (3.6) (green), increasing $D(C)$ given by (3.7) (red), and decreasing $D(C)$ given by (3.8) (black). (b) Solutions of Equation (3.13) at $t = 200$ with these three $D(C)$ functions. The dashed line is the initial distribution where $C(x, 0) = 1$ for $x \in [40, 60]$ and $C(x, 0) = 0$ elsewhere. (c) The evolution of $\mathcal{C}(t)$ with these three $D(C)$ functions. We set $M = 1$ and $P = 6/1000$ leading to $D_0 = 1/4$ and $\lambda = 6/1000$ in (b)–(c). (d) $H(C)$ associated with $D(C) = D_0C$ (green), $D(C) = D_0C^2$ (red) and $D(C) = D_0C^3$ (black). (e) Solutions of Equation (3.13) at $t = 2000$ with these three $D(C)$ functions. The dashed line is the initial distribution where $C(x, 0) = 1$ for $x \in [40, 60]$ and $C(x, 0) = 0$ elsewhere. (f) The evolution of $\mathcal{C}(t)$ with these three $D(C)$ functions. We set $M = 1$ and $P = 1/1000$ leading to $D_0 = 1/4$ and $\lambda = 1/1000$ in (e)–(f).

solutions of (3.13) at time $t = 2000$ in Figure 3.6(e), and $\mathcal{C}(t)$ in Figure 3.6(f). The results in Figure 3.6(d)–(f) for this class of power law $D(C)$ are consistent with the results in Figure 3.6(a)–(c). Results for $m = 1, 2$ and 3 lead to a reduction in flux relative to linear diffusion, but setting $m = 1$ still leads to sufficient spreading that a larger proportion of the domain has $C < A$ leading to extinction, whereas setting $m > 1$ reduces the spreading so that a smaller proportion of the domain has $C < A$ leading to survival.

Results in Figure 3.6 show that the change of flux influences the speed at which the population spreads in space. Due to the change of spreading speed, the initial width of the vertical strip needed for a population to survive changes as well. This suggests that the nonlinear diffusivity function affects the fate of bistable populations through influencing the flux of populations. However, in Figure 3.6, we fix the ratio of growth and movement, P/M, while P/M also influences the fate of bistable populations. Next, we are going to vary P/M and study the influence of nonlinear diffusion on the fate of a broader range of populations.

Our results so far show that the long-term survival of the population involves a complicated relationship between the width of the initial condition w, the time scale of migration M, the time scale of growth P, as well as the particular nonlinear diffusivity function $D(C)$. We now systematically explore this relationship by taking the $(w, P/M)$ phase space and discretising it uniformly for $w \in [0, 40]$ and $P/M \in [1/1000, 40, 1000]$, as shown in Figure 3.7. We vary P and fix $M = 1$ leading to $\lambda = P$ and $D_0 = 1/4$ in the continuum model. As we are interested in the long-term outcomes of bistable populations, we solve (3.13) and calculate $\mathcal{C}(T)$ for a sufficiently long period of time T, so that the outcome is either $\mathcal{C}(T) = 1$ or $\mathcal{C}(T) = 0$. With these simulation outcomes we identify the boundaries that separate survival and extinction on the phase diagram. Overall, results in Figure 3.7 show that large w encourages survival, and that for each value of w there is a threshold value of P/M that determines the eventual survival or extinction of the survival. In the Supplementary, we show that the boundaries generated from the discrete model are consistent with the boundaries identified using the continuum model. The main result in Figure 3.7 is that the curves that delineate the survival/extinction boundary depend upon the choice of $D(C)$, and we plot three curves for the linear diffusion model, the increasing $D(C)$ given by (3.7) and the decreasing $D(C)$ given by (3.8). The horizontal dashed line at $P/M = 0.006$ highlights results shown previously in Figure 3.4 and Figure 3.6, but this phase diagram summarises the long-term survival/extinction patterns for a much wider choice of parameters than we explored in these previous cases.

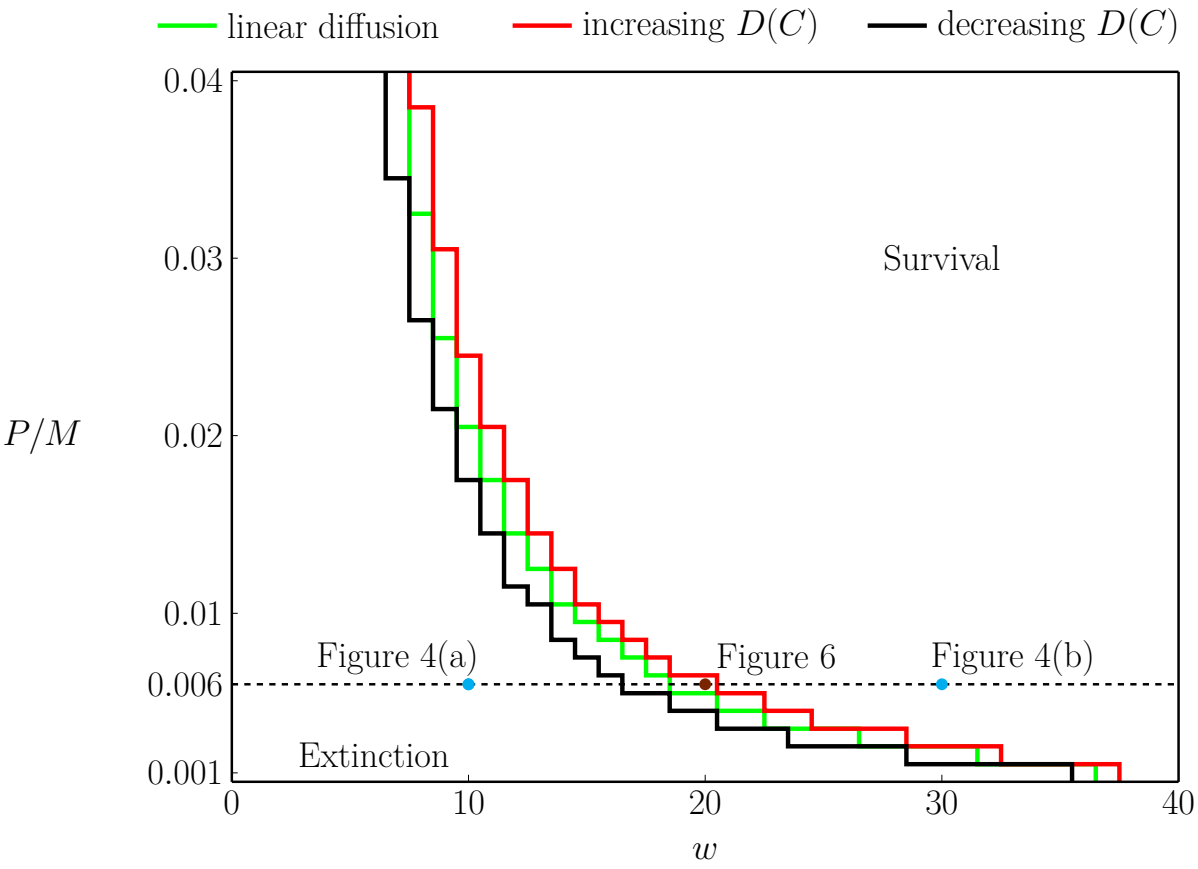

Figure 3.7: **Phase diagram for the survival and extinction of populations.** The phase space $(w, P/M)$ is uniformly discretised into a rectangular mesh with 41×40 nodes, where $w \in [0, 40]$ and $P/M \in [1/1000, 4/100]$. Three curves are the thresholds for the survival and extinction of populations in the continuum model with the linear diffusion given by (3.6) (green), increasing $D(C)$ given by (3.7) (red), and decreasing $D(C)$ given by (3.8) (black). Two cyan dots indicate the parameters $P/M = 6/1000$ and $w = 10$ or $w = 30$ considered in Figures 3.4. The brown dot indicates the parameters $P/M = 6/1000$ and $w = 20$ considered in Figure 3.6.

3.8 Conclusion and outlook

In this work we consider the question of population survival or extinction, with a focus on understanding how various migration mechanisms either encourage or suppress extinction. In the population biology modelling literature, the most common way to study population dynamics with spatial effects is to use a reaction-diffusion model with a linear diffusion term to represent migration and a bistable source term to represent birth-death processes. While most studies employ a linear diffusion mechanism for simplicity, there are many cases where linear diffusion is inadequate. For example, mathematical models based on a linear diffusion mechanism do not predict a well-defined front that is often observed experimentally or in the field. This limitation of linear diffusion is typically overcome by generalising the constant diffusivity, D, to a nonlinear diffusivity function $D(C)$. One of the main challenges of working with a nonlinear diffusion framework is the important question of how to choose the functional form of $D(C)$, and there are conflicting results in the literature. For example, in the cell migration modelling literature some studies have found that using a power law diffusivity function $D(C) = D_0 C^m$, with $m \geq 1$ can lead to a good match to experimental data (Sherratt and Murray 1990; Sengers et al. 2007; Jin et al. 2016b). One of the features of these models it that this nonlinear diffusivity is an increasing function of density. Curiously, other researchers working in precisely the same field have suggested that a decreasing nonlinear diffusivity function is appropriate, $D(C) = 1/(\alpha + C)$, with $\alpha > 0$ (Cai et al. 2007). This highlights the fact that choosing an appropriate nonlinear diffusivity function is not always straightforward.

In addition to understanding how to choose an appropriate nonlinear diffusivity function, a related challenge is to understand how different forms of $D(C)$ affect the long-term survival or extinction of bistable populations. While it has been established that different choices of $D(C)$ impacts the long-term survival of populations (Lee et al. 2006), an intuitive understanding of why different choices of $D(C)$ encourage or suppress extinction has been lacking. In this work we address this question by working with a very simple discrete modelling framework on a two-dimensional hexagonal lattice, where migration and birth/death events are controlled through relatively simple, easy-to-interpret crowding functions. In particular we work with a migration crowding function $G(C)$, which provides a very simple measure of how the ability of an individual agent to move is reduced as a function of density, C. Our discrete-to-continuum averaging arguments provides a mathematical relationship which allows us to either: (i) specify $G(C)$ and determine the associated nonlinear diffusivity function $D(C)$; or, (ii) specify $D(C)$ and determine the associated crowding function $G(C)$. This new relationship allows us to explore how the averaged population-level flux of agents varies relative to the classical linear diffusion model for a particular crowding function, $G(C)$. We find that choices of $G(C)$ that increase

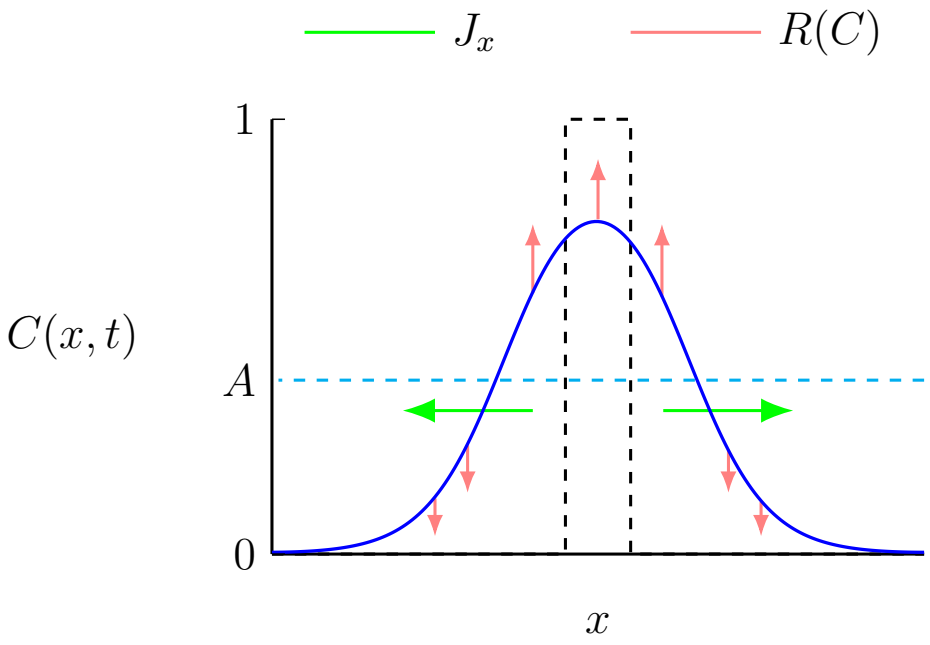

Figure 3.8: **Schematic profile of the spreading population (blue) superimposed on the Allee threshold $C = A$ (dashed cyan) and the initial density distribution $C(x, 0)$ (dashed black).** Spatial spreading of the population is controlled by the diffusive flux, J_x, that is proportional to the nonlinear diffusivity function, $D(C)$, and the direction of the flux is indicated (green arrows). This flux affects: (i) the proportion of the domain where $C < A$ giving rise to a negative source term (downward red arrows), and (ii) the proportion of the domain where $C > A$, giving rise to a positive source term (upward red arrows).

the flux encourage population extinction relative to the classical linear diffusion model, whereas choices of $G(C)$ that decrease the flux suppresses population extinction. These results are summarised in the conceptual diagram in Figure 3.8 showing that, for the initial conditions considered, increasing the flux of agents tends to reduce the density across the domain as the population spreads, meaning that a greater proportion of the domain has $C < A$, where the bistable source term acts to reduce the population and encourage extinction.

There are many ways that our work can be extended. For example, all simulation results presented here consider a very simple one-dimensional vertical strip initial condition. These results can be generalised to other initial shapes, such as circular, square or more complicated initial populations, and the mathematical and computational tools presented in this work can be applied directly to this generalisation. We show that nonlinear diffusion plays the same role as linear diffusion on the fate of populations when we consider the simple well-mixed initial distribution in the Supplementary Material. There are also many ways that the current modelling framework can be extended. For example, the discrete model can be extended to consider multiple interacting subpopulations, and the same discrete-to-continuum averaging approach could be used to construct a continuum limit

model, which would take the form of a system of coupled partial differential equation models (Shigesada et al. 1979; Painter and Sherratt 2003; Hughes et al. 2010; Martínez-García et al. 2020). We leave this extension for future consideration.

3.9 Additional results

3.9.1 Algorithm for discrete simulations

We consider an $L \times L$ domain with $L = 100$. Each lattice site is indexed by (i, j), and has a unique Cartesian coordinate,

$$(x, y) = \begin{cases} \left(i\Delta, j\dfrac{\Delta\sqrt{3}}{2} \right), & \text{if } j \text{ is even,} \\ \left(\left(i + \dfrac{1}{2} \right) \Delta, j\dfrac{\Delta\sqrt{3}}{2} \right), & \text{if } j \text{ is odd.} \end{cases} \tag{3.23}$$

To approximate the size of the domain in discrete simulations, we create a two-dimensional hexagonal lattice with 100×116 uniformly distributed nodes. The pseudo-code for a single realisation of the stochastic model is given in Algorithm 2.

Algorithm 2: Pseudo-code for a single realisation of the stochastic model

Create a two-dimensional $I \times J$ hexagonal lattice; Distribute agents with vertical strip initial conditions; The total number of lattice site is IJ;
Set $t = 0$; Calculate total agents $Q(t)$;
while $t < t_{\text{end}}$ and $Q(t) > 0$ and $Q(t) \leq IJ$ **do**
    $t = t + \tau$;
    $Q(t) = Q(t - \tau)$;
    $B_1 = 0$; $B_2 = 0$;
    Draw two random variables: $\beta_1 \sim U[0, 1]$, $\beta_2 \sim U[0, 1]$;
    while $B_1 < Q(t)$ **do**
        $B_1 = B_1 + 1$;
        Randomly choose an agent $\mathbf{s}$;
        if $\beta_1 < M$ **then**
            Calculate $\overline{K}_{\mathbf{s}}^{(\mathrm{m})}$ and $G(\overline{K}_{\mathbf{s}}^{(\mathrm{m})})$;
            Draw a random variable: $\gamma_1 \sim U[0, 1]$;
            if $\gamma_1 < G(\overline{K}_{\mathbf{s}}^{(\mathrm{m})})$ **then**
                Randomly choose a vacant site in $\mathcal{N}_1(\mathbf{s})$ and move agent to chosen site
            else
                Nothing happens;
            end
        else
            Nothing happens;
        end
    end
    while $B_2 < Q(t)$ **do**
        $B_2 = B_2 + 1$;
        Randomly choose an agent $\mathbf{s}$;
        if $\beta_2 < P$ **then**
            Calculate $K_{\mathbf{s}}^{(\mathrm{g})}$ and $F(\overline{K}_{\mathbf{s}}^{(\mathrm{g})})$;
            Draw a random variable: $\gamma_2 \sim U[0, 1]$;
            if $F(\overline{K}_{\mathbf{s}}^{(\mathrm{g})}) > 0$ **then**
                if $\gamma_2 < F(\overline{K}_{\mathbf{s}}^{(\mathrm{g})})$ **then**
                    Randomly choose a vacant site in $\mathcal{N}_4(\mathbf{s})$ and place a new agent on chosen site;
                    $Q(t) = Q(t) + 1$
            else if $F(\overline{K}_{\mathbf{s}}^{(\mathrm{g})}) < 0$ **then**
                if $\gamma_2 < -F(\overline{K}_{\mathbf{s}}^{(\mathrm{g})})$ **then**
                    Remove agent;
                    $Q(t) = Q(t) - 1$;
            else
                Nothing happens;
            end
        else
            Nothing happens;
        end
    end
end

3.9.2 Derivation of the continuum limit

Considering the spatial template with $r = 1$ for the movement mechanism and $r \geq 1$ for the growth mechanism of agents, the expected change in occupancy of site $\mathbf{s}$ during the time interval from t to $t + \tau$ is given as

$$\begin{aligned}\delta(\overline{C}_{\mathbf{s}}) =& \frac{M}{|\mathcal{N}_1|}(1-\overline{C}_{\mathbf{s}}) \sum_{\mathbf{s}' \in \mathcal{N}_1\{\mathbf{s}\}} \overline{C}_{\mathbf{s}'} \frac{G(\overline{K}^{(\mathrm{m})}_{\mathbf{s}'})}{1-\overline{K}^{(\mathrm{m})}_{\mathbf{s}'}} - M\overline{C}_{\mathbf{s}} G(\overline{K}^{(\mathrm{m})}_{\mathbf{s}}) \\ &+ \frac{P}{|\mathcal{N}_r|}(1-\overline{C}_{\mathbf{s}}) \sum_{\mathbf{s}' \in \mathcal{N}_r\{\mathbf{s}\}} \mathbb{H}(F(\overline{K}^{(\mathrm{g})}_{\mathbf{s}'}))\overline{C}_{\mathbf{s}'} \frac{F(\overline{K}^{(\mathrm{g})}_{\mathbf{s}'})}{1-\overline{K}^{(\mathrm{g})}_{\mathbf{s}'}} \\ &- (1-\mathbb{H}(F(\overline{K}^{(\mathrm{g})}_{\mathbf{s}}))P\overline{C}_{\mathbf{s}} F(\overline{K}^{(\mathrm{g})}_{\mathbf{s}}).\end{aligned} \tag{3.24}$$

As we know that the continuum limit of the last two terms in Equation (3.24) leads to a source term $\lambda C F(C)$ with $r \geq 1$ (Jin et al. 2016a), we focus on the movement mechanism, that is, the first two terms on the right hand side of Equation (3.24). For convenience, we will omit the overlines on notations in the following content.

It is useful to first write the general form of the Taylor series relating the occupancy of sites $(x + a, y + b)$,

$$\begin{aligned}C_{x+a,y+b} =& C_{x,y} + \frac{(a\Delta)^1}{1!}\frac{\partial C_{x,y}}{\partial x} + \frac{(b\Delta)^1}{1!}\frac{\partial C_{x,y}}{\partial y} \\ &+ \frac{(a\Delta)^2}{2!}\frac{\partial C^2_{x,y}}{\partial x^2} + \frac{2ab\Delta^2}{2!}\frac{\partial C^2_{x,y}}{\partial x \partial y} + \frac{(b\Delta)^2}{2!}\frac{\partial C^2_{x,y}}{\partial y^2} + \mathcal{O}(\Delta^3).\end{aligned} \tag{3.25}$$

We represent the six nearest neighbouring sites of site $\mathbf{s}$ located at (x, y) as site $\mathbf{s}_1$ with $(x - \Delta, y)$; site $\mathbf{s}_2$ with $(x + \Delta, y)$; site $\mathbf{s}_3$ with $(x - \Delta/2, y + \Delta\sqrt{3}/2)$; site $\mathbf{s}_4$ with $(x + \Delta/2, y + \Delta\sqrt{3}/2)$; site $\mathbf{s}_5$ with $(x - \Delta/2, y - \Delta\sqrt{3}/2)$ and site $\mathbf{s}_6$ with $(x + \Delta/2, y - \Delta\sqrt{3}/2)$. That is, $\mathcal{N}_1 = \{\mathbf{s}_1, \mathbf{s}_2, \mathbf{s}_3, \mathbf{s}_4, \mathbf{s}_5, \mathbf{s}_6\}$. The local density of $\mathbf{s}$ is obtained by summing the Taylor series of sites in $\mathcal{N}_1\{\mathbf{s}\}$, that is,

$$K^{(\mathrm{m})}_{\mathbf{s}} = \frac{1}{6}\sum_{\mathbf{s}'' \in \mathcal{N}_1\{\mathbf{s}\}} C_{\mathbf{s}''} = C_{\mathbf{s}} + \left(\frac{\partial^2 C_{\mathbf{s}}}{\partial x^2} + \frac{\partial^2 C_{\mathbf{s}}}{\partial y^2}\right)\frac{\Delta^2}{4} + \mathcal{O}(\Delta^3). \tag{3.26}$$

Similarly, the local density of $\mathbf{s_1}$ is obtained by summing the Taylor series of sites in $\mathcal{N}_1\{\mathbf{s}_1\}$, that is,

$$\begin{aligned}K^{(\mathrm{m})}_{\mathbf{s}_1} &= \frac{1}{6}\sum_{\mathbf{s}'' \in \mathcal{N}_1\{\mathbf{s}_1\}} C_{\mathbf{s}''} \\ &= C_{\mathbf{s}} - \frac{\partial C_{\mathbf{s}}}{\partial x}\Delta + \frac{\partial^2 C_{\mathbf{s}}}{\partial x^2}\frac{\Delta^2}{2} + \left(\frac{\partial^2 C_{\mathbf{s}}}{\partial x^2} + \frac{\partial^2 C_{\mathbf{s}}}{\partial y^2}\right)\frac{\Delta^2}{4} + \mathcal{O}(\Delta^3).\end{aligned} \tag{3.27}$$

For simplification we rewrite Equation (3.27) as $K_{\mathbf{s}_1}^{(\mathrm{m})} = C_{\mathbf{s}} + \widetilde{C}_{\mathbf{s}_1}$, where $\widetilde{C}_{\mathbf{s}_1} \sim \mathcal{O}(\Delta)$. Subsequently, the movement crowding function at $\mathbf{s}_1$ can be expanded as

$$\begin{aligned} G\left(K_{\mathbf{s}_1}^{(\mathrm{m})}\right) &= G\left(C_{\mathbf{s}} + \widetilde{C}_{\mathbf{s}_1}\right), \\ &= G\left(C_{\mathbf{s}}\right) + \frac{\mathrm{d}G\left(C_{\mathbf{s}}\right)}{\mathrm{d}C}\widetilde{C}_{\mathbf{s}_1} + \frac{\mathrm{d}^2G\left(C_{\mathbf{s}}\right)}{\mathrm{d}C^2}\frac{\widetilde{C}_{\mathbf{s}_1}^2}{2}. \end{aligned} \tag{3.28}$$

The expansions of $G(K_{\mathbf{s}_2}^{(\mathrm{m})})$, $G(K_{\mathbf{s}_3}^{(\mathrm{m})})$,...,$G(K_{\mathbf{s}_6}^{(\mathrm{m})})$ have similar forms to (3.28). We then go back to the first term on the right hand side of (3.24), which gives

$$\frac{M}{6}(1 - C_{\mathbf{s}}) \sum_{\mathbf{s}' \in \mathcal{N}_1\{\mathbf{s}\}} C_{\mathbf{s}'} \frac{G(K_{\mathbf{s}'}^{(\mathrm{m})})}{1 - K_{\mathbf{s}'}^{(\mathrm{m})}}. \tag{3.29}$$

For convenience we further drop the $\mathbf{s}$ notation so that $C_{\mathbf{s}}$ becomes C and $C_{\mathbf{s}_1}$ becomes C_1. Subsequently, (3.29) becomes

$$\frac{M}{6}(1 - C) \sum_{i=1}^{6} C_i \frac{G(K_{\mathbf{s}_i}^{(\mathrm{m})})}{1 - K_{\mathbf{s}_i}^{(\mathrm{m})}}. \tag{3.30}$$

Moreover, we will use two notations

$$\mathcal{A} = \left(\frac{\partial^2 C_{\mathbf{s}}}{\partial x^2} + \frac{\partial^2 C_{\mathbf{s}}}{\partial y^2}\right)\frac{\Delta^2}{4}, \quad \mathcal{B} = \left(\left(\frac{\partial C_{\mathbf{s}}}{\partial x}\right)^2 + \left(\frac{\partial C_{\mathbf{s}}}{\partial y}\right)^2\right)\frac{\Delta^2}{4}, \tag{3.31}$$

in the following content. Expanding the term related to site $\mathbf{s}_1$ in (3.30) gives

$$\begin{aligned} &\frac{M}{6}(1 - C)\left(C + \widetilde{C}_1 - \mathcal{A}\right)\frac{\left(G(C) + G'(C)\widetilde{C}_1 + G''(C)\dfrac{\widetilde{C}_1^2}{2}\right)}{1 - \left(C + \widetilde{C}_1\right)} \\ =&\frac{M}{6}\left[CG(C) + \left(CG'(C) + \frac{G(C)}{1 - C}\right)\widetilde{C}_1\right] \\ &+ \frac{M}{6}\left[\left(\frac{G(C)}{(1 - C)^2} + \frac{G'(C)}{1 - C} + \frac{CG''(C)}{2}\right)\widetilde{C}_1^2 - G(C)\mathcal{A}\right], \end{aligned}$$

to order of Δ^3. Here, the prime denotes the ordinary differentiation with respect to C. The terms related to other sites can be obtained in a similar way. Therefore, expanding all terms in (3.30) and neglecting terms of order $\mathcal{O}(\Delta^3)$ gives

$$\begin{aligned} &\frac{M}{6}\left[6CG(C) + \left(CG'(C) + \frac{G(C)}{1 - C}\right)\sum_{k=1}^{6}\widetilde{C}_k\right] \\ &+ \frac{M}{6}\left[\left(\frac{G(C)}{(1 - C)^2} + \frac{G'(C)}{1 - C} + \frac{CG''(C)}{2}\right)\sum_{k=1}^{6}\widetilde{C}_k^2 - 6G(C)\mathcal{A}\right]. \end{aligned} \tag{3.32}$$

Furthermore, since we have

$$\begin{aligned}\sum_{k=1}^{6}\widetilde{C}_k &= 12\left(\frac{\partial^2 C}{\partial x^2}+\frac{\partial^2 C}{\partial y^2}\right)\frac{\Delta^2}{4}+\mathcal{O}(\Delta^3),\\ &= 12\mathcal{A}+\mathcal{O}(\Delta^3),\end{aligned} \tag{3.33}$$

and

$$\begin{aligned}\sum_{k=1}^{6}\widetilde{C}_k^2 &= 12\left(\left(\frac{\partial C}{\partial x}\right)^2+\left(\frac{\partial C}{\partial y}\right)^2\right)\frac{\Delta^2}{4}+\mathcal{O}(\Delta^3),\\ &= 12\mathcal{B}+\mathcal{O}(\Delta^3),\end{aligned} \tag{3.34}$$

Equation (3.32) becomes

$$\begin{aligned}&MCG(C)+M\left(2CG'(C)-G(C)+\frac{2G(C)}{1-C}\right)\mathcal{A}\\ &+M\left(CG''(C)+\frac{2G(C)}{(1-C)^2}+\frac{2G'(C)}{1-C}\right)\mathcal{B}+\mathcal{O}(\Delta^3).\end{aligned} \tag{3.35}$$

Remind that the second term in (3.24) is

$$\begin{aligned}MCG(\overline{K}_{\mathbf{s}}^{(\mathrm{m})}) &= MCG(C)+MCG'(C)\widetilde{C},\\ &= MCG(C)+MCG'(C)\mathcal{A}+\mathcal{O}(\Delta^3).\end{aligned} \tag{3.36}$$

Then combining (3.35) and (3.36) gives

$$\begin{aligned}\delta(C_{\mathbf{s}}) &= \left(CG'(C)+\frac{1+C}{1-C}G(C)\right)M\mathcal{A}\\ &+\left(CG''(C)+\frac{2G(C)}{(1-C)^2}+\frac{2G'(C)}{1-C}\right)M\mathcal{B},\end{aligned} \tag{3.37}$$

to order of Δ^3. Dividing both sides of the resulting expression by τ, and letting $\Delta\to 0$ and $\tau\to 0$ jointly, with the ratio Δ^2/τ held constant, leads to the following nonlinear reaction-diffusion equation,

$$\frac{\partial C}{\partial t}=\nabla\cdot\left[D_0\left(CG'(C)+\frac{1+C}{1-C}G(C)\right)\nabla C\right]+\lambda CF(C), \tag{3.38}$$

where

$$D_0=\frac{M}{4}\lim_{\Delta,\tau\to 0}\frac{\Delta^2}{\tau},\quad \lambda=\lim_{\tau\to 0}\frac{P}{\tau}. \tag{3.39}$$

If we define

$$D(C)=D_0\left[CG'(C)+\frac{1+C}{1-C}G(C)\right], \tag{3.40}$$

then the continuum limit is written as

$$\frac{\partial C}{\partial t} = \nabla \cdot [D(C)\nabla C] + \lambda C F(C). \tag{3.41}$$

3.9.3 Numerical method

To numerically calculate solutions of the reaction-diffusion equation

$$\frac{\partial C}{\partial t} = \frac{\partial}{\partial x}\left(D(C)\frac{\partial C}{\partial x}\right) + R(C), \tag{3.42}$$

on $0 < x < L$, we first discretise the spatial derivative in Equation (3.42) with an $(I+1)$ uniformly distributed nodes with spacing $\delta x > 0$, which are indexed by x_i with $i = 0, 1, 2, ..., I$ satisfying $I = L/\delta x$. We leave the time derivative continuous and obtain

$$\begin{aligned}\frac{\mathrm{d}C_i}{\mathrm{d}t} =& \frac{1}{2\delta x^2}(D(C_{i+1}) + D(C_i))C_{i+1} \\ &- \frac{1}{2\delta x^2}(D(C_{i+1}) + 2D(C_i) + D(C_{i-1}))C_i \\ &+ \frac{1}{2\delta x^2}(D(C_i) + D(C_{i-1}))C_{i-1} \\ &+ R(C_i).\end{aligned} \tag{3.43}$$

This equation is valid for interior nodes, and is modified on the boundary nodes to simulate periodic boundary conditions. This system of I coupled ordinary differential equations is then integrated through time using MATLABs function ode45 (MATLAB 2020).

3.9.4 Discrete-continuum comparisons with power-law diffusivity

Figure 3.9 show the continuum and discrete results obtained with the nonlinear diffusivity functions $D(C) = D_0 C^m$ for $m = 1, 2, 3$ and the corresponding movement crowding functions. Discrete simulations are performed with parameters $M = 1$ and $P = 1/1000$, leading to $D_0 = 1/4$ and $\lambda = 1/1000$ in the continuum model. For the discrete model, we average the simulation data over 40 times of identically-prepared realisations, and initially locate agents in the middle of the domain with a vertical strip with width $w = 20$, which means that the initial condition for the continuum model is $C(x, 0) = 1$ for $x \in [40, 60]$ and $C(x, 0) = 0$ elsewhere. We compare $C(x, t)$ with $\langle C(x, t)\rangle$ in Figures 3.9(a)–(c), and compare $\mathcal{C}(t)$ with $\langle C(t)\rangle$ in Figures 3.9(d)–(f). Results in Figure 3.9 indicate that the match between the solutions of continuum model and the appropriately averaged data from discrete model is excellent.

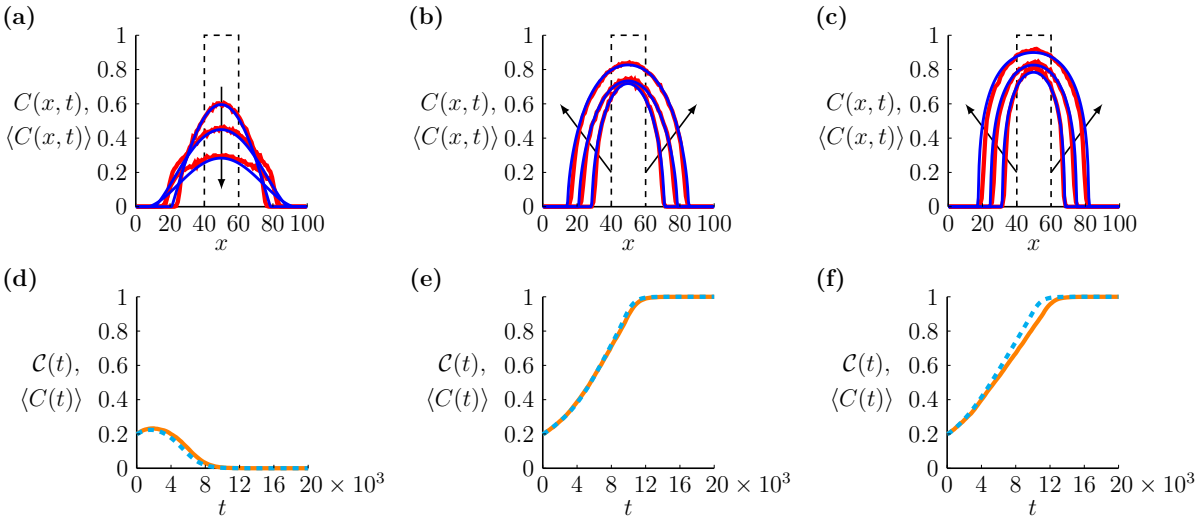

Figure 3.9: **Population dynamics with different nonlinear diffusivity functions.** (a) $C(x,t)$ (blue) obtained with $D(C) = D_0C$, $D(C) = D_0C^2$ and $D(C) = D_0C^3$, respectively, and $\langle C(x,t)\rangle$ (red) obtained with the corresponding $G(C)$, at $t = 1000, 3000, 5000$. The dashed lines in (a)–(c) indicate the initial distribution, where $C(x,0) = 1$ for $x \in [40,60]$ and $C(x,0) = 0$ elsewhere. The arrows in (a)–(c) show the direction of increasing time. (d)–(f) $\mathcal{C}(t)$ (dashed cyan) and $\langle C(t)\rangle$ (solid orange) obtained with $D(C) = D_0C$, $D(C) = D_0C^2$, $D(C) = D_0C^3$, respectively. Note that we consider $M = 1$ and $P = 1/1000$ leading to $D_0 = 1/4$ and $\lambda = 1/1000$.

3.9.5 Phase diagrams with the well-mixed or vertical strip initial distributions

We show the phase diagram for the survival and extinction of the well-mixed populations with $G(C) = 1 - C$, $G(C) = (1 - C)(1 + C/2)$ and $G(C) = (1 - C)(1 - C/2)$ in Figure 3.10(a)–(c), respectively. In our discrete simulations we randomly distribute a fixed number of agents on an $L \times L$ domain where $L = 100$, so that the density is, on average, B at any site. We consider the $(B, P/M)$ phase space and discretise it into 51×40 nodes, where we change $B \in [0.1, 0.6]$ and change $P/M \in [1/1000, 4/100]$ by varying P where $M = 1$ in the discrete model, and varying $\lambda = P$ where $D_0 = 1/4$ in the continuum model. Since different identically-prepared realisations of the stochastic model can lead to either survival or extinction of the population, for each pair of parameters w and P/M, we generate 40 identically-prepared realisations and compute the survival probability, $S \in [0, 1]$, as the fraction of realisations in which the population survives after a sufficiently long period of time $\mathcal{T}$, which we take $\mathcal{T} = max(30/P, 10^4)$ in practice. The blue shading in Figures 3.10(a)–(c) shows the survival probability S. For the well-mixed population, the continuum model simplifies to an ODE

$$\frac{\mathrm{d}C(t)}{\mathrm{d}t} = \lambda C(t) F(C(t)), \tag{3.44}$$

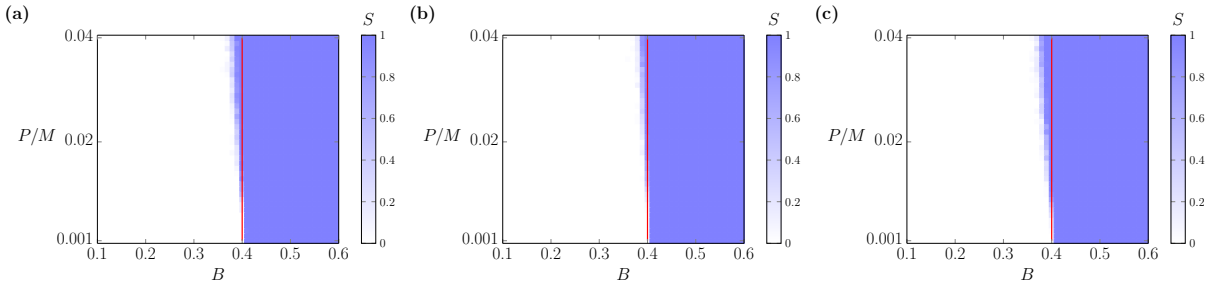

Figure 3.10: **Phase diagrams for the survival and extinction of populations with the well-mixed initial distribution and different $G(C)$.** (a)–(c) Phase diagrams with $G(C) = 1 - C$, $G(C) = (1 - C)(1 + C/2)$ and $G(C) = (1 - C)(1 - C/2)$, respectively. The phase space is descretised into a rectangular mesh with 51×40 nodes for $B \in [1/10, 1/60]$ and $P/M \in [1/1000, 4/100]$ where $M = 1$. The blue shading is the survival probability in the discrete model. The red line in each phase diagram indicates $B = 0.4$, which relates to the Allee threshold, $A = 0.4$, and is the survival/extinction boundary for the continuum model.

where $F(C) = 2.5(1 - C)(C - A)$ with the Allee threshold $A = 0.4$. Therefore, the boundary separating the survival and extinction of populations in the continuum model is always the vertical line $B = 0.4$, associated with the Allee threshold $A = 0.4$. Results in Figure 3.10 indicate that the three movement crowding functions lead to very similar boundaries for the survival and extinction of populations in the discrete model. This suggests that nonlinear diffusion plays the same role as linear diffusion on the fate of well-mixed populations.

We then consider the vertical strip initial distribution and compare the continuum and discrete results. We take the $(w, P/M)$ phase space and discretise it uniformly into a rectangular mesh with 41×40 nodes, where $w \in [0, 40]$ and $P/M \in [1/1000, 4/100]$. We vary P and fix $M = 1$ in the discrete model, leading to $\lambda = P$ and $D_0 = 1/4$ in the continuum model. We show the survival probability on the $(w, P/M)$ phase space in Figure 3.11, and overlap with the boundary that separates survival and extinction of the population in the continuum model. We show the results obtained with the linear diffusion, increasing $D(C)$ and decreasing $D(C)$ in Figure 3.11(a)–(c), respectively. The boundaries separating survival and extinction in discrete and continuum models are very close on the phase diagram, which indicates that the discrete and continuum models are consistent in generating the long-term outcomes of bistable populations.

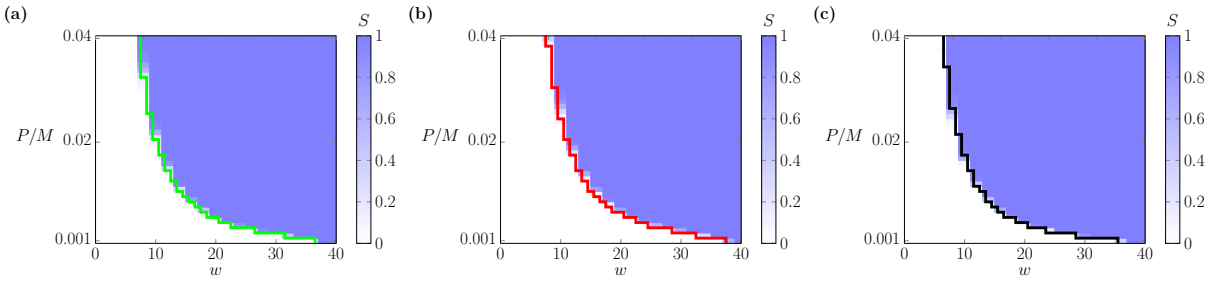

Figure 3.11: **Phase diagrams for the survival and extinction of populations with both discrete and continuum models.** (a)–(c) Phase diagrams for the survival and extinction of populations with $G(C) = 1$, $G(C) = (1 - C)(1 + C/2)$ and $G(C) = (1 - C)(1 - C/2)$, respectively. The phase space is descretised into a rectangular mesh with 41×40 nodes for $w \in [0, 40]$ and $P/M \in [1/1000, 4/100]$ where $M = 1$. The blue shading is the survival probability in the discrete model. The solid line in each phase diagram is the survival/extinction boundary obtained from the continuum model.

Chapter 4

Smooth travelling waves with nonlinear diffusion and logistic growth source terms

---

4.1 Preamble

This chapter is a paper published in the *Journal of Mathematical Biology*

Li, Y., van Heijster, P., Marangell, R., Simpson, M. J., 2020. Travelling wave solutions in a negative nonlinear diffusion–reaction model. *Journal of Mathematical Biology*, 81: 1495-1522. DOI:10.1007/s00285-020-01547-1. arXiv Preprint

In this chapter, we address the research question 3 of the thesis: What are the existence and stability properties of smooth travelling wave solutions with nonlinear diffusion and logistic growth source terms? We focus on a specific movement mechanism of individuals in a one-dimensional discrete model, which leads to a nonlinear diffusivity function that changes signs twice in the domain of our interest. We transform the reaction-diffusion equation to a system of first-order ODEs by using the travelling wave coordinate and a dynamical system approach. To address the problem of singularities in the ODE system, we desingularise the system by using a stretched variable. We then study the desingularised system with the method of phase plane analysis to prove the existence of travelling wave solutions. We also study the spectral stability of travelling wave solutions, and explore how the stability property relates to the speed of travelling wave solutions. Note that the geometric approach developed here acts as a reference approach for further studies in the next chapter, where extensions are made by adding higher order perturbation terms to the original equation.

4.2 Abstract

We use a geometric approach to prove the existence of smooth travelling wave solutions of a nonlinear diffusion-reaction equation with logistic kinetics and a convex nonlinear diffusivity function which changes sign twice in our domain of interest. We determine the minimum wave speed, c^*, and investigate its relation to the spectral stability of the travelling wave solutions.

4.3 Introduction

Invasion processes have been studied with mathematical models, especially partial differential equations (PDEs), for many years; see, for example, Murray (1989) and references therein. These models describe, for instance, how cells are transported to new areas in which they persist, proliferate, and spread (Mack et al. 2000). To incorporate information about individual-level behaviours in invasion processes, lattice-based discrete models are widely used (Deroulers et al. 2009; Johnston et al. 2017, 2012; Simpson et al. 2010c). In these discrete models, individual agents are permitted to move, proliferate and die on a lattice, and the average density of agents is related to PDE descriptions obtained using truncated Taylor series in the continuum limit (Anguige and Schmeiser 2009; Codling et al. 2008). The macroscopic behaviour described by the PDEs in terms of expected agent density reflects the individual microscopic behaviour. Travelling wave solutions are of particular interest among the macroscopic behaviours arising from these continuum models, as they reflect various modes of microscopic invasive behaviours. One famous model exhibiting travelling wave solutions is the Fisher-KPP equation (KPP refers to Kolmogorov, Petrovsky, Piskunov) proposed in 1937 to study population dynamics with linear diffusion and logistic growth (Fisher 1937; Kolmogorov et al. 1937). The existence and stability of travelling wave solutions of the Fisher-KPP equation has been widely studied, see, for instance, Aronson and Weinberger (1978); Fisher (1937); Harley et al. (2015); Kolmogorov et al. (1937); Larson (1978); Murray (1989).

The Fisher-KPP equation can be derived as a continuum limit of a discrete model under the assumption that the population of cells can be treated as a uniform population without any differences in subpopulations (Bramson et al. 1986). However, differences between individual and collective behaviour have been observed in cell biology and ecology in practice. For instance, in cell biology, isolated cells called *leader cells* are more motile than the grouped cells, called *follower cells* (Poujade et al. 2007). Also, contact interactions lead to different motility rates between isolated cells and grouped cells in the migration of breast cancer cells (Simpson et al. 2010c, 2014), glioma cells (Khain et al. 2011), would healing processes (Khain et al. 2007) and the development of the enteric nervous system

(Druckenbrod and Epstein 2007). In ecology, the population growth rate of some species decreases as their populations reach small sizes or low densities (Courchamp et al. 1999). This phenomenon is usually referred to as the Allee effect (Allee and Bowen 1932).

To describe the invasion process and reflect the difference between collective and individual behaviour, Johnston and coworkers introduced a discrete model considering birth, death and movement events of agents that are isolated or grouped on a simple one-dimensional lattice (Johnston et al. 2017). A discrete conservation statement describing δU_j, which is the change of the occupancy of a lattice site j during a time step τ, gives

$$\begin{aligned}
\delta U_j =& \frac{P_m^i}{2}[U_{j-1}(1-U_j)(1-U_{j-2}) + U_{j+1}(1-U_j)(1-U_{j+2}) \\
&- 2U_j(1-U_{j-1})(1-U_{j+1})] \\
&+ \frac{P_m^g}{2}[U_{j-1}(1-U_j) + U_{j+1}(1-U_j) - U_j(1-U_{j-1}) - U_j(1-U_{j+1})] \\
&- \frac{P_m^g}{2}[U_{j-1}(1-U_j)(1-U_{j-2}) + U_{j+1}(1-U_j)(1-U_{j+2}) \\
&- 2U_j(1-U_{j-1})(1-U_{j+1})] \\
&+ \frac{P_p^i}{2}[U_{j-1}(1-U_j)(1-U_{j-2}) + U_{j+1}(1-U_j)(1-U_{j+2})] \\
&+ \frac{P_p^g}{2}[U_{j-1}(1-U_j) + U_{j+1}(1-U_j)] \\
&- \frac{P_p^g}{2}[U_{j-1}(1-U_j)(1-U_{j-2}) + U_{j+1}(1-U_j)(1-U_{j+2})] \\
&- P_d^i[U_j(1-U_{j-1})(1-U_{j+1})] - P_d^g U_j + P_d^g[U_j(1-U_{j-1})(1-U_{j+1})].
\end{aligned} \tag{4.1}$$

Here, U_j represents the probability that an agent occupies lattice j, thus, $1-U_j$ represents the probability that lattice j is vacant (Simpson et al. 2010a). P_m^i and P_m^g represents the probability per time step that isolated or grouped agent, respectively, attempts to step to a nearest neighbour lattice site; P_p^i and P_p^g represents the probability per time step that an isolated or grouped agent, respectively, attempts to undergo a proliferation event and deposit a daughter agent at a nearest neighbour lattice site; P_d^i and P_d^g represents the probability per time step that an isolated or grouped agent, respectively, dies, and is removed from the lattice. See Figure 4.1a for a schematic of the lattice-based discrete model.

To obtain a continuous description, Johnston and coworkers treated U_j as a continuous function, $U(x,t)$, and divide (4.1) by the time step τ. Next, they expanded all terms in (4.1) in a Taylor series around $x = j\Delta$, where Δ is the lattice spacing, and neglect terms of $\mathcal{O}(\Delta^3)$ (Simpson et al. 2010a). As $\Delta \to 0$ and $\tau \to 0$ with the restriction that the ratio Δ^2/τ held constant (Codling et al. 2008; Simpson et al. 2010a), they obtained a nonlinear

diffusion-reaction equation

$$\frac{\partial U}{\partial t} = \frac{\partial}{\partial x}\left(D(U)\frac{\partial U}{\partial x}\right) + R\left(U\right), \tag{4.2}$$

where

$$D\left(U\right) = D_i\left(1 - 4U + 3U^2\right) + D_g\left(4U - 3U^2\right), \tag{4.3}$$

is the nonlinear diffusivity function, and

$$R\left(U\right) = \lambda_g U\left(1 - U\right) + \left(\lambda_i - \lambda_g - K_i + K_g\right) U\left(1 - U\right)^2 - K_g U, \tag{4.4}$$

is the kinetic term. Furthermore, the parameters are given by

$$\begin{aligned} D_g &= \lim_{\Delta,\tau\to 0} \frac{P_m^g \Delta^2}{2\tau}, & D_i &= \lim_{\Delta,\tau\to 0} \frac{P_m^i \Delta^2}{2\tau}, & \lambda_g &= \lim_{\tau\to 0} \frac{P_p^g}{\tau}, \\ \lambda_i &= \lim_{\tau\to 0} \frac{P_p^i}{\tau}, & K_g &= \lim_{\tau\to 0} \frac{P_d^g}{\tau}, & K_i &= \lim_{\tau\to 0} \frac{P_d^i}{\tau}, \end{aligned}$$

where we require that $P_p^i, P_p^g, P_d^i, P_d^g$ are $\mathcal{O}(\tau)$ (Simpson et al. 2010a). Here, $U(x,t)$ denotes the total density of the agents at position $x \in \mathbb{R}$ and time $t \in \mathbb{R}_+$; $D_i \geq 0$ and $D_g \geq 0$ are diffusivities of the isolated and grouped agents, respectively; $\lambda_i \geq 0$ and $\lambda_g \geq 0$ are the birth rates of isolated and grouped agents, respectively; $K_i \geq 0$ and $K_g \geq 0$ are the death rates of isolated and grouped agents, respectively (Johnston et al. 2017).

In this manuscript, we study the effect that aggregation, which is modelled with a nonlinear diffusivity function that goes negative (Simpson et al. 2010b), has on the dynamics of the model. Therefore, we assume that $D_i > 4D_g$ such that $D(U)$ given by (4.3) is convex and changes sign twice in our domain of interest (however, see Section 4.6.2 for a short discussion related to the other case). For simplicity, we furthermore assume equal proliferation rates, $\lambda = \lambda_i = \lambda_g$, and no agent death, $K_i = K_g = 0$. This way, the kinetic term simplifies to a logistic term

$$R\left(U\right) = \lambda U\left(1 - U\right), \tag{4.5}$$

and $D\left(U\right)$ has a sign condition:

$$D\left(U\right) > 0 \quad \text{for} \quad U \in [0, \alpha) \cup (\beta, 1], \quad D\left(U\right) < 0 \quad \text{for} \quad U \in (\alpha, \beta), \tag{4.6}$$

where the interval where $D(U) < 0$ is centred around $U = 2/3$, and α, β are given by

$$\alpha = \frac{2}{3} - \frac{\sqrt{D_i^2 + 4D_g^2 - 5D_iD_g}}{3\left(D_i - D_g\right)}, \quad \beta = \frac{2}{3} + \frac{\sqrt{D_i^2 + 4D_g^2 - 5D_iD_g}}{3\left(D_i - D_g\right)}, \tag{4.7}$$

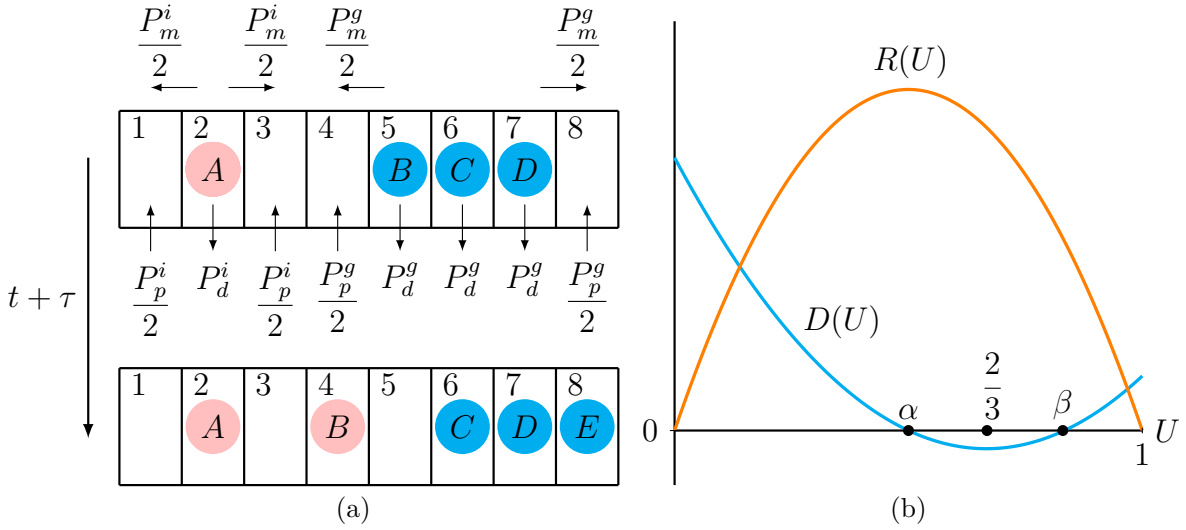

Figure 4.1: (a) describes one possible time step of the lattice-based discrete model of (Johnston et al. 2017): a new grouped agent (agent E) is born and the grouped agent B moves from lattice site 5 to lattice site 4 to become an isolated agent. Pink circles represent isolated agents with birth rate P_p^i, death rate P_d^i and motility rate related to P_m^i; cyan circles represent grouped agents with birth rate P_p^g, death rate P_d^g and motility rate P_m^g. (b) presents a diffusivity function $D(U)$, given by (4.3) (cyan curve) satisfying $D_i > 4D_g$ which makes $D(U)$ change sign twice on $(0,1)$, and the kinetic term $R(U)$, given by (4.5) (orange curve) which is positive on $(0,1)$ and zero at end points $U = 0$ and $U = 1$.

with $1/3 < \alpha < 2/3$ and $2/3 < \beta < 1$, see Figure 4.1b. That is, we have negative diffusion for $U \in (\alpha, \beta)$. The relation that D_i is larger than D_g indicates that isolated agents are more active than grouped agents, which agrees with the experimental observation that *leader cells* are more motile than *follower cells* (Poujade et al. 2007; Simpson et al. 2014).

Ferracuti et al. (2009) showed the existence of travelling wave solutions for a range of positive wave speeds for (4.2) with general convex $D(U)$ that changes sign twice on $(0,1)$ and $R(U)$ given by (4.5) based on the *comparison method* introduced by Aronson and Weinberger (1978). Related studies proved the existence of travelling wave solutions for a similar range of speeds for nonlinear diffusion-reaction equations with different $D(U)$ and different $R(U)$: Malaguti and Marcelli (2003) studied (4.2) with a logistic kinetic term and a nonlinear diffusivity function satisfying

$$D(0) = 0 \quad \text{and} \quad D(0) > 0 \quad \text{for all} \quad U \in (0,1].$$

Maini et al. (2006) studied (4.2) with a logistic kinetic term and a nonlinear diffusivity function satisfying

$$D(U) > 0 \quad \text{in} \quad (0,\theta) \quad \text{and} \quad D(U) < 0 \quad \text{in} \quad U \in (\theta,1), \tag{4.8}$$

for some given $\theta \in (0,1)$ and with $D(0) = D(\theta) = D(1) = 0$. In addition, Maini et al.

(2007) studied (4.2) with (4.8) and a bistable kinetic term satisfying

$$R(0) = R(\phi) = R(1) = 0,$$
$$R(U) < 0 \quad \text{in} \quad U \in (0, \phi), R(U) > 0 \quad \text{in} \quad U \in (\phi, 1).$$

In this manuscript, we show the following result:

Theorem 1 *Model (4.2) with (4.3) and (4.5) and $D_i > 4D_g$ supports smooth monotone nonnegative travelling wave solutions for*

$$c \geq 2\sqrt{\lambda D_i} =: c^*. \tag{4.9}$$

This theorem agrees with the result of Ferracuti et al. (2009), and because of the specific nonlinear diffusivity function, we can further extend their results. Moreover, instead of the comparison method used by Ferracuti et al. (2009), we use a geometric approach to prove the existence of travelling wave solutions. This geometric approach has the advantage that it can also be used to study shock-fronted travelling wave solutions (Harley et al. 2014a,b; Wechselberger and Pettet 2010). While shock-fronted travelling wave solutions are not the focus in this manuscript, we show in the final section that they do exist for (4.5) with different $D(U)$, see Figure 4.10a in Section 4.6.3. The lower bound c^* in Theorem 1 is often called the minimum wave speed as it represents the monotone nonnegative travelling wave solutions with the lowest wave speed (Murray 1989). Numerical simulations show that (4.2) with (4.3) and (4.5) indeed support smooth travelling wave solutions even though the nonlinear diffusivity function goes negative. Moreover, the speed relates to the initial condition, and the wave speed converges to the minimum wave speed c^* as the initial condition limits to the Heaviside initial condition, see Figure 4.2. We will also show the connection between the existence of smooth monotone nonnegative travelling wave solutions, the spectrum of the travelling wave solutions, and the minimum wave speed c^*.

This manucript is organised as follows. We prove Theorem 1 in Section 4.4 by using desingularisation techniques (Aronson 1980) and detailed phase plane analysis which have not been applied to (4.2) before. In Section 4.5, we determine the spectral properties of the travelling wave solutions and show how the minimum wave speed c^* is related to absolute instabilities (Kapitula and Promislow 2013; Sandstede 2002; Sherratt et al. 2014). Some interesting results for different nonlinear diffusivity functions with the same kinetic term (4.5) are discussed in Section 4.6. Here, we also discuss the implications of the analytical results for the discrete model.

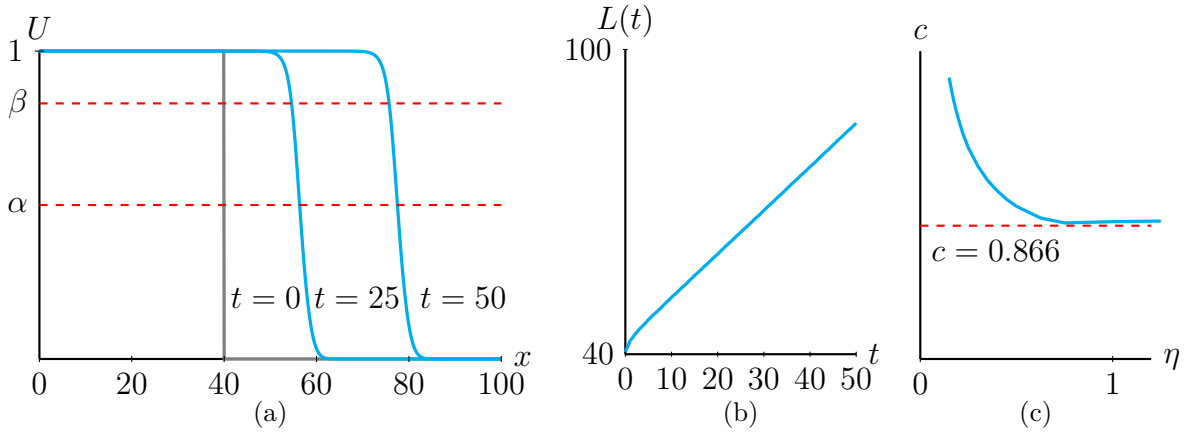

Figure 4.2: (a) shows the evolution of a Heaviside initial condition to a smooth travelling wave solution obtained by simulating (4.2) with (4.3) and (4.5) with parameters $D_i = 0.25$, $D_g = 0.05$ and $\lambda = 0.75$. We use a finite difference method with space step $\delta x = 0.1$, time step $\delta t = 0.01$ and no-flux boundary conditions. Notice that $D(U) = 0$ at $\alpha = 0.5$ and $\beta \approx 0.83$. (b) measures the position of the wave $L(t)$ by looking for the left-most leading edge point where U is smaller than 10^{-5}, indicating that the solution is travelling at a constant speed $c = 0.864$. (c) gives the wave speed as a function of the initial condition $U(x, 0) = 1/2 + \tanh(-\eta(x - 40))/2$. Notice that as η grows to infinity this initial condition limits to the Heaviside initial condition used for the simulation in (a), and the wave speed converges to $c \approx 0.864$. The minimum wave speed $c^* = 2\sqrt{\lambda D_i} \approx 0.866$ (4.9).

4.4 Existence of travelling wave solutions

4.4.1 Transformation and desingularisation

A travelling wave solution of (4.2) is a solution of the form $u(x - ct, t)$ that travels with constant speed c and constant wave shape, and that asymptotes to 1 as $x \to -\infty$ and to 0 as $x \to \infty$. We only consider positive wave speeds since (4.2) with (4.3) and (4.5) is monostable with a Fisher-KPP imprint, that is, $U \equiv 1$ is a PDE stable solution of (4.2), while $U \equiv 0$ is a PDE unstable solution. We introduce the travelling wave coordinate $z = x - ct$, where $z \in \mathbb{R}$, and write (4.2) in its travelling wave coordinate

$$\frac{\partial U}{\partial t} = \frac{\partial}{\partial z}\left(D(U)\frac{\partial U}{\partial z}\right) + c\frac{\partial U}{\partial z} + R(U). \tag{4.10}$$

A travelling wave solution to (4.2) is now a stationary solution to (4.10), that is, $\partial U/\partial t = 0$, and (4.10) simplifies to a second-order ordinary differential equation (ODE)

$$\frac{d}{dz}\left(D(u)\frac{du}{dz}\right) + c\frac{du}{dz} + R(u) = 0, \tag{4.11}$$

with asymptotic boundary conditions $\lim_{z\to-\infty} u = 1$ and $\lim_{z\to\infty} u = 0$. We use a dynamical systems approach to analyse (4.11). Upon introducing $p := D(u)du/dz$, it can be written as a system of first-order ODEs

$$\begin{cases} D(u)\dfrac{du}{dz} = p, \\ D(u)\dfrac{dp}{dz} = -cp - D(u)R(u). \end{cases} \tag{4.12}$$

Note that $p > 0$ if $du/dz < 0$ and $D(u) < 0$. Thus, while we expect that the derivative of a travelling wave solution is always negatvie, p is not necessarily always negative. Travelling wave solutions of (4.2) now correspond to heteroclinic orbits of (4.12) connecting $(1, 0)$ to $(0, 0)$. However, (4.12) is singular as $D(u)$ is zero for $u = \alpha$ and $u = \beta$, see (4.7). That is, we have two *walls of singularities* $u = \alpha$ and $u = \beta$ (Harley et al. 2014a; Pettet et al. 2000; Wechselberger and Pettet 2010). On these walls of singularities the right hand sides of (4.2) also dissappear if $p = 0$. That is, each wall of singularities has one (potential) *hole in the wall* (Harley et al. 2014a; Pettet et al. 2000; Wechselberger and Pettet 2010). In system (4.12), the holes are at $(\alpha, 0)$ and $(\beta, 0)$. To remove the singularities, we desingularise system (4.12) by introducing a stretched variable ξ satisfying $D(u)d\xi = dz$ (Aronson 1980; Murray 1989; Sánchez-Garduño and Maini 1994). Subsequently, system (4.12) becomes

$$\begin{cases} \dfrac{du}{d\xi} = p, \\ \dfrac{dp}{d\xi} = -cp - D(u)R(u). \end{cases} \tag{4.13}$$

When $D(u) > 0$, $d\xi/dz > 0$ and therefore trajectories on the phase planes of (4.12) and (4.13) have the same moving directions. In contrast, when $D(u) < 0$, $d\xi/dz < 0$ and trajectories on the two phase planes are in the opposite direction, see Figure 4.3. Therefore, heteroclinic orbits of (4.12) connecting $(1, 0)$ to $(0, 0)$ crossing the holes in the walls $(\alpha, 0)$ and $(\beta, 0)$, if they exist, are transformed and separated to heteroclinic orbits connecting $(1, 0)$ to $(\beta, 0)$, $(\alpha, 0)$ to $(\beta, 0)$ and $(\alpha, 0)$ to $(0, 0)$ of (4.13) and *vice versa*. Next, we will prove the existence of these heteroclinic orbits in system (4.13) for a range of wave speeds c.

4.4.2 Phase plane analysis of the desingularised system

We first study the desingularised system (4.13). It has nullclines $p = 0$ and

$$p = -\frac{D(u)R(u)}{c}. \tag{4.14}$$

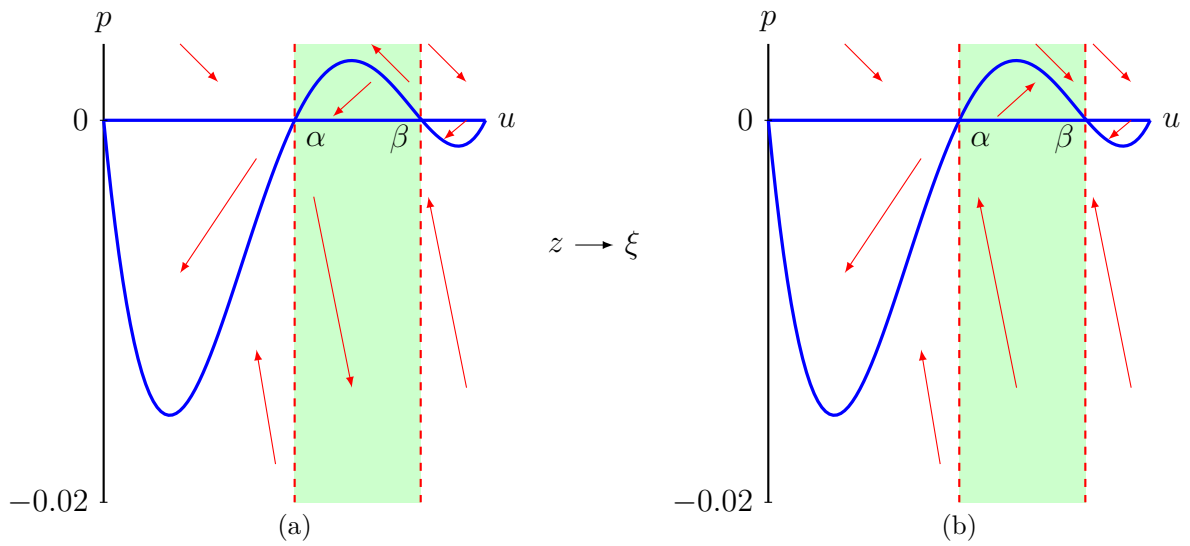

Figure 4.3: (a) is the phase plane of system (4.12) with parameters $D_i = 0.25$, $D_g = 0.05$, $\lambda = 0.75$ and $c = 0.866$. The vertical dashed lines are the walls of singularities $u = \alpha$ and $u = \beta$ and the solid blue lines are nullclines. Red arrows show the moving direction of trajectories. (b) is the phase plane of system (4.13) for the same parameter values and red lines are nullclines. For u in between α and β, the moving direction of the trajectories is opposite compared to (a), while the moving direction is the same for $u < \alpha$ and $u > \beta$.

The intersections of the two nullclines give four equilibrium points: $(0,0), (1,0), (\alpha,0), (\beta,0)$.

Lemma 1 *The equilibrium points* $(1,0)$ *and* $(\alpha,0)$ *are saddles. The equilibrium point* $(0,0)$ *is a stable node if*

$$c \geq 2\sqrt{D(0)R'(0)} = 2\sqrt{\lambda D_i} = c^*, \tag{4.15}$$

and a stable spiral otherwise. The equilibrium point $(\beta,0)$ *is a stable node if*

$$c \geq 2\sqrt{D'(\beta)R(\beta)}, \tag{4.16}$$

and a stable spiral otherwise.

Proof The Jacobian of system (4.13) is

$$J(u,p) = \begin{pmatrix} 0 & 1 \\ -F(u) & -c \end{pmatrix}, \quad \text{where} \quad F(u) := (D(u)R(u))'. \tag{4.17}$$

The Jacobian has eigenvalues and eigenvectors

$$\lambda_\pm = \frac{-c \pm \sqrt{c^2 - 4F(u)}}{2}, \quad E_\pm = (1, \lambda\pm).$$

For the equilibrium point $(1, 0)$ this reduces to

$$\lambda_{1\pm} = \frac{-c \pm \sqrt{c^2 - 4D(1)R'(1)}}{2}, \quad E_{1\pm} = (1, \lambda_{1\pm}). \tag{4.18}$$

The eigenvalues $\lambda_{1\pm}$ are real and negative since $D(1) = D_g > 0$ and $R'(1) = -\lambda < 0$. Thus $(1, 0)$ is a saddle.

Similarly, the Jacobian of the equilibrium point $(\alpha, 0)$ has eigenvalues and eigenvectors

$$\lambda_{\alpha\pm} = \frac{-c \pm \sqrt{c^2 - 4D'(\alpha)R(\alpha)}}{2}, \quad E_{\alpha\pm} = (1, \lambda_{\alpha\pm}). \tag{4.19}$$

Knowing that $D'(\alpha) < 0$ and $R(\alpha) > 0$, $\lambda_{\alpha+}$ is real and positive and $\lambda_{\alpha-}$ is real and negative. Thus $(\alpha, 0)$ is a saddle.

The Jacobian of the equilibrium point $(0, 0)$ has eigenvalues and eigenvectors

$$\lambda_{0\pm} = \frac{-c \pm \sqrt{c^2 - 4D(0)R'(0)}}{2}, \quad E_{0\pm} = (1, \lambda_{0\pm}). \tag{4.20}$$

The eigenvalues $\lambda_{0\pm}$ are real and negative if (4.15) holds since $D(0) = D_i > 0$ and $R'(0) = \lambda > 0$. Thus equilibrium point $(0, 0)$ is a stable node if (4.15) holds. Otherwise, $\lambda_{0\pm}$ are complex-valued with negative real parts and $(1, 0)$ is a stable spiral.

Similarly, the Jacobian of equilibrium point $(\beta, 0)$ has eigenvalues and eigenvectors

$$\lambda_{\beta\pm} = \frac{-c \pm \sqrt{c^2 - 4D'(\beta)R(\beta)}}{2}, \quad E_{\beta\pm} = (1, \lambda_{\beta\pm}). \tag{4.21}$$

The eigenvalues $\lambda_{\beta\pm}$ are real and negative if (4.16) holds since $D'(\beta) > 0$ and $R(\beta) > 0$. Thus the equilibrium point $(\beta, 0)$ is a stable node if (4.16) holds. Otherwise, $\lambda_{\beta\pm}$ are complex-valued with negative real parts and $(\beta, 0)$ is a stable spiral. ∎

Lemma 2 *For $D_i > 4D_g$, the thresholds of conditions (4.15) and (4.16) give*

$$c^* > 2\sqrt{D'(\beta)R(\beta)}. \tag{4.22}$$

Proof The right hand side of (4.22) is given by

$$2\sqrt{D'(\beta)R(\beta)} = 2\sqrt{3\lambda(D_i - D_g)\beta(1-\beta)(\beta-\alpha)}.$$

Since $c^* = 2\sqrt{\lambda D_i}$, proving relation (4.22) is equivalent to proving

$$D_i > 3(D_i - D_g)\beta(1-\beta)(\beta-\alpha),$$

which is equivalent to proving

$$\frac{D_i}{D_i - D_g} > 3\beta(1-\beta)(\beta-\alpha). \tag{4.23}$$

Knowing that $2/3 < \beta < 1$ and $0 < \beta - \alpha < 2/3$ gives $3\beta(1-\beta)(\beta-\alpha) < 2/3$. Since $D_i > 4D_g$, we have that $D_i/(D_i - D_g) > 1$ since $D_i > D_i - D_g$. Hence, (4.23) holds and thus (4.22) holds. ∎

For $c < c^*$, $(0,0)$ becomes a spiral node and hence we expect trajectories approaching $(0,0)$ to become negative which in the end would lead to travelling wave solutions become negative. Therefore, we now assume that $c \geq c^*$. To prove the existence of heteroclinic orbits between the equilibrium points, we construct invariant regions in the phase plane from which trajectories cannot leave, so that the Poincaré-Bendixson theorem can be applied (Jordan and Smith 1999), see Figure 4.4. The slope of nullcline (4.14) is $\chi(u) = -1/\left(cF(u)\right)$, where $F(u)$ is given by (4.17), while the slope of the unstable eigenvector of $(1,0)$ is λ_{1+}, see (4.18). We thus have

$$\begin{aligned}
\lambda_{1+} - \chi(1) =& \frac{-c + \sqrt{c^2 - 4D(1)R'(1)}}{2} + \frac{1}{c}D(1)R'(1) \\
=& \frac{c\sqrt{c^2 - 4D(1)R'(1)} - \left(c^2 - 2D(1)R'(1)\right)}{2c} \\
=& \frac{\sqrt{c^4 - 4c^2D(1)R'(1)} - \sqrt{c^4 - 4c^2D(1)R'(1) + 4\left(D(1)R'(1)\right)^2}}{2} < 0.
\end{aligned} \tag{4.24}$$

That is, the unstable eigenvector of $(1,0)$ has a smaller slope than nullcline (4.14) at $(1,0)$. In other words, the trajectory leaving $(1,0)$ with decreasing u initially lies above the nullcline (4.14).

Similarly, the slope of the unstable eigenvector of $(\alpha,0)$ is $\lambda_{\alpha+}$, see (4.19). We have, after similar computation as (4.24), $\lambda_{\alpha+} - \chi(\alpha) < 0$. Thus, the unstable eigenvector of $(\alpha,0)$ has a smaller slope than nullcline (4.14) at $(\alpha,0)$. Therefore, the trajectory leaving $(\alpha,0)$ with decreasing u initially lies above the nullcline (4.14), while the trajectory leaving $(\alpha,0)$ with increasing u initially lies below the nullcline (4.14).

Under condition (4.15), the least negative slope of the stable eigenvectors of equilibrium point $(0,0)$ is λ_{0+}, see (4.20). This gives, after a similar computation as (4.24), $\lambda_{0+} - \chi(0) < 0$. Thus, both eigenvectors of $(0,0)$ have slopes that are more negative than nullcline (4.14) at $(0,0)$. In other words, the eigenvectors of $(0,0)$ initially lie under the nullcline (4.14) for $u > 0$.

Similarly, under condition (4.16), the least negative slope of the stable eigenvectors of $(\beta,0)$ is $\lambda_{\beta+}$, see (4.21). This gives $\lambda_{\beta+} - \chi(\beta) < 0$. Thus, both eigenvectors have slopes

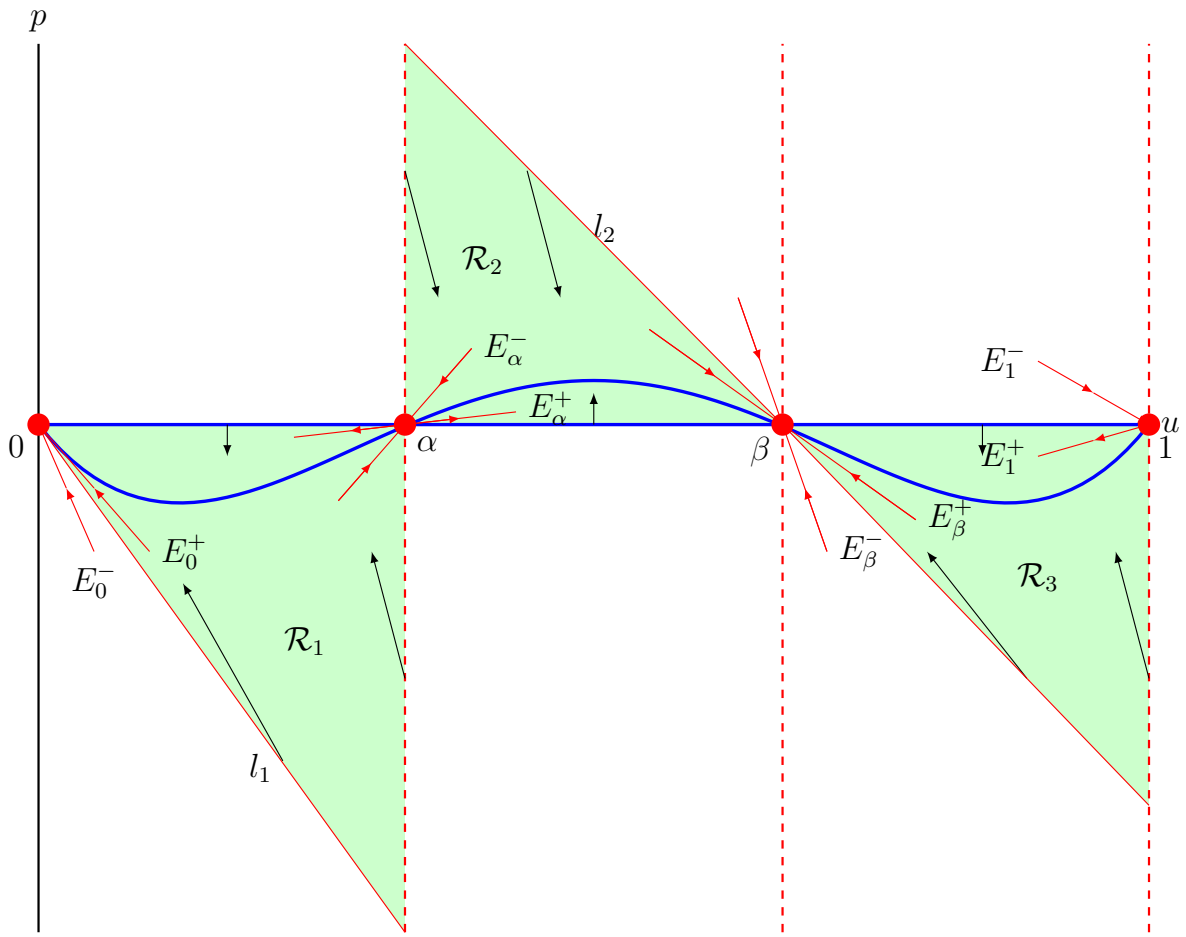

Figure 4.4: A qualitative phase plane of system (4.13). The three dashed lines are $u = \alpha$, $u = \beta$ and $u = 1$. The blue lines are the nullclines $p = 0$ and $p = -D(u)R(u)/c$. Region $\mathcal{R}_1$ is bounded by $p = 0$, $u = \alpha$ and a straight line l_1 with negative slope passing through $(0, 0)$. Region $\mathcal{R}_2$ is bounded by $p = 0$, $u = \alpha$ and a straight line l_2 with negative slope passing through $(\beta, 0)$. Region $\mathcal{R}_3$ is bounded by $p = 0$, $u = 1$ and l_2.

that are more negative than nullcline (4.14) at $(\beta, 0)$. Therefore, the trajectory moving in $(\beta, 0)$ with decreasing u initially lies under the nullcline (4.14) for $u > \beta$, while they lie above the nullcline (4.14) for $u < \beta$, see also Figure 4.4.

Next, we consider the region $\mathcal{R}_1$ bounded by $p = 0$, $u = \alpha$ and a straight line l_1 through $(0, 0)$ with a negative slope μ_1. We aim to prove that for $c \geq c^*$, there always exists a slope μ_1 so that no trajectories in region $\mathcal{R}_1$ can cross through its boundaries. Trajectories starting on $p = 0$ have negative vertical directions since $du/d\xi = p = 0$ and $dp/d\xi = -D(u)R(u) < 0$ for $u \in (0, \alpha)$. Thus, trajectories in $\mathcal{R}_1$ cannot cross through $p = 0$. Trajectories starting on $u = \alpha$ with negative p values point into region $\mathcal{R}_1$ since $du/d\xi = p < 0$ and $dp/d\xi = -cp > 0$. Trajectories starting on l_1 satisfy $p = \mu_1 u$, and they point into $\mathcal{R}_1$ only if

$$\left.\frac{dp}{du}\right|_{p=\mu_1 u} = -c - \frac{D(u)R(u)}{\mu_1 u} \leq \mu_1, \quad \text{for} \quad u \in (0, \alpha).$$

After rearranging and recalling that $\mu_1 < 0$, we obtain

$$\mu_1(\mu_1 + c) \leq -\frac{D(u)R(u)}{u} = -\lambda D(u)(1-u), \quad \text{for} \quad u \in (0, \alpha). \tag{4.25}$$

Lemma 3 *For $c \geq c^*$, there exists a μ_1 such that inequality (4.25) is valid for any $u \in (0, \alpha)$.*

Proof Proving inequality (4.25) is equivalent to proving

$$\mu_1(\mu_1 + c) \leq -\lambda \sup_{u \in (0,\alpha)} D(u)(1-u). \tag{4.26}$$

The left hand side of inequality (4.26) is minimal when $\mu_1 = -c/2$. Setting $\mu_1 = -c/2$ and substituting into inequality (4.26) gives a lower bound for the speed

$$c_1 = 2\sqrt{\lambda} \sup_{u \in (0,\alpha]} \sqrt{D(u)(1-u)}, \tag{4.27}$$

such that (4.26) holds for $c \geq c_1$. The right hand side of (4.27) gives

$$2\sqrt{\lambda} \sup_{u \in (0,\alpha)} \sqrt{D(u)(1-u)} = 2\sqrt{\lambda D(0)} = 2\sqrt{\lambda D_i},$$

since $D(u)$ and $(1-u)$ are both decreasing functions on $u \in (0, \alpha)$. Thus, $c_1 = c^*$. Hence, for $c \geq c^*$, inequality (4.26) is valid for $\mu_1 = -c/2$. ∎

Knowing that for $c \geq c^*$ inequality (4.25) is valid, trajectories on l_1 with $\mu_1 = -c/2$ point into region $\mathcal{R}_1$. Thus, based on the Poincaré-Bendixson theorem (Jordan and Smith 1999), the trajectory leaving from the equilibrium point $(\alpha, 0)$ with decreasing u and decreasing p must connect with the equilibrium point $(0, 0)$ without going negative in u.

Similarly, we consider the region $\mathcal{R}_2$ bounded by $p = 0$, $u = \alpha$ and a straight line l_2 through $(\beta, 0)$ with a negative slope μ_2, and the region $\mathcal{R}_3$ bounded by $p = 0$, $u = 1$ and l_2. Trajectories starting on $p = 0$ have positive vertical directions for $u \in (\alpha, \beta)$ since $du/d\xi = p = 0$ and $dp/d\xi = -D(u)R(u) > 0$ and they have negative vertical directions since for $u \in (\beta, 1)$, $du/d\xi = 0$ and $dp/d\xi = -D(u)R(u) < 0$. Trajectories starting on $u = \alpha$ with positive p point into region $\mathcal{R}_2$ since $du/d\xi = p > 0$ and $dp/d\xi = -cp < 0$. Similarly, trajectories starting on $u = 1$ with negative p point into region $\mathcal{R}_3$. In addition, requiring the existence of a slope μ_2 such that trajectories starting on l_2 point into regions $\mathcal{R}_2$ and $\mathcal{R}_3$ leads to the condition

$$\mu_2(\mu_2 + c) \leq -\frac{D(u)R(u)}{u - \beta} = -3(D_i - D_g)(u - \alpha)R(u), \quad \text{for} \quad u \in (\alpha, 1). \tag{4.28}$$

Lemma 4 *For $c \geq c^*$, there exists a μ_2 such that inequality (4.25) is valid for any $u \in (\alpha, 1)$.*

Proof The proof of Lemma 4 is analogous to the proof of Lemma 3 and we will omit some of the details. Again, there exist a lower bound c_2

$$c_2 = 2\sqrt{3(D_i - D_g)} \sup_{u\in(\alpha,1)} \sqrt{(u-\alpha)R(u)},$$

such that (4.28) holds for $c \geq c_2$. Next, we show that $c_2 < c^*$. That is, we show that

$$2\sqrt{\lambda D_i} > 2\sqrt{3(D_i - D_g)} \sup_{u\in(\alpha,1)} \sqrt{(u-\alpha)R(u)}.$$

This is equivalent to proving $D_i/(D_i - D_g) > 3u(1-u)(u-\alpha)$ for $u \in (\alpha, 1)$. Noticing that $u - \alpha < 2/3$, and $u(1-u) \leq 1/4$, we obtain $3u(1-u)(u-\alpha) < 1/2$. Subsequently, we have

$$\frac{D_i}{D_i - D_g} > 1 > \frac{1}{2} > 3u(1-u)(u-\alpha),$$

since $D_i > 4D_g$ by assumption. Thus, $c_2 < c^*$. ∎

Knowing that for $c \geq c^*$ the inequality (4.28) is valid, trajectories on l_2 in between α and β point into region $\mathcal{R}_2$. Thus, based on the Poincaré-Bendixson theorem (Jordan and Smith 1999), the trajectory leaving from the equilibrium point $(\alpha, 0)$ with increasing u and increasing p must connect with the equilibrium point $(\beta, 0)$. Analogously, the trajectory leaving from the equilibrium point $(1, 0)$ with decreasing u and decreasing p must connect with the equilibrium point $(\beta, 0)$.

In summary, for $c \geq c^*$ there exist heteroclinic orbits connecting $(1, 0)$ to $(\beta, 0)$, $(\alpha, 0)$ to $(\beta, 0)$ and $(\alpha, 0)$ to $(0, 0)$ in system (4.13). Since trajectories in $u \in (0, \alpha) \cup (\beta, 0)$ in system (4.12) have the same moving direction as in system (4.13), there exist trajectories connecting $(1, 0)$ to the hole in the wall $(\beta, 0)$ and trajectories connecting the hole in the wall $(\alpha, 0)$ to $(0, 0)$ in system (4.12). For $u \in (\alpha, \beta)$, trajectories of system (4.12) have the opposite moving direction compared to (4.12). The trajectory leaving from $(\alpha, 0)$ with increasing u, positive p and connecting to $(\beta, 0)$ in system (4.13) becomes a trajectory leaving from $(\beta, 0)$ with decreasing u, positive p and connecting to $(\alpha, 0)$ in system (4.12). Thus, there exists an orbit connecting $(\beta, 0)$ to $(\alpha, 0)$ in system (4.12). Combining the above, we get that for $c \geq c^*$, there exists a heteroclinic orbit with $u \geq 0$ connecting $(1, 0)$ to $(0, 0)$ passing through holes in the walls $(\alpha, 0)$ and $(\beta, 0)$ in system (4.12). Hence, there exist smooth monotone travelling wave solutions of (4.2) with positive speed $c \geq c^*$. This completes the proof of Theorem 1.

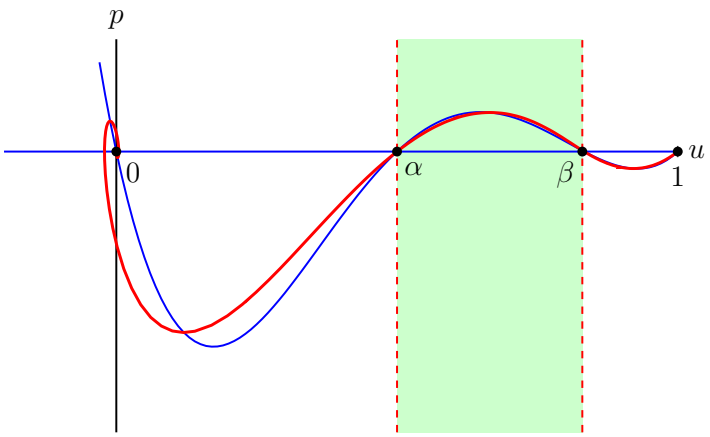

Figure 4.5: Phase plane of system (4.13) with parameters $D_i = 0.25$, $D_g = 0.05$, $\lambda = 0.75$ and $c = 0.4$. The latter is smaller than $c^* \approx 0.866$ but larger than $2\sqrt{D'(\beta)R(\beta)} \approx 0.289$. The blue lines are the nullclines $p = 0$ and $p = -D(u)R(u)/c$. The red lines are the heteroclinic orbits connecting $(0, 0)$, $(\alpha, 0)$, $(\beta, 0)$, and $(1, 0)$.

For $2\sqrt{D'(\beta)R(\beta)} < c < c^*$ the equilibrium point $(\beta, 0)$ is still a stable node, while $(0, 0)$ is a stable spiral, see Lemma 1. We can use similar techniques as above to show that system (4.13) still possesses heteroclinic orbits connecting $(1, 0)$ to $(\beta, 0)$, $(\alpha, 0)$ to $(\beta, 0)$ and $(\alpha, 0)$ to $(0, 0)$, see also Figure 4.5. However, this latter heteroclinic orbit now spirals into $(0, 0)$. Consequently, also for $2\sqrt{D'(\beta)R(\beta)} < c < c^*$ there exists a heteroclinic orbit connecting $(1, 0)$ to $(0, 0)$ passing through holes in the walls $(\alpha, 0)$ and $(\beta, 0)$ in system (4.12). However, these correspond to smooth travelling wave solutions of (4.2) with (4.3) and (4.5) that are not monotone and instead oscillate around 0. These solutions are not feasible as U represents the population density in the discrete model and thus cannot be negative.

4.5 Stability analysis

We showed that, similar to the Fisher-KPP equation (Harley et al. 2015, e.g.), (4.2) with (4.3) and (4.5) supports smooth travelling wave solutions for $c > 2\sqrt{D'(\beta)R(\beta)}$, but that only the travelling wave solutions with $c \geq c^*$ (4.9) are feasible. The minimal wave speed for the Fisher-KPP equation is closely related to the onset of absolute instabilities. Roughly speaking, absolute instabilities imply that perturbations to a travelling wave solution will grow for all time and at every point in space (Sherratt et al. 2014). These instabilities are related to the absolute spectrum of the travelling wave solution and are fully determined by the asymptotic behaviour ($z \to \pm\infty$) of the travelling wave solution (Kapitula and Promislow 2013; Sandstede 2002). The travelling wave solutions of (4.2) with (4.3) and (4.5) as constructed in Section 4.4 asymptote to 0 and 1 and the nonlinear diffusivity function $D(U)$ is positive near $U = 0$ and $U = 1$, see (4.6). That is, near these points (4.2) with (4.3) and (4.5) has a Fisher-KPP imprint and we therefore expect

that the minimal wave speed c^* of (4.2) is also closely related to the onset of absolute instabilities. In other words, we expect that the travelling wave solutions of (4.2) with (4.3) and (4.5) are absolutely unstable for $2\sqrt{D'(\beta)R(\beta)} < c < c^*$. Therefore, we expect perturbations to these travelling wave solutions to always grow and we will never observe them in, for instance, numerical simulations. Consequently, while (4.2) with (4.3) and (4.5) support these unfeasible travelling wave solutions that go negative, they will never be observed and thus do not effect the feasibility of the model.

Below, we briefly describe how to determine the absolute spectrum of a travelling wave solution, for a more detailed and complete mathematical description, we refer to Davis et al. (2017); Kapitula and Promislow (2013); Sandstede (2002). To determine the absolute spectrum of a travelling wave solution $\hat{u}(z)$, we add a small perturbation $q(z,t)$ to the travelling wave solution and determine how this perturbation evolves under the PDE in its moving frame. That is, we substitute $u(z,t) = \hat{u}(z) + q(z,t)$ into (4.10) and, upon ignoring higher-order perturbative terms $\mathcal{O}(q^2)$, we get

$$\begin{aligned}
&\frac{\partial q}{\partial t} = \mathcal{L}q, \\
&\mathcal{L} := D(\hat{u})\frac{\partial^2}{\partial z^2} + \left(2D'(\hat{u})\frac{d\hat{u}}{dz} + c\right)\frac{\partial}{\partial z} + \left(D'(\hat{u})\frac{d^2\hat{u}}{dz^2} + D''(\hat{u})\left(\frac{d\hat{u}}{dz}\right)^2 + R'(\hat{u})\right).
\end{aligned}$$

The associated eigenvalue problem, which is obtained by setting $q(z,t) = e^{\Lambda t}q(z)$, is given by

$$\mathcal{L}q = \Lambda q. \tag{4.29}$$

The spectral stability of the travelling wave solution $\hat{u}$ is now determined by the spectrum of the linear operator $\mathcal{L}$, that is, the $\Lambda \in \mathbb{C}$ for which $\mathcal{L} - \Lambda$ is not invertible. In particular, if the spectrum is in the open left half plane, or the origin, then we call the travelling wave solution $\hat{u}$ spectrally stable and unstable otherwise. This spectrum naturally breaks up into two sets, the point spectrum and the essential spectrum (Kapitula and Promislow 2013; Sandstede 2002). Roughly speaking, the essential spectrum of the travelling wave solution deals with instabilities at infinity and it is related to the spectrum of the background linear operator $\mathcal{L}$ as $z \to \pm\infty$, while the point spectrum deals with the stability of the actual wave front.

Obviously, the spectral properties of $\mathcal{L}$ depend on the space we allow the perturbations q to be taken from. A natural choice is the space of square integrable functions whose first (weak) derivative (in z) is also square integrable, that is, the Sobolev space $\mathbb{H}^1(\mathbb{R})$. Another choice is the related weighted space $\mathbb{H}^1_\nu(\mathbb{R})$ defined as $q \in \mathbb{H}^1_\nu(\mathbb{R})$ if and only if $e^{\nu z}q \in \mathbb{H}^1(\mathbb{R})$ (Kapitula and Promislow 2013; Sattinger 1977). For positive ν the weight forces q to decay at a rate faster than $e^{-\nu z}$ as $z \to \infty$, while it is allowed to grow exponentially, but at a rate less than $e^{-\nu z}$, as $z \to -\infty$. That is, the weight provides information whether

the travelling wave solution is more sensitive to perturbations at plus or minus infinity (Davis et al. 2017). The weighting of $\mathbb{H}^1(\mathbb{R})$ does not influence the point spectrum of $\mathcal{L}$, however, it does shift the essential spectrum (Kapitula and Promislow 2013). That is, a travelling wave solution can be unstable with respect to perturbations in $\mathbb{H}^1(\mathbb{R})$, while it is stable with respect to perturbations in an appropriately weighted space $\mathbb{H}^1_\nu(\mathbb{R})$. This is, for instance, the case for the Fisher-KPP equation and a particular Keller-Segel model (Davis et al. 2017, 2019). The absolute spectrum of a travelling wave solution, which is strictly speaking not always part of the spectrum, is not affected by the weighting of the space and gives an indication on how far the essential spectrum can be weighted (as the absolute spectrum is always to the left of the rightmost boundary of the essential spectrum (Davis et al. 2017)). In other words, if the absolute spectrum of a travelling wave solution contains part of the right half plane then the essential spectrum cannot be weighted into the open left half plane and the travelling wave solution is said to be absolutely unstable.

The eigenvalue problem (4.29) can be written as a system of first order ODEs

$$\mathcal{T}(\Lambda)\begin{pmatrix} q \\ s \end{pmatrix} := \left(\frac{d}{dz} - A(z;\Lambda)\right)\begin{pmatrix} q \\ s \end{pmatrix} = 0\,, \quad \text{where} \quad A(z;\Lambda) := \begin{pmatrix} 0 & 1 \\ \mathcal{B} & \mathcal{C} \end{pmatrix},$$

with

$$\mathcal{B} = -\frac{1}{D(\hat{u})}\left(D'(\hat{u})\frac{d^2\hat{u}}{dz^2} + D''(\hat{u})\left(\frac{d\hat{u}}{dz}\right)^2 + R'(\hat{u}) - \Lambda\right),$$
$$\mathcal{C} = -\frac{1}{D(\hat{u})}\left(2D'(\hat{u})\frac{d\hat{u}}{dz} + c\right).$$

The unweighted essential spectrum and the absolute spectrum of the operator $\mathcal{L}$ are determined by the asymptotic behaviour of the operator $\mathcal{T}(\Lambda)$ since the operator is a relatively compact perturbation of the operator when you plug in $z = \pm\infty$ (Kapitula and Promislow 2013). Therefore, we define the asymptotic matrices

$$A_+(\Lambda) := \lim_{z\to+\infty} A(z,\Lambda) = \begin{pmatrix} 0 & 1 \\ \dfrac{-R'(0)+\Lambda}{D(0)} & -\dfrac{c}{D(0)} \end{pmatrix},$$

and

$$A_-(\Lambda) := \lim_{z\to-\infty} A(z,\Lambda) = \begin{pmatrix} 0 & 1 \\ \dfrac{-R'(1)+\Lambda}{D(1)} & -\dfrac{c}{D(1)} \end{pmatrix}.$$

More specifically, for the problem at hand the boundary of the unweighted essential spectrum of $\mathcal{L}$ is determined by those Λ for which $A_\pm(\Lambda)$ has a purely imaginary eigenvalue.

In contrast, the absolute spectrum at $\pm\infty$ is determined by those Λ for which the

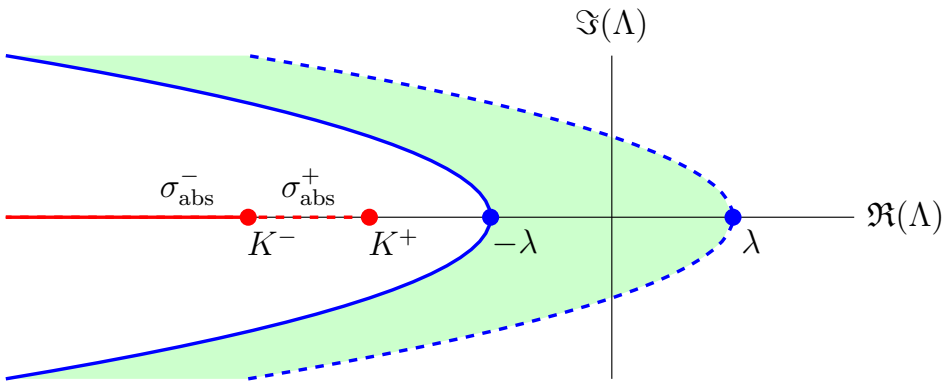

Figure 4.6: The unweighted essential spectrum and the absolute spectrum of the linear operator $\mathcal{L}$ for $c > c^*$. The boundary of the unweighted essential spectrum is determined by the dispersion relations of A_+ (dashed blue curve) and A_- (solid blue curve) and the green region is the interior of the unweighted essential spectrum. The solid red line is the absolute spectrum σ^-_{abs} (4.33), while the dashed red line is the absolute spectrum σ^+_{abs} (4.32).

eigenvalues of $A_\pm(\Lambda)$ have the same real part (Sandstede 2002). The eigenvalues of A_+ are

$$\mu^\pm_+ = \frac{-c \pm \sqrt{c^2 - 4D(0)R'(0) + 4D(0)\Lambda}}{2D(0)}, \tag{4.30}$$

and those of A_- are

$$\mu^\pm_- = \frac{-c \pm \sqrt{c^2 - 4D(1)R'(1) + 4D(1)\Lambda}}{2D(1)}. \tag{4.31}$$

Hence, the boundary of the unweighted essential spectrum is given by the so-called dispersion relations

$$\Lambda_+ = -D(0)k^2 + ick + R'(0), \quad \text{and} \quad \Lambda_- = -D(1)k^2 + ick + R'(1),$$

where $k \in \mathbb{R}$ and where $\mu^+_\pm = ik$ are the purely imaginary spatial eigenvalue of $A_\pm$. These dispersion relations form two parabolas, opening leftward and intersecting the real axis at $R'(0) = \lambda > 0$ and $R'(1) = -\lambda < 0$, see Figure 4.6. That is, all travelling wave solutions of (4.2) with (4.3) and (4.5) have unweighted essential spectrum in the right half plane.

From (4.30) we get that the absolute spectrum at $+\infty$ is given by

$$\sigma^+_{\text{abs}} = \left\{ \Lambda \in \mathbb{R} \;\middle|\; \Lambda < -\frac{c^2}{4D(0)} + R'(0) = -\frac{c^2}{4D_i} + \lambda =: K^+ \right\}. \tag{4.32}$$

Similarly, from (4.31) we get that the absolute spectrum at $-\infty$ is given by

$$\sigma^-_{\text{abs}} = \left\{ \lambda \in \mathbb{R} \;\middle|\; \Lambda < -\frac{c^2}{4D(1)} + R'(1) = -\frac{c^2}{4D_g} - \lambda =: K^- \right\}. \tag{4.33}$$

That is, σ^-_{abs} is always fully contained in the open left half plane including the origin, while σ^+_{abs} is only fully contained in the open left half plane including the origin for $c \geq c^* = 2\sqrt{\lambda D_i}$, see Figure 4.6.

In conclusion, a travelling wave solution with speed $2\sqrt{D'(\beta)R(\beta)} < c < c^*$ is absolutely unstable and no weights exist to shift its unweighted essential spectrum into the open left half plane. In contrast, the absolute spectrum of a travelling wave solution with speed $c \geq c^*$ is fully contained in the open left half plane including the origin and weights can be found that shift the unweighted essential spectrum into this region.

Remark 1 *To fully establish spectral stability of the operator $\mathcal{L}$, we also need to determine the point spectrum of $\mathcal{L}$ and show that it is contained in the open left half plane including the origin when $c \geq c_*$ provided our perturbations stay in an appropriately chosen Hilbert space $\mathcal{X}$. With this in mind, we define*

$$w(z) := D(\hat{u})q(z)e^{\int c/(2D(\hat{u}(t)))dt}. \tag{4.34}$$

Then if $\mathcal{L}q = \Lambda q$ (4.29) we have that w will solve

$$\mathcal{M}w(z) := D(\hat{u})w_{zz} + \left(R'(\hat{u}) - \frac{c\,(c + 2D'(\hat{u})\hat{u}_z)}{4D(\hat{u})}\right) w(z) = \Lambda w(z).$$

We have thus reduced the problem to showing that $\mathcal{M}$ is negative semi-definite on some appropriately chosen Hilbert space $\mathcal{X}$. Unfortunately, the natural choice for such a Hilbert space in these problems is the one with"inner product"

$$(u, v) := \int \frac{uv}{D(\hat{u})} dz,$$

but the sign change in $D(\hat{u})$ means that this is actually no longer an inner product (it is strictly negative for a localised pulse near where $D(\hat{u})$ is negative for instance).

However, if we instead work with the desingularised system (4.13)*, then for a perturbation $\tilde{q}$ about $\hat{u}$, linearising gives the eigenvalue problem for the linearised desingularised system*

$$\tilde{q}_{\xi\xi} + c\tilde{q}_\xi + F(\hat{u})\tilde{q} = \Lambda\tilde{q}\,, \tag{4.35}$$

where $F(u)$ is defined in (4.17)*. The standard Liouville transformation $\tilde{w}(\xi) := \tilde{q}(\xi)e^{c\xi/2}$ now does lead to a self adjoint eigenvalue problem in terms of $\tilde{w}(\xi)$*

$$\tilde{w}_{\xi\xi} + \left(F(\hat{u}) - \frac{c^2}{4}\right)\tilde{w}(\xi) = \Lambda\tilde{w}(\xi)\,.$$

Here, one can show explicitly that the operator

$$\tilde{\mathcal{M}} := \frac{d^2}{d\xi^2} + \left(F(\hat{u}) - \frac{c^2}{4} \right)$$

is negative semi-definite precisely when $c \geq c_*$. Indeed, as we are assuming that $D_i > 4D_g$, the potential term in $\tilde{\mathcal{M}}$ satisfies

$$\left(F(\hat{u}) - \frac{c^2}{4} \right) < \frac{1}{4} \left(-c^2 + \lambda D_i (4 - 32\hat{u} + 63\hat{u}^2 - 36\hat{u}^3) \right)$$

and the polynomial term $4 - 32\hat{u} + 63\hat{u}^2 - 36\hat{u}^3$ has a maximum value of 4 when $\hat{u} \in [0, 1]$ (at $\hat{u} = 0$). So, we have that $F(\hat{u}) - c^2/4 \leq 0$ when $c \geq c_* = 2\sqrt{\lambda D_i}$. Thus, $\tilde{\mathcal{M}}$ is a negative semidefinite operator in the space of perturbations which decay faster than $e^{c\xi}$, that is, $\mathbb{H}^1_c$. This is usually referred to as a transient instability in the stability literature (Sandstede 2002; Sherratt et al. 2014).

Lastly, we remark that given what was just shown, the only remaining step in the proof of stability of these travelling wave solutions for $c \geq c_*$ is how to relate the eigenvalue problem of the desingularised system (4.35) *to the spectrum of the operator $\mathcal{L}$. Due to the singular nature of the operator, it is unclear how to even define the 'natural' Hilbert spaces which should act as domains for the original linearised problem. Further, the weighting given in* (4.34) *involves a nonlinear, singular exponential weight, and to the best of our knowledge there is no such work which describes the dynamic effects of stability or instability in these cases. So, we cannot even say whether we would have only a transient instability even if we could show that the 'natural' operator was negative definite on an appropriate domain.*

4.6 Conclusion and outlook

4.6.1 Summary of results

We started this manuscript with a lattice-based discrete model reflecting the differences in individual and collective cell behaviour introduced in Johnston et al. (2017). Based on Johnston et al. (2017), the discrete model has the continuous description (4.2) obtained by using truncated Taylor series in the continuum limit. Our analysis focused on the case where $D_i > 4D_g$ so that we can obtain a convex nonlinear diffusivity function $D(U)$, given by (4.3) which changes sign twice in our domain of interest. Furthermore, the assumption of equal proliferation rates and zero death rates leads to a logistic kinetic term $R(U)$, given by (4.5). The associated numerical simulations of (4.2) with (4.3) and (4.5), see Figure 4.2, provided evidence of the existence of smooth monotone travelling wave solutions. To study

these travelling wave solutions of (4.2), we used a travelling wave coordinate $z = x - ct$ and looked for stationary solutions in the moving frame. Consequently, (4.2) was transformed into the singular second-order ODE (4.11) which we transformed into a singular system of first-order ODEs (4.12). To remove the singularities, we used the stretched variable $D(u)d\xi = dz$ and transformed (4.12) into system (4.13). Next, we analysed the phase plane of the desingularised system (4.13) and proved the existence of heteroclinic orbits connecting the equilibrium points $(0,0), (\alpha,0), (\beta,0)$ and $(1,0)$ for wave speeds $c \geq c^*$, given by (4.9). Subsequently, based on the relation between the phase planes of (4.12) and (4.13), we proved the existence of a heteroclinic orbit in (4.12) connecting the equilibrium points $(1,0)$ and $(0,0)$ passing through $(\alpha,0)$ and $(\beta,0)$, that are special points on the phase plane called a hole in the wall of singularities. That is, we proved the existence of smooth monotone travelling wave solutions of (4.2) for $c \geq c^*$. In the end, we showed that the travelling wave solutions of (4.2) with wave speeds $c < c^*$ are absolutely unstable, which in turn explained that the numerical simulations only provided travelling wave solutions with wave speeds $c \geq c^*$.

Based on our analysis, one-dimensional agent density profiles will eventually spread with a speed $c \geq c^*$ if the two types of agents have equal proliferation rates, zero death rates and different diffusivities satisfying $D_i > 4D_g$. Notice that $c^* = 2\sqrt{\lambda D_i}$, hence, the lowest speed for the travelling wave only relates to the diffusivity of individuals and is independent of the diffusivity of the gouped agents. That is, the diffusivity of grouped agents which is smaller than that of isolated agents ($D_i > 4D_g$) does not give restrictions for the lowest speed of the moving front. Consequently, we infer that the speed of invasion processes for organisms, for instance, cells, is mainly determined by the behaviour of individuals. Furthermore, the Fisher-KPP equation also has a minimum wave speed for the existence of smooth monotone travelling wave solutions (Fife 2013; Kolmogorov et al. 1937). Hence, a discrete mechanism of invasion processes considering the differences in individual and collective behaviours can lead to the similar macroscopic behaviour as the discrete mechanism with no differences in isolated and grouped agents.

4.6.2 Smooth travelling wave solutions for positive *D(U)*

If $D_i < 4D_g$, then the nonlinear diffusivity function $D(U)$ is positive for $U \in [0,1]$, see Figure 4.7a. Thus the corresponding system of first-order ODEs (4.12) is not singular, and the nullcline $p = -D(u)R(u)/c$ does not cross u-axis, see Figure 4.7b. In other words, $(0,0)$ and $(1,0)$ are the only equilibrium points. Following the same method as applied in

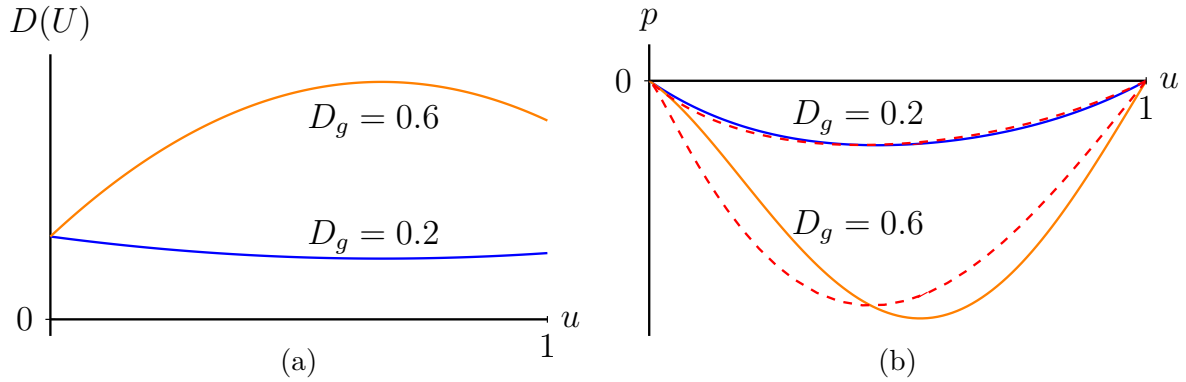

Figure 4.7: (a) shows $D(U)$ with $D_i = 0.25$ and two different D_g. (b) gives the corresponding phase planes of system (4.12) for $\lambda = 0.75$, $c = 1$, $D_i = 0.25$, $D_g = 0.2$ and $D_g = 0.6$, respectively. The two solid curves are the nullclines $p = -D(u)R(u)/c$ with $D_g = 0.2$ (blue curve) and $D_g = 0.6$ (orange curve), respectively. The red dashed lines are the corresponding heteroclinic orbits representing travelling wave solutions in (4.2).

Section 4.4.2, we obtain the lower bound

$$S_1 = \sup_{u\in(0,1)} 2\sqrt{\frac{D(u)R(u)}{u}} = \sup_{u\in(0,1)} 2\sqrt{\lambda(1-u)D(u)},$$

such that there exist smooth monotone travelling wave solutions of (4.2) for $c \geq S_1$. The origin is still a stable node for $c \geq 2\sqrt{\lambda D_i} := S_2$ and $S_1 \geq S_2$. So, if $S_1 \neq S_2$, $c \geq S_1$ is only a sufficient condition because there may exist smooth monotone travelling wave solutions of (4.2) for wave speeds $S_2 \leq c < S_1$. Thus, we can only conclude that the minimum wave speed is in the range

$$S_2 \leq \hat{c} \leq S_1, \tag{4.36}$$

such that there exist smooth monotone nonnegative travelling wave solutions of (4.2) for $c \geq \hat{c}$. Note that the minimum wave speed $\hat{c}$ can be different from the minimum wave speed c^* in Theorem 1, and Lemma 2 does not necessarily hold.

This estimate is consistent with the result in Malaguti and Marcelli (2003) obtained based on the *comparison method* introduced by Aronson and Weinberger (1978). The corresponding numerical simulations also give the expected results, see Figure 4.8. Witelski (1994) obtained an asymptotic travelling wave solution for a PDE motivated by polymer diffusion with a positive nonlinear diffusivity function and logistic kinetics for wave speeds greater than a minimum wave speed which is greater than S_2. This is consistent with the estimate of the minimum wave speed in (4.36). For solutions with an asymptotic wave speed equal to S_2, the front of the travelling wave is called a *pulled front*; for solutions with asymptotic speeds greater than S_2, the front of the travelling wave is called a *pushed*

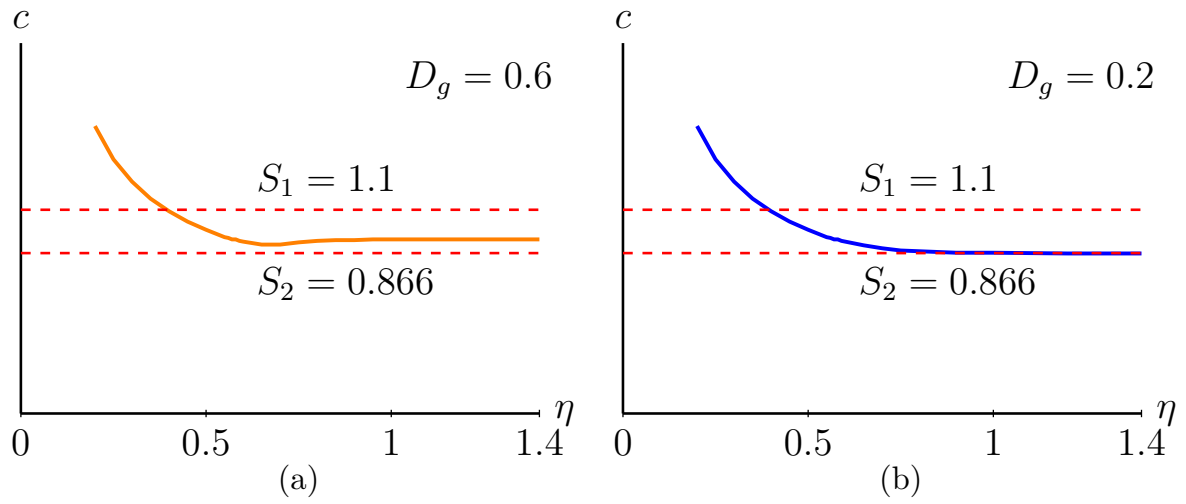

Figure 4.8: (a) gives the wave speed as a function of the initial condition $U(x,0) = 1/2 + \tanh(-\eta(x-40))/2$. Notice that as η grows to infinity this initial condition limits to the Heaviside initial condition. Parameters are $\lambda = 0.75$, $D_i = 0.25$ and $D_g = 0.6$. The wave speed reaches its minimum which is between S_1 and S_2 and then converges to a bigger value which is still between S_1 and S_2. In (b), $D_g = 0.2$ while the other parameters are the same. In this case, the wave speed converges to S_2.

front (van Saarloos 2003). Unravelling the differences in wave speed selection remains to be explored.

4.6.3 Shock-fronted travelling waves

In Section 4.4, we mainly considered the equilibrium point $(0,0)$ as a stable node in the phase plane of system (4.13). With $(0,0)$ a stable node, $(\beta,0)$ is also a stable node based on (4.22). However, (4.22) does not hold for any convex $D(U)$ which changes sign twice. For instance, for

$$\hat{D}(U) = (U-0.1)(U-0.3), \tag{4.37}$$

condition (4.15) and condition (4.16) become

$$c \geq 2\sqrt{\hat{D}(0)R'(0)} = 0.3, \quad c \geq 2\sqrt{\hat{D}'(0.3)R(0.3)} \approx 0.355.$$

With the nonlinear diffusivity function $\hat{D}(U)$, the equilibrium point $(0,0)$ is a stable node and the equilibrium point $(\beta,0)$ is a stable spiral for speeds $0.3 < c < 0.355...$ in (4.13). In this case, only shock-fronted travelling wave solutions of (4.2) can exist since (4.13) no longer possesses heteroclinic orbits connecting to $(\beta,0)$ that do not cross the walls of singularities, see Figure 4.9. The corresponding numerical simulation of (4.2) indeed gives a shock-fronted travelling wave solution with a speed $c = 0.3$, see Figure 4.10.

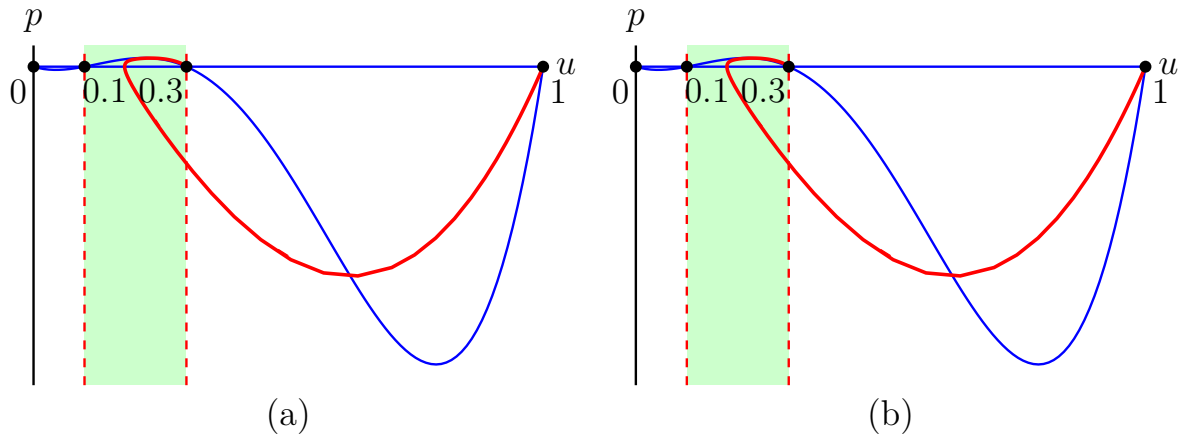

Figure 4.9: (a) is the phase plane of the desingularised system (4.13) with $\hat{D}(u)$, $c = 0.3$ and $\lambda = 0.75$. The vertical dashed lines are the wall of singularities at $u = 0.1$ and $u = 0.3$. The blue lines are the nullclines $p = 0$ and $p = -D(u)R(u)/c$. The red line is the heteroclinic orbit connecting $(1, 0)$ to $(0.3, 0)$. (b) is the phase plane of system (4.12) with $\hat{D}(u)$, $c = 0.3$ and $\lambda = 0.75$. The vertical dashed lines are the walls of singularities $u = 0.1$ and $u = 0.3$. The blue lines are the nullclines $p = 0$ and $p = -D(u)R(u)/c$. The red line shows the opposite moving directions of the same trajectory in (a) on different sides of the wall of singularities $u = 0.3$.

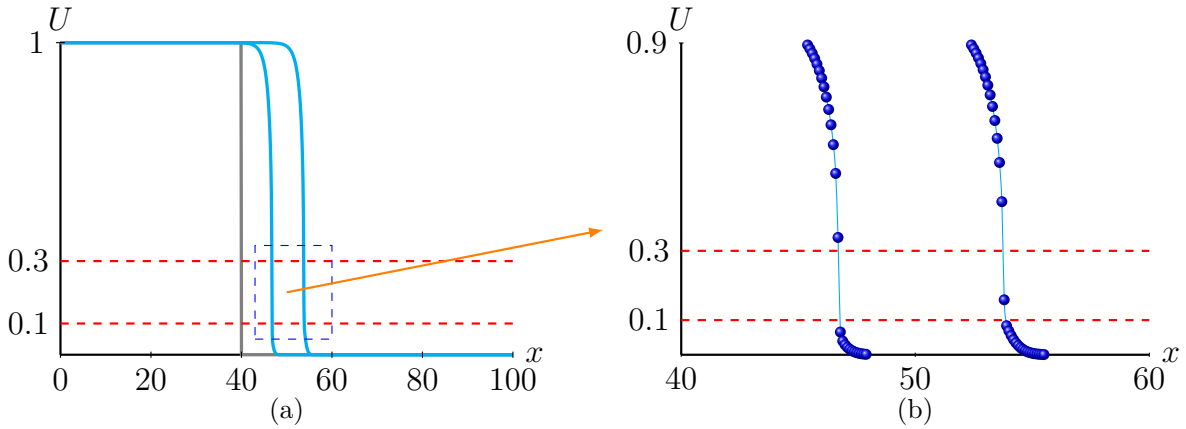

Figure 4.10: (a) shows the evolution of a Heaviside initial condition to a smooth travelling wave solution obtained by simulating (4.2) with (4.37) and (4.5) with $\lambda = 0.75$ at $t = 0$, $t = 25$ and $t = 50$. Notice that $D(U) = 0$ at $\alpha = 0.1$ and $\beta = 0.3$. The travelling wave solution eventually has a constant positive speed, $c = 0.3$. (b) amplifies the region around the shock. Blue dots represent the numerical simulations of the corresponding travelling wave solutions which indicate the existence of a shock.

It is not a surprise to see shock-fronted travelling wave solutions in negative nonlinear diffusion equations. Shocks in negative nonlinear diffusion equations with no kinetic terms have been studied in the context of many physical phenomena, such as the movement of moisture in partially saturated porous media (DiCarlo et al. 2008); the motion of nanofluids (Landman and White 2011) and these kinds of PDEs also arise in the study of Cahn-Hilliard models (Witelski 1995b). Numerical simulations of (4.2) with nonlinear diffusivity function (4.3) and Allee kinetics (4.4) also lead to shock-fronted solutions, see Johnston et al. (2017). In addition, Allee kinetics support shock-fronted travelling wave solutions for reaction-diffusion-advection equations with small diffusion coefficients (Sewalt et al. 2016; Wang et al. 2019). The analysis of shock-fronted travelling wave solutions in nonlinear diffusion-reaction equations with generic diffusivity functions and logistic kinetics is left for future work.

Chapter 5

Shock-fronted travelling waves with nonlinear diffusion and strong Allee effect source terms

---

5.1 Preamble

This chapter is a paper published in the *Physica D: Nonlinear Phenomenon*

Li, Y., van Heijster, P., Simpson, M.J., Wechselberger, M., 2021. Shock-fronted travelling waves in a reaction-diffusion model with nonlinear forward-backward-forward diffusion. *Physica D: Nonlinear Phenomena.* 423: 132916. DOI:10.1016/j.physd.2021.132916. arXiv Preprint

In this chapter, we address the research question 4 of the thesis: Do shock-fronted travelling wave solutions exist with nonlinear diffusion and strong Allee effect source terms? We extend the geometric approach developed in Section 4 by considering two smaller higher order perturbation terms, so that we can regularise the original system and study the properties of shock-fronted travelling wave solutions in an ODE system with higher dimensions. With these two regularisations, we explore how to identify the profile of shocks, and how to calculate the speed of shock-fronted travelling wave solutions.

5.2 Abstract

Reaction-diffusion equations (RDEs) are often derived as continuum limits of lattice-based discrete models. Recently, a discrete model which allows the rates of movement, proliferation and death to depend upon whether the agents are isolated has been proposed, and this approach gives various RDEs where the diffusion term is convex and can become negative (Johnston et al., Sci. Rep. 7, 2017), i.e. forward-backward diffusion. Numerical simulations suggest these RDEs support shock-fronted travelling waves when the reaction term includes an Allee effect. In this work we formalise these preliminary numerical observations by analysing the shock-fronted travelling waves through embedding the RDE into a larger class of higher order partial differential equations (PDEs). Subsequently, we use geometric singular perturbation theory to study this larger class of equations and prove the existence of these shock-fronted travelling waves. Most notable, we show that different embeddings yield shock-fronted travelling waves with different properties.

5.3 Introduction

Reaction-diffusion equations (RDEs) are widely used to study population dynamics in cell biology and ecology (Murray 1989). Often, $U(x,t)$ represents a population density and provides a macroscopic description of individual behaviour. For RDEs established from the continuum limit of stochastic models, a solution of the RDE not only shows the macroscopic evolution of $U(x,t)$, but it also reflects how microscopic behaviour of individuals influences the macroscopic outcomes (Anguige and Schmeiser 2009; Deroulers et al. 2009; Johnston et al. 2017, 2012; Li et al. 2020; Simpson et al. 2010a). Johnston et al. (2017) introduced a lattice-based stochastic model to study how a population of individuals can undergo motility, proliferation and death events with the aim of studying biological and ecological invasion, see Figure 5.1. By considering different behaviours of isolated and grouped agents, including motility, proliferation and death events, an RDE with a nonlinear diffusivity function and a logistic or Allee type reaction term was derived as the continuum limit. In particular,

$$\frac{\partial U}{\partial t} = \frac{\partial}{\partial x}\left(D(U)\frac{\partial U}{\partial x}\right) + R\left(U\right), \tag{5.1}$$

where $U(x,t)$ represents the total population density at position $x \in \mathbb{R}$ and time $t \in \mathbb{R}_+$.

The nonlinear diffusivity function is given by

$$D\left(U\right) = 3(D_i - D_g)U^2 - 4(D_i - D_g)U + D_i, \tag{5.2}$$

where $D_i \geq 0$ and $D_g \geq 0$ are diffusivities of the isolated and grouped agents, respectively.

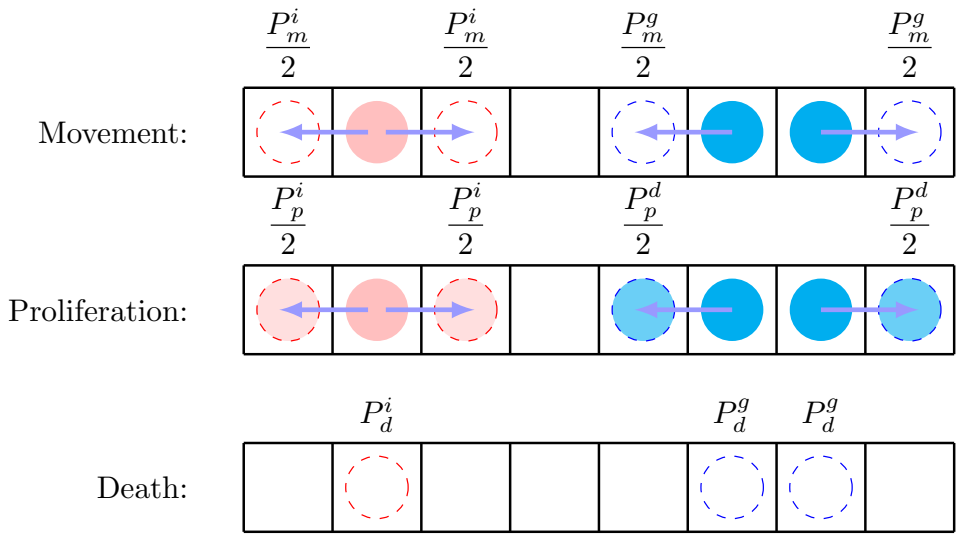

Figure 5.1: Schematic depiction of the evolution rules of the lattice-based model introduced in Johnston et al. (2017). Pink discs represent isolated agents and blue discs represent grouped agents. During each time step of duration τ, isolated agents attempt to move to nearest neighbour lattice sites with a probability P_m^i, to proliferate to form new agents in neighbour sites with a probability P_p^i and to die with a probability P_d^i. Similarly, grouped agents attempt to move to neighbour sites with a probability P_m^g, to proliferate to form new agents in neighbour sites with a probability P_p^g and to die with a probability P_d^g. The attempts that would move to an occupied site or place an agent on an occupied site are aborted.

When $D_i > 4D_g$, $D(U)$ has two real roots, α and β, which are centred around $2/3$, and are given by

$$\alpha = \frac{2}{3}\left(1 - \sqrt{\frac{D_i - 4D_g}{4(D_i - D_g)}}\right), \quad \beta = \frac{2}{3}\left(1 + \sqrt{\frac{D_i - 4D_g}{4(D_i - D_g)}}\right), \tag{5.3}$$

and $D(U) < 0$ for $U \in (\alpha, \beta)$. While the negativity of a nonlinear diffusivity function is sometimes related to aggregation in the underlying discrete model (Simpson et al. 2010b), here it is actually a macroscopic effect of the isolated and the grouped motility of the agents, together with competition for space, that leads to a net *aggregation effect* (Johnston et al. 2017). The condition $D_i > 4D_g$ implies that the motility rate of isolated agents is greater than the motility rate of grouped agents, which is consistent with the common biological observation that isolated *leader cells* are more motile than *follower cells* (Poujade et al. 2007; Simpson et al. 2014). Note that D_i and D_g are related to P_m^i and P_m^g, respectively, in the lattice-based model in Figure 5.1. Full details of the discrete model and the continuum limit derivation are given in Johnston et al. (2017).

The reaction term, whose parameters are also related to parameters in the lattice-based model depicted in Figure 5.1, is given by

$$R(U) = \lambda_g U(1-U) + (\lambda_i - \lambda_g - K_i + K_g)U(1-U)^2 - K_g U, \tag{5.4}$$

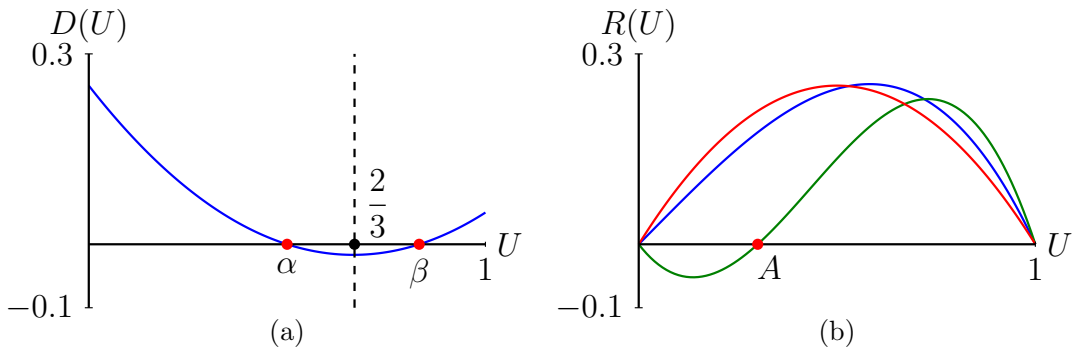

Figure 5.2: (a) The nonlinear diffusivity function $D(U)$ (5.2) centred around 2/3 (dashed line). (b) The reaction term $R(u)$ corresponding to the logistic growth with $\lambda_g = 1$ (red), the weak Allee effect with $r = 0.8$ and $A = -0.9$ (blue), and the strong Allee effect with $r = 3$ and $A = 0.3$ (green).

where $\lambda_i \geq 0$ and $\lambda_g \geq 0$ are the proliferation rates of isolated and grouped agents, respectively; $K_i \geq 0$ and $K_g \geq 0$ are the death rates of isolated and grouped agents, respectively Johnston et al. (2017). If the proliferation mechanism is the same for isolated and grouped agents and no death event occurs, that is, $\lambda_i = \lambda_g$ and $K_i = K_g = 0$, then (5.4) simplifies to a logistic reaction term

$$R(U) = \lambda_g U(1 - U). \tag{5.5}$$

If the proliferation and death mechanisms are either competitive or co-operative, that is, $\lambda_i \neq \lambda_g$ and $K_i \neq K_g$ (Stephens et al. 1999; Taylor and Hastings 2005), then the reaction term takes the form of an Allee effect (Taylor and Hastings 2005). For simplicity, but without loss of generality, we assume $K_g = 0$.[1] Subsequently, (5.4) simplifies to

$$R(U) = rU(1 - U)(U - A), \tag{5.6}$$

where $r = K_i - \lambda_i + \lambda_g$ is the intrinsic growth rate and $A = 1 - \lambda_g/r$ is the Allee parameter Johnston et al. (2017). If $r > \lambda_g$, which is equivalent to $K_i > \lambda_i$ and thus implies that isolated agents have a higher death rate than proliferation rate, then $0 < A < 1$ and $R(U) < 0$ in $(0, A)$ and $R(U) > 0$ in $(A, 1)$. This represents the strong Allee effect. Conversely, if $0 < r < \lambda_g$, which implies that isolated agents have a higher birth rate than death rate, then $A < 0$ and $R(U) > 0$ in $(0, 1)$. This is called the weak Allee effect Johnston et al. (2017). See Figure 5.2 for the different potential forms of $R(U)$. For simplicity, we assume that $A \neq \alpha$ and $A \neq \beta$.

Understanding travelling wave solutions, that is, solutions that propagate through

[1] Although we assume $K_i = K_g = 0$ to obtain the logistic reaction term (5.5) and $K_g = 0$ to obtain the Allee reaction term (5.6), similar reaction terms are obtained without these assumptions by scaling the population density $U(x, t)$ (Johnston et al. 2017).

space with a fixed shape and a constant speed, is important in the study of biological and ecological invasion processes (Ducrot et al. 2021; El-Hachem et al. 2020; Harley et al. 2014a; Sewalt et al. 2016). In this work, we are interested in travelling wave solutions supported by (5.1) with $D_i > 4D_g$, such that the nonlinear diffusivity function is negative for $U \in (\alpha, \beta)$, see (5.3). In this case, the nonlinear diffusivity function can be written as

$$D(U) = k(U-\alpha)(U-\beta), \qquad k := 3(D_i - D_g). \tag{5.7}$$

With the implicit finite difference method introduced in Johnston et al. (2017), numerical solutions of (5.1) with $D(U)$ as in (5.7) and with either logistic or weak Allee forms for $R(U)$ lead to smooth travelling wave solutions with positive speeds, while simulations of (5.1) with $D(U)$ as in (5.7) and strong Allee forms for $R(U)$ lead to shock-fronted travelling wave solutions with either positive or negative speeds (Johnston et al. 2017; Li et al. 2020), see Figure 5.3 for different travelling wave solutions at $t = t_1, t_2, t_3$, with $t_1 < t_2 < t_3$. To calculate the wave speed, we locate the front of the wave by looking for the left-most coordinate x_l satisfying $U(x_l, t) < 10^{-3}$. Then, we estimate the speed from the distance the front of the wave has travelled from t_2 to t_3. Interestingly, the speeds of the shock-fronted travelling wave solutions are much smaller than the speeds of the smooth travelling wave solutions, which potentially indicates that the mechanisms giving rise to shock-fronted travelling waves are fundamentally different to the mechanisms that give rise to smooth travelling waves. Note that with the nonlinear diffusivity function $D(U)$ centred around 2/3 given by (5.2) we only observe shock-fronted travelling wave solutions with the strong Allee effect. However, a forward-backward-forward nonlinear diffusivity function which is not centred around 2/3 may also lead to shock-fronted travelling wave solutions with logistic or weak Allee forms of $R(U)$, see Figures 9 and 10 in Li et al. (2020) for an example.

Ferracuti et al. (2009) showed that there exist smooth travelling wave solutions of (5.1) with logistic $R(U)$ for a range of positive wave speeds based on the *comparison method* (Aronson 1980). Kuzmin and Ruggerini (Kuzmin and Ruggerini 2011) provided necessary conditions for the existence of smooth travelling wave solutions of (5.1) with $R(U)$ that takes the form of an Allee effect and the speed of the wave can be either negative or positive according to the shape of $D(U)$ and $R(U)$. However, to the best of our knowledge, the existence of shock-fronted travelling wave solutions to (5.1) with $D(U)$ (5.7) and $R(U)$ taking the form of an Allee effect is an open question. The methods used in Kuzmin and Ruggerini (2011) can also be used to identify necessary conditions for the existence of shock-fronted

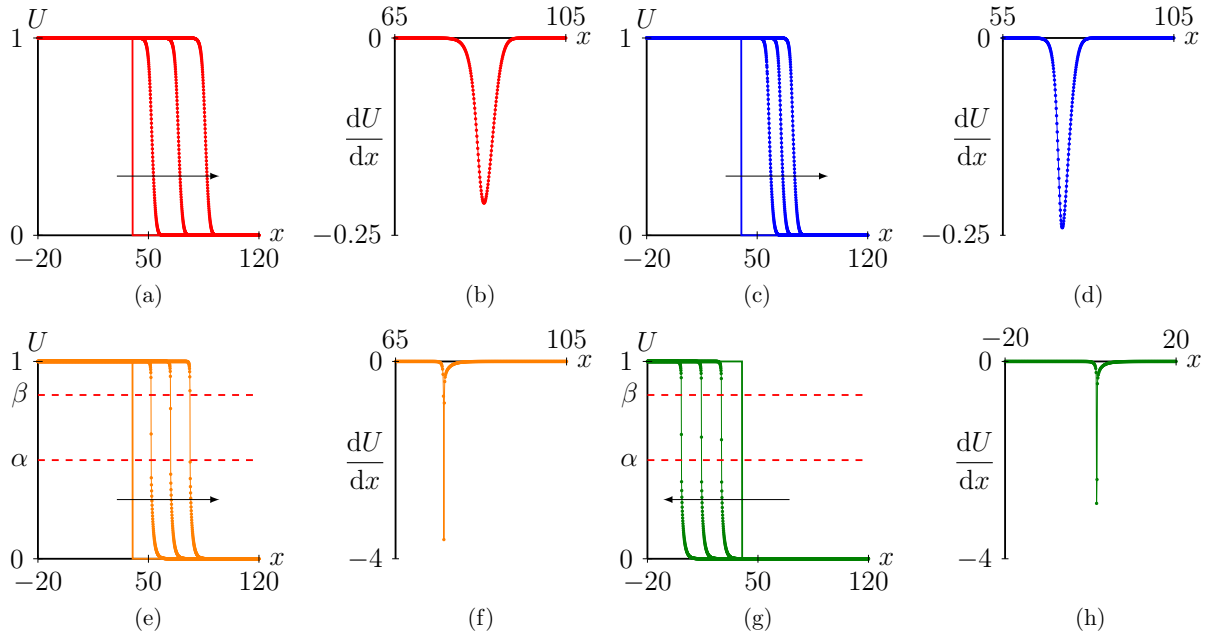

Figure 5.3: Travelling wave solutions of (5.1) evolving from a Heavidside initial condition, $U = 1$ for $x \in [-20, 40]$ and $U = 0$ for $x \in (40, 120]$, with $D_i = 0.25$ and $D_g = 0.05$ such that $D(U) = 0.6U^2 - 0.8U + 0.25$ and for different $R(U)$. The implicit finite difference method we used had no-flux boundary conditions, a time step $\delta t = 0.01$, a space step $\delta x = 0.1$ and an error tolerance 10^{-6}. With a logistic type $R(U) = 0.75U(1 - U)$, (a) shows a travelling wave solution with speed $c \approx 0.86$ at $t_1 = 20$, $t_2 = 40$, $t_3 = 60$. With a weak Allee type $R(U) = 0.5U(1 - U)(U + 0.2)$, where $\lambda_i = 0.5$, $\lambda_g = 0.6$ and $K_i = 0.4$, (c) shows a smooth travelling wave solution with $c \approx 0.99$ at $t_1 = 15$, $t_2 = 30$, $t_3 = 45$. With a strong Allee type $R(U) = 0.5U(1 - U)(U - 0.2)$, where $\lambda_i = 0.4$, $\lambda_g = 0.4$ and $K_i = 0.5$, (e) shows a shock-fronted travelling wave solution with positive speed $c = 0.0123$ at $t_1 = 1000$, $t_2 = 2000$, $t_3 = 3000$. With a different strong Allee type $R(U) = 0.3U(1 - U)(U - 1/3)$, where $\lambda_i = 0.4$, $\lambda_g = 0.2$ and $K_i = 0.5$, (h) shows a shock-fronted travelling wave solution with negative speed $c = -0.0127$ at $t_1 = 500$, $t_2 = 1000$, $t_3 = 1500$. (b) & (d) show the derivatives of the last simulated travelling wave solutions in (a) & (c) and highlight the smoothness of the waves. (f) & (h) show the derivatives of the last simulated travelling wave solutions in (e) & (g) and highlight the shocks in these waves.

travelling wave solutions. In particular, let U_1 and U_2 (with $U_1 \leq \alpha < \beta \leq U_2$) denote the U-values at the endpoints of the shock, then a necessary condition for the existence of a monotonically decreasing shock-fronted left-travelling wave solution is

$$\int_0^{U_a} D(U)R(U)\mathrm{d}U < 0\,, \tag{5.8}$$

for all $U_a \in (0, U_1)$.

Similarly, a necessary condition for the existence of a monotonically decreasing shock-fronted right-travelling wave solution is

$$\int_{U_b}^1 D(U)R(U)\mathrm{d}U > 0\,, \tag{5.9}$$

for all $U_b \in (U_2, 1)$. We refer to Section 5.7.1 for a derivation, inspired by Kuzmin and Ruggerini (2011), of these necessary conditions. Heuristically this means that for shock-fronted travelling wave solutions with a positive speed, the A value in $R(U)$, in order to satisfy (5.9), should not be too close to 1. Since $A = 1 - \lambda_g/r$ where $r = K_i - \lambda_i + \lambda_g$, this implies that a relatively much higher death rate of isolated agents compared to the birth rate of isolated agents will not result in a successful invasion event. Similarly, a very small birth rate of grouped agents will also not result in a successful invasion event.

In Li et al. (2020), we derived, among other things, the same condition as in Ferracuti et al. (2009) for the existence of smooth travelling wave solutions of (5.1) with logistic $R(U)$ by using a geometric approach. Furthermore, geometric approaches have been used to study shock-fronted travelling wave solutions. For example, in Harley et al. (2014a) and Sewalt et al. (2016), the authors studied shock-fronted travelling wave solutions in an advection-reaction-diffusion equation for malignant tumour invasion using geometric singular perturbation theory (GSPT) (Fenichel 1979; Hek 2010; Jones 1995) and canard theory (Szmolyan and Wechselberger 2001; Wechselberger 2012; Wechselberger and Pettet 2010). In this work, we use GSPT to further explore the existence of shock-fronted travelling wave solutions of (5.1) with $\lim_{x\to-\infty} U(x,t) = 1$ and $\lim_{x\to\infty} U(x,t) = 0$.[2] Moreover, we assume $D_i > 4D_g$ – such that $D(U) < 0$ for $U \in (\alpha, \beta)$ – and $K_g = 0$ and $r > \lambda_g$ – such that we have a strong Allee effect type $R(U)$. To apply GSPT, we smooth out the shock and regularise (5.1) by adding a small higher order perturbation term. This embeds (5.1) into a larger class of PDEs. Regularisation of RDEs is typically considered in one of two ways (Padrón 2004; Pego and Penrose 1989). The first method of regularisation accounts for non-local effects by adding a small fourth-order spatial derivative term (Pego

[2] $U \equiv 0$ and $U \equiv 1$ are both constant solutions of (5.1) with the logistic $R(U)$ and the weak and strong Allee type $R(U)$. However, $U \equiv 0$ and $U \equiv 1$ are both PDE stable for the strong Allee type $R(U)$, while only $U \equiv 1$ is PDE stable for the logistic $R(U)$ and the weak Allee type $R(U)$. Therefore, it is no surprise that left-moving traveling wave solutions are only found for the strong Allee type $R(U)$, see Figure 5.3.

and Penrose 1989; Witelski 1995b). In particular, equation (5.1) becomes

$$\frac{\partial U}{\partial t} = \frac{\partial}{\partial x}\left(D(U)\frac{\partial U}{\partial x}\right) + R(U) - \varepsilon^2 \frac{\partial^4 U}{\partial x^4}, \quad 0 \leq \varepsilon \ll 1. \tag{5.10}$$

The second method of regularisation accounts for viscous relaxation by adding a small mixed derivative term (Novick-Cohen and Pego 1991; Padrón 2004; Witelski 1996). In particular, equation (5.1) becomes

$$\frac{\partial U}{\partial t} = \frac{\partial}{\partial x}\left(D(U)\frac{\partial U}{\partial x}\right) + R(U) + \varepsilon \frac{\partial^3 U}{\partial x^2 \partial t}, \quad 0 \leq \varepsilon \ll 1. \tag{5.11}$$

It is important that the sign of the perturbation terms in (5.10) and (5.11) is such that setting $\varepsilon > 0$ generally leads to well-posed problems. However, see Li et al. (2020) and references therein, for a further discussion related to the well-posedness of (5.1). Also note that other types of regularisations have been used to smooth out shocks (Barenblatt et al. 1993).

In Section 5.4, we study travelling wave solutions of (5.10) and first derive a higher-dimensional slow-fast system of ordinary differential equations (ODEs). The related reduced singular limit ODE systems give useful information of underlying shock-fronted travelling wave solutions of (5.1) and (5.10) based on GSPT and Fenichel theory (Fenichel 1979). Because the reduced systems are algebraically intractable, we use a numerical ODE solver to determine the speed of the shock-fronted travelling wave solutions. In Section 5.5, we use a similar approach to establish a different higher-dimensional system of ODEs based on the viscous relaxation PDE (5.11) and find shock-fronted travelling wave solutions with different properties. Note that in this case, GSPT has to be extended since the critical manifold loses normal hyperbolicity near a fold point. Although (5.10) and (5.11) are the same in the singular limit $\varepsilon = 0$, they yield shock-fronted travelling wave solutions with different speeds and different shock sizes when $\varepsilon > 0$. Finally, we discuss various extensions of the current work including the relationship between the discrete model and the continuous description, the option of including different regularisation terms, the possibility of shock-fronted travelling wave solutions with logistic $R(U)$ and the spectral stability of travelling wave solutions of (5.1).

Remark 1 *In the remainder of this article we will use nonlinear diffusivity functions* $D(U)$ (5.2) *and reaction terms* $R(U)$ (5.4) *that are larger than the* $D(U)$ *and* $R(U)$ *used in Figure 5.3 to generate larger speeds. As the model based on* (5.1) *is dimensionless, those larger parameters in* $D(U)$ *and* $R(U)$ *still correspond to the parameters introduced in the latticed-based model in Figure 5.1 upon rescaling space and/or time. However, note that the connection between the discrete and continuum models is only accurate when the rate of motility of both the grouped and isolated agents is much greater than rate of proliferation*

and death of both the grouped and isolated agents and this should be kept in mind when rescaling space and/or time. For more details, see Johnston et al. (2017).

5.4 Non-local regularisation

In this section, we look for shock-fronted travelling wave solutions of (5.10) connecting $U = 1$ to $U = 0$. We first introduce a travelling wave coordinate to transform (5.10) into a fourth-order ODE. Next, we use a dynamical system approach to transform the ODE into a four-dimensional singular perturbed slow-fast system. The four-dimensional system has two equivalent forms as $\varepsilon \neq 0$. However, these forms produce different lower-dimensional subsystems, called the *reduced problem* and the *layer problem* in the singular limit $\varepsilon = 0$.[3] The concatenation of solutions of each of the subsystems yields a solution of the four-dimensional system in the singular limit. We give an outline, and conclude based on GSPT, that it persists for ε sufficiently small in the full four-dimensional system. This solution corresponds to a travelling wave solution of (5.10).

5.4.1 Preliminary observations

A travelling wave solution of (5.10) is a solution of the form $U(x,t) = u(x - ct) = u(z)$, where $c \in \mathbb{R}$ is the constant speed of the travelling wave solution and $z = x - ct$ is the travelling wave coordinate. Writing (5.10) in its travelling wave coordinate leads to

$$\frac{\partial U}{\partial t} = \frac{\partial}{\partial z}\left(\varepsilon^2 \frac{\partial^3 U}{\partial z^3} - cU - \frac{\partial}{\partial z}(F(U))\right) - R(U), \tag{5.12}$$

where $F(U) = \int D(U)\mathrm{d}U$ and the reaction term $R(U)$ (5.6) is of strong Allee effect type. A travelling wave solution $u(z)$ is a stationary solution to (5.12) that asymptotes to one as $z \to -\infty$ and to zero as $z \to \infty$. Thus, it satisfies

$$0 = \frac{\mathrm{d}}{\mathrm{d}z}\left(\varepsilon^2 \frac{\mathrm{d}^3 u}{\mathrm{d}z^3} - cu - \frac{\mathrm{d}}{\mathrm{d}z}(F(u))\right) - R(u). \tag{5.13}$$

Upon defining

$$p := \varepsilon^2 \frac{\mathrm{d}^3 u}{\mathrm{d}z^3} - cu - \frac{\mathrm{d}}{\mathrm{d}z}(F(u)), \quad v := \varepsilon^2 \frac{\mathrm{d}^2 u}{\mathrm{d}z^2} - F(u), \quad w := \varepsilon \frac{\mathrm{d}u}{\mathrm{d}z}, \tag{5.14}$$

[3] The reduced problem is called the *slow reduced system* and the layer problem is called the *fast reduced system* in studies of phase separation, see for example, Doelman et al. (2009).

(5.13) transforms into a four-dimensional singular perturbed slow-fast dynamical system

$$\begin{cases} \varepsilon \dfrac{\mathrm{d}u}{\mathrm{d}z} & = w, \\ \varepsilon \dfrac{\mathrm{d}w}{\mathrm{d}z} & = v + F(u), \\ \dfrac{\mathrm{d}p}{\mathrm{d}z} & = R(u), \\ \dfrac{\mathrm{d}v}{\mathrm{d}z} & = p + cu. \end{cases} \tag{5.15}$$

Here, $(u, w) \in \mathbb{R}^2$ are fast variables and $(p, v) \in \mathbb{R}^2$ are slow variables. By using a stretched, or fast variable, $\xi = z/\varepsilon$ Fenichel (1979), (5.15) is transformed into an equivalent fast system, provided $\varepsilon \neq 0$,

$$\begin{cases} \dfrac{\mathrm{d}u}{\mathrm{d}\xi} & = w, \\ \dfrac{\mathrm{d}w}{\mathrm{d}\xi} & = v + F(u), \\ \dfrac{\mathrm{d}p}{\mathrm{d}\xi} & = \varepsilon R(u), \\ \dfrac{\mathrm{d}v}{\mathrm{d}\xi} & = \varepsilon(p + cu). \end{cases} \tag{5.16}$$

The three fixed points[4] of the two equivalent systems (5.15) and (5.16) are

$$P_\varepsilon^0 = (0, 0, 0, -F(0)),\ P_\varepsilon^1 = (1, 0, -c, -F(1)),\ P_\varepsilon^A = (A, 0, -cA, -F(A)), \tag{5.17}$$

and we are interested in heteroclinic orbits connecting P_ε^1 with P_ε^0 as these correspond to travelling wave solutions of (5.10) that asymptote to 1 as $x \to -\infty$ and to 0 as $x \to \infty$. Note that due to the symmetry $(w, p, z, c) \mapsto (-w, -p, -z, -c)$ of system (5.15), the existence of a heteroclinic orbit connecting P_ε^1 with P_ε^0 also implies the existence of a heteroclinic orbit connecting P_ε^0 with P_ε^1 and this latter orbit corresponds to a travelling wave solution of (5.10) that asymptotes to 0 as $x \to -\infty$ and to 1 as $x \to \infty$ and moves in the opposite direction.

The characteristic equation of the Jacobian of (5.16) is given by

$$\tau^4 - D(u)\tau^2 - \varepsilon\tau c - \varepsilon^2 R'(u) = 0, \tag{5.18}$$

where we used that $F'(u) = D(u)$ and observe that $u = 0, 1$ or A at a fixed point. Upon substituting a regular expansion $\tau = \tau_0 + \varepsilon\tau_1 + \mathcal{O}(\varepsilon^2)$ into (5.18), we obtain an expansion

[4] Even though the fixed points are independent of ε, we use the subscript ε to indicate that these are fixed points of the full four-dimensional systems (5.15) and (5.16).

for the four eigenvalues of the Jacobian

$$\begin{aligned}\tau_1^{\pm}(u) &= \frac{-c \pm \sqrt{c^2 - 4D(u)R'(u)}}{2D(u)}\varepsilon + \mathcal{O}(\varepsilon^2),\\ \tau_2^{\pm}(u) &= \pm\sqrt{D(u)} + \frac{c}{2D(u)}\varepsilon + \mathcal{O}(\varepsilon^2).\end{aligned} \tag{5.19}$$

At P_ε^0, $R'(0) < 0$, $D(0) > 0$, thus $\tau_{1,2}^+(0) > 0$, $\tau_{1,2}^-(0) < 0$. Similarly, at P_ε^1, $R'(1) < 0$, $D(1) > 0$ and $\tau_{1,2}^+(1) > 0$, $\tau_{1,2}^-(1) < 0$. That is, both the stable and unstable manifolds $P_\varepsilon^{0,1}$ are two-dimensional. At P_ε^A, the stable and unstable manifolds depend on the sign of c. If $c > 0$, the stable manifold of P_ε^A is three-dimensional and the unstable manifold of P_ε^A is one-dimensional, while the situation for the stable and unstable manifolds of P_ε^A is the opposite for $c < 0$. For $c = 0$, that is, for a standing wave, we again have that the stable and unstable manifold of P_ε^A are two-dimensional.

While the slow system (5.15) and the fast system (5.16) are equivalent for $\varepsilon \neq 0$, they have different singular limits. The singular limit of the fast system, that is, the layer problem, describes the dynamics near the shock and the fast variables (u, w) will change significantly here while the slow variables (p, v) are to leading order constant. In contrast, the singular limit of the slow system, that is, the reduced problem, describes the dynamics away from the shock and here the fast variables will be slaved to the slow variables.

5.4.2 Layer problem

The layer problem is obtained by letting $\varepsilon \to 0$ in the fast system (5.16), which gives

$$\begin{cases}\dfrac{\mathrm{d}u}{\mathrm{d}\xi} &= w,\\ \dfrac{\mathrm{d}w}{\mathrm{d}\xi} &= v + F(u),\end{cases} \tag{5.20}$$

as well as $\mathrm{d}p/\mathrm{d}\xi = 0$ and $\mathrm{d}v/\mathrm{d}\xi = 0$, that is, $(p, v) \in \mathbb{R}^2$ are constants in (5.20). The union of fixed points of (5.20)

$$\mathcal{M}_0 := \{(u, w, p, v) \in \mathbb{R}^4 : w = 0,\ F(u) = -v\}, \tag{5.21}$$

forms a two-dimensional invariant manifold, which is the so-called critical manifold (Jones 1995), see Figure 5.4.

The Jacobian of (5.20) is

$$J = \begin{pmatrix} 0 & 1 \\ D(u) & 0 \end{pmatrix},$$

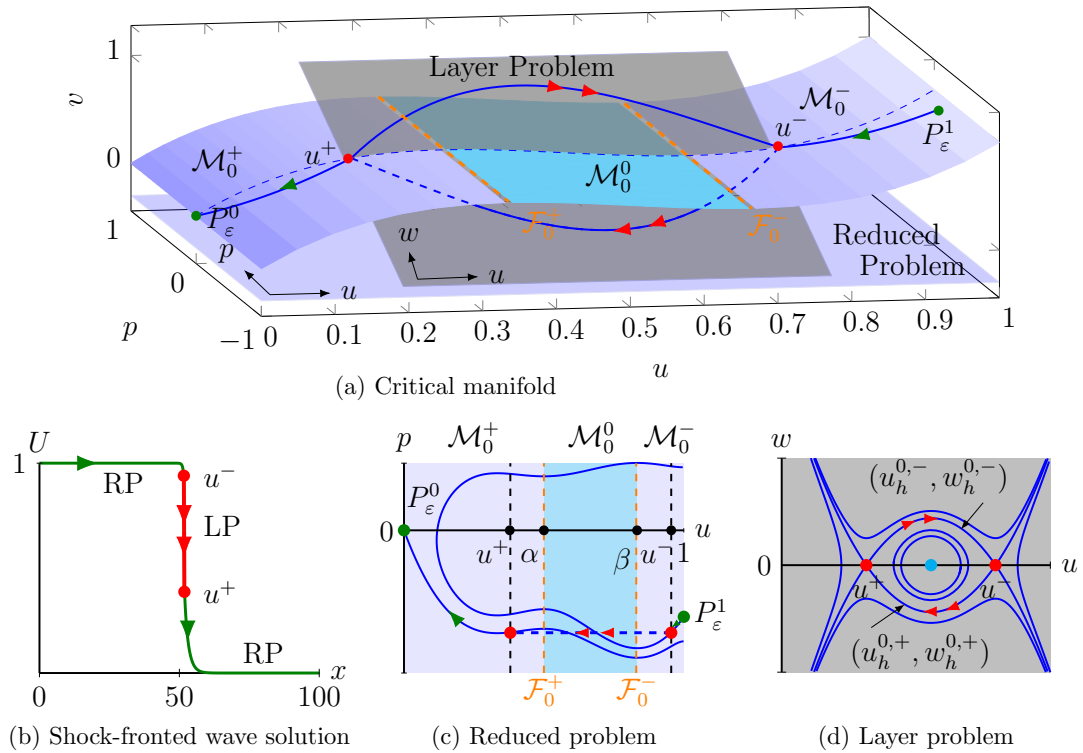

(a) Critical manifold

(b) Shock-fronted wave solution

(c) Reduced problem

(d) Layer problem

Figure 5.4: (a) A projection of the four-dimensional phase plane of (5.15) and the critical manifold $\mathcal{M}_0$. A shock-fronted travelling wave solution of (5.10) as shown in (b) corresponds to a heteroclinic orbit (indicated in blue in (a)) that starts at P_ε^1 on the normally hyperbolic branch $\mathcal{M}_0^-$ of $\mathcal{M}_0$ and that follows the dynamics of the reduced problem (RP), whose projection on the (u, p)-plane is shown in (c), before it jumps to the other normally hyperbolic branch $\mathcal{M}_0^+$ according to the dynamics of the layer problem (LP). The projection of the layer dynamics on the (u, w)-plane, since p and v are constant, is shown in (d) and the two blue curves connecting u^- and u^+ in (a) correspond to the heteroclinic orbits $\left(u_h^{0,\pm}, w_h^{0,\pm}\right)$ in (d). On $\mathcal{M}_0^+$, the heteroclinic orbit again follows the dynamics of the reduced problem and asymptotes to P_ε^0. A shock-fronted travelling wave solution is thus composed by orbits in the reduced problem and the layer problem as indicated in (b).

with eigenvalues

$$\tau_{\pm}(u,w) = \pm\sqrt{D(u)}. \tag{5.22}$$

Therefore, the manifold $\mathcal{M}_0$ loses normal hyperbolicity when $D(u) \leq 0$, that is, for $u \in [\alpha, \beta]$ the eigenvalues $\tau_{\pm}$ (5.22) are purely imaginary. As such, we split the critical manifold $\mathcal{M}_0$ into two two-dimensional normally hyperbolic saddle-type branches

$$\mathcal{M}_0^+ := \{(u,w,p,v) \in \mathbb{R}^4 : w = 0,\ F(u) = -v,\ u \in [0,\alpha)\},$$
$$\mathcal{M}_0^- := \{(u,w,p,v) \in \mathbb{R}^4 : w = 0,\ F(u) = -v,\ u \in (\beta,1]\},$$

a two-dimensional not normally hyperbolic centre-type branche

$$\mathcal{M}_0^0 := \{(u,w,p,v) \in \mathbb{R}^4 : w = 0,\ F(u) = -v,\ u \in (\alpha,\beta)\},$$

and the two one-dimensional boundary sets

$$\mathcal{F}_0^+ := \{(u,w,p,v) \in \mathbb{R}^4 : w = 0,\ F(u) = -v,\ u = \alpha\},$$
$$\mathcal{F}_0^- := \{(u,w,p,v) \in \mathbb{R}^4 : w = 0,\ F(u) = -v,\ u = \beta\}.$$

The layer problem (5.20) describes the dynamics near the shock away from the critical manifold. It is a Hamiltonian system and, as such, we are looking for a heteroclinic orbit connecting $\mathcal{M}_0^-$ with $\mathcal{M}_0^+$. The Hamiltonian of (5.20) is given by

$$H(u,w) = -\frac{1}{2}w^2 + G(u) + vu,$$

where $G(u) = \int F(u)\,\mathrm{d}u$. Any solution is confined to a level set of the Hamiltonian and we have that

$$G(u^+) + vu^+ = G(u^-) + vu^-,$$

where $u^{\pm} \in \mathcal{M}_0^{\pm}$ are the end-points of the heteroclinic orbit such that $0 < u^+ < \alpha < \beta < u^- < 1$. This is equivalent to the integral equation

$$\int_{u^+}^{u^-} (F(u) + v)\,\mathrm{d}u = 0, \tag{5.23}$$

which is the well-known *equal area rule*, see, for example, Witelski (1995b). Recall that $F(u) = \int D(u)\,\mathrm{d}u$ and $F(u)$ thus has an integration constant. Therefore, for a specific $F(u)$ the value of v satisfying the equal area rule (5.23) is unique. In 5.7.2 we show that (5.20) supports two heteroclinic orbits connecting $(u^+,0)$ and $(u^-,0)$ and these heteroclinic

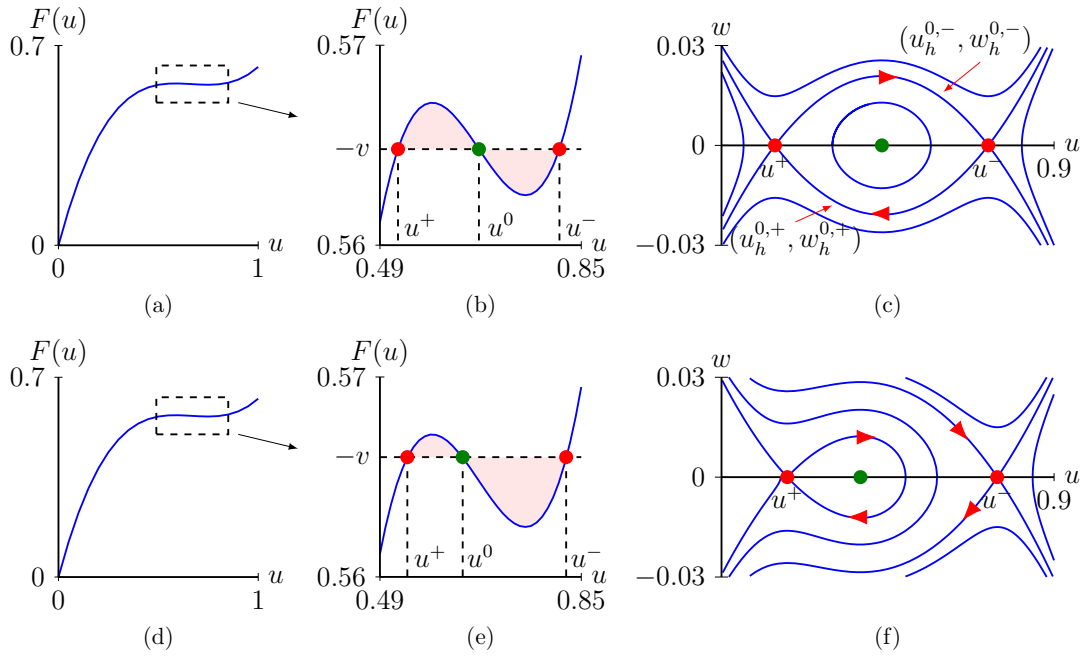

Figure 5.5: (a) & (b) The case when u^+ and u^- satisfy the equal area rule (5.23) with $D(u) = 6(u - 7/12)(u - 3/4)$ leading to $F(u) = 2u^3 - 4u^2 + 21u/8$ and $v = -61/108$. (c) The related phase plane of (5.20) including the two heteroclinic orbits $\left(u_h^{0,\pm}, w_h^{0,\pm}\right)$. (d) & (e) The case when u^+ and u^- do not satisfy the equal area rule with $v = -163/288$. (f) The related phase plane.

orbits $\left(u_h^{0,\pm}, w_h^{0,\pm}\right)$ are given by

$$u_h^{0,\pm}(\xi) = \frac{u^- + u^+}{2} \pm \frac{u^- - u^+}{2} \tanh\left(-\frac{a(u^- - u^+)}{2}\xi\right),$$
$$w_h^{0,\pm}(\xi) = \mp\frac{a(u^- - u^+)^2}{4} \operatorname{sech}^2\left(-\frac{a(u^- - u^+)}{2}\xi\right),$$

where $a = \sqrt{(D_i - D_g)/2}$ and we recall that $u^- > u^+$ by construction. See Figure 5.5.

5.4.3 Reduced problem

The reduced problem is obtained from (5.15) by letting $\varepsilon \to 0$, which gives

$$\begin{cases} \dfrac{\mathrm{d}p}{\mathrm{d}z} &= R(u), \\ \dfrac{\mathrm{d}v}{\mathrm{d}z} &= p + cu, \end{cases} \tag{5.24}$$

and the two algebraic constraints $w = 0$ and $v + F(u) = 0$. Hence, (5.24) simplifies to

$$\begin{cases} -D(u)\dfrac{\mathrm{d}u}{\mathrm{d}z} &= p + cu, \\ \dfrac{\mathrm{d}p}{\mathrm{d}z} &= R(u). \end{cases} \tag{5.25}$$

Morever, since $w = 0$ and $F(u) = -v$, (5.25) governs the flow on the critical manifold $\mathcal{M}_0$. The reduced problem is singular along the two lines $u = \alpha$ and $u = \beta$ since $D(\alpha) = D(\beta) = 0$. Therefore, we transform (5.25) into a desingularised system[5] by using a stretched variable $\mathrm{d}\psi = \mathrm{d}z/D(u)$ (Aronson 1980; Li et al. 2020)

$$\begin{cases} \dfrac{\mathrm{d}u}{\mathrm{d}\psi} &= -p - cu, \\ \dfrac{\mathrm{d}p}{\mathrm{d}\psi} &= D(u)R(u). \end{cases} \tag{5.26}$$

It is important to note that, while the stretching changes the speed along a trajectory in a nonlinear fashion, the trajectories of the phase portraits of the reduced problem (5.25) and the desingularised problem (5.26) are the same. However, the orientation along a trajectory is reversed for $u \in (\alpha, \beta)$ as $D(u) < 0$.

System (5.26) has five fixed points $(0, 0)$, $(\alpha, -c\alpha)$, $(A, -cA)$, $(\beta, -c\beta)$ and $(1, -c)$. The eigenvalues and eigenvectors of the Jacobian of (5.26) are given by

$$\tau_\pm = \frac{-c \pm \sqrt{c^2 - 4(D(u)R'(u) + D'(u)R(u))}}{2}, \quad E_\pm = (1, -\tau_\mp).$$

If we let χ_1 be the minimum of the set $\{A, \alpha, \beta\}$, χ_3 its maximum, and χ_2 the remaining element, then the characteristics of $D(u)$ and $R(u)$ yield the following results:

- $(0, 0), (1, -c)$ and $(\chi_2, -c\chi_2)$ are saddles; and
- $(\chi_i, -c\chi_i)$, $i \in \{1, 3\}$, is a(n)
  - stable node for $c > 2\sqrt{D(\chi_i)R'(\chi_i)}$;
  - stable spiral for $0 < c < 2\sqrt{D(\chi_i)R'(\chi_i)}$;
  - centre for $c = 0$;
  - unstable spiral for $-2\sqrt{D(\chi_i)R'(\chi_i)} < c < 0$; and
  - unstable node for $c < -2\sqrt{D(\chi_i)R'(\chi_i)}$.

[5] Deriving the desingularised system from (5.25) is, strictly speaking, not necessary for our analysis as we only need to consider (5.25) on $\mathcal{M}_0^\pm$ away from α and β since the heteroclinic orbit of the layer problem jumps from $\mathcal{M}_0^- \ni u^- > \beta$ to $\in \mathcal{M}_0^+ \ni u^+ < \alpha$, see Figures 5.4 and 5.5. However, the desingularised system is more amenable to analysis and we thus study the dynamics of this desingularised system.

5.4.4 The construction of the heteroclinic orbit in the singular limit

Since the fixed points $P_\varepsilon^{0,1}$ (5.17) are on the normally hyperbolic branches $\mathcal{M}_0^\pm$ of the critical manifold $\mathcal{M}_0$, a shock-fronted travelling wave solution to (5.10) corresponds to a heteroclinic orbit of (5.15) that, to leading order, starts on $\mathcal{M}_0^-$, follows the dynamics of the reduced problem (5.25) before it jumps, according to the layer dynamics (5.20), to the other normally hyperbolic branch $\mathcal{M}_0^+$ on which it asymptotes to P_ε^0 following the dynamics of (5.25) again. In particular, if we split the spatial domain $z \in (-\infty, \infty)$ into three parts:

$$\begin{aligned} &z \in I_s^- := (-\infty, -\sqrt{\varepsilon} + z^*)\,, \quad z \in I_f := [-\sqrt{\varepsilon} + z^*, \sqrt{\varepsilon} + z^*]\,, \\ &z \in I_s^+ := (\sqrt{\varepsilon} + z^*, \infty)\,, \end{aligned} \tag{5.27}$$

then the heteroclinic orbit is, to leading order, on $\mathcal{M}_0^\pm$ and governed by the reduced problem (5.25) for $z \in I_s^\pm$, while it is, to leading order, governed by the layer problem (5.20) for $z \in I_f$, see Figure 5.4. Note that due to translation invariance of (5.12) we can, without loss of generality, set $z^* = 0$ in (5.27).

Since $w = 0$ and $F(u) = -v$ on the critical manifold, the fixed points $(0, 0)$ and $(1, -c)$ of the reduced problem (5.25) correspond to P_ε^0 and P_ε^1, respectively. Furthermore, the analysis of the layer problem (5.20) – which is independent of the speed c – indicates there may exist shocks with endpoints u^- $(> \beta)$ and u^+ $(< \alpha)$. Consequently, if there exists a shock-fronted travelling wave solution of (5.10) with a shock from u^- to u^+, it relates to two trajectories in system (5.25), see also Figure 5.4. These, in turn, relate to two corresponding trajectories in the desingularised system (5.26). One is the unique trajectory γ^+, for a given speed c, that starts on the line $\{(u^+, p^+), p^+ \in \mathbb{R}\}$ and approaches $(0, 0)$ as $\psi \to \infty$, while the other one is the unique trajectory γ^- that arrives at the line $\{(u^-, p^-), p^- \in \mathbb{R}\}$ and approaches $(1, -c)$ as $\psi \to -\infty$. Note that these unique trajectories can intersect the lines $\{(u^\pm, p^\pm), p^\pm \in \mathbb{R}\}$ multiple times, see, for instance, Figure 5.6a. However, only the first intersections may lead to monotone travelling wave solutions. We are mainly interested in monotone travelling wave solutions since nonmonotonic travelling wave solutions are often PDE unstable Volpert et al. (1994). Therefore, we only look for these first intersections. As p is a slow variable, it should, to leading order, hold constant at the endpoints of the shock ($\mathrm{d}p/\mathrm{d}\xi = 0$ in the singular limit). Hence, we are interested in the speeds c_0 for which the p-value of the trajectory γ^- at u^-, say p_*^-, is the same as the p-value of the trajectory γ^+ at u^+, say p_*^+, see Figure 5.6b. These c-values determine the actual speed of the shock-fronted travelling wave solution.

As the stable and unstable manifolds of $(0, 0)$ and $(1, -c)$ are algebraically too complicated to study analytically, we use numerical tools to detect the speeds leading

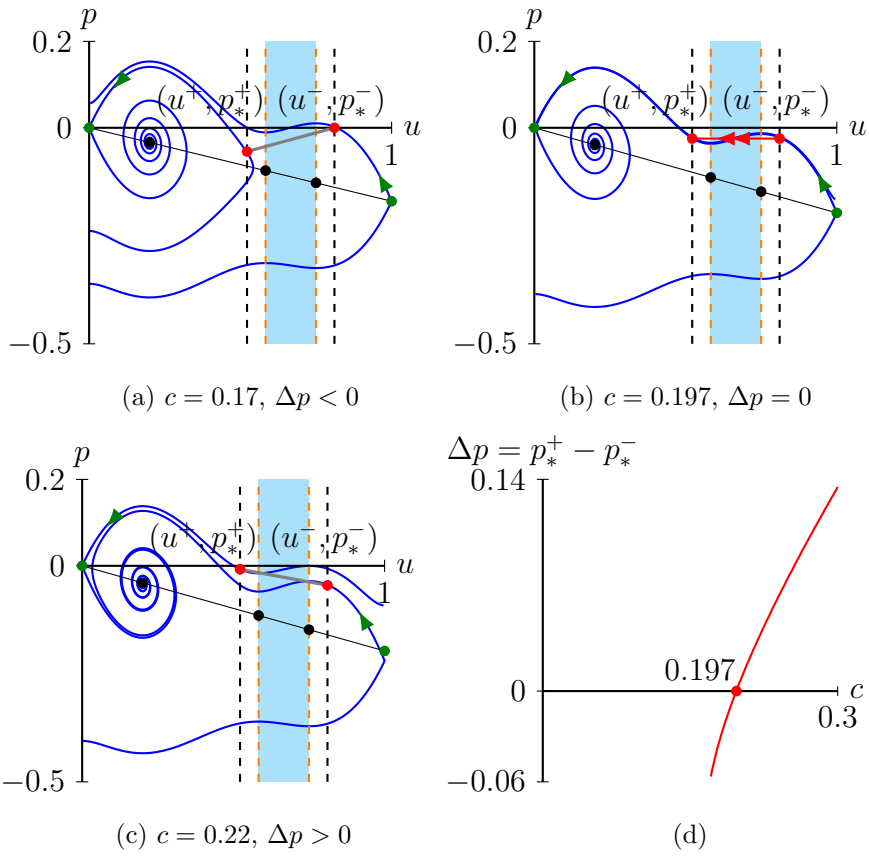

(a) $c = 0.17$, $\Delta p < 0$ (b) $c = 0.197$, $\Delta p = 0$

(c) $c = 0.22$, $\Delta p > 0$ (d)

Figure 5.6: (a) – (c) Phase planes of the desingularised system (5.26) for different values of c with $D(u) = 6(u - 7/12)(u - 3/4)$ and $R(u) = 5u(1 - u)(u - 1/5)$. The green and black dots are fixed points and red points are the endpoints $u^{\pm}$ of the fast jump (as derived from the layer problem). The black solid lines are the nullclines $p = -cu$. The red straight solid line in (b) indicates the shock from (u^-, p_*^-) to (u^+, p_*^+), while the grey straight lines in (a) & (c) cannot lead to shocks as $p_*^+ \neq p_*^-$. With $c = 0.197$, it leads to a feasible desingularised system where $p_*^+ = p_*^-$. (d) The difference $\Delta p = p_*^+ - p_*^-$ as a function of c shows that $\Delta p = 0$ for $c = c_0 \approx 0.197$.

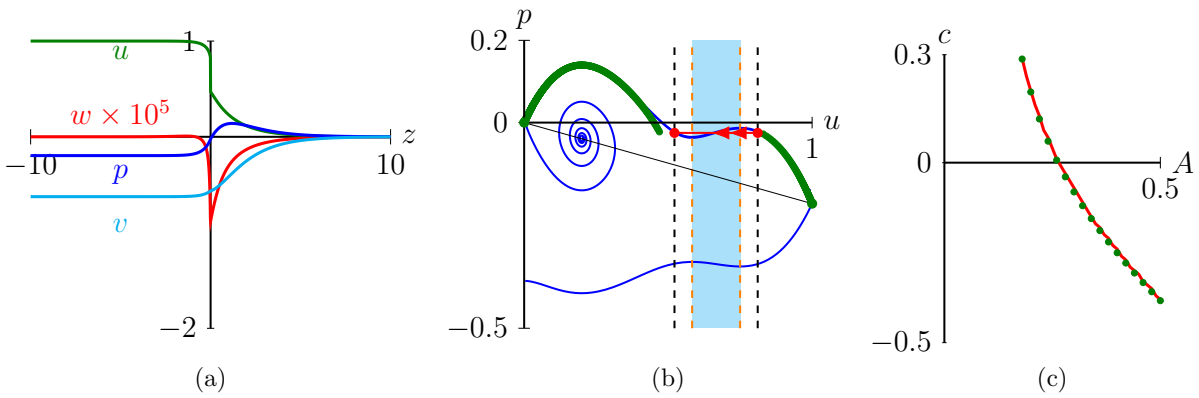

Figure 5.7: The comparison between numerical and analytical results. (a) Numerical simulation of (5.15) with $D(u) = 6(u - 7/12)(u - 3/4)$, $R(u) = 5u(1 - u)(u - 1/5)$ and $\varepsilon = 10^{-5}$ obtained using Matlab ODE solver 'bvp4c'. Boundary conditions are $u(-L) = 1, w(-L) = 0, w(L) = 0, p(-L) = -c, v(L) = -F(0)$ and $q(-L) = -5$ (where $\mathrm{d}q/\mathrm{d}z = u$). The numerically obtained speed is $c = 0.196$, which is close to the analytically obtained speed $c_0 = 0.197$. (b) The numerically obtained (u, p)-trajectory in terms of the stretched variable ψ (green line) superimposed onto the phase plane of the desingularised system (5.26) with $c = c_0 = 0.197$. (c) The numerically (green) and analytically (red) obtained speeds for a varying reaction term of the form $R(U) = 5U(1 - u)(u - A)$ with $A \in (0, 0.5)$.

to a feasible desingularised system (5.26). In particular, we use the function *ode45* in MATLAB to obtain the phase plane of (5.26) and then calculate $\Delta p := p_*^+ - p_*^-$ for different speeds c. Note that we locate the initial points of trajectories approaching $(0, 0)$ or $(1, -c)$ with a small step along their eigenvectors. We find the crossing point of the trajectory leaving from $(1, -c)$ and the straight line $u = u^-$ as (u^-, p_*^-) and the crossing point of the trajectory arriving at $(0, 0)$ and the straight line $u = u^+$ as (u^+, p_*^+). Finally, we calculate Δp as function of c.

As shown in Figure 5.6, for a given prototypical $D(u) = 6(u - 7/12)(u - 3/4)$ and $R(u) = 5u(1 - u)(u - 1/5)$, the difference between two p-values at $u^\pm$ is zero when $c = c_0 \approx 0.197$, that is, the phase plane of (5.26) aligns the endpoints of the shock $u^- \to u^+$ when $c = c_0 \approx 0.197$. Thus, in the singular limit $\varepsilon \to 0$, we expect that (5.10), with the given $D(u)$ and $R(u)$, supports a shock-fronted right-travelling wave solution with speed $c = c_0 \approx 0.197$, see Figure 5.3b.

Due to the complexity of numerically simulating a singularly perturbed fourth-order PDE like (5.10), we simulate solutions of the perturbed ODE system (5.15) with Matlab's ODE solver 'bvp4c' and compare it with our analytical results from the singular limit. With the diffusivity function and reaction term as above, the numerical results and analytical results coincide (to leading order), see Figure 5.7. Furthermore, in Figure 5.7c we compare the numerical and analytical speeds for reaction terms of the form $R(u) = 5u(1-u)(u-A)$ with varying A. Again, the numerical and analytical speeds coincide (to leading order).

5.4.5 Persistence analysis

For $c = c_0$, the orbit in the layer problem connecting u^- to u^+ and the orbits in the reduced problem and desingularised problem connecting 1 to u^- and connecting u^+ to 0 form a complete heteroclinic orbit connecting 1 to 0 in the singular limit $\varepsilon \to 0$. Below we will argue that such solution persists in the four-dimensional system (5.15) for sufficiently small ε, i.e. $0 < \varepsilon \ll 1$. Note that we do not present the full proof for the persistence claim – which follows from geometric singular perturbation theory (GSPT) based on Fenichel's persistence theorems Fenichel (1979); Hek (2010); Jones (1995) since $\mathcal{M}_0^{\pm}$ are normally hyperbolic – because this is rather standard, but quite technical, at this stage. Instead, we provide some heuristic arguments for the persistence.

The endpoints of the heteroclinic orbit in the full system (5.15) are P_ε^0 and P_ε^1 (5.17) and the heteroclinic orbit lies in the intersection of the two-dimensional stable manifold of P_ε^0, $\mathcal{W}^s(P_\varepsilon^0)$, and the two-dimensional unstable manifold of P_ε^1, $\mathcal{W}^u(P_\varepsilon^1)$, see (5.19). This intersection will generically not be transversal since the full system is four-dimensional, i.e. $2 + 2 - 1 < 4$. Therefore, we extend the full system (5.15) to a five-dimensional system by appending it with an equation for the unknown speed $\{c' = 0\}$. That is, we threat c as a variable and not as an unknown parameter. In the extended system the heteroclinic orbit now lies in the intersection of the three-dimensional centre stable manifold $\mathcal{W}^{cs}(P_\varepsilon^0)$ and the three-dimensional centre unstable manifold $\mathcal{W}^u(P_\varepsilon^1)$ and this intersection will generically be transversal since the full system is five-dimensional, i.e. $3 + 3 - 1 = 5$. Typically, transversality follows from a Melnikov-type analysis (Hek 2010; Robinson 1983; Szmolyan 1991). We decided to omit this calculation, but its proof is numerically verified in Figure 5.6(b) and (d). As a result, and for sufficiently small ε, the heteroclinic orbit will persist with a nearby speed $c(\varepsilon)$, with $c(0) = c_0$, the speed found in the singular limit. Finally, recall that such a heteroclinic orbit corresponds to a shock-fronted travelling wave solution of (5.10).

5.5 Viscous relaxation

In this section, we study shock-fronted travelling wave solutions in (5.11) and we use similar mathematical techniques as in Section 5.4 to obtain a three-dimensional singular perturbed slow-fast system. The reduced problem is the same as in Section 5.4, however, it has different algebraic constraints. In contrast, the layer problem is different and only one-dimensional which leads to shocks with different characteristics. Since the methodology of the analysis is similar, we only present a succinct and brief derivation of the main results.

5.5.1 Preliminary observations

The travelling wave solution of (5.11) of interest here is a solution of

$$\frac{\mathrm{d}}{\mathrm{d}z}\left(\varepsilon c\frac{\mathrm{d}^2u}{\mathrm{d}z^2}-cu-\frac{\mathrm{d}}{\mathrm{d}z}(F(u))\right)=R(u), \tag{5.28}$$

that asymptotes to one as $z\to-\infty$ and to zero as $z\to\infty$. Here, $z:=x-ct$ is again the travelling wave coordinate. Next, with some abuse of notation, we define

$$p:=\varepsilon c\frac{\mathrm{d}^2u}{\mathrm{d}z^2}-cu-\frac{\mathrm{d}}{\mathrm{d}z}(F(u)),\quad v:=\varepsilon c\frac{\mathrm{d}u}{\mathrm{d}z}-F(u), \tag{5.29}$$

and transform (5.28) into a three-dimensional singular perturbed slow-fast dynamical system

$$\begin{cases}\varepsilon\dfrac{\mathrm{d}u}{\mathrm{d}z} &= \dfrac{1}{c}(v+F(u)),\\ \dfrac{\mathrm{d}p}{\mathrm{d}z} &= R(u),\\ \dfrac{\mathrm{d}v}{\mathrm{d}z} &= p+cu,\end{cases} \tag{5.30}$$

where $u\in\mathbb{R}$ is fast variable and $(p,v)\in\mathbb{R}^2$ are slow variables. By using a stretched variable $\xi=z/\varepsilon$, (5.30) is transformed into an equivalent fast system, provided $\varepsilon\neq0$,

$$\begin{cases}\dfrac{\mathrm{d}u}{\mathrm{d}\xi} &= \dfrac{1}{c}(v+F(u)),\\ \dfrac{\mathrm{d}p}{\mathrm{d}\xi} &= \varepsilon R(u),\\ \dfrac{\mathrm{d}v}{\mathrm{d}\xi} &= \varepsilon(p+cu).\end{cases} \tag{5.31}$$

The fixed points of the two equivalent systems (5.30) and (5.31) are

$$Q_\varepsilon^0=(0,0,-F(0)),\quad Q_\varepsilon^A=(A,-cA,-F(A)),\quad Q_\varepsilon^1=(1,-c,-F(1)),$$

and we are interested in heteroclinic orbits connecting Q_ε^0 with Q_ε^1. The Jacobian of (5.31) has three eigenvalues with the expansion of ε

$$\begin{aligned}\tau_1^{\pm}(u)&=\frac{-c\pm\sqrt{c^2-4D(u)R'(u)}}{2D(u)}\varepsilon+\mathcal{O}(\varepsilon^2),\\ \tau_2(u)&=\frac{D(u)}{c}+\frac{c}{D(u)}\varepsilon+\mathcal{O}(\varepsilon^2).\end{aligned}$$

At Q_ε^0, $R'(0) < 0$, $D(0) > 0$, thus, $\tau_1^+(0) > 0$, $\tau_1^-(0) < 0$ and $\tau_2(0) > 0$. Similarly, at Q_ε^1, $R'(1) < 0$, $D(1) > 0$, thus, $\tau_1^+(1) > 0$, $\tau_1^-(1) < 0$ and $\tau_2(1) > 0$. That is, the stable manifolds of $Q_\varepsilon^{0,1}$ are one-dimensional and the unstable manifolds of $Q_\varepsilon^{0,1}$ are two-dimensional. At Q_ε^A, for positive speeds, the stable manifold is two-dimensional and the unstable manifold is one-dimensional; for negative speeds, the stable manifold is one-dimensional and the unstable manifold is two-dimensional.

5.5.2 Layer problem

Letting $\varepsilon \to 0$ in (5.31) gives the layer problem

$$\frac{\mathrm{d}u}{\mathrm{d}\xi} = \frac{1}{c}(v + F(u)), \tag{5.32}$$

and $\mathrm{d}p/\mathrm{d}\xi = 0$ and $\mathrm{d}v/\mathrm{d}\xi = 0$. Thus, we have a two-dimensional critical manifold

$$\hat{\mathcal{M}}_0 := \{(u, p, v) \in \mathbb{R}^3 : F(u) = -v\}.$$

Upon recalling that $F'(u) = D(u)$, we observe that the critical manifold loses normal hyperbolicity along the one-dimensional set

$$\hat{\mathcal{F}} := \{(u, p, v) \in \hat{\mathcal{M}}_0 : D(u) = 0\},$$

which has two branches

$$\hat{\mathcal{F}} = \hat{\mathcal{F}}^+ \cup \hat{\mathcal{F}}^- := \{(u, p, v) \in \hat{\mathcal{M}}_0 : u = \alpha\} \cup \{(u, p, v) \in \hat{\mathcal{M}}_0 : u = \beta\}.$$

Thus, we split the critical manifold into five branches $\hat{\mathcal{M}}_0 = \hat{\mathcal{M}}_0^- \cup \hat{\mathcal{F}}^- \cup \hat{\mathcal{M}}_0^0 \cup \hat{\mathcal{F}}^+ \cup \hat{\mathcal{M}}_0^+$, with

$$\hat{\mathcal{M}}_0^+ := \{(u, p, v) \in \mathbb{R}^3 : u < \alpha\}, \quad \hat{\mathcal{M}}_0^- := \{(u, p, v) \in \mathbb{R}^3 : u > \beta\},$$

repelling manifolds for $c > 0$ and attracting manifolds for $c < 0$. Similarly

$$\hat{\mathcal{M}}_0^0 = \{(u, p, v) \in \mathbb{R}^3 : \alpha < u < \beta\},$$

is an attracting manifold for $c > 0$ and an unstable manifold for $c < 0$, see Figure 5.8.

Considering the stability of the different branches of critical manifold, there may exist connections between $\hat{\mathcal{M}}_0^\pm$ and $\hat{\mathcal{M}}_0^0$ and between $\hat{\mathcal{M}}_0^\pm$ and $\hat{\mathcal{F}}^\mp$. In contrast to the previous section, we are now interested in connections between $\hat{\mathcal{M}}_0^\pm$ and $\hat{\mathcal{F}}^\mp$ since we are looking for travelling wave solutions that connect $u = 0$ and $u = 1$, and both of these points are on $\hat{\mathcal{M}}_0^\pm$. There are two ways to establish these connections. If $c > 0$, $\hat{\mathcal{M}}_0^\pm$ are repelling

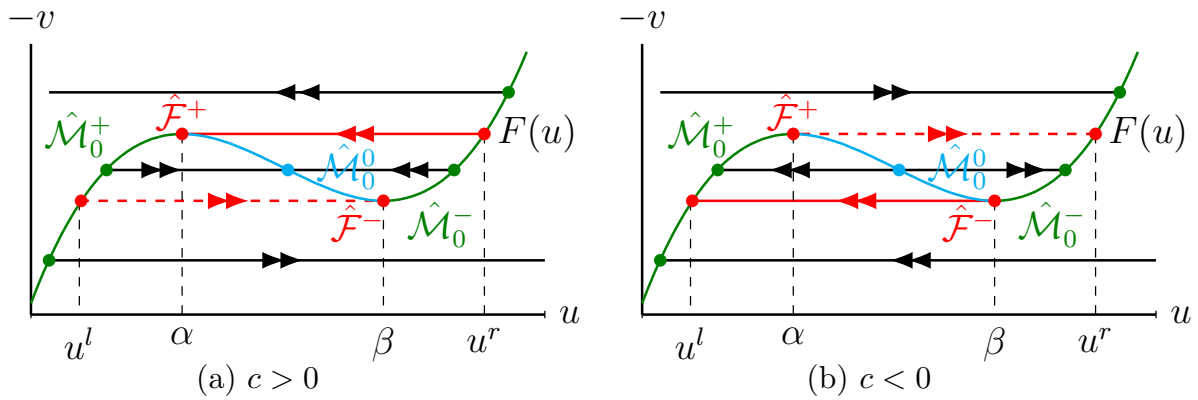

Figure 5.8: (a) Connections from $\hat{\mathcal{M}}_0^{\pm}$ to $\hat{\mathcal{F}}_{\mp}$ for $c > 0$. (b) These connections are reversed for $c < 0$.

and $F(u) = -v$ has two non-repeating real roots β and u^l ($< \alpha$), or $u = \alpha$ and u^r ($> \beta$). In this case, the related shocks are $u^r \to \alpha$ and $u^l \to \beta$, see Figure 5.8a. If $c < 0$, $\hat{\mathcal{M}}_0^{\pm}$ are attracting. and the related shocks are in the opposite direction $\alpha \to u^r$ and $\beta \to u^l$, see Figure 5.8b.

5.5.3 Reduced problem

The reduced problem of (5.30), obtained by letting $\varepsilon \to 0$, is the same as the reduced problem (5.25) of the previous section and is given by

$$\begin{cases} -D(u)\dfrac{\mathrm{d}u}{\mathrm{d}z} &= p + cu, \\ \dfrac{\mathrm{d}p}{\mathrm{d}z} &= R(u). \end{cases}$$

Similarly, its desingularised system[6] is the same and given by

$$\begin{cases} \dfrac{\mathrm{d}u}{\mathrm{d}\psi} &= -p - cu, \\ \dfrac{\mathrm{d}p}{\mathrm{d}\psi} &= D(u)R(u). \end{cases} \tag{5.33}$$

However, note that the slow variable p is defined differently, see (5.14) and (5.29), and thus has a different meaning.

[6] The desingularised system is required this time because we need to study the dynamics around $u = \alpha$ and $u = \beta$ where the reduced problem is singular.

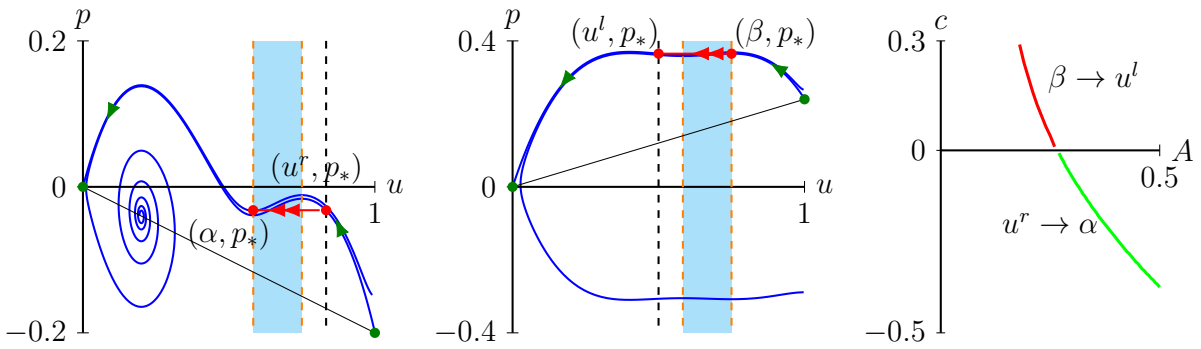

(a) $A = 0.2,\ c = 0.199$ (b) $A = 0.4,\ c = -0.241$ (c)

Figure 5.9: (a) and (b) Phase planes of the desingularised system (5.26) with $D(u) = 6(u - 7/12)(u - 3/4)$ and $R(u) = 5u(1 - u)(u - A)$ with $A = 0.2$ (a) and $A = 0.4$ (b). In the former case, we observe a shock $u^r \to \alpha$ with a positive speed $c = c_0 = 0.199$, while in the latter case we have a shock $\beta \to u^l$ with a negative speed $c = c_0 = -0.241$. (c) The change of speed as function of A where the line with positive speed represents shocks $u^r \to \alpha$ and the line with negative speed represents shocks $\beta \to u^l$. We remark that we could not find an Allee type $R(u)$ for which both types of travelling wave solutions exist simultaneously.

5.5.4 The construction of the heteroclinic orbit in the singular limit

From the analysis of the layer problem (5.32), the shocks $u^r \to \alpha$ and $u^l \to \beta$ have positive speeds, while the shocks in the opposite directions, $\alpha \to u^r$ and $\beta \to u^l$, have negative speed. The shocks $u^r \to \alpha$ and $\beta \to u^l$ potentially relate, in the singular limit, to trajectories of (5.30) leaving from $u = 1$ and arriving at $u = 0$, that is, they have the asymptotic conditions $\lim_{z\to-\infty} u = 1$ and $\lim_{z\to\infty} u = 0$ we are interested in. In contrast, the shocks $u^l \to \beta$ and $\alpha \to u^r$ correspond to trajectories with the opposite asymptotic conditions $\lim_{z\to-\infty} u = 0$ and $\lim_{z\to\infty} u = 1$. Thus, we are interested in positive speeds c for which there exist trajectories of the desingularised system (5.33) that connect $(1, -c)$ with (u^r, p_*) and (α, p_*) with $(0, 0)$ (both in forward ψ). Similarly, we are interested in negative speeds c for which there exist trajectories of the desingularised system (5.33) that connect $(1, -c)$ with (β, p_*) and (u^l, p_*) with $(0, 0)$.

Following the same procedure as in the previous section using *ode45* in MATLAB, we can now construct orbits of the correspond to heteroclinic orbits in the singular limit of (5.30), and thus to shock-fronted travelling wave solutions of (5.11). See Figure 5.9 for two prototypical examples of these orbits. One corresponding to a shock-fronted travelling wave solution with positive speed and one with negative speed.

5.5.5 Persistence analysis

To show that these singular orbits indeed persist for ε sufficient small, and thus correspond to shock-fronted travelling wave solutions of (5.11), we have to proceed in a similar fashion as in the previous section and extend the full three-dimensional system (5.30) with an equation for the speed $\{c' = 0\}$ (since the stable and unstable manifold $\mathcal{W}^{s,u}(Q_\varepsilon^{0,1})$ are respectively one and two-dimensional and $1 + 2 - 1 < 3$) such that transversality is generically possible. Transversality again follows from a Melnikov-type argument, but we have to extend Fenichel theory near the regular fold point $\hat{\mathcal{F}}^{\pm}$, where the critical manifold loses normal hyperbolicity – one of the necessary conditions for Fenichel's persistence theorems. This way, we can show that the orbits persist even though in the singular limit we leave, or arrive at, the critical manifold at a fold point $\hat{\mathcal{F}}^{\pm}$. We decided to not go into the details of this analysis and refer to Beck et al. (2008), and references therein, instead, for an outline how the persistence of these singular orbits can be shown. In the end, this shows the persistence of the heteroclinic orbit for sufficiently small ε and with nearby speed $c(\varepsilon)$, with $c(0) = c_0$, the speed found in the singular limit.

5.6 Conclusion and outlook

In this article, we studied shock-fronted travelling wave solutions supported by the RDE (5.1) with a convex nonlinear diffusivity function $D(U)$ (5.2) that is negative for $U \in (\alpha, \beta)$ (5.3), and with an Allee-type reaction-term $R(U)$ (5.6). This RDE with forward-backward diffusion was previously derived by Johnston et al. (2017) from a lattice-based stochastic model modelling a population of individuals and groups that can undergo movement, birth and death events to describe the its macroscopic behaviour. We studied the RDE by adding two different small regularisations; a non-local regularisation $-\varepsilon^2 \partial^4 U/\partial x^4$, with ε small, see (5.10) and Section 5.4, and a viscous relaxation $\varepsilon \partial^3 U/(\partial x^2 \partial t)$, see (5.11) and Section 5.5. Note that in the singular limit $\varepsilon \to 0$ both PDEs reduce to (5.1).

These two regularisations allowed us to use a dynamical systems approach to study the shock-fronted travelling wave solutions. In particular, for the non-local regularisation the PDE (5.10) could be reduced to a singularly perturbed four-dimensional system of ODEs (5.15). As the regularisation term is assumed to be small there is a scale separation in this system of ODEs. This allowed for a further reduction by investigating (5.15) singular limit in the fast and slow scaling. The singular limit in the fast scaling, called the layer problem (5.20), described the dynamics near the shock of a shock-fronted travelling wave solutions, and was a two-dimensional Hamiltonian system independent of the speed c, see Figure 5.5. The singular limit in the slow scaling, called the reduced problem (5.24), was a singular two-dimensional system of ODEs. It is constraint to the critical manifold $\mathcal{M}_0$

(5.21) and described the dynamics away from the shock. Note that we use MATLAB to investigate the reduced problem as it is algebraically too involved to determine the sought after trajectories. A shock-fronted travelling wave solution can now be constructed, in the singular limit, upon concatenating the three parts of the solution, see Figures 5.4 and 5.6. Subsequently, GSPT can be used to show that the solution persists for sufficiently small ε. Note that the details of this final calculation were omitted, instead it was shown that the dynamics of the full ODE (5.15) agrees with the obtained results in the singular limit, see Figure 5.7.

For the viscous relaxation the PDE (5.10) could be reduced to a singularly perturbed three-dimensional system of ODEs (5.30). Whilst this ODE had the same reduced problem as with the non-local regularisation, it had a different layer problem (5.32). This difference can lead to shock-fronted travelling wave solutions with different characteristics for same nonlinear diffusivity function $D(U)$ (5.2) and reaction-term $R(U)$ (5.6), see Figure 5.10. In addition, as the shock-connection in the layer problem is at a point where the critical manifold loses normal hyperbolicity, GSPT has to be extended to prove the persistence of the singular orbit for sufficiently small ε. Again, details of this computation were omitted.

5.6.1 Regularisations and the lattice-based stochastic model

While the two regularised PDEs have the same singular limit (5.1), the different regularisations yielded shock-fronted travelling wave solutions with different characteristics. Therefore, we mainly compared the singular limit results of the two models with the travelling wave ODE systems, and not with the numerical results of (5.1). The reason for this is that the numerical schemes used to simulate (5.1) naturally introduce artificial regularisation (and error) terms and, as shown in this article, different regularisations yield shock-fronted travelling wave solutions with different characteristics. The connection between the numerical results of (5.1) and the analytical results therefore needs to be further explored.

In addition, (5.1) was derived from a lattice-based stochastic model and during this derivation of the continuous description small higher order terms were omitted. Including some of these small higher order terms would potentially result in a (differently) regularised version of (5.1), which in turn could lead to shock-fronted travelling wave solutions with different properties. Therefore, studying the connection between the lattice-based stochastic models and the regularisations is also an interesting topic.

For instance, a natural question to ask is what happens when we consider a linear combination of the non-local regularisation (considered in Section 5.4) and viscous

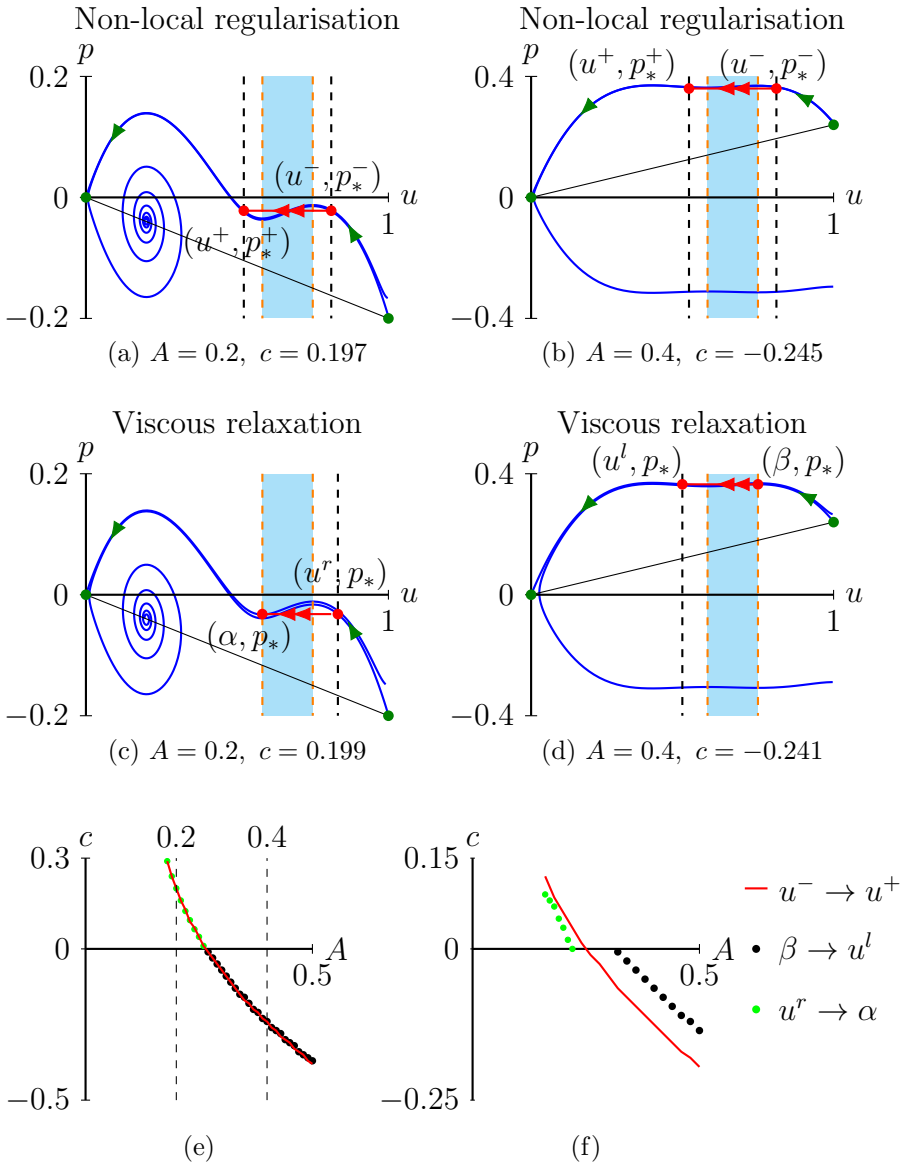

Figure 5.10: (a) – (d) Phase planes of the desingularised system (5.26)/(5.33) with $D(u) = 6(u - 7/12)(u - 3/4)$ and $R(u) = 5u(1 - u)(u - A)$ with $A = 0.2$ (a) & (c) and $A = 0.4$ (b) & (d). For $A = 0.2$ in the non-local regularisation we observe a shock $u^- \to u^+$ for $c = 0.197$, while for $A = 0.2$ in the viscous relaxation we observe a shock $u^r \to \alpha$ for $c = 0.199$. For $A = 0.4$ in the non-local regularisation we observe a shock $u^- \to u^+$ for $c = -0.245$, while for $A = 0.4$ in the viscous relaxation we observe a shock $\beta \to u^l$ for $c = -0.241$. (e) The three different types of shock, $u^- \to u^+$, $u^r \to \alpha$ and $\beta \to u^l$, for changing A from 0 to 0.5. The dashed line $A = 0.2$ relates to (a) & (b) and the dashed line $A = 0.4$ relates to (c) & (d). (f) For a $D(U)$ not centred around 2/3 the differences among the speeds of the shocks is more prevalent. In particular, $D(u) = 6(u - 2/5)(u - 3/4)$.

regularisation (considered in Section 5.5)

$$\frac{\partial U}{\partial t} = \frac{\partial}{\partial x}\left(D(U)\frac{\partial U}{\partial x}\right) + R(U) + (1-\mu)\varepsilon\frac{\partial^3 U}{\partial x^2 \partial t} - \mu\varepsilon^2\frac{\partial^4 U}{\partial x^4},$$

where $\mu \in [0,1]$ is a constant. Note that $\mu = 0$ corresponds to the viscous regularisation (5.11) and $\mu = 1$ corresponds to the non-local regularisation (5.10). The associated four-dimensional slow-fast system[7] is given by

$$\begin{cases} \varepsilon\mu\dfrac{\mathrm{d}u}{\mathrm{d}z} &= (\mu-1)\,cu + w, \\ \varepsilon\dfrac{\mathrm{d}w}{\mathrm{d}z} &= v + F(u), \\ \dfrac{\mathrm{d}p}{\mathrm{d}z} &= R(u), \\ \dfrac{\mathrm{d}v}{\mathrm{d}z} &= p + cu. \end{cases}$$

The corresponding layer problem, for $\mu \neq 0$, is

$$\begin{cases} \dfrac{\mathrm{d}u}{\mathrm{d}\xi} &= \left(1 - \dfrac{1}{\mu}\right)cu + \dfrac{1}{\mu}w, \\ \dfrac{\mathrm{d}w}{\mathrm{d}\xi} &= v + F(u). \end{cases} \tag{5.34}$$

If v is such that (5.34) has three fixed points (u^-, w^-), (u^0, w^0) and (u^+, w^+), where $u^+ < \alpha < u^0 < \beta < u^-$. Then, for $\mu \neq 1$, (5.34) does not have heteroclinic orbits connecting (u^-, w^-) with (u^+, w^+). Hence, we do not expect shock-fronted travelling wave solutions in this case.

5.6.2 Generalisations

In this article, we concentrated on a specific quadratic nonlinear diffusivity function $D(U)$ (5.2) centred around 2/3 and a specific Allee-type reaction-term $R(U)$ (5.6) as these were derived from an underlying lattice-based stochastic model (Johnston et al. 2017). However, the techniques used in this article can in fact be easily extended to more general nonlinear diffusivity functions and reaction terms. For instance, if we change the reaction term from an Allee type (5.6) to a logistic type (5.5) (as studied in Li et al. (2020)), we can still construct the higher-dimensional systems based on the two regularisations (5.10) and (5.11). Since the two layer problems (5.20) and (5.32) only depend on $F(u)$, the anti-derivative of $D(u)$, and not on $R(u)$, we obtain the same conditions for the shocks as for the Allee type reaction term. That is, for the non-local regularisation the shocks

[7] For $\mu = 0$ this slow-fast system is actually three-dimensional and given by (5.30).

will have, to leading order, endpoints u^- and u^+, while the shocks will have, to leading order, endpoints u^r and α or u^l and β for the viscous relaxation. In other words, the size of the shock depends on the relaxation and the nonlinear diffusivity function $D(U)$, but not the reaction term $R(U)$. For both regularisations, the reduced desingularised problem has four fixed points which are determined by the roots of the product of the nonlinear diffusivity function $D(U)$ and the reaction term $R(U)$. In particular, the fixed points are $(0,0)$, $(1,-c)$, $(\alpha,-c\alpha)$ and $(\beta,-c\beta)$. In the desingularised system, the fixed point $(0,0)$ is a stable node or stable spiral for $c>0$ and an unstable node or unstable spiral for $c<0$. For shock-fronted travelling wave solutions with the asymptotic conditions $\lim_{z\to-\infty}U=1$ and $\lim_{z\to\infty}U=0$, we expect $(0,0)$ to be stable in the desingularised problem. Therefore, we expect those travelling wave solutions to have positive speeds. Hence, if the reaction term is logistic, we do not expect shock-fronted travelling wave solutions with negative speeds. However, using other boundary conditions may provide novel characteristics, see El-Hachem et al. (2020); Fadai and Simpson (2020a) for examples of moving boundary problems with logistic type reaction terms.

5.6.3 Stability

Another natural extension of this work is to analyse the stability of the constructed shock-fronted travelling wave solutions. This was partly done for smooth travelling wave solution supported by (5.1) with $D(U)$ as in (5.2) and logistic reaction term $R(U)$ (5.5) in Li et al. (2020). In that article we studied the absolute spectrum of the associated desingularised stability problem and showed that for speeds above the minimal wave speed, the essential spectrum (Kapitula and Promislow 2013; Sandstede 2002) of the desingularised system can always be weighted into the left-half plane, while this is not possible for speeds below the minimal wave speed (Li et al. 2020). This analysis can be repeated for the shock-fronted travelling wave solutions constructed in this article since the essential spectrum is related to the behaviour of the wave at *infinity* and thus only determined by the asymptotic end states of the shock-fronted travelling wave solution under consideration. For brevity we decided not to show this computation and instead refer to Li et al. (2020). In short, the computation shows that the essential spectrum of the associated desingularised stability problems of (5.1), (5.10) and (5.11) are all fully contained in the left-half plane, see Figure 5.11, thus there are no absolute instabilities. However, what remains to be determined is the point spectrum, as well as the connection of the essential spectrum of the associated desingularised stability problem and the original stability problem, to complete the linear stability analysis. This is part of future work, see also the discussion in Li et al. (2020).

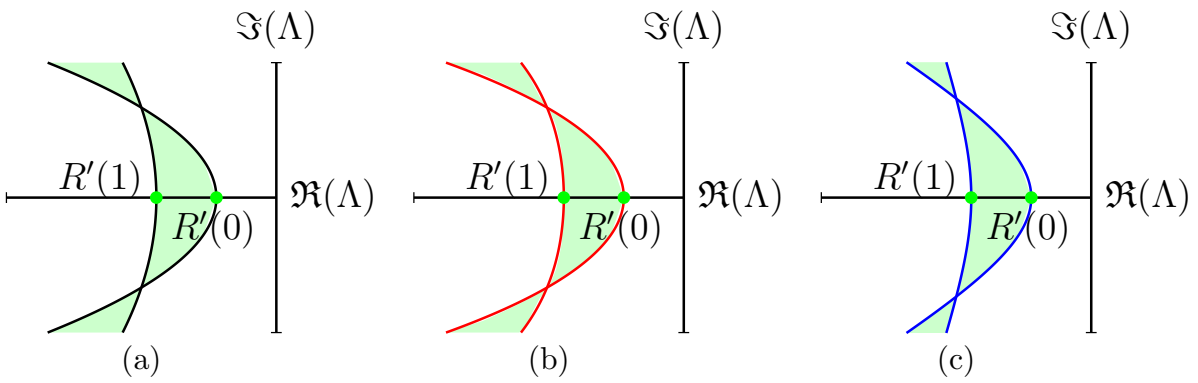

Figure 5.11: The essential spectrums (shaded green regions plus boundaries) of the desingularised stability problems associated to (5.1) (a), (5.10) (b) and (5.11) (c) with $\varepsilon = 0.1$. Note that the essential spectrums are to leading order the same and fully contained in the left-half plane.

5.7 Additional results

5.7.1 Necessary conditions for shock-fronted travelling wave solutions

In this section, we follow Kuzmin and Ruggerini (2011) and derive the two necessary conditions (5.8) and (5.9) for the existence of shock-fronted travelling wave solutions as mentioned in the Introduction. A shock-fronted travelling wave solutions of (5.1) solves the travelling wave ODE

$$c\frac{\mathrm{d}u}{\mathrm{d}z} + \frac{\mathrm{d}}{\mathrm{d}z}\left(D(u)\frac{\mathrm{d}u}{\mathrm{d}z}\right) + R(u) = 0,$$

where $z := x - ct$ is the travelling wave coordinate. Define $g(u) := D(u)\mathrm{d}u/\mathrm{d}z$ in $(0, u_1) \cup (u_2, 1)$, that is, $g(u)$ is defined in the region where the travelling wave solution u is smooth. As we focus on monotonically decreasing travelling wave solutions we have that $g(u) < 0$. The travelling wave ODE can now be written as

$$g(u)\left(\frac{\mathrm{d}(g(u))}{\mathrm{d}u} + c\right) = -R(u)D(u). \tag{5.35}$$

Integrating both sides (5.35) between 0 and $u_a (< u_1)$ gives

$$\int_0^{u_a} g(u)\mathrm{d}g(u) + c\int_0^{u_a} g(u)\mathrm{d}u = -\int_0^{u_a} R(u)D(u)\mathrm{d}u,$$

which leads to

$$c = -\frac{\int_0^{u_a} R(u)D(u)\mathrm{d}u + \frac{1}{2}(g(u_a))^2}{\int_0^{u_a} g(u)\mathrm{d}u}.$$

Thus, for $c < 0$ a necessary condition for the existence of a shock-fronted travelling wave solution is

$$\int_0^{u_a} R(u)D(u)\mathrm{d}u < -\frac{1}{2}(g(u_a))^2 < 0\,.$$

Similarly, integrating (5.35) between $u_b(> u_2)$ and 1 gives

$$c = -\frac{\int_{u_b}^{1} R(u)D(u)\mathrm{d}u - \frac{1}{2}(g(u_b))^2}{\int_{u_b}^{1} g(u)\mathrm{d}u},$$

which, for $c > 0$, leads to the necessary condition

$$\int_{u_b}^{1} R(u)D(u)\mathrm{d}u > \frac{1}{2}(g(u_b))^2 > 0.$$

5.7.2 The heteroclinic orbits of the layer problem

We derive the analytic expressions for the heteroclinic orbits given in the layer problem supported by

$$\begin{cases} \dfrac{\mathrm{d}u}{\mathrm{d}\xi} &= w, \\ \dfrac{\mathrm{d}w}{\mathrm{d}\xi} &= v + F(u), \end{cases}$$

where v is a constant. Based on its Hamiltonian, we require

$$H(u, w) = -\frac{1}{2}w^2 + G(u) + vu = 0,$$

on the heteroclinic orbits $\left(u_h^{0,\pm}, w_h^{0,\pm}\right)$. Subsequently, we obtain

$$w = \pm\sqrt{2\left(G(u) + vu\right)}.$$

Note that $G(u)$ has two integration constants. With specific integration constants, $w(u)$ can become a second-order polynomial with specific roots. That is, we can write w as

$$w(u) = \pm\sqrt{2\left(G(u) + vu\right)} = \pm\sqrt{a^2(u - B_1)^2(u - B_2)^2}.$$

Furthermore, as $w(u^{\pm}) = 0$, we can write w as

$$w(u) = \pm a\left(u - u^{+}\right)\left(u - u^{-}\right),$$

where $a = \sqrt{(D_i - D_g)/2} > 0$. If we assume $w < 0$ in (u^{+}, u^{-}), then we have

$$\frac{\mathrm{d}u}{\mathrm{d}\xi} = a(u - u^{+})(u - u^{-}). \tag{5.36}$$

Deriving the equation (5.36) gives

$$u_h^{0,+}(\xi) = \frac{u^{+} + u^{-}}{2} + \frac{u^{-} - u^{+}}{2}\tanh\left(-\frac{a(u^{-} - u^{+})}{2}\xi\right).$$

Subsequently, we obtain the expression of $w(\xi)$:

$$w_h^{0,+}(\xi) = -\frac{a(u^{-} - u^{+})^2}{4}\mathrm{sech}^2\left(-\frac{a(u^{-} - u^{+})}{2}\xi\right),$$

which satisfies $\lim_{\xi\to\pm\infty} w(\xi) = 0$. Similarly, for the asymptotic conditions $\lim_{\xi\to-\infty} u(\xi) = u^{+}$ and $\lim_{\xi\to\infty} u(\xi) = u^{-}$, we have

$$\frac{\mathrm{d}u}{\mathrm{d}\xi} = -a(u - u^{+})(u - u^{-}). \tag{5.37}$$

Subsequently, solving (5.37) gives the expressions of $u_h^{0,-}(\xi)$ and $w_h^{0,-}(\xi)$:

$$u_h^{0,-}(\xi) = \frac{u^{-} + u^{+}}{2} - \frac{u^{-} - u^{+}}{2}\tanh\left(-\frac{a(u^{-} - u^{+})}{2}\xi\right),$$
$$w_h^{0,-}(\xi) = \frac{a(u^{-} - u^{+})^2}{4}\mathrm{sech}^2\left(-\frac{a(u^{-} - u^{+})}{2}\xi\right).$$

Chapter 6

Conclusions

In this chapter we summarise the results and novel contributions of this work. We then outline possible extensions for further investigation.

6.1 Summary

In this thesis, we explore the influence of nonlinear diffusion on population dynamics in reaction-diffusion models. We pay particular attention to the role of nonlinear diffusion on the survival or extinction of bistable populations, and the role of nonlinear diffusion on the properties of travelling waves.

In Chapter 2 and 3, we construct a novel discrete-continuum modelling framework that connects the behaviour of individuals influenced by crowding effects in a two-dimensional lattice-based model to population dynamics described by reaction-diffusion equations. This framework can be used to study a wide range of macroscopic phenomena including linear diffusion, nonlinear diffusion, as well as logistic growth and strong Allee kinetics. We first consider a simple movement mechanism associated with linear diffusion in Chapter 2, and explore the role of initial shape of spatial distributions on the fate of bistable populations. Both discrete and continuum results indicate that the initial shape of spatial population distributions is a key factor in determining whether a bistable population will survive or go extinct. A bistable population may survive with one initial spatial distribution, and go extinct with another initial spatial distribution. This suggests the importance of considering the influence of spatial arrangements of individuals in studies of population dynamics.

We then consider more complicated movement mechanisms associated with nonlinear diffusion in Chapter 3, and identify whether a given nonlinear diffusivity function will encourage or suppress extinction relative to the classical linear diffusion model. Through the discrete-continuum framework, we build a new relationship between the nonlinear diffusivity function and the movement mechanisms of individuals. This relationship allows

us to explore how the averaged population-level flux of individuals varies with different choices of nonlinear diffusivity functions. Our results show that choices of nonlinear diffusivity function that decrease the flux suppress population extinction relative to the classical linear diffusion model. In contrast, choices of nonlinear diffusivity function that increase the flux encourage population extinction.

In mathematical biology, most continuum models are derived using arguments based on population-level phenomena. While some discrete models incorporate the movement mechanism of individuals into a discrete-continuum framework and derive the well-defined continuum limit equations, the form of nonlinear diffusivity functions is often limited by the particular movement mechanism of individuals (Deroulers et al. 2009; Anguige and Schmeiser 2009; Yates et al. 2015). In contrast, our discrete-continuum framework provides a general form of nonlinear diffusivity function associated with a wide range of movement mechanisms of individuals, as well as a general form of source term associated with a wide range of proliferation and death mechanisms of individuals. Not only can we derive the nonlinear diffusivity function from a particular movement mechanism of individuals, but we can also find the movement mechanism for a given nonlinear diffusivity function. This framework can be applied to study a broad range of population dynamics and to interpret the population-level phenomena based on the individual-level mechanisms.

In Chapter 4 and 5, we develop a geometric approach to study properties of travelling waves in reaction-diffusion models. We consider a reaction-diffusion equation derived from the continuum limit of a one-dimensional lattice-based discrete model, which has a nonlinear diffusivity function that changes signs twice in the domain from zero to carrying capacity density. In Chapter 4, we use a travelling wave coordinate and transform the reaction-diffusion equation into a singular system of ODEs. To remove singularities, we use a stretched variable and transform the original system to a desingularised system. Through analysing the phase plane of the desingularised system, we prove the existence of travelling wave solutions with speeds greater than a minimum wave speed. In addition, we show that travelling wave solutions with speeds smaller than the minimum wave speed are absolutely unstable, which supports the numerical observations.

We then extend the geometric approach to study the characteristics of shock-fronted travelling wave solutions with nonlinear diffusion and strong Allee kinetics in Chapter 5. We studied the reaction-diffusion equation by adding two different small regularisations, so that we can use a dynamical systems approach to study shock-fronted travelling wave solutions. Since the regularisation term is assumed to be small, there is a scale separation in this system. This allows us to investigate singular limits of the system in the fast and slow scaling, so that we can construct the shock-fronted travelling wave solutions by concatenating the dynamics in singular limits. Our analysis and numerical results identify the profile of shocks and the speed of shock-fronted travelling wave solutions. Moreover,

we show that different regularisations yield shock-fronted travelling wave solutions with different characteristics.

Since the reaction-diffusion equation is derived from the continuum limit of a discrete model, the travelling wave solutions intuitively indicate the agent density profiles. As the Fisher-KPP equation also has a minimum wave speed for the existence of smooth travelling wave solutions (Kolmogorov et al. 1937; Fife 2013), our analysis indicates that a discrete mechanism of invasion processes considering the differences in individual and collective behaviours can lead to the similar macroscopic behaviour as the discrete mechanism with no differences in isolated and grouped agents. Unlike the infinite number of smooth travelling wave solutions associated with logistic kinetics, we only find several shock-fronted travelling wave solutions associated with strong Allee kinetics. The characteristics of shock-fronted travelling wave solutions are closely related to the regularisation terms. The geometric approach developed in Chapter 4 and 5 addresses the limitation of the previous method which can not be used to study shock-fronted travelling wave solutions (Ferracuti et al. 2009).

Overall, we explored the role of initial shape of spatial distributions and the role of nonlinear diffusion on the fate of populations. We further studied the existence and stability of travelling wave solutions in reaction-diffusion equations with nonlinear diffusion. Nonlinear diffusion affects population extinction, as well as the properties of travelling waves in reaction-diffusion models. Since we study population dynamics in reaction-diffusion models with a discrete-continuum framework, the influence of nonlinear diffusion in population dynamics is related to the movement mechanism of individuals described by the discrete model. For a bistable population located on a finite domain, the movement mechanism of individuals determines the population-level flux and influences the long-term survival or extinction. For a population that spreads through space with a travelling wave, the movement mechanism of individuals determines the speed and the profile of travelling waves.

6.2 Future work

While the modelling framework presented in this thesis is relatively general and considers various scenarios where nonlinear diffusion plays a crucial role in governing population dynamics, there are many ways that it could be extended. We now discuss these potential extensions.

6.2.1 Exploring the role of various initial conditions on the fate of bistable populations in reaction-diffusion models

In Section 2, we consider several shapes of initial population distributions on a finite $L \times L$ domain with periodic boundary conditions. There are many shapes of initial distributions and other initial conditions which have not been investigated. However, similar numerical explorations of the long-term survival or extinction of populations can be conducted using our discrete-continuum framework. In Section 2.9.7, we show that no-flux boundary conditions lead to the same result as when we consider periodic boundary conditions. Other boundary conditions, such as homogeneous Dirichlet boundary conditions representing the situation where individuals leak through boundaries, may lead to different outcomes relative to periodic boundary conditions and no-flux boundary conditions. Similarly, in Section 3 we only consider a simple one-dimensional vertical strip initial distribution. Nonlinear diffusion may play a different role on the fate of bistable populations if we consider other shapes or boundary conditions. For example, in Section 3.9.5 we consider the well-mixed initial distribution, which leads to the results indicating that nonlinear diffusion plays the same role as linear diffusion on contributing to the eventual survival or extinction of bistable populations. Furthermore, although we have highlighted the influence of dimensionality on the fate of bistable populations in Chapter 2, our discrete simulations are only performed on two-dimensional domains. Considering a three-dimensional population model, which may represent a population of cells in tumour spheroids (Nyga et al. 2011; Kopanska et al. 2016), is an interesting extension for exploring the role of initial spatial arrangements on the fate of bistable populations.

6.2.2 Extending the framework for studying interacting species

Although in this thesis we only consider the situation where individuals in a population follow the same mechanism influenced by crowding effects, the discrete model can be extended to study population dynamics of interacting species (Simpson et al. 2009a). The same averaging approach could be used to derive the continuum limit, which would take the form of a system of coupled partial differential equations (Shigesada et al. 1979; Painter and Sherratt 2003; Hughes et al. 2010; Martínez-García et al. 2020). If the dynamics of subpopulations incorporate strong Allee effects, interactions can also play an important role in determining the eventual survival or extinction of any of the subpopulations (Taylor et al. 2020; Krause and Van Gorder 2020).

6.2.3 Extending the framework for studying biased migration

Another feature of this framework that could be explored is to consider other interesting movement mechanisms. In particular, a directed movement mechanism of individuals could be incorporated to mimic the biased migration of populations (Cai et al. 2006). For example, extracellular signals cause cells to migrate in a biased way towards the source of the attractant (Mason et al. 2001). This would extend our reaction-diffusion models to advection-reaction-diffusion models.

6.2.4 Investigating the influence of stochasticity on population dynamics in the discrete model

In this thesis we use the stochastic discrete model to generate averaged data that matches well with solutions of the continuum model. However, there are additional information of population dynamics in the discrete model that cannot be easily extracted from the continuum model. For example, since the evolution of population in the discrete model is a stochastic process, different identically-prepared realisations may lead to different outcomes. This is different to the continuum equations, which always generate the same result. We estimate the robustness of the stochastic simulations in Section 2.9.8. The result indicates that stochasticity influences the fate of bistable populations when parameters are close to the boundary separating survival and extinction in the continuum model. Therefore, care must be taken when different identically-prepared realisations generate different outcomes as reaction-diffusion equations ignore the influence of stochasticity.

6.2.5 Studying shock-fronted travelling waves in reaction-diffusion equations with other diffusion terms

In Section 4 the discrete model constrains the choices of nonlinear diffusivity functions. However, other choices of nonlinear diffusivity function changing signs twice may lead to shock-fronted travelling wave solutions as shown in Figure 4.10. One possible extension of our work is to analyse shock-fronted travelling wave solutions in reaction-diffusion equations with generic diffusivity functions and logistic kinetics or strong Allee kinetics. We anticipate that the analysis can follow the same geometric approach used in this thesis, since the approach is relatively general in studying travelling wave solutions of reaction-diffusion equations with nonlinear diffusion that changes signs.

6.2.6 Exploring the connection between the discrete model and the regularisations

Since we use truncated Taylor series in the discrete-to-continuum averaging approach to arrive at the continuum limit equation, there are indeed small higher order terms that we ignore in derivations. It is interesting to explore the relationship between the regularisations and the discrete model, so that we can find the shock-fronted travelling waves in the discrete model, and in turn gain insight into the individual-level mechanisms leading to shock-fronted travelling waves. We note that the ignored higher order terms may not have the same form as the two regularisations considered in our thesis, while there could be more feasible regularisations leading to shock-fronted travelling waves. For example, we may expand the choices of regularisations by considering a linear combination of the two regularisations considered in our thesis, as suggested in Section 5.6.1.

6.2.7 Calculating the point spectrum to complete the stability analysis of travelling wave solutions

In this thesis we determine the absolute spectrum for both smooth and shock-fronted travelling wave solutions. The property of absolute stability of travelling wave solutions supports our numerical observations. However, to fully establish the spectral stability of these travelling wave solutions, we need to calculate the point spectrum. The remaining challenge of calculating the point spectrum is to connect a desingularised stability problem to the original stability problem. In our scope of knowledge, there is currently no available method to solve this issue.

6.3 Final remarks

In this thesis, we have explored the influence of nonlinear diffusion on population dynamics in reaction-diffusion models. The discrete-continuum modelling framework suggests that the spatial-temporal population dynamics described by the reaction-diffusion equation relate to the movement, proliferation and death of individuals. The diffusion mechanism of populations relates to the movement of individuals, and the reaction mechanism of populations relates to the proliferation and death of individuals. In particular, nonlinear diffusion reflects how crowding effects influence the movement of individuals. Studying population dynamics in reaction-diffusion models based on the discrete-continuum framework reveals how the behaviour of individuals influence the evolution of populations. This work shows the usefulness of reaction-diffusion models in studying the survival or extinction of populations and biological invasion processes.

Bibliography

[1] Ablowitz, M.J., Zeppetella, A., 1979. Explicit solutions of Fisher's equation for a special wave speed. *Bulletin of Mathematical Biology.* 41, 835–840.

[2] Abramowitz, M., Stegun, I.A., 1964. *Handbook of mathematical functions with formulas, graphs, and mathematical tables.* volume 55. Dover, New York, NY.

[3] Alber, M., Chen, N., Glimm, T., Lushnikov, P.M., 2006. Multiscale dynamics of biological cells with chemotactic interactions: From a discrete stochastic model to a continuous description. *Physical Review E.* 73, 051901.

[4] Alkhayuon, H., Tyson, R.C., Wieczorek, S., 2021. Phase tipping: how cyclic ecosystems respond to contemporary climate. *Proceedings of the Royal Society A: Mathematical, Physical and Engineering Sciences.* 477, 20210059.

[5] Allee, W., Bowen, E.S., 1932. Studies in animal aggregations: Mass protection against colloidal silver among goldfishes. *Journal of Experimental Zoology.* 61, 185–207.

[6] Ames, W.F., 2014. *Numerical methods for partial differential equations.* Academic press, Boston.

[7] Anguige, K., Schmeiser, C., 2009. A one-dimensional model of cell diffusion and aggregation, incorporating volume filling and cell-to-cell adhesion. *Journal of Mathematical Biology.* 58, 395.

[8] Aronson, D.G., 1980. Density-dependent interaction-diffusion systems, in: Dynamics and Modelling of Reactive Systems. Elsevier, pp. 161–176.

[9] Aronson, D.G., Weinberger, H.F., 1978. Multidimensional nonlinear diffusion arising in population genetics. *Advances in Mathematics.* 30, 33–76.

[10] Arroyo-Esquivel, J., Hastings, A., 2020. Spatial dynamics and spread of ecosystem engineers: Two patch analysis. *Bulletin of Mathematical Biology.* 82, 149.

[11] Axelrod, R., Axelrod, D.E., Pienta, K.J., 2006. Evolution of cooperation among tumor cells. *Proceedings of the National Academy of Sciences.* 103, 13474–13479.

[12] Baker, R.E., Simpson, M.J., 2010. Correcting mean-field approximations for birth-death-movement processes. *Physical Review E.* 82.

[13] Barenblatt, G.I., Bertsch, M., Passo, R.D., Ughi, M., 1993. A degenerate pseudoparabolic regularization of a nonlinear forward-backward heat equation arising in the theory of heat and mass exchange in stably stratified turbulent shear flow. *SIAM Journal on Mathematical Analysis.* 24, 1414–1439.

[14] Beck, M., Jones, C.K.R.T., Schaeffer, D., Wechselberger, M., 2008. Electrical waves in a one-dimensional model of cardiac tissue. *SIAM Journal on Applied Dynamical Systems.* 7, 1558–1581.

[15] Benoit, E., 1981. Chasse au canard. *Collectanea Mathematica.* 32, 37–119.

[16] Berger, J., 1990. Persistence of different-sized populations: An empirical assessment of rapid extinctions in bighorn sheep. *Conserv. Biol.* 4, 91–98.

[17] Böttger, K., Hatzikirou, H., Voss-Böhme, A., Cavalcanti-Adam, E.A., Herrero, M.A., Deutsch, A., 2015. An emerging Allee effect is critical for tumor initiation and persistence. *PLoS Computational Biology.* 11, e1004366.

[18] Bradford, E., Philip, J.R., 1970a. Stability of steady distributions of asocial populations dispersing in one dimension. *Journal of Theoretical Biology.* 29, 13–26.

[19] Bradford, E., Philip, J.R., 1970b. Note on asocial populations dispersing in two dimensions. *Journal of Theoretical Biology.* 29, 27–33.

[20] Bramson, M., Calderoni, P., De Masi, A., Ferrari, P., Lebowitz, J., Schonmann, R.H., 1986. Microscopic selection principle for a diffusion-reaction equation. *Journal of Statistical Physics.* 45, 905–920.

[21] Bubba, F., Lorenzi, T., Macfarlane, F.R., 2020. From a discrete model of chemotaxis with volume-filling to a generalized Patlak–Keller–Segel model. *Proceedings of the Royal Society A: Mathematical, Physical and Engineering Sciences.* 476, 20190871.

[22] Buenzli, P.R., Lanaro, M., Wong, C.S., McLaughlin, M.P., Allenby, M.C., Woodruff, M.A., Simpson, M.J., 2020. Cell proliferation and migration explain pore bridging dynamics in 3D printed scaffolds of different pore size. *Acta Biomaterialia.* 114, 285–295.

[23] Cai, A.Q., Landman, K.A., Hughes, B.D., 2006. Modelling directional guidance and motility regulation in cell migration. *Bulletin of Mathematical Biology.* 68, 25.

[24] Cai, A.Q., Landman, K.A., Hughes, B.D., 2007. Multi-scale modeling of a wound-healing cell migration assay. *Journal of Theoretical Biology.* 245, 576–594.

[25] Cantrell, R.S., Cosner, C., 1998. On the effects of spatial heterogeneity on the persistence of interacting species. *Journal of Mathematical Biology.* 37, 103–145.

[26] Cantrell, R.S., Cosner, C., 2004. *Spatial ecology via reaction-diffusion equations.* John Wiley & Sons, New York.

[27] Chaplain, M.A.J., Lorenzi, T., Macfarlane, F.R., 2020. Bridging the gap between individual-based and continuum models of growing cell populations. *Journal of Mathematical Biology.* 80, 343–371.

[28] Chappelle, G., Yates, C.A., 2019. Pulling in models of cell migration. *Physical Review E.* 99, 062413.

[29] Chowdhury, D., Schadschneider, A., Nishinari, K., 2005. Physics of transport and traffic phenomena in biology: From molecular motors and cells to organisms. *Physics of Life Reviews.* 2, 318–352.

[30] Codling, E.A., Plank, M.J., Benhamou, S., 2008. Random walk models in biology. *Journal of the Royal Society Interface.* 5, 813–834.

[31] Courchamp, F., Berec, L., Gascoigne, J., 2008. *Allee effects in ecology and conservation.* Oxford University Press, Oxford.

[32] Courchamp, F., Clutton-Brock, T., Grenfell, B., 1999. Inverse density dependence and the Allee effect. *Trends in Ecology & Evolution.* 14, 405–410.

[33] Davis, P.N., van Heijster, P., Marangell, R., 2017. Absolute instabilities of travelling wave solutions in a Keller–Segel model. *Nonlinearity.* 30, 4029.

[34] Davis, P.N., van Heijster, P., Marangell, R., 2019. Spectral stability of travelling wave solutions in a Keller–Segel model. *Applied Numerical Mathematics.* 141, 54–61.

[35] Deroulers, C., Aubert, M., Badoual, M., Grammaticos, B., 2009. Modeling tumor cell migration: From microscopic to macroscopic models. *Physical Review E.* 79, 031917.

[36] DiCarlo, D.A., Juanes, R., LaForce, T., Witelski, T.P., 2008. Nonmonotonic traveling wave solutions of infiltration into porous media. *Water Resources Research.* 44, W02406.

[37] Doelman, A., van Heijster, P., Kaper, T.J., 2009. Pulse dynamics in a three-component system: Existence analysis. *Journal of Dynamics and Differential Equations.* 21, 73–115.

[38] Drake, J.M., 2004. Allee effects and the risk of biological invasion. *Risk Analysis.* 24, 795–802.

[39] Druckenbrod, N.R., Epstein, M.L., 2005. The pattern of neural crest advance in the cecum and colon. *Developmental Biology.* 287, 125–133.

[40] Druckenbrod, N.R., Epstein, M.L., 2007. Behavior of enteric neural crest-derived cells varies with respect to the migratory wavefront. *Developmental Dynamics.* 236, 84–92.

[41] Ducrot, A., Liu, Z., Magal, P., 2021. Large speed traveling waves for the Rosenzweig–Macarthur predator–prey model with spatial diffusion. *Physica D: Nonlinear Phenomena.* 415, 132730.

[42] Dumortier, F., Roussarie, R., Roussarie, R.H., 1996. *Canard cycles and center manifolds*. volume 577. American Mathematical Society.

[43] Edelstein-Keshet, L., 2005. *Mathematical models in biology.* SIAM, Philadelphia.

[44] El-Hachem, M., McCue, S.W., Jin, W., Du, Y., Simpson, M.J., 2019. Revisiting the fisher–kolmogorov–petrovsky–piskunov equation to interpret the spreading–extinction dichotomy. *Proceedings of the Royal Society A: Mathematical, Physical and Engineering Sciences.* 475, 20190378.

[45] El-Hachem, M., McCue, S.W., Simpson, M.J., 2020. A sharp-front moving boundary model for malignant invasion. *Physica D: Nonlinear Phenomena.* 412, 132639.

[46] Etienne, R., Wertheim, B., Hemerik, L., Schneider, P., Powell, J., 2002. The interaction between dispersal, the Allee effect and scramble competition affects population dynamics. *Ecological Modelling.* 148, 153–168.

[47] Fadai, N.T., Johnston, S.T., Simpson, M.J., 2020. Unpacking the Allee effect: determining individual-level mechanisms that drive global population dynamics. *Proceedings of the Royal Society A: Mathematical, Physical and Engineering Sciences.* 476, 20200350.

[48] Fadai, N.T., Simpson, M.J., 2020a. New travelling wave solutions of the Porous–Fisher model with a moving boundary. *Journal of Physics A: Mathematical and Theoretical.* 53, 095601.

[49] Fadai, N.T., Simpson, M.J., 2020b. Population dynamics with threshold effects give rise to a diverse family of Allee effects. *Bulletin of Mathematical Biology.* 82, 74.

[50] Fenichel, N., 1979. Geometric singular perturbation theory for ordinary differential equations. *Journal of Differential Equations.* 31, 53–98.

[51] Fernando, A.E., Landman, K.A., Simpson, M.J., 2010. Nonlinear diffusion and exclusion processes with contact interactions. *Physical Review E.* 81, 011903.

[52] Ferracuti, L., Marcelli, C., Papalini, F., 2009. Travelling waves in some reaction-diffusion-aggregation models. *Advances in Dynamical Systems and Applications.* 4, 19–33.

[53] Fife, P.C., 1979. Long time behavior of solutions of bistable nonlinear diffusion equationsn. *Archive for Rational Mechanics and Analysis.* 70, 31–36.

[54] Fife, P.C., 2013. *Mathematical aspects of reacting and diffusing systems.* volume 28. Springer, Berlin.

[55] Fife, P.C., McLeod, J.B., 1977. The approach of solutions of nonlinear diffusion equations to travelling front solutions. *Archive for Rational Mechanics and Analysis.* 65, 335–361.

[56] Fisher, R.A., 1937. The wave of advance of advantageous genes. *Annals of Eugenics.* 7, 355–369.

[57] Gerlee, P., Altrock, P.M., Krona, C., Nelander, S., 2021. Autocrine signaling explains the emergence of Allee effects in cancer cell populations. *bioRxiv.* doi:10.1101/2021.07.14.452320.

[58] Grindrod, P., 1991. *The theory and applications of reaction-diffusion equations: Patterns and waves.* Oxford University Press, Oxford.

[59] Hadeler, K.P., Rothe, F., 1975. Travelling fronts in nonlinear diffusion equations. *Journal of Mathematical Biology.* 2, 251–263.

[60] Harley, K., van Heijster, P., Marangell, R., Pettet, G.J., Wechselberger, M., 2014a. Existence of traveling wave solutions for a model of tumor invasion. *SIAM Journal on Applied Dynamical Systems.* 13, 366–396.

[61] Harley, K., van Heijster, P., Marangell, R., Pettet, G.J., Wechselberger, M., 2014b. Novel solutions for a model of wound healing angiogenesis. *Nonlinearity.* 27, 2975.

[62] Harley, K., van Heijster, P., Marangell, R., Pettet, G.J., Wechselberger, M., 2015. Numerical computation of an Evans function for travelling waves. *Mathematical Biosciences.* 266, 36–51.

[63] Hastings, A., Cuddington, K., Davies, K.F., Dugaw, C.J., Elmendorf, S., Freestone, A., Harrison, S., Holland, M., Lambrinos, J., Malvadkar, U., Melbourne, B.A., Moore, K., Taylor, C., Thomson, D., 2005. The spatial spread of invasions: new developments in theory and evidence. *Ecology Letters.* 8, 91–101.

[64] Hek, G., 2010. Geometric singular perturbation theory in biological practice. *Journal of Mathematical Biology.* 60, 347–386.

[65] Holmes, E.E., Lewis, M.A., Banks, J.E., Veit, R.R., 1994. Partial differential equations in ecology: Spatial interactions and population dynamics. *Ecology.* 75, 17–29.

[66] Hughes, B.D., 1995. *Random walks and random environments: random walks.* volume 1. Oxford University Press, Oxford.

[67] Hughes, N.K., Price, C.J., Banks, P.B., 2010. Predators are attracted to the olfactory signals of prey. *PloS One.* 5, 1–4.

[68] Jin, W., Penington, C.J., McCue, S.W., Simpson, M.J., 2016a. Stochastic simulation tools and continuum models for describing two-dimensional collective cell spreading with universal growth functions. *Physical Biology.* 13, 056003.

[69] Jin, W., Shah, E.T., Penington, C.J., McCue, S.W., Chopin, L.K., Simpson, M.J., 2016b. Reproducibility of scratch assays is affected by the initial degree of confluence: Experiments, modelling and model selection. *Journal of Theoretical Biology.* 390, 136–145.

[70] Johnston, S.T., Baker, R.E., McElwain, D.L.S., Simpson, M.J., 2017. Co-operation, competition and crowding: a discrete framework linking Allee kinetics, nonlinear diffusion, shocks and sharp-fronted travelling waves. *Scientific Reports.* 7, 42134.

[71] Johnston, S.T., Simpson, M.J., Baker, R.E., 2012. Mean-field descriptions of collective migration with strong adhesion. *Physical Review E.* 85, 051922.

[72] Johnston, S.T., Simpson, M.J., Crampin, E.J., 2020. Predicting population extinction in lattice-based birth-death-movement models. *Proceedings of the Royal Society A: Mathematical, Physical and Engineering Sciences.* 476, 20200089.

[73] Jones, C.K.R.T., 1995. Geometric singular perturbation theory, in: Dynamical systems: Lectures given at the 2nd session of the Centro Internazionale Matematico Estivo (C.I.M.E.) held in Montecatini Terme, Italy, June 13–22, 1994. Springer, Berlin, pp. 44–118.

[74] Jordan, D.W., Smith, P., 1999. *Nonlinear Ordinary Differential Equations: An Introduction to Dynamical Systems.* volume 2. Oxford University Press, Oxford.

[75] Kapitula, T., Promislow, K., 2013. *Spectral and dynamical stability of nonlinear waves.* Springer, New York.

[76] Khain, E., Katakowski, M., Hopkins, S., Szalad, A., Zheng, X., Jiang, F., Chopp, M., 2011. Collective behavior of brain tumor cells: the role of hypoxia. *Physical Review E.* 83, 031920.

[77] Khain, E., Sander, L.M., Schneider-Mizell, C.M., 2007. The role of cell-cell adhesion in wound healing. *Journal of Statistical Physics.* 128, 209–218.

[78] Kolmogorov, A., Petrovsky, I., Piscounov, N., 1937. Étude de l'équation de la diffusion avec croissance de la quantité de matière et son application à un problème biologique. *Moscow University Mathematics Bulletin.* 1, 1–25.

[79] Kopanska, K.S., Alcheikh, Y., Staneva, R., Vignjevic, D., Betz, T., 2016. Tensile forces originating from cancer spheroids facilitate tumor invasion. *PloS One.* 11, 1–23.

[80] Korolev, K.S., Xavier, J.B., Gore, J., 2014. Turning ecology and evolution against cancer. *Nature Reviews Cancer.* 14, 371–380.

[81] Kot, M., 2001. *Elements of mathematical ecology.* Cambridge University Press, Cambridge.

[82] Kot, M., Lewis, M.A., van den Driessche, P., 1996. Dispersal data and the spread of invading organisms. *Ecology.* 77, 2027–2042.

[83] Krause, A.L., Van Gorder, R.A., 2020. A non-local cross-diffusion model of population dynamics II: Exact, approximate, and numerical traveling waves in single- and multi-species populations. *Bulletin of Mathematical Biology.* 82, 113.

[84] Kuzmin, M., Ruggerini, S., 2011. Front propagation in diffusion-aggregation models with bi-stable reaction. *Discrete & Continuous Dynamical Systems-B.* 16, 819–833.

[85] Kéfi, S., Rietkerk, M., Roy, M., Franc, A., de Ruiter, P.C., Pascual, M., 2011. Robust scaling in ecosystems and the meltdown of patch size distributions before extinction. *Ecology Letters.* 14, 29–35.

[86] Landman, K.A., White, L.R., 2011. Terraced spreading of nanofilms under a nonmonotonic disjoining pressure. *Physics of Fluids.* 23, 012004.

[87] Larson, D.A., 1978. Transient bounds and time-asymptotic behavior of solutions to nonlinear equations of Fisher type. *SIAM Journal on Applied Mathematics.* 34, 93–104.

[88] Lee, Y., McIntire, L.V., Zygourakis, K., 1994. Analysis of endothelial cell locomotion: Differential effects of motility and contact inhibition. *Biotechnology and Bioengineering.* 43, 622–634.

[89] Lee, Y.H., Sherbakov, L., Taber, J., Shi, J., 2006. Bifurcation diagrams of population models with nonlinear, diffusion. *Journal of Computational and Applied Mathematics.* 194, 357–367.

[90] Lewis, M.A., Kareiva, P., 1993. Allee dynamics and the spread of invading organisms. *Theoretical Population Biology.* 43, 141–158.

[91] Lewis, M.A., Petrovskii, S.V., Potts, J.R., 2016. *The mathematics behind biological invasions.* volume 44. Springer, Berlin.

[92] Li, Y., van Heijster, P., Marangell, R., Simpson, M.J., 2020. Travelling wave solutions in a negative nonlinear diffusion–reaction model. *Journal of Mathematical Biology.* 81, 1495–1522.

[93] Li, Y., van Heijster, P., Simpson, M.J., Wechselberger, M., 2021. Shock-fronted travelling waves in a reaction–diffusion model with nonlinear forward–backward–forward diffusion. *Physica D: Nonlinear Phenomena.* 423, 132916.

[94] Li, Y., Johnston, S.T., Buenzli, P.R., van Heijster, P., Simpson, M.J., 2022. Extinction of bistable populations is affected by the shape of their initial spatial distribution. *Bulletin of Mathematical Biology.* 84, 21.

[95] Liggett, T.M., 2013. *Stochastic interacting systems: contact, voter and exclusion processes.* volume 324. Springer, Berlin.

[96] Liggett, T.M., Liggett, T.M., 1985. *Interacting particle systems.* volume 2. Springer, Berlin.

[97] Lushnikov, P.M., Chen, N., Alber, M., 2008. Macroscopic dynamics of biological cells interacting via chemotaxis and direct contact. *Physical Review E.* 78, 061904.

[98] Lutscher, F., 2019. *Integrodifference equations in spatial ecology.* Springer, Berlin.

[99] Lutscher, F., Nisbet, R.M., Pachepsky, E., 2010. Population persistence in the face of advection. *Theoretical Ecology.* 3, 271–284.

[100] Macfarlane, F.R., Lorenzi, T., Chaplain, M.A.J., 2018. Modelling the immune response to cancer: an individual-based approach accounting for the difference in movement between inactive and activated T cells. *Bulletin of Mathematical Biology.* 80, 1539–1562.

[101] Maciel, G.A., Lutscher, F., 2015. Allee effects and population spread in patchy landscapes. *Journal of Biological Dynamics.* 9, 109–123.

[102] Mack, R.N., Simberloff, D., Mark Lonsdale, W., Evans, H., Clout, M., Bazzaz, F.A., 2000. Biotic invasions: Causes, epidemiology, global consequences, and control. *Ecological Applications.* 10, 689–710.

[103] Maini, P.K., Malaguti, L., Marcelli, C., Matucci, S., 2006. Diffusion-aggregation processes with mono-stable reaction terms. *Discrete and Continuous Dynamical Systems Series B.* 6, 1175–1189.

[104] Maini, P.K., Malaguti, L., Marcelli, C., Matucci, S., 2007. Aggregative movement and front propagation for bi-stable population models. *Mathematical Models and Methods in Applied Sciences.* 17, 1351–1368.

[105] Maini, P.K., McElwain, D.L.S., Leavesley, D., 2004a. Traveling wave model to interpret a wound-healing cell migration assay for human peritoneal mesothelial cells. *Tissue Engineering.* 10, 475–482.

[106] Maini, P.K., McElwain, D.L.S., Leavesley, D., 2004b. Travelling waves in a wound healing assay. *Applied Mathematics Letters.* 17, 575–580.

[107] Malaguti, L., Marcelli, C., 2003. Sharp profiles in degenerate and doubly degenerate Fisher-Kpp equations. *Journal of Differential Equations.* 195, 471–496.

[108] Malfliet, W., 1992. Solitary wave solutions of nonlinear wave equations. *American Journal of Physics.* 60, 650–654.

[109] Martínez-García, R., Fleming, C.H., Seppelt, R., Fagan, W.F., Calabrese, J.M., 2020. How range residency and long-range perception change encounter rates. *Journal of Theoretical Biology.* 498, 110267.

[110] Martínez-García, R., Murgui, C., Hernández-García, E., López, C., 2015. Pattern formation in populations with density-dependent movement and two interaction scales. *PLoS One.* 10, 1–14.

[111] Mason, H.A., Ito, S., Corfas, G., 2001. Extracellular signals that regulate the tangential migration of olfactory bulb neuronal precursors: Inducers, inhibitors, and repellents. *Journal of Neuroscience.* 21, 7654–7663.

[112] MATLAB, 2020. ode45 documentation. url: `https://www.mathworks.com/help/matlab/ref/ode45.html`.

[113] McCue, S.W., El-Hachem, M., Simpson, M.J., 2021. Exact sharp-fronted travelling wave solutions of the Fisher–KPP equation. *Applied Mathematics Letters.* 114, 106918.

[114] McCue, S.W., Jin, W., Moroney, T.J., Lo K-Y, Chou S-E, Simpson, M.J., 2019. Hole-closing model reveals exponents for nonlinear degenerate diffusivity functions in cell biology. *Physica D: Nonlinear Phenomena.* 398, 130–140.

[115] Murray, J.D., 1989. *Mathematical biology.* Springer, New York.

[116] Neufeld, Z., von Witt, W., Lakatos, D., Wang, J., Hegedus, B., Czirok, A., 2017. The role of Allee effect in modelling post resection recurrence of glioblastoma. *PLoS Computational Biology.* 13, e1005818.

[117] Novick-Cohen, A., Pego, R.L., 1991. Stable patterns in a viscous diffusion equation. *Transactions of the American Mathematical Society.* 324, 331–351.

[118] Nyga, A., Cheema, U., Loizidou, M., 2011. 3D tumour models: novel in vitro approaches to cancer studies. *Journal of Cell Communication and Signaling.* 5, 239.

[119] Ovaskainen, O., Meerson, B., 2010. Stochastic models of population extinction. *Trends in Ecology & Evolution.* 25, 643–652.

[120] Padrón, V., 2004. Effect of aggregation on population recovery modeled by a forward-backward pseudoparabolic equation. *Transactions of the American Mathematical Society.* 356, 2739–2756.

[121] Painter, K.J., Sherratt, J.A., 2003. Modelling the movement of interacting cell populations. *Journal of Theoretical Biology.* 225, 327–339.

[122] Pego, R.L., Penrose, O., 1989. Front migration in the nonlinear Cahn-Hilliard equation. *Proceedings of the Royal Society A: Mathematical, Physical and Engineering Sciences.* 422, 261–278.

[123] Petrovskii, S., Shigesada, N., 2001. Some exact solutions of a generalized Fisher equation related to the problem of biological invasion. *Mathematical Biosciences.* 172, 73–94.

[124] Pettet, G.J., McElwain, D.L.S., Norbury, J., 2000. Lotka-Volterra equations with chemotaxis: Walls, barriers and travelling waves. *Mathematical Medicine and Biology: A Journal of the IMA.* 17, 395–413.

[125] Poujade, M., Grasland-Mongrain, E., Hertzog, A., Jouanneau, J., Chavrier, P., Ladoux, B., Buguin, A., Silberzan, P., 2007. Collective migration of an epithelial monolayer in response to a model wound. *Proceedings of the National Academy of Sciences.* 104, 15988–15993.

[126] Robinson, C., 1983. Sustained resonance for a nonlinear system with slowly varying coefficients. *SIAM Journal on Mathematical Analysis.* 14, 847–860.

[127] van Saarloos, W., 2003. Front propagation into unstable states. *Physics Reports.* 386, 29–222.

[128] Saltz, D., Rubenstein, D.I., 1995. Population dynamics of a reintroduced asiatic wild ass (*Equus hemionus*) herd. *Ecological Applications.* 5, 327–335.

[129] Sánchez-Garduño, F., Maini, P.K., 1994. Existence and uniqueness of a sharp travelling wave in degenerate non-linear diffusion Fisher-Kpp equations. *Journal of Mathematical Biology.* 33, 163–192.

[130] Sandstede, B., 2002. Stability of travelling waves, in: Handbook of dynamical systems. Elsevier. volume 2, pp. 983–1055.

[131] Sarapata, E.A., de Pillis, L.G., 2014. A comparison and catalog of intrinsic tumor growth models. *Bulletin of Mathematical Biology.* 76, 2010–2024.

[132] Sattinger, D., 1977. Weighted norms for the stability of traveling waves. *Journal of Differential Equations.* 25, 130–144.

[133] Sengers, B.G., Please, C.P., Oreffo, R.O., 2007. Experimental characterization and computational modelling of two-dimensional cell spreading for skeletal regeneration. *Journal of the Royal Society Interface.* 4, 1107–1117.

[134] Sewalt, L., Harley, K., van Heijster, P., Balasuriya, S., 2016. Influences of allee effects in the spreading of malignant tumours. *Journal of Theoretical Biology.* 394, 77–92.

[135] Sherratt, J.A., Dagbovie, A.S., Hilker, F.M., 2014. A mathematical biologist's guide to absolute and convective instability. *Bulletin of Mathematical Biology.* 76, 1–26.

[136] Sherratt, J.A., Murray, J.D., 1990. Models of epidermal wound healing. *Proceedings of the Royal Society B: Biological Sciences.* 241, 29–36.

[137] Shigesada, N., 1980. Spatial distribution of dispersing animals. *Journal of Mathematical Biology.* 9, 85–96.

[138] Shigesada, N., Kawasaki, K., Teramoto, E., 1979. Spatial segregation of interacting species. *Journal of Theoretical Biology.* 79, 83–99.

[139] Simpson, M.J., 2009. Depth-averaging errors in reactive transport modeling. *Water Resources Research.* 45, W02505.

[140] Simpson, M.J., Baker, R.E., McCue, S.W., 2011. Models of collective cell spreading with variable cell aspect ratio: a motivation for degenerate diffusion models. *Physical Review E.* 83, 021901.

[141] Simpson, M.J., Haridas, P., McElwain, D.L.S., 2014. Do pioneer cells exist? *PLoS One.* 9, e85488.

[142] Simpson, M.J., Landman, K.A., Hughes, B.D., 2009a. Multi-species simple exclusion processes. *Physica A: Statistical Mechanics and its Applications.* 388, 399–406.

[143] Simpson, M.J., Landman, K.A., Hughes, B.D., 2009b. Pathlines in exclusion processes. *Physical Review E.* 79, 031920.

[144] Simpson, M.J., Landman, K.A., Hughes, B.D., 2010a. Cell invasion with proliferation mechanisms motivated by time-lapse data. *Physica A: Statistical Mechanics and its Applications.* 389, 3779–3790.

[145] Simpson, M.J., Landman, K.A., Hughes, B.D., Fernando, A.E., 2010b. A model for mesoscale patterns in motile populations. *Physica A: Statistical Mechanics and its Applications.* 389, 1412–1424.

[146] Simpson, M.J., Towne, C., McElwain, D.L.S., Upton, Z., 2010c. Migration of breast cancer cells: Understanding the roles of volume exclusion and cell-to-cell adhesion. *Physical Review E.* 82, 041901.

[147] Skellam, J.G., 1951. Random dispersal in theoretical populations. *Biometrika.* 38, 196–218.

[148] Soboleva, T.K., Shorten, P.R., Pleasants, A.B., Rae, A.L., 2003. Qualitative theory of the spread of a new gene into a resident population. *Ecological Modelling.* 163, 33–44.

[149] Stephens, P.A., Sutherland, W.J., Freckleton, R.P., 1999. What is the Allee effect? *Oikos.* 87, 185–190.

[150] Surendran, A., Plank, M.J., Simpson, M.J., 2020. Population dynamics with spatial structure and an Allee effect. *Proceedings of the Royal Society A: Mathematical, Physical and Engineering Sciences.* 476, 20200501.

[151] Szmolyan, P., 1991. Transversal heteroclinic and homoclinic orbits in singular perturbation problems. *Journal of Differential Equations.* 92, 252–281.

[152] Szmolyan, P., Wechselberger, M., 2001. Canards in $\mathbb{R}^3$. *Journal of Differential Equations.* 177, 419–453.

[153] Taylor, C.M., Hastings, A., 2005. Allee effects in biological invasions. *Ecology Letters.* 8, 895–908.

[154] Taylor, N.P., Kim, H., Krause, A.L., Van Gorder, R.A., 2020. A non-local cross-diffusion model of population dynamics I: Emergent spatial and spatiotemporal patterns. *Bulletin of Mathematical Biology.* 82, 112.

[155] Treloar, K.K., Simpson, M.J., McElwain, D.L.S., Baker, R.E., 2014. Are in vitro estimates of cell diffusivity and cell proliferation rate sensitive to assay geometry? *Journal of Theoretical Biology.* 356, 71–84.

[156] Tremel, A., Cai, A., Tirtaatmadja, N., Hughes, B., Stevens, G., Landman, K., O'Connor, A., 2009. Cell migration and proliferation during monolayer formation and wound healing. *Chemical Engineering Science.* 64, 247–253.

[157] Turner, S., Sherratt, J.A., Painter, K.J., Savill, N.J., 2004. From a discrete to a continuous model of biological cell movement. *Physical Review E.* 69, 021910.

[158] Volpert, A.I., Volpert, V.A., Volpert, V.A., 1994. *Traveling wave solutions of parabolic systems.* volume 140. American Mathematical Society, Providence.

[159] Vortkamp, I., Schreiber, S.J., Hastings, A., Hilker, F.M., 2020. Multiple attractors and long transients in spatially structured populations with an Allee effect. *Bulletin of Mathematical Biology.* 82, 82.

[160] Wang, Y., Shi, J., Wang, J., 2019. Persistence and extinction of population in reaction–diffusion–advection model with strong Allee effect growth. *Journal of mathematical biology.* 78, 2093–2140.

[161] Wechselberger, M., 2012. À propos de canards (Apropos canards). *Transactions of the American Mathematical Society.* 364, 3289–3309.

[162] Wechselberger, M., Pettet, G.J., 2010. Folds, canards and shocks in advection–reaction–diffusion models. *Nonlinearity.* 23, 1949.

[163] West, J., Hasnain, Z., Macklin, P., Newton, P.K., 2016. An evolutionary model of tumor cell kinetics and the emergence of molecular heterogeneity driving gompertzian growth. *SIAM Review.* 58, 716–736.

[164] Witelski, T.P., 1994. An asymptotic solution for traveling waves of a nonlinear-diffusion Fisher's equation. *Journal of Mathematical Biology.* 33, 1–16.

[165] Witelski, T.P., 1995a. Merging traveling waves for the Porous-Fisher's equation. *Applied Mathematics Letters.* 8, 57–62.

[166] Witelski, T.P., 1995b. Shocks in nonlinear diffusion. *Applied Mathematics Letters.* 8, 27–32.

[167] Witelski, T.P., 1996. The structure of internal layers for unstable nonlinear diffusion equations. *Studies in Applied Mathematics.* 97, 277–300.

[168] Yates, C.A., Parker, A., Baker, R.E., 2015. Incorporating pushing in exclusion-process models of cell migration. *Physical Review E.* 91, 052711.

[169] Zhang, S., Chong, A., Hughes, B.D., 2019. Persistent exclusion processes: Inertia, drift, mixing, and correlation. *Physical Review E.* 100, 042415.